I) De l'optique quantique aux condensats de Bose-Einstein II) Contribution à l'étude du pompage optique de l'hélium 3 pour des applications médicales

Alice Sinatra

▶ **To cite this version:**

Alice Sinatra. I) De l'optique quantique aux condensats de Bose-Einstein II) Contribution à l'étude du pompage optique de l'hélium 3 pour des applications médicales. Physique Atomique [physics.atom-ph]. Université Pierre et Marie Curie - Paris VI, 2006. tel-00117282

HAL Id: tel-00117282
https://theses.hal.science/tel-00117282

Submitted on 30 Nov 2006

HAL is a multi-disciplinary open access archive for the deposit and dissemination of scientific research documents, whether they are published or not. The documents may come from teaching and research institutions in France or abroad, or from public or private research centers.

L'archive ouverte pluridisciplinaire **HAL**, est destinée au dépôt et à la diffusion de documents scientifiques de niveau recherche, publiés ou non, émanant des établissements d'enseignement et de recherche français ou étrangers, des laboratoires publics ou privés.

DÉPARTEMENT DE PHYSIQUE
DE L'ÉCOLE NORMALE SUPÉRIEURE

LABORATOIRE KASTLER BROSSEL

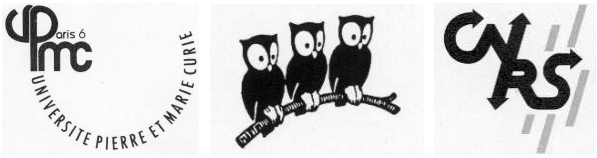

HABILITATION À DIRIGER LES RECHERCHES DE L'UNIVERSITÉ PARIS VI

présentée par

Alice SINATRA

I
DE L'OPTIQUE QUANTIQUE AUX CONDENSATS DE BOSE-EINSTEIN

II
CONTRIBUTION A L'ÉTUDE DU POMPAGE OPTIQUE DE L'HÉLIUM 3 POUR DES APPLICATIONS MÉDICALES

soutenue le 17 mai 2006 devant le jury composé de :

M. Ennio Arimondo	Rapporteur
M. Mikhail Kolobov	Rapporteur
M. Franck Laloë	
Mme Claire Lhuillier	
M. Klaus Mølmer	Rapporteur
M. Christophe Salomon	

Table des matières

Chapitre 1

Structure du mémoire

J'ai divisé la matière de mon mémoire en trois chapitres : un chapitre sur les travaux d'optique quantique, un chapitre sur les gaz dégénérés et un chapitre sur le pompage optique de l'hélium 3. Dans chaque chapitre il y a un petit paragraphe introductif, suivi de différents paragraphes correspondant aux différents travaux que je veux décrire. J'ai essayé de résumer les points importants de chaque travail et de le situer par rapport aux travaux existants et par rapport à mon parcours scientifique. La où j'ai voulu donner plus de détails, j'ai inclus une ou plusieurs publications.

Chapitre 2

Parcours scientifique et personnel

Que ça soit pour étudier et manipuler les propriétés quantiques de la lumière comme on le fait en optique quantique, ou celles de la matière à l'aide de gaz dégénérés, ou encore dans un régime classique à des fins d'applications médicales, j'ai étudié des systèmes de physique atomique simples, constitués d'atomes, éventuellement en interaction entre eux ou avec de la radiation électromagnétique. Tout en ayant débuté dans un groupe purement théorique, j'ai souvent travaillé en connextion étroite avec des expériences jusqu'à m'y impliquer d'abord pour les atomes froids, puis pour l'hélium polarisé.

J'ai débuté mon travail de recherche dans le groupe de Luigi Lugiato à Milan en étudiant des modèles théoriques pour la production d'états comprimés de la lumière. Lugiato collaborait avec Philippe Grangier de l'Institut d'Optique d'Orsay qui menait à l'époque des expériences de compression de bruit et de mesures quantiques non destructives (QND) avec des atomes froids. L'expérience QND d'Orsay m'a tout suite intriguée. J'ai donc modélisé cette expérience pour pouvoir à la fois comparer les résultats aux prédictions théoriques et pour pouvoir guider l'expérience vers les conditions de fonctionnement optimales dans un espace de paramètres *a priori* vaste. Cette opération a été un indiscutable succès. Les mesures QND de Grangier étaient alors les meilleures effectuées sur des variables continues, et l'accord entre théorie et expérience remarquable.

La possibilité de prédire précisément les résultats d'une expérience avec une théorie microscopique (interaction champ-matière et équation pilote) m'a passionnée et m'a convertie à la physique atomique. Comme les mesures QND n'avaient pas été traitées auparavant dans le groupe de Lugiato, j'ai mis au point ma propre méthode (bien qu'il existe d'autres méthodes équivalentes) pour le calcul des coefficients destinés à caractériser une mesure QND non idéale. Le reste de ma recherche s'est effectuée au Laboratoire Kastler Brossel. Je suis rentrée en contact avec l'équipe Atomes Froids du LKB grâce à un ancien membre du groupe de Grangier, Jean-François Roch, et j'ai pu travailler dans cette équipe de haut niveau grâce à quelques mois de salaire pris sur un réseau européen de Jean Dalibard, puis une Bourse Marie Curie Individuelle, puis un poste temporaire de Maître de Conférence au Collège de France attaché à la chaire de Claude Cohen-Tannoudji. En 1997, lors de mon arrivée, il y avait une grande excitation autour des atomes froids ; le premier condensat réalisé à l'École Normale, puis le Prix Nobel de Claude Cohen-Tannoudji y contribuaient. J'ai travaillé pendant à peu près deux ans dans le groupe de théorie d'Yvan Castin qui devait ensuite devenir mon mari. Les sujets que j'ai attaqués étaient relativement proches de l'optique quantique. D'abord les effets des pertes de particules sur les résurgences de la phase relative entre deux condensats (particulièrement intéressant pour qui veut créer des chat de Schrödinger avec des condensats) puis la dynamique de phase (et la dynamique spatiale) d'un condensat à deux composantes. Des expériences étaient alors en cours dans le groupe d'Eric Cornell avec lequel nous avons pu interagir. Bien que nos calcules aient

pu assez bien reproduire la dynamique spatiale des condensats (séparation des deux composantes et amortissement des oscillations), avec notre théorie à température nulle nous n'étions pas parvenus à expliquer les relativement courts temps de cohérence de phase observés par Eric Cornell. Entre temps, j'avais pris goût aux systèmes d'atomes dégénérés et à la physique plus riche des systèmes multimodes. J'ai donc attaqué un nouveau projet pour décrire la dynamique des condensats à température non nulle. Avec Yvan Castin, nous avons proposé et montré la viabilité de l'utilisation de la fonction de Wigner pour décrire le champ atomique à température non nulle, mais initialement assez faible pour que le gaz soit bien décrit dans l'approximation de Bogoliubov. L'idée de pouvoir appliquer cette méthode aux différentes situations physiques rencontrées dans les expériences était très excitante et avait suscité un certain intérêt dans la communauté. L'excitation passée, une analyse approfondie nous a permis d'en quantifier les limites et les avantages par rapport à d'autres méthodes. À la fin de ma bourse post-doctorale, j'avais décidé de m'installer en France. Claude Cohen-Tannoudji et Michèle Leduc m'ont proposé de travailler sur leur expérience de refroidissement et piègeage d'atomes d'hélium métastable en vue de l'obtention d'un condensat de Bose-Einstein. Grâce à Christophe Salomon qui m'avait accueillie en stage dans son équipe "lithium" pendant ma bourse Marie Curie, ce n'était pas ma "première" expérimentale. Je me suis occupée d'informatiser l'expérience puis, avec les autres doctorants et visiteurs post-doc, du système d'imagerie et de l'optimisation du piège magnéto-optique. Il était important de comprendre les facteurs limitant la densité dans notre piège, dont les collisions autoionisantes de Penning que j'aurai rencontrées aussi plus tard dans ma carrière. En 2000, je candidate sur différents postes permanents de chercheur et d'enseignant chercheur à Paris. J'obtiens un poste de maître de conférence à Paris VI pour travailler dans l'équipe de Pierre-Jean Nacher à l'École Normale avec un projet de recherche :"Imagerie médicale par résonance magnétique utilisant des gaz rares polarisés". Voila un tournant dans ma vie. Je vais enfin faire quelque chose de directement utile. L'idée de Pierre-Jean était d'effectuer le pompage optique dans un champ magnétique fort pour pouvoir supprimer certains canaux de relaxation de la polarisation nucléaire et arriver à polariser l'hélium par échange de métastabilité à une plus forte pression que dans les conditions usuelles ($<$1 mbar). Ceci simplifierait considérablement l'étape de compression du gaz, qui doit être porté à la pression atmosphérique pour pouvoir être inhalé, donc la préparation des échantillons pour l'imagerie. Avec Marie Abboud, dont j'ai co-encadré la thèse, et Xavier Maître du Laboratoire U2R2M, nous avons obtenu des résultats qui montrent en effet une substantielle diminution de la relaxation à fort champ et qui étendent le domaine d'application du pompage optique par échange de métastabilité jusqu'à des pressions presque 100 fois plus élevées que celles usuelles. J'espère vivement que ces résultats très encourageants soient mis à profit pour l'imagerie avec les gaz polarisés. Xavier a le projet de construire un prototype de polariseur à fort champ. Je lui ai promis mon soutien quand il se mettra à la tâche. Après quatre ans de travail sur le pompage à fort champ, j'ai maintenant envie de revenir à la physique quantique et aux condensats, et aux applications des condensats pour l'information quantique en particulier.

Chapitre 3

Optique quantique

Les numéros entre crochets font référence à la liste de mes publications, disponible en fin de document.

3.1 États comprimés de la lumière et mesures QND en optique

Dans ce chapitre, nous nous intéressons à la dynamique de systèmes constitués d'atomes interagissant avec des modes du champ électromagnétique dans une cavité optique. Il s'agit de systèmes ouverts couplés à un réservoir qui introduit dans le système des pertes et des fluctuations. Le régime qui nous intéresse est celui d'un grand nombre de photons et de couplage faible (où l'échelle de temps de l'évolution cohérente du système pour un photon et un atome est beaucoup plus grande que le temps de vie $1/\kappa$ du photon dans la cavité). Dans ce régime, l'évolution des valeurs moyennes des observables, essentiellement classique, conduit à un état stationnaire dans lequel s'équilibrent la dissipation et l'effet d'une excitation en continu du système. Le caractère quantique du système reste toutefois dans les petites "fluctuations" autour de la valeur stationnaire et se manifeste dans les moment d'ordre supérieure des observables : typiquement les variances. Puisque les fluctuations sont petites par rapport aux valeurs moyennes, un traitement linéarisé en général suffit.

3.1.1 Rappels : états comprimés du champ électromagnétique

Considérons un mode du champ électromagnétique de pulsation ω dans une boîte de volume V. Nous savons que ce mode peut être décrit comme un oscillateur harmonique si bien que le champ électrique est donné par

$$E(t) = \mathcal{E}_0(a\, e^{-i\omega t} + a^\dagger\, e^{-i\omega t})\,. \tag{3.1}$$

a et $a^\dagger$ sont les opérateurs d'annihilation et de création d'un photon dans le mode, $\mathcal{E}_0$ est l'amplitude du champ électrique dans les fluctuations du vide

$$\mathcal{E}_0 = \sqrt{\frac{\hbar\omega}{2\epsilon_0 V}} \tag{3.2}$$

où ϵ_0 est la permittivité diélectrique du vide. On introduit les *quadratures* du champ

$$X_\phi = a\, e^{-i\phi} + a^\dagger e^{i\phi} \qquad\qquad Y_\phi = i(a^\dagger\, e^{i\phi} - a\, e^{-i\phi}) = X_{\phi+\pi/2} \tag{3.3}$$

De la non commutativité de a et $a^\dagger$ suit

$$\Delta X_\phi \, \Delta Y_\phi \leq \frac{1}{2} |\langle [X_\phi, Y_\phi] \rangle| = 1 \,. \tag{3.4}$$

Il y a donc des fluctuations intrinsèques au champ électromagnétique venant de sa nature quantique. L'étude et la manipulation du champ électromagnétique au niveau des fluctuations quantiques constitue le domaine de l'optique quantique.

Pour l'état vide on a $\Delta X_\phi = \Delta Y_\phi = 1$. Les mêmes écarts type $\Delta X_\phi = \Delta Y_\phi = 1$ se retrouvent dans l'*état cohérent* $|\alpha\rangle$ état propre de l'opérateur a avec valeur propre α, qui s'obtient à partir de l'état vide par l'action de l'opérateur "déplacement" $D(\alpha)$:

$$|\alpha\rangle = D(\alpha)|0\rangle \qquad\qquad D(\alpha) = \exp[\alpha a^\dagger - \alpha^* a] \,. \tag{3.5}$$

Le bruit quantique de l'état cohérent est dit *bruit quantique standard*.

On dit que le mode est dans un état comprimé si la variance pour l'une des quadratures est inférieure à celle du vide, par exemple :

$$\Delta X_\phi < 1 \qquad\qquad (\text{et} \quad \Delta Y_\phi > 1) \,. \tag{3.6}$$

À partir du vide on crée un état de vide comprimé par l'action de l'opérateur unitaire de compression $S(\xi)$:

$$|\xi\rangle = S(\xi)|0\rangle \quad \text{avec} \quad S(\xi) = \exp[(\xi^* a^2 - \xi a^{\dagger 2})/2] \,, \quad \text{et} \quad \xi = r \, e^{2i\theta} \,. \tag{3.7}$$

Les opérateurs quadratures X_θ et Y_θ sont transformés en

$$S^\dagger(\xi) X_\theta S(\xi) = X_\theta e^{-r} \qquad\qquad S^\dagger(\xi) Y_\theta S(\xi) = Y_\theta e^{r} \,. \tag{3.8}$$

Ils ont donc une moyenne nulle et des écarts type $\Delta X_\phi = e^{-r} < 1$ et $\Delta Y_\phi = e^r > 1$. Tout comme le vide peut être déplacé, ce qui donne lieu à un état cohérent avec $\langle a \rangle \neq 0$, on peut déplacer le vide comprimé pour donner lieu à un état comprimé

$$|\alpha, \xi\rangle = D(\alpha) S(\xi) |0\rangle \,. \tag{3.9}$$

Un état comprimé est non classique dans le sens où ses fluctuations ne peuvent pas être reproduites par une distribution de probabilité classique positive. Plus techniquement la distribution de Glauber-Sudarshan $P(\alpha)$ n'est pas positive pour un état comprimé.

D'après les équations (3.7) et (3.8), il est clair que des Hamiltoniens du type $H = \kappa a^2 + \kappa^* a^{\dagger 2}$, qui décrivent la formation de photons par paires, ou des processus d'amplification dépendant de la phase peuvent donner lieu à des états comprimés. En général, des processus non linéaires sont nécessaires. Pour ce qui concerne ce mémoire, la non linéarité viendra des atomes situés dans une cavité optique dans laquelle on injecte des champs dans un état cohérent.

3.1.2 Rappels : mesures quantiques non destructives

Comme nous l'avons dit au début du chapitre, nous nous intéressons aux "petites" fluctuations quantiques des quadratures du champ électromagnétique. La variance dans la quadrature amplitude $X_{\phi=0}$ du champ peut être mesurée directement en envoyant le faisceau sur un photodétecteur (figure 3.1). Toutefois cette détection est destructive, non seulement pour notre observable mais pour le système tout entier puisque le faisceau est absorbé. En général pour effectuer une mesure *non destructive*, on se sert d'un deuxième

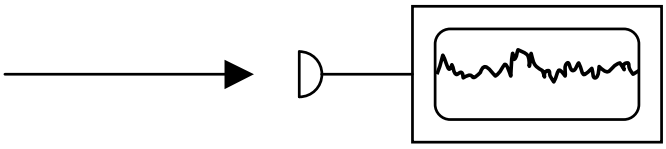

FIG. 3.1 – Une mesure directe et destructive des fluctuation d'intensité d'un faisceau lumineux.

système (dit le *mètre*) couplé au système sur lequel nous voulons effectuer la mesure (dit le *signal*) et sur lequel on effectue une mesure destructive dont on déduit de l'information sur le *signal*. Pour être dans le domaine quantique, on veut mesurer à mieux que le bruit quantique standard. En outre, pour que la mesure soit QND, il faut que le bruit de rétro-action introduit par la mesure dans le système ne retombe pas, dans la suite de l'évolution hamiltonienne, sur la variable mesurée.

Pour nous, le *mètre* et le *signal* seront deux faisceaux laser. Imaginons vouloir mesurer les fluctuations de la quadrature X_s du *signal* en effectuant une mesure sur la quadrature Y_m du faisceau *mètre*. Pour caractériser les mesures QND réelles sur des faisceaux propageants, trois coefficients ont été introduits relativement à trois propriétés de la mesure :

- Un coefficient C_m qui nous renseigne sur la quantité d'information sur X_s extraite de la mesure de Y_m.

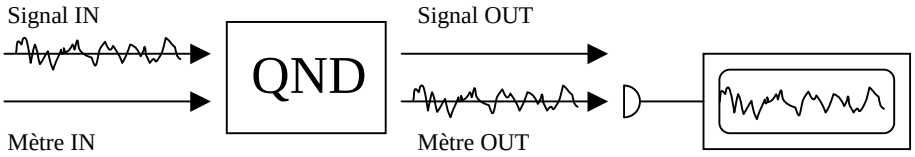

FIG. 3.2 – Information sur X_s que nous avons acquise par la mesure de Y_m.

En terme des fonctions de corrélation entre X_s et Y_m,

$$C_m = \frac{|\langle X_s^{in} Y_m^{out}\rangle|^2}{\langle X_s^{in} X_s^{in}\rangle \langle Y_m^{out} Y_m^{out}\rangle} \tag{3.10}$$

avec

$$\langle AB\rangle = \int dt\, e^{-i\omega t}\, \langle \delta A(t)\delta B + \delta B \delta A(t)\rangle/2 \tag{3.11}$$

où δA représente l'écart de l'observable A à sa valeur moyenne stationnaire.

- Un coefficient C_s qui nous donne le degré de non destructivité de la mesure de X_s.

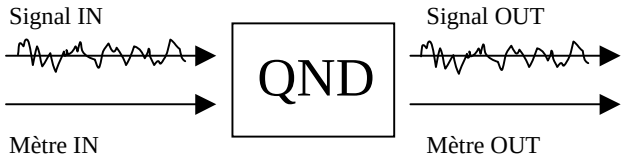

FIG. 3.3 – Non-destructivité de la mesure.

$$C_s = \frac{|\langle X_s^{in} X_s^{out}\rangle|^2}{\langle X_s^{in} X_s^{in}\rangle \langle X_s^{out} X_s^{out}\rangle} \tag{3.12}$$

- La variance conditionnelle $V[s|m]$ nous donne la variance résiduelle dans la quadrature X_s connaissant le résultat de la mesure sur Y_m : c'est la variance qui reste dans le signal après avoir utilisé aux mieux l'information acquise par mesure QND pour reduire ses fluctuations.

$$V[s|m] = \langle X_s^{out} X_s^{out} \rangle \left(1 - \frac{|\langle X_s^{out} Y_m^{out} \rangle|^2}{\langle X_s^{out} X_s^{out} \rangle \langle Y_m^{out} Y_m^{out} \rangle} \right) \tag{3.13}$$

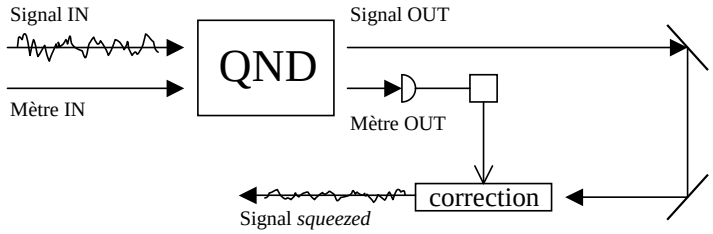

FIG. 3.4 – Variance conditionnelle.

Pour une mesure QND idéale : $C_m = 1$, $C_s = 1$ et $V[s|m] = 0$.

3.1.3 Notre étude

Les modèles que j'ai étudiés décrivent des atomes à trois niveaux en "cascade" Ξ ou en "lambda" Λ, en interaction avec deux modes du champ dans une cavité optique. Comme je l'ai montré, ces systèmes constituent un schéma favorable pour la production d'états comprimés de la lumière et pour la réalisation de mesures quantiques non destructives.

Au contraire des traitements antérieurs à notre travail, nous avons choisi, pour étudier ces systèmes, de développer des modèles théoriques aussi complets et généraux que possible, sans faire d'hypothèse *a priori* sur les paramètres du système. Cette approche a permis d'effectuer des comparaisons quantitatives avec les expériences. Nous avons décrit de façon entièrement quantique les degrés de liberté internes des atomes et la dynamique du champ en cavité, en utilisant une équation pilote qui prend en compte l'émission spontanée des atomes et les pertes du champ dans la cavité.

Une grande partie de mon travail de thèse a été effectuée en collaboration avec l'équipe de Philippe Grangier à l'Institut d'Optique, où des expériences sur les états comprimés de la lumière et sur les mesures QND le l'intensité lumineuse, à partir d'un jet d'atomes de Na et d'atomes piégés de Rb, étaient en cours.

3.2 Le schéma à "transition fantôme" et l'expérience de l'Institut d'Optique.

3.2.1 Mesure QND par effet Kerr croisé

On injecte dans la cavité un faisceau intense, le faisceau "signal", dont on souhaite mesurer les fluctuations d'intensité, et un faisceau peu intense, le faisceau "mètre".

Le faisceau signal est à résonance avec la transition $|2\rangle - |3\rangle$ du schéma en Λ, (Fig. 3.5). Sa présence a principalement deux effets : (1) habiller la transition atomique $|2\rangle - |3\rangle$, ce qui produit un clivage de Rabi de l'état excité c'est-à-dire ce qui donne naissance à deux états habillés $|\pm\rangle$ dont la séparation en énergie est proportionnelle à l'amplitude

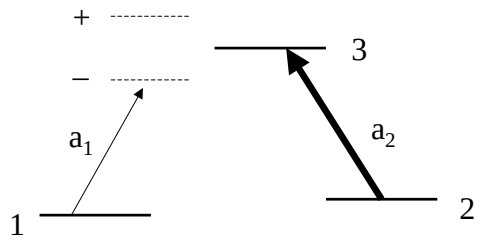

FIG. 3.5 – Système en Λ dans la configuration transition fantôme. Trait plain : niveaux d'énergie de l'atome seul. Trait pointillé : niveaux d'énergie de l'atome habillé.

du champ signal, et (2) transférer la population atomique dans l'autre état fondamental $|1\rangle$ par pompage optique. Comme la population de $|2\rangle$ est très faible, le faisceau signal n'est pratiquement pas absorbé, ce qui sera essentiel pour le caractère non destructif de la mesure.

Le faisceau mètre travaille sur la transition $|1\rangle - |3\rangle$. Son déphasage et son absorption dépendent alors de son désaccord en fréquence avec les transitions $|1\rangle - |\pm\rangle$, donc de l'intensité du faisceau signal. Ceci permet de réaliser une mesure quantique non destructive des fluctuations d'intensité du faisceau signal, en effectuant une mesure directe (et destructive) sur le faisceau mètre.

Dans la proposition initiale de ce schéma par K. Gheri et al. en 1992, les champs étaient résonnants avec la cavité contenant les atomes. Nous avons généralisé cette idée en dehors de ce point de fonctionnement très particulier. Nos calculs ont permis de fournir à l'équipe de Philippe Grangier à l'Institut d'Optique des indications précises pour une réalisation expérimentale optimale du schéma décrit. Ils ont aussi permis d'interpréter quantitativement et en grand détail les résultats obtenus, qui représentent les meilleures performances QND obtenues à ce jour [5,7].

3.2.2 États comprimés du champ obtenus par "rétroaction" optique

L'étude de la configuration à transition fantôme dans le cas où les champs sont hors de résonance avec la cavité optique nous a permis de mettre en évidence un nouveau mécanisme de réduction du bruit quantique par "rétroaction". Dans le cas non résonnant, en effet, les fluctuations du faisceau mètre, pilotées par les fluctuations d'intensité du faisceau signal, sont ramenées sur le faisceau signal d'une façon qui peut en réduire le bruit d'intensité. Cet effet a aussi été observé à l'Institut d'Optique, en utilisant deux transitions en cascade de l'atome de sodium [1].

3.2.3 Publications jointes

VOLUME 78, NUMBER 4 PHYSICAL REVIEW LETTERS 27 JANUARY 1997

Quantum Nondemolition Measurements using Cold Trapped Atoms

J.-F. Roch, K. Vigneron, Ph. Grelu, A. Sinatra,* J.-Ph. Poizat, and Ph. Grangier
Institut d'Optique, B.P. 147, F-91403 Orsay Cedex, France
(Received 3 September 1996)

We have investigated possible implementations of optical quantum nondemolition measurements, using rubidium atoms in a magneto-optical trap as a nonlinear medium. Using a Λ-type three-level system in the $D1$ line of ^{87}Rb, the observed performances are quantitatively the best obtained so far for a single back action evading measurement. Moreover, the magneto-optical trap and the quantum nondemolition effect are both running continuously at the same time and mutual perturbations have been avoided by using a "dark spot" technique. This experiment demonstrates clearly the interest of using cold atoms for controlling the quantum fluctuations of light. [S0031-9007(96)02247-8]

PACS numbers: 42.50.Lc, 32.80.Pj, 42.65.Pc

Significant effort was made during recent years for implementing the idea of "quantum nondemolition" (QND) measurements, which was initially introduced theoretically by Braginsky [1] and Thorne [2]. The principle of QND measurements is to overcome the measurement noise, which is introduced in a physical system when a quantum measurement is performed, by repeatedly "hiding" this noise in an observable which is not of interest. A scheme where the measurement noise is entirely kept in an observable which is conjugated with the measured quantity is usually said to be "back-action evading" (BAE). Though proposed and initially studied for mechanical oscillators [3,4], QND ideas were first implemented in quantum optics [5–14]. In the standard situation encountered with propagating laser beams, where the quantum fluctuations are small compared to the mean intensities, quantitative criteria have been developed for evaluating the QND or BAE efficiency of a given experimental setup [15,16]. An important quantity to look at is the quantum correlation between the two outputs of the measurement system (signal and meter), which can be measured through the conditional variance $V_{S|M}$ of the signal output S, given the measurement M [15,16]. It is also necessary to consider the transfer coefficients T_S and T_M, which quantify the transfer of the signal to (quantum) noise ratio of the input signal beam towards, respectively, the output signal and meter [16,17]. These quantities have boundaries which define necessary conditions for QND operation of the device [16]: Giving the conventional value 1 to the signal shot-noise level (SNL), $V_{S|M} < 1$ indicates nonclassical operation, in the same sense as used for squeezed states of light [18]. For a coherent input signal [16], a value of $T_S + T_M$ larger than 1, up to the maximum of 2, can only be obtained by using a phase-sensitive device, and is therefore related to noiseless amplification methods [19].

Many experiments have been devoted to the demonstration of BAE measurements [6–14]. These works culminated in the recent demonstration of repeated BAE measurements, which constitutes a full demonstration of the QND original idea [14]. This experiment, like several previous ones [11–13], uses second-order ($\chi^{(2)}$) optical nonlinearities, which have the important advantages of being well understood, and of adding very small excess noise to the output light beams. On the other hand, third-order ($\chi^{(3)}$) optical nonlinearities are usually accompanied by significant excess noise from the nonlinear medium [6–10]. Third-order nonlinearities in atomic media have, nevertheless, the advantage of having extremely large values, and can operate with very small optical power. Moreover, theoretical analysis done for motionless atoms predicts that it should be possible to achieve very good QND efficiency provided that appropriate laser powers and detunings are used [20]. However, such calculations do not include the atomic motion, which causes Doppler effect and excess fluctuations in the refractive index, even in an atomic beam [10], and therefore degrades quantum noise reduction effects. An open way for reducing motion-induced fluctuations is clearly to use a medium of cold trapped atoms; an encouraging result was the recent observation of transient squeezing from a cloud of falling atoms released from a magneto-optical trap (MOT) [21].

In this Letter we present the implementation of a BAE device using trapped rubidium atoms to provide a nonlinear coupling between two light beams: The intensity of a "signal" beam is thus read out on the phase of a "meter" beam. By tuning the two lasers close to the resonances of a Λ-type three-level system, the measured performances are $V_{S|M} = 0.45$, $T_S = 0.90$, and $T_M = 0.65$, which are the best obtained so far in a single BAE device. The optical powers used in the experiment are in the microwatt range, emphasizing the very high values of the effective nonlinearities. Special care has been taken to minimize the mutual perturbations of the trapping and QND effect, by using two different optical transitions and a "dark spot" configuration for the trap [22]. As a consequence, both the MOT and the QND effect are running continuously at the same time.

The MOT is built in a large ultrahigh vacuum (UHV) chamber, designed in order to set up the sensitive parts of the experiment directly around the cold atom cloud. The

 0031-9007/97/78(4)/634(4)$10.00 © 1997 The American Physical Society

present setup uses ^{87}Rb, with nuclear spin $I = 3/2$. The trap is loaded by slowing down an atomic beam using the standard chirped-frequency technique [23]. The atoms are trapped using a standard six-beam $\sigma+/\sigma-$ MOT configuration [24]. The trapping lasers are two 100 mW laser diodes, injection locked to a master laser and detuned by four natural linewidths $[\Gamma/(2\pi) = 6$ MHz] to the red of the $F = 2$-$F' = 3$ transition (see Fig. 1). The total power on the trap is typically 3×30 mW, with a beam diameter of 20 mm. A repumping beam locked on the $F = 1$ to $F' = 2$ line pumps back the atoms from the $F = 1$ ground state. This beam is superimposed with the trapping beams along two axes, and its central part is screened by a dark spot imaged at the trap location [22]. This allows one to have about 90% of the population of the cloud in the $F = 1$ ground state, and will be essential for the continuous operation of the QND effect. The diameter of the trap, measured either in fluorescence ($F = 2$) or in absorption ($F = 1$), is close to 3.5 mm FWHM. The estimated population in the $F = 1$ dark state is 10^9 atoms, corresponding to a density of 5×10^{10} atoms/cm^3. For the following experiments, the Doppler width of the atomic medium has to be smaller than the natural linewidth Γ; this is easily fulfilled by the techniques that are used here.

A schematic overview of the optics of the QND experiment is shown in Fig. 2. The signal and meter beams are emitted by two independent frequency-stabilized titanium-sapphire lasers, which are shot-noise limited in both intensity and phase for noise analysis frequencies above 2 MHz. The two beams are carried onto the optical table by optical fibers, which ensure very good spatial mode quality, and then mode matched to the vertical optical cavity which is set up inside the UHV chamber around the cold atom cloud. The signal and meter beams have orthogonal linear polarization inside the cavity, and the input and output beams are separated using polarization beam splitters and Faraday rotators (see Fig. 2). The cavity mirrors have a 60 mm radius of curvature, and their distance is adjustable from 64 to 68 mm, using screws and piezo-electric transducers which are outside the UHV chamber. The lower, input/output cavity mirror has a 5% transmissivity. The upper mirror has a low transmissivity ($T < 10^{-4}$), which is used to monitor the intracavity intensities using two photomultipliers and another polarization beam splitter. The cavity finesse is 125, and typical mode-matching efficiency in the cavity fundamental mode is above 99%. The output signal beam is directly detected, while the meter beam is detected after interfering with a "local oscillator" beam (phase-sensitive homodyne detection [18]). The maximum fringe visibility of this interferometer (or homodyne efficiency) is 96%. The quantum efficiency of all photodiodes is 92%. The transmission of the optical system (not including the photodiodes) is 90%, and the on-resonance losses of the cavity are negligibly small.

The level scheme which is used for the QND effect is shown in Fig. 1. While the trapping and repumping lasers are tuned on the D2 line at 780 nm, the signal and meter beams are tuned on the D1 line at 795 nm. The linearly polarized signal is tuned close to the $5s_{1/2}$ $F = 2$ to $5p_{1/2}$ $F' = 2$ transition, with a typical input power of 15 μW. The signal acts therefore as a "depumper" with respect to the trap, increasing the population of the ground $F = 1$ level. The meter beam, on the $F = 1$ and $F' = 2$ transition, is linearly polarized orthogonally to the signal, and is detuned negatively (to the red) with respect to the dressed levels due to the signal-atom coupling. The typical meter input power is 0.25 μW. The contributions of the different Zeeman sublevels to the two-beam coupling is shown in the inset of Fig. 1. Note that, if this system was considered alone, all the population should be pumped in the $F = 2$, $m = 0$ ground state. However,

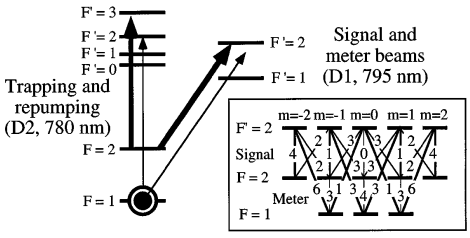

FIG. 1. Level scheme used in the experiment. The inset shows the relevant relative oscillator strengths for coupling the signal and meter beams, which have orthogonal linear polarizations.

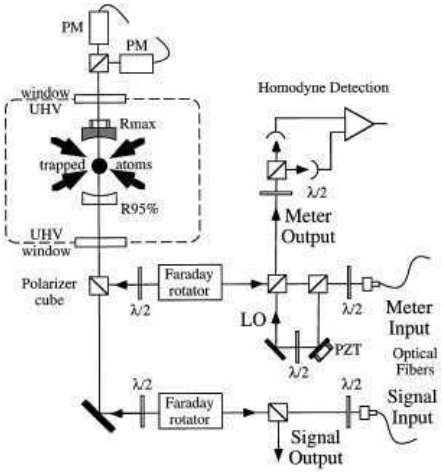

FIG. 2. Simplified view of the experimental setup. The input signal and meter beams are mode matched to an optical cavity surrounding the trapped atoms. Output beams are separated from the input ones using Faraday rotators. The signal beam is directly detected, while the meter beam undergoes a phase-sensitive homodyne detection.

the MOT laser recycles very efficiently the atoms which could be lost in this level, and most of the coupling comes from the two Λ level schemes with the largest Clebsch-Gordan coefficients. This system is therefore very close to the "ghost transition" scheme, which was studied theoretically in Ref. [20] and predicted to have good QND performances. In this scheme, the strong signal beam optically pumps the atoms into a ground level (here, the $F = 1$ level), from which the weak meter beam can probe the light shift induced by the signal on the upper level. The signal acts therefore on a nearly transparent transition, and its intensity fluctuations are almost unperturbed. Using experimental values [25] in the model described in Ref. [20], and correcting for losses in the optics, the calculated values are within a few percent of the results obtained in the experiment. This analysis, including the behavior of the mean fields, will be presented in another publication.

We note that the frequency difference between the signal and meter beam has to be close to the ground state hyperfine splitting of ^{87}Rb, which is 6.83 GHz. Since both beams also have to be resonant in the cavity, this detuning has to be close to an integer number of free spectral range (FSR) of the cavity. This is indeed the case when the cavity length is 66 mm, corresponding to a FSR of 2.27 GHz: The two frequencies are then approximately 3 FSR apart. We note also that the two standing wave patterns from the signal and meter beams have to be in phase at the atom location, so that the atoms see the appropriate Rabi frequencies [25] from each beam. This is achieved by placing the trapped atoms' cloud at one-third of the cavity length.

The experimental procedure for measuring the QND criteria is the following. A weak intensity modulation at 5 MHz, about 20 dB above the SNL, is applied on the signal beam. Then the detunings of the two beams are iteratively adjusted while scanning both the cavity and the homodyne detection, in order to maximize the transfer of the modulation from the signal onto the meter beam, while minimizing the degradation of the signal. This adjustment can be completed at a cavity position where both fields resonate together inside the cavity [10]. When the optimum detunings are found, the cavity scan is stopped at the resonance peak, and the noise levels are measured by scanning the spectrum analyzer (SA) around 5 MHz. Typical results are shown in Fig. 3. The lower trace (a) shows the SNL and the modulation of the output signal beam, taken off cavity resonance without the atoms; the width of the modulation peak is the 100 kHz rf resolution bandwidth of the SA. Over this trace are also shown as dots the SNL and modulation of the output signal beam, taken while the cavity is stopped at resonance in the presence of the atoms (operating conditions). There is clearly neither attenuation nor change in the noise of the signal beam. The nondemolition coefficient T_S is therefore limited only by the passive optical transmission of the system, which relates the output signal without atoms to the input one, i.e., $T_S = 0.90$ (-0.5 dB). From T_S and Fig. 3, one gets the input beam

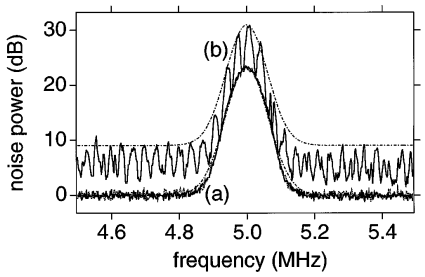

FIG. 3. Measurement of the transfer coefficient T_M. Curve (a), normalized to the SNL, corresponds to the output signal, modeled by a Gaussian peak (dash-dotted line). Two curves are actually displayed, and show no observable difference: one taken off resonance without atoms (line), and one taken on operating conditions (dots). Curve (b) is the outcoming meter, also taken on operating conditions, and modulated by scanning the phase of the homodyne detection. The upper envelope is fitted by a Gaussian peak of same width as in (a). The signal-to-noise ratios are obtained as the differences (in dB) between the fitted peaks and the flat backgrounds.

signal-to-noise ratio, which is 23.8 dB. The upper trace (b) is the phase-dependent noise and modulation of the output meter beam, taken in operating conditions while scanning the phase of the homodyne detection. The SNL of the meter beam has been electronically set at the same level as the one for the signal beam. The upper envelope of the fringes gives the meter phase information, and yields the output meter signal-to-noise ratio, which is equal to 21.9 dB. The measurement transfer coefficient is thus -1.9 dB, or $T_M = 0.65$. Finally, it can be shown that the conditional variance of the signal, given the measurement, is also the minimum noise which can be obtained when recombining the output signal and meter photocurrents, the latter being appropriately attenuated [14,16]. This recombined photocurrent is shown in Fig. 4, while scanning the phase of the homodyne detection. For optimum attenuation (12 dB) of the meter photocurrent, the recombined noise reaches a minimum value 3.5 dB below the SNL, which gives a conditional variance $V_{S|M} = 0.45$. Estimated uncertainties on T_S, T_M, and $V_{S|M}$ are ± 0.05. The values quoted here, which are corrected for the amplifier noise but not for the detector quantum efficiencies, are typical of many experiments which were done for different values of the input beam powers and detunings.

We also tried several other level schemes, using either "Λ" or "V" configurations, which, however, did not give as good results. Generally speaking, the experiment requires one to get control both on optical pumping effects, in order to avoid that the atoms be pumped outside the three-level scheme of interest, and on light-induced forces, so that the signal and meter beams do not expel the atoms from the interaction region or even from the trap. Further improvements, now under theoretical analysis, could be obtained if the atoms were attracted and trapped

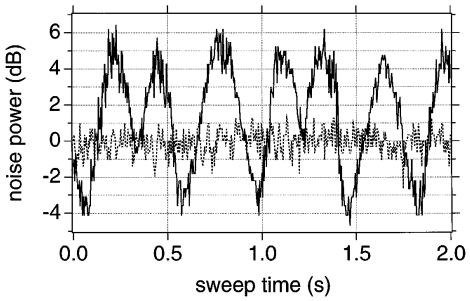

FIG. 4. Measurement of the conditional variance $V_{S|M}$. The dotted line is the signal beam shot-noise level at a noise analysis frequency of 5 MHz (rf bandwidth 100 kHz, video bandwidth 300 Hz). The full line is the noise from the recombined signal and meter photocurrents, recorded as the phase of the homodyne detection is scanned. The conditional variance appears as the minimum noise level on this curve.

at the common antinodes of the coupled beams; though we could not clearly demonstrate this effect so far, the used scheme yields, in principle, rectified dipole force [26] able to attract the atoms at the right position.

To summarize, we have observed very good BAE performances from a cloud of trapped rubidium atoms in an optical cavity, in a level configuration where the trap and the quantum noise effects are running continuously at the same time. This is obtained by controlling both the optical pumping and the light forces induced by the signal and meter beams. Beyond its success as a BAE device, this experiment demonstrates clearly that cold atoms do provide a very efficient and low-noise nonlinear medium for achieving control of the quantum fluctuations of light.

This research has been supported in part by the Direction des Recherches, Etudes et Techniques (DRET/DGA). We acknowledge the work of Tony Van der Veldt and Pierre Fournet in setting up the experiment, and the constant help of Alain Aide with the electronics. Thanks are due to Helmut Ritsch for discussions within the framework of Amadeus project 95.44.25. Institut d'Optique is Unité de Recherche Associée 14 du Centre National de la Recherche Scientifique (CNRS).

*Permanent address: Dipartimento di Fisica dell'Università, via Celoria 16, 20133 Milano, Italy.

[1] V. B. Braginsky and Yu. I. Vorontsov, Usp. Fiz. Nauk **114**, 41 (1974) [Sov. Phys. Usp. **17**, 644 (1975)]; V. B. Braginsky, Yu. I. Vorontsov, and F. Ya. Khalili, Zh. Eksp. Teor. Fiz. **73**, 1340 (1975) [Sov. Phys. JETP **46**, 705 (1977)].

[2] K. S. Thorne, R. W. P. Drever, C. M. Caves, M. Zimmerman, and V. D. Sandberg, Phys. Rev. Lett. **40**, 705 (1978).

[3] W. G. Unruh, Phys. Rev. D **19**, 2888 (1979).

[4] C. M. Caves, K. S. Thorne, R. W. P. Drever, V. D. Sandberg, and M. Zimmerman, Rev. Mod. Phys. **52**, 341 (1980).

[5] G. J. Milburn and D. F. Walls, Phys. Rev. A **28**, 2055 (1983); N. Imoto, H. A. Haus, and Y. Yamamoto, Phys. Rev. A **32**, 2287 (1985); B. Yurke, J. Opt. Soc. Am. B **2**, 732 (1985).

[6] M. D. Levenson, R. M. Shelby, M. Reid, and D. F. Walls, Phys. Rev. Lett. **57**, 2473 (1986).

[7] S. R. Friberg, S. Machida, and Y. Yamamoto, Phys. Rev. Lett. **69**, 3165 (1992).

[8] M. D. Levenson, M. J. Holland, D. F. Walls, P. J. Manson, P. T. H. Fisk, and H. A. Bachor, Phys. Rev. A **44**, 2023 (1991).

[9] P. Grangier, J. F. Roch, and G. Roger, Phys. Rev. Lett. **66**, 1418 (1991).

[10] J. Ph. Poizat and P. Grangier, Phys. Rev. Lett. **70**, 271 (1993).

[11] A. LaPorta, R. E. Slusher, and B. Yurke, Phys. Rev. Lett. **62**, 28 (1989).

[12] J. A. Levenson, I. Abram, T. Rivera, P. Fayolle, J. C. Garreau, and P. Grangier, Phys. Rev. Lett. **70**, 267 (1993).

[13] S. F. Pereira, Z. Y. Ou, and H. J. Kimble, Phys. Rev. Lett. **72**, 214 (1994).

[14] K. Bencheikh, J. A. Levenson, Ph. Grangier, and O. Lopez, Phys. Rev. Lett. **75**, 3422 (1995).

[15] M. J. Holland, M. Collett, D. F. Walls, and M. D. Levenson, Phys. Rev. A **42**, 2995 (1990).

[16] J. Ph. Poizat, J.-F. Roch, and P. Grangier, Ann. Phys. (Paris) **19**, 265 (1994).

[17] Defining $R = \langle X \rangle^2 / \Delta X^2$ as the signal to (quantum) noise ratio of the observable X, one has $T_S = R_S^{\text{out}}/R_S^{\text{in}}$ and $T_M = R_M^{\text{out}}/R_S^{\text{in}}$. In this equation, $\langle X \rangle$ is the amplitude of a classical modulation at a given frequency, and ΔX^2 is the noise power at the same frequency. This definition should be used in a linear or linearized system.

[18] See, e.g., special issue [J. Opt. Soc. Am. B **4**, 1450 (1987)].

[19] C. M. Caves, Phys. Rev. D **26**, 1817 (1982).

[20] K. M. Gheri, P. Grangier, J. Ph. Poizat, and D. F. Walls, Phys. Rev. A **46**, 4276 (1992).

[21] A. Lambrecht, T. Coudreau, A. M. Steinberg, and E. Giacobino, Europhys. Lett. **36**, 93 (1996).

[22] W. Ketterle, K. Davis, M. Joffe, A. Martin, and D. Pritchard, Phys. Rev. Lett. **70**, 2253 (1993).

[23] B. Sheehy, S. Q. Shang, R. Watts, S. Hatamian, and H. Metcalf, J. Opt. Soc. Am. B **6**, 2165 (1989).

[24] E. Raab, M. Prentiss, A. Cable, S. Chu, and D. Pritchard, Phys. Rev. Lett. **59**, 2631 (1987).

[25] Parameters to be used in the model of Ref. [20] are the signal and meter Rabi frequencies, detunings, and cooperativities, which are, respectively, $\Omega_s = 35$, $\Omega_m = 6$, $\Delta_s = 0$, $\Delta_m = -45$ (in $\Gamma/2$ units), and $C_s = 90$, $C_m = 135$.

[26] R. Grimm, Y. B. Ovchinnikov, A. I. Sidorov, and V. S. Lethokov, Phys. Rev. Lett. **65**, 1415 (1990).

PHYSICAL REVIEW A VOLUME 57, NUMBER 4 APRIL 1998

Quantum-nondemolition measurements using cold trapped atoms: Comparison between theory and experiment

A. Sinatra,* J. F. Roch, K. Vigneron, Ph. Grelu, J.-Ph. Poizat, Kaige Wang,† and P. Grangier
Institut d'Optique, Boîte Postale 147, F-91403 Orsay Cedex, France
(Received 15 July 1997)

In this paper we present a detailed theoretical analysis of a recent quantum-nondemolition experiment in optics using cold atoms in a magneto-optical trap as a nonlinear medium. A signal beam and a meter beam from two independent lasers are coupled within a Λ-type three-level scheme in the $D1$ line of ^{87}Rb atoms. The experimental results for the relevant quantum correlations of the fields, that represent up to now the best achievements for a single back-action evading measurement, are found in a remarkably good agreement with the theoretical predictions from a fully quantum model for three-level atoms in a doubly resonant cavity. [S1050-2947(98)05203-2]

PACS number(s): 42.50.Lc, 32.80.Pj, 42.50.Dv, 42.65.Pc

I. INTRODUCTION

A. General features

As summed up by the Heisenberg uncertainty relation, noise is introduced into a physical system when a quantum measurement is performed on a given observable. The principle of quantum nondemolition (QND) measurements, which was first introduced theoretically by Braginsky and co-workers [1] and Thorne *et al.* [2], is to overcome this measurement noise by repeatedly ''hiding'' it in another observable which is not of interest. In the case where the noise is entirely kept into an observable which is conjugate with the measured quantity, the measurement is said to be back-Action evading (BAE). Though initially proposed for mechanical oscillators, these ideas were greatly developed, both theoretically and experimentally, in the field of quantum optics.

In particular, quantum measurements performed on propagating laser beams are very good candidates for implementing QND or BAE schemes. The basic idea of these schemes is to couple two light beams, usually called ''signal'' and ''meter'' beams, via an optically nonlinear medium (see Ref. [3] for theoretical proposals). Then, for an appropriately designed coupling, direct or homodyne detection of the meter beam will perform a BAE measurement on the signal beam [4–10]. The nonlinear medium may display either second-order ($\chi^{(2)}$) or third-order ($\chi^{(3)}$) optical nonlinearities. The former have the important advantages of being well understood, and of adding very small excess noise to the interacting light beams; they were used in several successful experiments (see, e.g., Ref. [9] and references therein). On the other hand, the latter ($\chi^{(3)}$) nonlinearities are usually accompanied by significant excess noise from the nonlinear medium, which has been attributed to thermally excited Brillouin scattering in optical fibers [4,7], or to absorption and/or spontaneous emission noise in quasiresonant media [11,6]. Nevertheless the last word about the exploitation of ($\chi^{(3)}$) nonlinearities for quantum nondemolition experiments has not yet been pronounced.

A theoretical analysis done for motionless atoms [12] predicted that it should be possible to obtain almost full control of absorption and spontaneous emission processes, provided that appropriate laser powers and detunings are used. On the other hand, the atomic media used so far, which are atomic beams or vapor cells, also exhibit other types of fluctuations, associated with collisions and/or atomic motion [8]. Atomic motion causes fluctuations in the refractive index due to the fluctuating number of atoms in the interaction region, and thus degrades quantum noise reduction effects. An open way to improve atomic media is then clearly to use a medium of cold trapped atoms [13]; in these media, in fact, the time scale of the fluctuations in the number of interacting particles, characterized by the transit time of the atoms across the interaction region, is about three orders of magnitude slower than in atomic beams or vapor cells. In other words, atom number fluctuations in traps have characteristic frequencies that are typically in the kHz range, and do no affect the noise analysis that is performed in the MHz range (see, for example, Sec. V). Moreover, despite the lower densities usually obtained in traps with respect to atomic beams or vapor cells, the elimination of the Doppler broadening of the atomic lines allows one to control small atomic detunings accurately, and consequently to achieve large nonlinear effects. Though these arguments have only a qualitative character, it will be shown below that, when compared to atomic beam experiments [6,8,14], QND experiments performed with cold atoms do achieve both an improved efficiency and an improved agreement with theoretical models.

B. Motivations of the work

In this article we give a detailed theoretical analysis of a recent experiment [10], where QND measurements are performed using rubidium atoms in a magneto-optical trap (MOT) as a nonlinear medium. Using a Λ-type three-level system in the $D1$ line of ^{87}Rb, the observed performances are quantitatively the best obtained so far for a single back-action-evading measurement. Moreover, the MOT and the

*Permanent address: Istituto Nazionale Fisica della Materia, Dipartimento di Fisica dell'Università, Via Celoria 16, 20133 Milano, Italy.
†Permanent address: Department of Physics, Beijing Normal University, Beijing 100875, China.

 © 1998 The American Physical Society

QND effect are both running continuously at the same time, and mutual perturbations have been avoided by using different optical transitions and a ''dark-spot'' technique [15]. From the theoretical viewpoint, we extend the analysis done in [12] on QND measurements using three-level atoms in a ghost transition scheme, by including the case in which the fields are not resonant in the cavity. How this scheme can be realized and optimized in a real experiment will be analyzed in detail, by taking explicitly into account the constraints imposed by the optical cavity and by the atomic energy-level configuration.

C. Overview of the paper

In Sec. II we briefly introduce the criteria that were developed to evaluate the efficiency of a real quantum nondemolition device. The model is presented in Sec. III. In Sec. IV we illustrate the configuration used to perform the QND measurement, and show how we can choose the adjustable parameters of our system in order to optimize the QND performances. In Sec. V we present the setup of our experiment. Finally, in Sec. VI we compare the results of the model with the experimental results.

II. CHARACTERIZATION OF A REAL QND MEASUREMENT

A. Introduction

Appropriate criteria for evaluating the efficiency of system as a ''real'' (i.e., nonideal) QND device were discussed in several papers [16,17]. It is now generally admitted that three necessary criteria for BAE operation of a device are given by looking, on the one hand, at its input-output properties, and on the other hand at the quantum correlations established between the signal and meter outputs.

More precisely, we are interested in the small time-dependent quantum fluctuations $\delta X_s(t)$ of the *signal* field *amplitude quadrature* about its steady-state value, defined by the relation:

$$X_s(t)-\langle X_s\rangle_{\rm st}=\delta X_s(t), \tag{1}$$

and we are willing to ''read out'' those fluctuations in the meter field *phase quadrature* fluctuations $\delta Y_s(t)$ about the steady-state value which are defined in the same fashion:

$$Y_m(t)-\langle Y_m\rangle_{\rm st}=\delta Y_m(t). \tag{2}$$

With a larger generality, the signal field amplitude may carry out a small *coherent modulation* $X_s'(t)$, the amplitude and the frequency of the modulation being much smaller than the mean amplitude and the optical frequency of the field, respectively. The steady state of the system is thus ''modulated'' about the stable time independent solution $\langle X_s\rangle_{\rm st}$, $\langle Y_m\rangle_{\rm st}$, and one has

$$X_s(t)-\langle X_s\rangle_{\rm st}=X_s'(t)+\delta X_s(t), \tag{3}$$

$$Y_m(t)-\langle Y_m\rangle_{\rm st}=Y_m'(t)+\delta Y_m(t), \tag{4}$$

where, as in Eqs. (1) and (2), the terms which are kept on the right-hand side are small and will be treated linearly. By regarding the QND device as a black box with two input channels and two output channels represented by the incoming and outcoming signal and meter fields, we are interested in describing how the incoming signal amplitude fluctuations $\delta X_s^{\rm in}(t)$ or modulations $X_s'^{\rm in}(t)$ are transferred to the two output channels of the device represented by the signal and the meter outputs. In an ideal QND device, the incoming fluctuations or modulations of the signal amplitude are left unchanged at the signal output, and they are at the same time perfectly reproduced by the meter output, allowing us to perform an ideally accurate and nondestructive measurement. For real experiments three criteria were developed to quantify the efficiency of a system as a QND device, by taking inspiration from the possible applications of the nondestructive measurements as detailed below.

B. Input-output transfer coefficients and correlations

A first important application of the QND measurement, for example in the field of telecommunications, is related to the possibility of reading an amount of information encoded in a beam without adding noise. Let us assume, for example, that the experimenter gives a classical modulation to the signal amplitude at a certain frequency. We would like to ''read'' the modulation, which represents the information carried by the signal field, without degrading it, thus leaving the information available for other users along the same transmission line.

By restricting ourselves to the linearized regime for quantum fluctuations and coherent modulations, we can consider the QND device as a linear amplifier, and study how the modulation and the noise are transferred from the signal input channel to the signal output and the meter output channels. In the frequency space, by introducing the Fourier transform (denoted with the tilde) of the time dependent quantities defined above, one has

$$\tilde{X}'^{\rm out}_s(\omega)=g_s\tilde{X}'^{\rm in}_s(\omega), \tag{5}$$

$$\delta\tilde{X}^{\rm out}_s(\omega)=g_s\delta\tilde{X}^{\rm in}_s(\omega)+B^{\rm add}_s(\omega) \tag{6}$$

for the signal output channel, and

$$\tilde{Y}'^{\rm out}_m(\omega)=g_m\tilde{X}'^{\rm in}_s(\omega), \tag{7}$$

$$\delta\tilde{Y}^{\rm out}_m(\omega)=g_m\delta\tilde{X}^{\rm in}_s(\omega)+B^{\rm add}_m(\omega) \tag{8}$$

for the meter output channel, where g_s and g_m represent the gains of the amplifier in the signal output and in the meter output channel, respectively, which are the same for the signal input noise and the modulation, while $B_s^{\rm add}$ and $B_m^{\rm add}$ represent the extra noises added by the amplifier in the two channels, which could come for example from the atomic noise or from the input meter noise and the signal phase noise $[\delta\tilde{Y}^{\rm in}_s(\omega)]$ processed by the system. By assuming that the fields injected in the QND device are in a coherent state, we suppose that $B_s^{\rm add}$ and $B_m^{\rm add}$ are not correlated with $\delta\tilde{X}^{\rm in}_s(\omega)$; a more general treatment was given in Ref. [17]. The signal-to-noise ratio (SNR) for the input channel of the signal field is then defined as the ratio between the intensity of the small classical modulation given to the signal field

amplitude quadrature at a certain frequency and the quantum noise power in the same quadrature at the same frequency:

$$R_s^{\rm in}=\left|\frac{\langle \widetilde{X'}_s^{\rm in}(\omega)\rangle^2}{\langle \delta\widetilde{X}_s^{\rm in}(\omega)^2\rangle}\right|, \tag{9}$$

and the same quantity can be defined for the two output channels:

$$R_s^{\rm out}=\left|\frac{\langle \widetilde{X'}_s^{\rm out}(\omega)\rangle^2}{\langle \delta\widetilde{X}_s^{\rm out}(\omega)^2\rangle}\right| \quad \text{and} \quad R_m^{\rm out}=\left|\frac{\langle \widetilde{Y'}_m^{\rm out}(\omega)\rangle^2}{\langle \delta\widetilde{Y}_m^{\rm out}(\omega)^2\rangle}\right|. \tag{10}$$

One can then define two quantities T_s and T_m, which describe how the incoming SNR (9) is transmitted to two output channels of the QND device:

$$T_s=\frac{R_s^{\rm out}}{R_s^{\rm in}} \quad \text{and} \quad T_m=\frac{R_m^{\rm out}}{R_s^{\rm in}}. \tag{11}$$

From Eqs. (5)–(8), one has

$$T_s=\frac{\langle \delta\widetilde{X}_s^{\rm in}(\omega)^2\rangle}{\langle \delta\widetilde{X}_s^{\rm in}(\omega)^2\rangle+\langle[\,\delta B_s^{\rm add}(\omega)/g_s]^2\rangle} \quad \text{and}$$

$$T_m=\frac{\langle \delta\widetilde{X}_s^{\rm in}(\omega)^2\rangle}{\langle \delta\widetilde{X}_s^{\rm in}(\omega)^2\rangle+\langle[\,\delta B_m^{\rm add}(\omega)/g_m]^2\rangle}. \tag{12}$$

The coefficient T_s evaluates to what extent the measurement is nondestructive, i.e., how the signal-to-noise ratio is degraded after the measurement: $T_s=1$ for an ideal nondestructive measurement, while $T_s=0$ if the measurement is totally destructive. Similarly, T_m evaluates the efficiency of the measurement: a perfectly accurate measurement would correspond to $T_m=1$, while $T_m=0$ if no information is gained. For achieving QND performances, one requires that $T_s+T_m>1$, which can be obtained only by using a phase-sensitive device. On the other hand, $T_s+T_m=1$ is the performance of a simple beam splitter [17]. These transfer coefficients are very useful because they are directly accessible in an experiment. The SNR values can indeed be visualized very easily on a spectrum analyzer, and it is then straightforward to measure the various SNR and to work out the transfer coefficients.

From a formal point of view, it is also possible to consider the normalized correlations between the meter or signal output and the signal input quantum fluctuations, which were first introduced by Holland *et al.* in Ref. [16], and which we will calculate theoretically. Precisely one defines

$$C_s=\frac{|\langle \delta X_s^{\rm in}\delta X_s^{\rm out}\rangle_\omega|^2}{\langle \delta X_s^{\rm in}\delta X_s^{\rm in}\rangle_\omega\langle \delta X_s^{\rm out}\delta X_s^{\rm out}\rangle_\omega},$$

$$C_m=\frac{|\langle \delta X_s^{\rm in}\delta Y_m^{\rm out}\rangle_\omega|^2}{\langle \delta X_s^{\rm in}\delta X_s^{\rm in}\rangle_\omega\langle \delta Y_m^{\rm out}\delta Y_m^{\rm out}\rangle_\omega}, \tag{13}$$

where $\langle AB\rangle_\omega$ denotes the Fourier transform of the symmetrized correlation function between the two operators in brackets:

$$\langle AB\rangle_\omega=\int_{-\infty}^{+\infty} e^{-i\omega t}\langle A(t)B\rangle_{\rm sym}dt \quad \text{with}$$

$$\langle A(t)B\rangle_{\rm sym}=\langle A(t)B+BA(t)\rangle/2. \tag{14}$$

Contrary to the previous ones, these quantities cannot be measured directly in a single BAE experiment, because the input fluctuations are not known in advance. However, it can be shown that in the linearized regime for fluctuations and small modulations, and for coherent input states of the fields into the QND device, one simply has

$$C_s=T_s \quad \text{and} \quad C_m=T_m, \tag{15}$$

and the correlation coefficients can be therefore calculated and used as the transfer coefficients; we emphasize, however, that this is not generally true when the input beam has phase-dependent excess noise, in which case some precautions are required [17].

C. Conditional variance

A second application of the QND measurement concerns the situation where we are interested directly in the quantum fluctuations of the fields. If the intensity fluctuations of an incoming beam are measured in a nondestructive way, the acquired information can be used, at the output of the QND device, to correct the signal beam by reducing its fluctuations. The third QND criterion, relative to this application, is given by the output conditional variance of the signal field, given the result of a measurement on the meter field:

$$V_{s|m}=\langle \delta X_s^{\rm out}\delta X_s^{\rm out}\rangle_\omega(1-C_{\rm sm}), \tag{16}$$

where $C_{\rm sm}$ is a normalized correlation between the meter and the signal outputs,

$$C_{\rm sm}=\frac{|\langle \delta X_s^{\rm out}\delta Y_m^{\rm out}\rangle_\omega|^2}{\langle \delta X_s^{\rm out}\delta X_s^{\rm out}\rangle_\omega\langle \delta Y_m^{\rm out}\delta Y_m^{\rm out}\rangle_\omega}, \tag{17}$$

and where $\langle AB\rangle_\omega$ is defined as in Eq. (14).

For an ideal QND device, $C_{\rm sm}=1$ and $V_{s|m}=0$, while in a real device one requires that the information gained by the measurement is sufficient to reduce the intensity fluctuation of the initial beam under the shot-noise level, corresponding to $V_{s|m}<1$.

In a QND experiment, the signal noise reduction is usually not implemented, and the conditional variance $V_{s|m}$ is measured electronically by subtracting the photocurrent of the meter readout $Y_m^{\rm out}$ from the photocurrent of the outgoing signal $X_s^{\rm out}$, with an appropriate gain or attenuation. More precisely, the quantum fluctuations of these recombined currents will be given by the spectral variance of $(X_s^{\rm out}-gY_m^{\rm out})$, where g is an electronic gain or attenuation. In the ideal case, the meter beam will reproduce the actual noise of the output signal beam up to a multiplicative factor, and it will be possible to correct exactly the signal noise by bringing the variance of $(X_s^{\rm out}-gY_m^{\rm out})$ to zero. In the general case, the variance of $(X_s^{\rm out}-gY_m^{\rm out})$ is

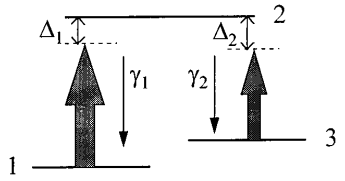

FIG. 1. Energy-level scheme of the Λ three-level atoms.

$$V_{s|m}^{(g)}=\langle \delta X_s^{\rm out}\delta X_s^{\rm out}\rangle_\omega+|g|^2\langle \delta Y_m^{\rm out}\delta Y_m^{\rm out}\rangle_\omega -2\,{\rm Re}(g\langle \delta X_s^{\rm out}\delta Y_m^{\rm out}\rangle_\omega); \tag{18}$$

the minimum value of this quantity is obtained by choosing

$$g=\langle \delta X_s^{\rm out}\delta Y_m^{\rm out}\rangle_\omega^*/\langle \delta Y_m^{\rm out}\delta Y_m^{\rm out}\rangle_\omega, \tag{19}$$

for which choice one has in fact

$$V_{s|m}^{(g)}=V_{s|m}, \tag{20}$$

with $V_{s|m}$ given by Eq. (16). In a real experimental situation, the amplitude and phase of the g factor are adjusted using an attenuator and a delay line in order to minimize the photocurrent difference. The minimum noise level obtained using this procedure gives the value of $V_{s|m}$.

III. MODEL

A. Equations

We consider a three-level atomic medium at rest, inside an optical ring cavity; $\mathcal{L}$ is the roundtrip length of the cavity, occupied by the medium for a length L. Two laser fields of carrier frequencies ω_1 and ω_2 are injected in the cavity; the fields are supposed to be close to resonance with two atomic transitions frequencies ω_r and ω_s, and with two cavity eigenfrequencies ω_{c1} and ω_{c2}. The cavity is single ended for each field, T_i ($i=1$ and 2) being the transmissivity of the coupling mirror. We introduce the decay constants of the fields amplitudes inside the empty (lossless) cavity:

$$\kappa_1=\frac{cT_1}{2\mathcal{L}},\quad \kappa_2=\frac{cT_2}{2\mathcal{L}}, \tag{21}$$

where c is the speed of light in vacuum, and the normalized empty cavity detunings:

$$\theta_1=\frac{\omega_{c1}-\omega_1}{\kappa_1},\quad \theta_2=\frac{\omega_{c2}-\omega_2}{\kappa_2}. \tag{22}$$

The atoms are described as sets of three energy levels disposed in a lambda configuration (Fig. 1). By γ_1 and γ_2 we denote the decay rate constants of the atomic population from the excited level $|2\rangle$ towards levels $|1\rangle$ and $|3\rangle$, respectively, while γ_w, defined as half of the total population decay rate from the upper level,

$$\gamma_w=\frac{\gamma_1+\gamma_2}{2}, \tag{23}$$

is the decay rate constant of the atomic polarizations 1-2 and 3-2 in the radiative limit. We define Δ_1 and Δ_2 the normalized atomic detunings:

$$\Delta_1=\frac{\omega_r-\omega_1}{\gamma_w},\quad \Delta_2=\frac{\omega_s-\omega_2}{\gamma_w}; \tag{24}$$

please note that with definitions (24) positive detunings are red detunings ($\omega_{\rm atom}<\omega_{\rm laser}$). The operators describing the atoms are the polarization operators: σ_{12}, σ_{13}, and σ_{23} obeying the commutation rules

$$[\sigma_{ij},\sigma_{kl}]=\delta_{jk}\sigma_{il}-\delta_{li}\sigma_{kj},\quad i,j=1,2,3, \tag{25}$$

where the δ_{ij} are Kronecker deltas, and the population inversions: $r_3=1/2(\sigma_{22}-\sigma_{11})$ and $s_3=1/2(\sigma_{22}-\sigma_{33})$. The resonant cavity modes are described by the usual boson creation and annihilation operators $a_i^\dagger$ and a_i ($i=1$ and 2), with

$$[a_i,a_i^\dagger]=1,\quad i,j=1,2. \tag{26}$$

The evolution of the system is governed by a master equation for the system density operator ρ, which, in the interaction picture, has the form

$$\frac{\partial\rho}{\partial t}=[-i(L_a+L_f+L_{\rm ext}+L_{\rm af})+\Lambda_a+\Lambda_f]\rho, \tag{27}$$

where

$$L_a\rho=\tfrac{2}{3}\{(2\omega_r-\omega_s)[R_3,\rho]+(2\omega_s-\omega_r)[S_3,\rho]\},$$

$$L_f\rho=(\omega_{c1}-\omega_1)[a_1^\dagger a_1,\rho]+(\omega_{c2}-\omega_2)[a_2^\dagger a_2,\rho],$$

$$L_{\rm ext}\rho=i\{\kappa_1[(\varepsilon_1 a_1^\dagger-\varepsilon_1^* a_1),\rho]+\kappa_2[(\varepsilon_2 a_2^\dagger-\varepsilon_2^* a_2),\rho]\},$$

$$L_{\rm af}\rho=i\{g_1[(a_1^\dagger R^- - a_1 R^+),\rho]+g_2[(a_2^\dagger S^- - a_2 S^+),\rho]\},$$

$$\Lambda_a\rho=\sum_{n=1}^{N}\frac{\gamma_1}{2}([\sigma_{12}^n\rho,\sigma_{21}^n]+[\sigma_{12}^n,\rho\sigma_{21}^n]) +\frac{\gamma_2}{2}([\sigma_{23}^n\rho,\sigma_{32}^n]+[\sigma_{23}^n,\rho\sigma_{32}^n]),$$

$$\lambda_f\rho=\kappa_1\{[a_1\rho,a_1^\dagger]+[a_1,\rho a_1^\dagger]\}+\kappa_2\{[a_2\rho,a_2^\dagger]+[a_2,\rho a_2^\dagger]\}.$$

In this master equation we introduced the collective atomic operators R^+, R^-, S^+, S^-, T^+, T^-, R_3, and S_3 constructed from the single-atom operators σ_{21}^n, σ_{12}^n, σ_{32}^n, σ_{23}^n, σ_{31}^n, σ_{13}^n, r_3^n, and s_3^n, respectively, as described in Ref. [18], and obeying the same commutation rules. The term $L_a\rho$ describes the free evolution of the atoms according to the single-atom Schrödinger Hamiltonian

$$H_a=\tfrac{2}{3}\hbar[r_3(2\omega_r-\omega_s)+s_3(2\omega_s-\omega_r)], \tag{28}$$

where we have conveniently defined the energy of level $|2\rangle$ as $E_{|2\rangle}=\hbar(\omega_s+\omega_r)/3$ in order to get rid of constant factors. Similarly, $L_f\rho$ describes the free evolution of the two cavity modes and $L_{\rm ext}\rho$ accounts for the driving fields ε_1 and ε_2 injected in the cavity. The interaction term $L_{af}\rho$ describes the coupling between fields and atoms, which is written in

the dipole and rotating-wave approximations, g_1 and g_2 being the coupling constants for the transitions 1-2 and 3-2, respectively. The non-Hamiltonian term $\Lambda_a\rho$ accounts for the decay of the atomic polarizations and population inversions (N is the number of atoms), while $\Lambda_f\rho$ accounts for the decay of the intracavity fields due to the escape of photons from the semireflecting cavity mirrors. For simplicity, here we neglect the contributions due to collisions to the decay of the atomic polarization, restricting ourselves to the radiative limit.

By introducing the normalized classical variables, representing mean values of the atomic operators,

$$v=-\frac{\sqrt{2}}{N}\langle R^-\rangle,\quad w=-\frac{\sqrt{2}}{N}\langle S^-\rangle,\quad z=-\frac{1}{N}\langle T^-\rangle,$$

$$m=-\frac{2}{N}\langle R_3\rangle,\quad n=-\frac{2}{N}\langle S_3\rangle, \tag{29}$$

and the normalized Rabi frequencies proportional to the intracavity and input fields E_i and $E_i^{\rm in}$ ($i=1$ and 2),

$$x_i=\frac{\sqrt{2}g_i}{\gamma w}E_i\quad\text{with}\quad E_i=\langle a_i\rangle\quad (i=1,2),$$

$$y_i=\frac{\sqrt{2}q_i}{\gamma_w}\frac{2}{\sqrt{T_i}}E_i^{\rm in}\quad\text{with}\quad E_i^{\rm in}=\varepsilon_i\frac{\sqrt{T_i}}{2}\quad (i=1,2), \tag{30}$$

the semiclassical equations for the normalized variables read

$$\dot{x}_1=-\kappa_1[(1+i\theta_1)x_1-y_1+2C_1v], \tag{31}$$

$$\dot{x}_2=-\kappa_2[(1+i\theta_2)x_2-y_2+2C_2w], \tag{32}$$

$$\dot{v}=-\gamma_w[(1+i\Delta_1)v-x_1m+x_2z], \tag{33}$$

$$\dot{w}=-\gamma_w[(1+i\Delta_2)w-x_2n+x_1z^*], \tag{34}$$

$$\dot{z}=-\gamma_w\left[i(\Delta_1-\Delta_2)z-\frac{1}{2}(x_1w^*+x_2^*v)\right], \tag{35}$$

$$\dot{m}=-\gamma_1\left[\frac{1}{3}(\eta+2)(m+n-1)+\frac{\gamma_w}{\gamma_1}(x_1v^*+x_1^*v)+\frac{\gamma_w}{2\gamma_1}(x_2w^*+x_2^*w)\right], \tag{36}$$

$$\dot{n}=-\gamma_1\left[\frac{1}{3}(1+2\eta)(m+n-1)+\frac{\gamma_w}{2\gamma_1}(x_1v^*+x_1^*v)+\frac{\gamma_w}{\gamma_1}(x_2w^*+x_2^*w)\right], \tag{37}$$

where we have introduced the ratio $\eta=\gamma_2/\gamma_1$ and the cooperativity parameters

$$C_1=\frac{g_1^2N}{2\kappa_1\gamma_w},\quad C_2=\frac{g_2^2N}{2\kappa_2\gamma_w} \tag{38}$$

proportional to the number of atoms that characterize the strength of the coupling between atoms and the two fields.

B. Steady state

Due to the high degree of symmetry of the equations for the lambda system, it is possible to calculate analytically the steady-state solution for the mean values of the atomic operators (29) and the intracavity fields x_1 and x_2, as a function of the input fields intensities and the remaining system parameters.

In the following we give the exact analytical solution for the intracavity fields in the general case for the system parameters. The steady-state mean values are calculated by solving the system of nonlinear equations obtained by setting the right-hand sides of Eqs. (31)–(37) to zero.

By suitable redefinition of the phases of the polarization variables and of the input fields, it is possible have the intracavity fields x_1 and x_2 real numbers at steady state. In particular we introduce the new variables $\tilde{v}=ve^{-i\phi_1^s}$, $\tilde{w}=we^{-i\phi_2^s}$, $\tilde{z}=ze^{-i(\phi_1^s-\phi_2^s)}$, $\tilde{y}_i=y_ie^{-i\phi_i^s}$, and $\tilde{x}_i=|x_i|$ ($i=1$ and 2), where ϕ_i ($i=1$ and 2) is the phase of the ith field at steady state. We shall use these variables in the following, although we omit the ''tildes'' for typing convenience.

1. Solution in the general case

As we said, it is possible to solve exactly the Bloch equations (33)–(37) at steady state, finding the analytical dependence of the atomic variables on the fields variables (x_1,x_2) and system parameters. By substituting the solutions of the Bloch equations in Eqs. (31) and (32) at steady state, one obtains the solutions for the fields, which read

$$x_1^2=\frac{|y_1|^2}{[1+2C_1b^2I_2\Pi]^2+[\theta_1+2C_1bI_2(\eta I_1+I_2-b\Delta_1)\Pi]^2}, \tag{39}$$

$$x_2^2=\frac{|y_2|^2}{[1+2C_2b^2\eta I_1\Pi]^2+[\theta_2-2C_2bI_1(\eta I_1+I_2+b\eta\Delta_2)\Pi]^2}, \tag{40}$$

where we have defined

$$\gamma=2\frac{\gamma_w}{\gamma_1},\quad I_1=x_1^2,\quad I_2=x_2^2,\quad b=2(\Delta_1-\Delta_2),\quad (41)$$

and where

$$\Pi=\Big\{\eta I_1^3+I_2^3+(2\eta+1)I_1^2I_2+(\eta+2)I_1I_2^2+2b\Delta_2\eta I_1^2 -2b\Delta_1I_2^2+b\Big[\frac{3}{2}\gamma b+(1+\eta)(\Delta_2-\Delta_1)\Big]I_1I_2+b^2\eta(\Delta_2^2+1)I_1+b^2(\Delta_1^2+1)I_2\Big\}^{-1}. \quad (42)$$

2. Phases of the input and output fields

Let us consider Eqs. (31) and (32) at the steady state; from Eq. (30), one has

$$E_1^{\rm in}=M_1[(1+i\theta_1)x_1+2C_1v], \quad (43)$$

$$E_2^{\rm in}=M_2[(1+i\theta_2)x_2+2C_2w], \quad (44)$$

where $M_i=(\gamma_w\sqrt{T_i})(2\sqrt{2}g_i)^{-1}$ are proportionality constants. The phases $\Theta_1^{\rm in}$ and $\Theta_2^{\rm in}$ of the input fields are then calculated as $\Theta_1^{\rm in}=\arctan[{\rm Im}(E_i^{\rm in})/{\rm Re}(E_i^{\rm in})]$ for ($i=1$ and 2). By using Eqs. (30), (43), and (44), and the boundary condition for our single-port cavity,

$$E_i^{\rm out}+E_i^{\rm in}=\sqrt{T_i}E_i\quad (i=1,2), \quad (45)$$

one has

$$E_1^{\rm out}=-M_1[(-1+i\theta_1)x_1+2C_1v], \quad (46)$$

$$E_2^{\rm out}=-M_2[(-1+i\theta_2)x_2+2C_2w], \quad (47)$$

from which the phases the phases $\Theta_1^{\rm out}$ and $\Theta_2^{\rm out}$ of the output fields are calculated in the same way.

3. Double-resonance condition

By using the steady-state solutions (39) and (40), we may easily find the condition in which both fields are resonant in the cavity at the same time. This situation is particularly favorable for the QND experiment [12], and it can be expressed as a precise requirement on the cavity detunings and input fields amplitudes, given certain values of the intracavity fields intensities I_1, and I_2, and atomic detunings Δ_1 and Δ_2. Such requirements read

$$\theta_1=-2C_1bI_2(\eta I_1+I_2-b\Delta_1)\Pi, \quad (48)$$

$$\theta_2=2C_2bI_1(\eta I_1+I_2+b\eta\Delta_2)\Pi, \quad (49)$$

$$|y_1|=\sqrt{I_1}(1+2C_1b^2I_2\Pi), \quad (50)$$

$$|y_2|=\sqrt{I_2}(1+2C_2b^2\eta I_1\Pi). \quad (51)$$

It should be noted that, in practice, it will not be trivial to realize the double-resonance condition for a given cavity and for a given atomic system. On the one hand, the choice of the laser frequencies fixes the cavity and atomic detunings, and, on the other hand, for the fields to be resonant, these quantities have to linked by relations (48) and (49). This constraint will be discussed below.

C. Constraint on the detunings

We think it is worth considering in some detail how the double-resonance conditions (48)–(51) can be achieved in an experiment; to this aim, we introduce the normalized detunings

$$\Delta_A=\frac{\omega_r-\omega_s}{\gamma_w},\quad \Delta_C=\frac{\omega_{c1}-\omega_{c2}}{\kappa_1}, \quad (52)$$

representing the distance in frequency between the two lower atomic levels and between the two cavity eigenfrequencies nearly resonant with the input fields, respectively. We point out that, due to its normalization, Δ_C does not depend on the cavity length. By construction, a relation holds between the cavity and the atomic detunings introduced so far:

$$\theta_1=\left(\frac{\kappa_2}{\kappa_1}\right)\theta_2=(\Delta_1-\Delta_2-\Delta_A)\frac{\gamma_w}{\kappa_1}+\Delta_C. \quad (53)$$

Equation (53) tells us that once the distance in frequency between the two lasers is fixed, for example, by our choice of the atomic detunings, the difference between the cavity detunings is automatically fixed by the properties of the cavity through Δ_C, κ_1, and κ_2. On the other hand, if we need both fields at resonance in the cavity, the cavity detunings should compensate for the phase shifts introduced by the atoms, which impose that:

$$\theta_1-\left(\frac{\kappa_2}{\kappa_1}\right)\theta_2=F(C_1,C_2,I_1,I_2,\Delta_1,\Delta_2), \quad (54)$$

where F is a function of the indicated parameters which is obtained easily from Eq. (48) and (49). Equations (53) and (54) represent thus two independent requirements on the quantity $\theta_1-(\kappa_2/\kappa_1)\theta_2$ which should be fulfilled at the same time. In particular, the right-hand sides of Eqs. (53) and (54) should be equal, which constraints, for a given cavity and a given medium, the possible values of the atomic detunings and intracavity fields for which the double-resonance condition can be achieved.

We will return to this constraint on parameters in Sec. IV B by considering in particular the case of our experimental setup and the mean fields configuration that we use to perform the QND measurements. Before this, however, we would like to go back to Eq. (53) and make some further remarks. Equation (53) is a relation between the cavity and the atomic detunings that is automatically fulfilled in a real experiment, suggesting that the four parameters of our model should not be considered as independent. In order to evaluate the significance of this relation in the different experimental situations, we rewrite Eq. (53) as

$$\theta_1-\left(\frac{\kappa_2}{\kappa_1}\right)\theta_2=\frac{4\pi}{T_1}\left(\frac{1}{\lambda_2}-\frac{1}{\lambda_1}\right)\mathcal{L}+\Delta_C, \tag{55}$$

where we used Eqs. (21), (24), and (52). Now several situations are possible. Suppose first that the frequencies ω_1 and ω_2 of the input fields are well separated on the optical-frequency scale (as, for example, in the experiments described in Refs. [6, 8]). Equation (55) shows that extremely small adjustments of the cavity length $\mathcal{L}$, on the order of $1/[(1/\lambda_1)-(1/\lambda_2)]\sim\lambda$, are in this case sufficient to adjust at will the difference $\theta_1-(\kappa_2/\kappa_1)\theta_2$ once the two laser frequencies have already been fixed. In such conditions, atomic and cavity detunings can in fact be considered as independent parameters; and in particular the double-resonance conditions (48) and (49) can be realized without any restriction on the atomic detunings Δ_1 and Δ_2. Let us now consider the opposite case in which the two frequencies ω_1 and ω_2 are very close one another. This could be, for example, the case when the two ground levels of the lambda scheme are degenerate Zeeman sublevels. If ω_1 and ω_2 are only a few MHz apart, adjustments of the cavity length on the order of the *meter* (that is of course out of reach in an experiment) would be necessary in order to change the difference $\theta_1-(\kappa_2/\kappa_1)\theta_2$ by some units when the laser frequencies have already been fixed. In this case Eq. (53) represents a serious constraint that cannot be overcome by adjustments of the cavity length. In between the two limiting cases considered above, there are situations in which, if on the one hand Eq. (53) represents a real constraint, still some room is left for small adjustments of the cavity detunings by significant changes of $\mathcal{L}$. A similar situation is encountered in the experiment with cold atoms that we consider in detail in this paper (Sec. V), where the two ground levels of the lambda scheme are hyperfine sublevels 6.83 GHz apart.

D. Quantum noise analysis

In order to calculate the QND coefficients defined in Sec. II, we are interested in the time-dependent correlation functions of the fields whose amplitude and phase fluctuate around a steady-state mean value. We consider the case in which the the fluctuations are small with respect to the mean values and a linearized treatment of the fluctuations is possible. Let Ξ_i^{ϕ} be a certain quadrature of the ith field ($i=1$ and 2), relative to the reference phase ϕ:

$$\Xi_i^{\phi}=a_i e^{-i\phi}+a_i^{\dagger}e^{i\phi}. \tag{56}$$

In the notations of Sec. II, and referring to the phases of the input and output fields at steady state introduced in Sec. III B, one has

$$\delta X_s^{\rm in}=\delta\Xi_2^{\Theta_2^{\rm in}} \quad \delta X_s^{\rm out}=\delta\Xi_2^{\Theta_2^{\rm out}}$$

$$\delta Y_m^{\rm in}=\delta\Xi_1^{\Theta_1^{\rm in}(\pi/2)} \quad \delta Y_m^{\rm out}=\delta\Xi_1^{\Theta_1^{\rm out}+(\pi/2)} \tag{57}$$

where by $\delta\Xi_i^{\phi}$ we denote the time-dependent fluctuation of the operator Ξ_i^{ϕ} around a steady-state point in the Heisenberg picture:

$$\delta\Xi_i^{\phi}=\delta a_i e^{-i\phi}+\delta a_i^{\dagger}e^{i\phi}, \quad \text{with} \quad \delta a_i=a_i-\langle a_i\rangle \quad (i=1,2). \tag{58}$$

By using the the input-output relations [19]

$$a_i^{\rm out}+a_i^{\rm in}=\sqrt{2\kappa_i}a_i \quad (i=1 \quad \text{and} \quad 2), \tag{59}$$

whose classical counterpart is represented by Eq. (45), and assuming that the input fields are in a coherent state, one obtains

$$\begin{aligned}\langle \delta X_s^{\rm in}(t)\,\delta Y_m^{\rm out}\rangle_{\rm sym}=i\sqrt{\kappa_1\kappa_2}\;\Theta(t)[&\langle[\alpha_1^{\dagger}(t),\alpha_2]\rangle e^{i(\Theta_1^{\rm out}-\Theta_2^{\rm in})}\\ &-\langle[\alpha_1^{\dagger}(t),\alpha_2^{\dagger}]\rangle e^{i(\Theta_1^{\rm out}+\Theta_1^{\rm in})}\\ &-\langle[\alpha_1(t),\alpha_2]\rangle e^{-i(\Theta_1^{\rm out}+\Theta_2^{\rm in})}\\ &+\langle[\alpha_1(t),\alpha_2^{\dagger}]\rangle e^{-i(\Theta_1^{\rm out}-\Theta_2^{\rm in})}],\end{aligned} \tag{60}$$

$$\begin{aligned}\langle \delta X_s^{\rm in}(t)\,\delta X_s^{\rm out}\rangle_{\rm sym}=\kappa_2\Theta(t)[&-\langle[\alpha_2(t),\alpha_2]\rangle e^{-i(\Theta_2^{\rm out}+\Theta_2^{\rm in})}\\ &+\langle[\alpha_2^{\dagger}(t),\alpha_2^{\dagger}]\rangle e^{i(\Theta_2^{\rm out}+\Theta_2^{\rm in})}\\ &+\langle[\alpha_2^{\dagger}(t),\alpha_2]\rangle e^{-i(\Theta_2^{\rm out}-\Theta_2^{\rm in})}\\ &-\langle[\alpha_2(t),\alpha_2^{\dagger}]\rangle e^{i(\Theta_2^{\rm out}-\Theta_2^{\rm in})}]\\ &-\delta(t)\cos(\Theta_2^{\rm out}-\Theta_2^{\rm in}),\end{aligned} \tag{61}$$

$$\begin{aligned}\langle \delta X_s^{\rm out}(t)\,\delta Y_m^{\rm out}\rangle_{\rm sym}=-2i\sqrt{\kappa_1\kappa_2}[&-\langle:\alpha_1(t)\alpha_2:\rangle\\ &\times e^{-i(\Theta_1^{\rm out}+\Theta_2^{\rm out})}+\langle:\alpha_1^{\dagger}(t)\alpha_2:\rangle\\ &\times e^{i(\Theta_1^{\rm out}-\Theta_2^{\rm out})}-\langle:\alpha_1(t)\alpha_2^{\dagger}:\rangle\\ &\times e^{-i(\Theta_1^{\rm out}-\Theta_2^{\rm out})}+\langle:\alpha_1(t)^{\dagger}\alpha_2^{\dagger}:\rangle\\ &\times e^{i(\Theta_1^{\rm out}+\Theta_2^{\rm out})}],\end{aligned} \tag{62}$$

where the dots in Eq. (62) mean time and normal ordering:

$$\langle:\alpha_i(t)\alpha_j^{\dagger}:\rangle=\langle\alpha_j^{\dagger}\alpha_i(t)\rangle,$$

$$\langle:\alpha_i(t)^{\dagger}\alpha_j:\rangle=\langle\alpha_i(t)^{\dagger}\alpha_j\rangle,$$

$$\langle:\alpha_i(t)\alpha_j:\rangle=\Theta(-t)\langle\alpha_j\alpha_i(t)\rangle+\Theta(t)\langle\alpha_i(t)\alpha_j\rangle,$$

$$\langle:\alpha_i(t)^{\dagger}\alpha_j^{\dagger}:\rangle=\Theta(-t)\langle\alpha_i(t^{\dagger})\alpha_i^{\dagger}\rangle+\Theta(t)\langle\alpha_j^{\dagger}\alpha_i(t)^{\dagger}\rangle,$$

where $\Theta(t)$ is the step-function taking the values 1, $\frac{1}{2}$ or 0, when t is larger than, equal to, or smaller than zero, respectively, and where for brevity we have introduced the notation

$$\alpha_i=\delta a_i=a_i-\langle a_i\rangle \quad (i=1 \quad \text{and} \quad 2). \tag{63}$$

By taking the Fourier transforms of the symmetrized correlations (60)–(62), we are eventually concerned with the calculation of response functions

$$R_{jk}(\omega)=\int_{-\infty}^{+\infty}\Theta(\tau)\langle[\beta_j(\tau),\beta_k]\rangle e^{-i\omega\tau}d\tau \quad (j,k=1,2,3,4). \tag{64}$$

and normally ordered correlation functions

$$S_{jk}(\omega)=\int_{-\infty}^{\infty}\langle:\beta_j(\tau)\beta_k:\rangle e^{-i\omega\tau}d\tau, \quad (j,k=1,2,3,4), \tag{65}$$

where we have introduced the vector β_j ($j=1$ and 12) of system operator fluctuations:

$$\beta=[\alpha_1,\alpha_1^\dagger,\alpha_2,\alpha_2^\dagger,\delta R^-,\delta R^+,\delta S^-,\delta S^+,\delta T^-,\delta T^+,\delta R_3,\delta S_3]^T. \tag{66}$$

In the linearized regime Eqs. (64) and (65) can be easily calculated by using the master equation. We carefully checked that our method, relying on the master equation formalism and the quantum regression theorem [20], gives results identical to the method based on linear-response theory in the frequency domain developed by Courty and Grangier [21], and with the method using the input-output formalism of Collett and Gardiner in the time domain [19,12]. The result for the response functions is

$$R_{jk}(\omega)=[(A+i\omega I)^{-1}C^0]_{jk}, \tag{67}$$

where A is the (12×12) drift matrix obtained linearizing Eqs. (31)–(37) [and the complex conjugates of Eqs. (31)–(35)], and C^0 is the matrix of the equal-time commutators, i.e.,

$$C^0_{ij}=\langle[\beta_i,\beta_j|]\rangle. \tag{68}$$

For the normally ordered correlation functions, one has, instead

$$S_{jk}(\omega)=[(A+i\omega I)^{-1}D_N(A^T-i\omega I)^{-1}]_{jk}, \tag{69}$$

where D_N is the normally ordered diffusion matrix that we report for completeness in the Appendix. The results for the interesting correlations between input and output fields are

$$\langle\delta X_s^{\rm in}\delta Y_m^{\rm out}\rangle_\omega=i\sqrt{\kappa_1\kappa_2}[R_{23}e^{i(\Theta_i^{\rm out}-\Theta_2^{\rm in})}-R_{24}e^{i(\Theta_1^{\rm out}+\Theta_2^{\rm in})}-R_{13}e^{-i(\Theta_1^{\rm out}+\Theta_2^{\rm in})}+R_{14}e^{-i(\Theta_1^{\rm out}-\Theta_2^{\rm in})}], \tag{70}$$

$$\langle\delta X_s^{\rm in}\delta X_s^{\rm out}\rangle_\omega=-\cos(\Theta_2^{\rm out}-\Theta_2^{\rm in})+\kappa_2[-R_{33}e^{-i(\Theta_2^{\rm out}+\Theta_2^{\rm in})}+R_{44}e^{i(\Theta_{2\rm out}+\Theta_2^{\rm in})}+R_{34}e^{-i(\Theta_2^{\rm out}-\Theta_2^{\rm in})}-R_{43}e^{i(\Theta_2^{\rm out}-\Theta_2^{\rm in})}]. \tag{71}$$

The useful correlations involving only the output fields are instead

$$\langle\delta X_s^{\rm out}\delta Y_m^{\rm out}\rangle_\omega=-2i\sqrt{\kappa_1\kappa_2}[-S_{13}e^{-i(\Theta_1^{\rm out}+\Theta_2^{\rm out})}+S_{23}e^{i(\Theta_1^{\rm out}-\Theta_2^{\rm out})}-S_{14}e^{-i(\Theta_1^{\rm out}-\Theta_2^{\rm out})}+S_{24}e^{i(\Theta_1^{\rm out}+\Theta_2^{\rm out})}], \tag{72}$$

$$\langle\delta X_s^{\rm out}\delta X_s^{\rm out}\rangle_\omega=1+2\kappa_2[S_{34}+S_{43}+S_{33}e^{-i2\Theta_2^{\rm out}}+S_{44}e^{i2\Theta_2^{\rm out}}], \tag{73}$$

$$\langle\delta Y_m^{\rm out}\delta Y_m^{\rm out}\rangle_\omega=1+2\kappa_1[S_{12}+S_{21}-S_{11}e^{-i2\Theta_1^{\rm out}}-S_{22}e^{i2\Theta_1^{\rm out}}]. \tag{74}$$

IV. WORKING POINT FOR QND: THEORETICAL ANALYSIS

In this section we analyze, from a theoretical viewpoint, the configuration necessary to perform the QND measurement which was used in the experiment with cold atoms described in Sec. V. Rather then repeating a general analysis of the scheme, which was done in Ref. [12], we shall give some details on how the scheme can be realized and optimized in a real experiment by taking explicitly into account the constraints imposed by the optical cavity and by the atomic energy-level configuration.

A. Ghost transition scheme

We consider a configuration proposed by Gheri *et al.* [12], using a very intense signal field and a much weaker meter field driving the transitions 3-2 and 2-1 of the three-level atoms respectively. The strong signal has the double effect of (1) dressing the atomic transition 3-2 to which it is applied, and (2) transferring most of the atomic population to the ''bare'' ground level $|1\rangle$. The coupling between the two fields is achieved by tuning the meter in proximity of one of the two Rabi-split levels, originating from the bare excited state $|2\rangle$, whose separation depends upon the intensity of the strong field. In particular, under the proper conditions, a very efficient coupling between the signal intensity and the meter phase can be exploited for the QND measurement. Moreover, due to the large difference in strength between the meter and the signal field, nearly all the atomic population remains in the ground level $|1\rangle$ with the consequent advantage of keeping signal-absorption (and spontaneous emission) low. To a first approximation the signal is applied to an empty transition. This is why this configuration was called ''ghost transition scheme'' in Ref. [12].

In Figs. 2 and 3(a), we report two examples of the QND performances of the Λ scheme in the ghost transition configuration with parameters which are typical of our experiment. The QND criteria are calculated, at a fixed frequency of analysis, as a function of the meter atomic detuning which is scanned across the two Rabi-split levels, the meter being exactly tuned on one of the two dressed levels for $\Delta_1=$

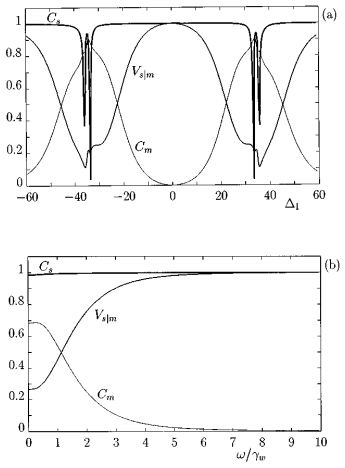

FIG. 2. (a) QND coefficients for $\omega=0$ as a function of the meter atomic detuning Δ_1. (b) QND coefficients for $\Delta_1=40.5$ as a function of the frequency of analysis ω/γ_w. Other parameters: $I_1=2$, $I_2=2450$, $\Delta_2=0$, $\Delta_1=40.5$, $C_1=135$, $C_2=90$, and $\kappa_1=\kappa_2=3\gamma_w$.

∓ 35 in both figures. Since the signal is taken at resonance with the atoms, the curves are symmetric with respect to $\Delta_1=0$. In these pictures, following the treatment in Ref. [12], we supposed both fields to be at resonance with the cavity, and we arbitrarily fixed the intracavity fields intensities I_1 and I_2 in a convenient range inspired from the experiment. The two figures differ in the value of I_1 which is four times larger in Fig. 3 than in Fig. 2. In both cases $I_2 \gg I_1$, as required by the ghost transition scheme. A convenient choice for the meter tuning is in proximity of the Rabi-split levels,

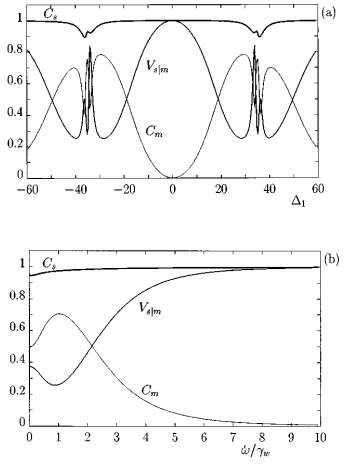

FIG. 3. (a) QND coefficients for $\omega=0.9\gamma_w$ as a function of the meter atomic detuning Δ_1. (b) QND coefficients for $\Delta_1=40.5$ as a function of the frequency of analysis ω/γ_w. Other parameters: $I_1=8$, $I_2=2450$, $\Delta_2=0$, $\Delta_1=40.5$, $C_1=135$, $C_2=90$, and $\kappa_1=\kappa_2=3\gamma_w$.

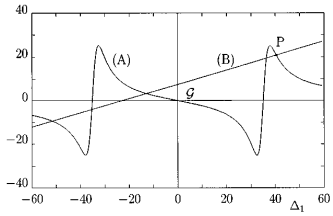

FIG. 4. Curve (A) [double-resonance condition (54)] and curve (B) [constraint relation (53) on the detunings], as functions of the meter atomic detuning Δ_1. Parameters: $I_1=8$, $I_2=2450$, $\Delta_2=0$, $C_1=135$, $C_2=90$, $\kappa_1=\kappa_2=3.05\gamma_w$, $\Delta_A=2276.6667$, $\Delta_C=753.9822$, and $\mathcal{G}=7.49$.

keeping, however, a certain detuning from the resonance with the Rabi levels in order to avoid strong meter absorption and consequent degradation of the ghost transition scheme [12].

In Figs. 2 and 3(b), we show the frequency dependence of the QND criteria for $\Delta_1=40.5$ in both cases. The frequency is normalized to γ_w, which in our case is about $\gamma_w/2\pi=3$ MHz. The case represented in Fig. 3(b), corresponding to $I_1=8$, $I_2=2450$, $\Delta_1=40.5$, and $\Delta_2=0$, seems more convenient from the experimental point of view, displaying the best QND performances ($C_s\simeq 0.9$, $C_m\simeq 0.7$, and $V_{s|m}\simeq 0.2$) around 3 MHz, which is above low-frequency technical noise.

B. Choice of the input fields and cavity parameters

By using our model, we wish to calculate the proper amplitudes and cavity detunings of the input fields, such that the favorable case represented in Fig. 3(b) is actually recovered in a realistic system.

We already know from Sec. III C that there is no complete freedom in choosing the cavity and the atomic detunings, and that Eqs. (53) and (54) should be fulfilled at the same time in order to have both fields at resonance in the cavity. We have represented these two conditions graphically in Fig. 4 as a function of the meter atomic detuning Δ_1. Curve (A) represents Eq. (54) when I_1, I_2, and Δ_2 are the same as in Fig. 3(b) (note that in the limit of strong signal and weak meter this curve represents as well the meter dispersion or phase shift). Curve (B) represents Eq. (53), with the parameters of our experiment and for a given value of the cavity length. At the intersection points between the two curves, both relations are satisfied, and Eqs. (48)–(51) can be used to calculate the exact values of the cavity detunings and input field amplitudes in order that the fields are set simultaneously at resonance in the cavity, with given values of I_1, I_2, and Δ_2 and with a value of Δ_1 corresponding to the intersection point we have chosen. In particular, for the intersection point P corresponding to $\Delta_1=40.5$, one recovers exactly the situation of Fig. 3(b).

The curves in Fig. 4 make it clear that, due to the constraint relation (53), the simultaneous resonance of the fields in the cavity can be achieved *only* for some particular sets of values of the atomic and cavity detunings. On the other hand, we have already pointed out that in many cases of interest the constraint coming from Eq. (53) can be overcome by

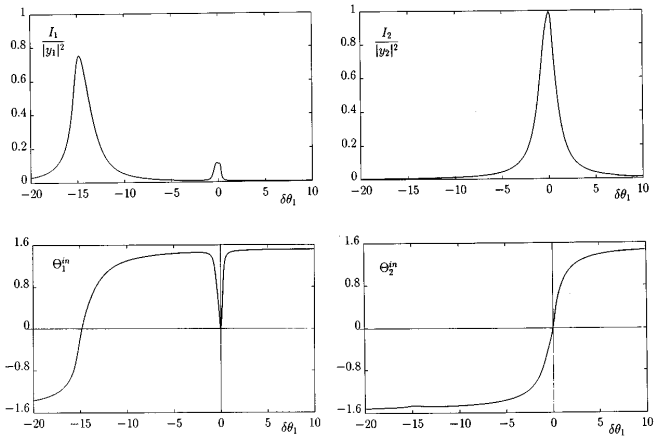

FIG. 5. Steady-state intensities (top) and phases (bottom) for the meter (left) and signal (right) fields as functions of the cavity detuning. The intensities I_1 and I_2 are normalized to the input intensities $|y_1|^2$ and $|y_2|^2$, respectively. Parameters: $y_1=8.6526$ $y_2=49.7193$, $\Delta_1=40.5$, $\Delta_2=0$, $C_1=135$, $C_2=90$, $\kappa_1=\kappa_2=3.05\gamma_w$, $\theta_{01}=20.9095$, $\theta_{02}=0.1360$, and $\mathcal{G}=7.49$.

adjusting the cavity length. In Fig. 4 these adjustments would correspond roughly to translate curve (B) thus ''choosing'' within some range the intersection point with curve (A). In a real experiment, in fact, what can be set precisely is not directly the cavity length but the $\mathcal{L}$-dependent quantity

$$\mathcal{G}=-\Delta_A\frac{\gamma_w}{\kappa_1}+\Delta_C, \tag{75}$$

accurately measured as the distance (in κ_1 units) between the empty-cavity resonances of the two fields when those are tuned exactly on the atomic resonances. This can be easily seen by setting $\Delta_1=\Delta_2=0$ in Eq. (53), which gives $\theta_1-(\kappa_2/\kappa_1)\theta_2=-\Delta_A(\gamma_w/\kappa_1)+\Delta_C$. In Fig. 4 (for $\Delta_2=0$) the quantity $\mathcal{G}$ is just the height of curve (B) at $\Delta_1=0$, equal in this case to $\mathcal{G}=7.5$.

C. Mean fields across the cavity scan

In order to understand more clearly how the double-resonance condition of the fields is achieved in the cavity, and to compare the theory with the experimental results, it is useful to plot the mean-field intensities of the signal and the meter when the cavity is scanned across the field resonance. In the experiment, this is done by sweeping in time the cavity length by a small amount $\pm\delta\mathcal{L}$ around the value $\mathcal{L}_0$ for which both fields are resonant in the cavity. To simulate the experimental procedure in our model, we decompose the cavity detunings θ_i $(i=1$ and $2)$ in Eqs. (31) and (32) as sums of two terms $\theta_i=\theta_{0i}+\delta\theta_i$, where θ_{0i} is a fixed initial cavity detuning, and $\delta\theta_i$ is a change in the detuning due to the variation of the cavity length. It is easy to verify that the $\delta\theta_i$ must satisfy

$$\delta\theta_1=\frac{\lambda_2 T_2}{\lambda_1 T_1}\,\delta\theta_2 \tag{76}$$

where λ_i $(i=1$ and $2)$ are the wavelengths of the modes, and T_i are the mirror transmission coefficients.[1] We plot an example in Fig. 5, where the input parameters are chosen as described in Sec. IV B. On the left we show the meter field intensity (upper curve) and phase (lower curve) across the cavity scan, and the same is shown on the right for the signal field. While the signal intensity curve displays the usual Lorenzian shape centered about the cavity resonance, the meter intensity curve displays two peaks: the ''proper'' resonance peak, shifted from its empty-cavity position $\delta\theta_1=-\theta_{01}$ by the linear and nonlinear dispersive responses of the atoms to the meter field alone; and a second peak, of necessarily nonlinear origin, induced in the meter at the signal resonance position for $\delta\theta_1=0$. Intuitively, the extra resonance in the meter field appears if the phase shift induced in the meter by the resonant signal equals the initial difference between the empty-cavity resonances of the two fields. In this very point of the cavity scan, where both fields are at resonance in the cavity (i.e., $\delta\theta_1=\delta\theta_2=0$), the configuration in Fig. 3(b) is in fact realized.

In Fig. 6 we show the corresponding QND coefficients calculated, at a fixed frequency of analysis $(\omega/2\pi=2.7$ MHz), along the cavity scan in the region of the induced peak where the fields are favorably coupled for QND. The best point of the scan is achieved at about $\delta\theta_1=0$, proving that the double-resonance condition of the two fields is actually the most favorable for the QND measurement. With this result in mind, parameters optimization, at least in principle, looks simpler: as a first step one adjusts the cavity

[1]When the cavity length is varied by a small amount $\mathcal{L}=\mathcal{L}_0+\delta\mathcal{L}$ from the definitions (22) and (21), and $\omega_{ci}=n_i 2\pi c/\mathcal{L}$ with $(i=1,2)$ and n_i an integer, one has $\theta_i=\theta_{0i}+\delta\theta_i$, with

$$\delta\theta_1=\frac{4\pi}{T_1}\frac{1}{\lambda_1}\,\delta\mathcal{L},\quad \delta\theta_2=\frac{4\pi}{T_2}\frac{1}{\lambda_2}\,\delta\mathcal{L},$$

from which Eq. (76) follows. In the case of our experiment, with $[(\lambda_2-\lambda_1)/\lambda_1]\simeq 10^{-5}$ and $T_1=T_2$, along the cavity scan we can approximate $\delta\theta_1=\delta\theta_2$.

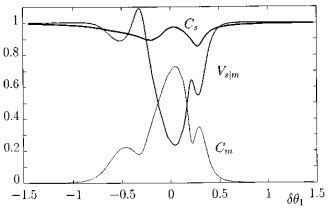

FIG. 6. QND coefficients for $\omega=0.9\gamma_w$ as a function of the cavity detuning in the region of the double-resonance position ($\delta\theta_1=0$). Parameters as in Fig. 5.

length as described in Sec. IV B. Then one adjusts the fields input powers, the laser frequencies, and the cavity detuning, in order to recover the favorable double-resonance configuration. If the result is not satisfactory, the whole process can be iteratively repeated for another cavity length.

V. EXPERIMENTAL SETUP

A. Magneto-optical trap

The MOT is built in a large ultrahigh vacuum (UHV) chamber, designed in order to set up the optical cavity directly around the cold atom cloud. The present setup uses ^{87}Rb atoms, with nuclear spin $I=\frac{3}{2}$, whose ground state $5S_{1/2}$ and excited states $5P_{3/2}$ ($D2$ line) and $5P_{1/2}$ ($D1$ line) are shown in Fig. 7 with their hyperfine sublevel structures. The trap is loaded by slowing down an atomic beam using the standard chirped-frequency technique [22]. The atomic beam part is separated from the UHV chamber containing the trap by a differential pumping aperture, which allows us to obtain a UHV pressure of a few 10^{-10} mbar in operating conditions. The central part of the chamber is about 80 cm far from the oven; at this point the atomic beam has a diameter of about 7 mm, and it is offset from the trap center by 1 cm. The ''slowing'' diode is swept on the quasiclosed $F=2$ to $F'=3$ transition on the $D2$ line at 780 nm (see Fig. 7), and a ''repumping'' diode is swept simultaneously on the $F=1$ to $F'=2$ transition. Both of them are free-running single-mode laser diodes (Hitachi HL 7851G and Mitsubishi ML 64110N-01). The powers sent onto the atoms are 30 (slowing) and 15 mW (repumping), with a 15-mm-diameter light beam whose part which could hit the trapped atomic cloud is carefully screened.

The atoms are trapped using a standard six-beams σ^+/σ^- MOT configuration [23]. A quadrupole magnetic field with a 8-G/cm gradient on axis is provided by two anti-Helmholtz

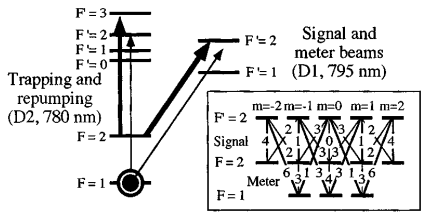

FIG. 7. Energy-level scheme of ^{87}Rb. The inset shows the relative strength for coupling the signal and meter beams which have linear orthogonal polarization.

coils spaced by about 50 mm, with a current of 20 A. The trapping lasers are two 100-mW laser diodes (SDL-5411-H2), injection locked to a master laser, which is a grating-extended laser diode locked to an appropriate saturated absorption line. An acousto-optical frequency shifter ensures an adjustable detuning. During the experiment, the trapping beams were detuned four natural linewidths to the red of the $F=2$ to $F'=3$ transition of the $D2$ line of rubidium atoms. The total power on the trap is typically three times 30 mW, with a beam diameter of 20 mm. As it is for the slowing process, a repumping laser diode (Mitsubishi ML 64110N-01) is locked on the $F=1$ to $F'=2$ transition, and pumps back into the trapping cycles the atoms which were lost in the $F=1$ ground state. This beam is superimposed on the trapping beams along two of the three axes. Its central part is screened thus forming a ''dark spot'' in the fields transverse profile [15], which is imaged at the trap location. In this way, the atoms in the trap cannot be repumped in the trapping cycle and, on average, about 90% of the population of the cloud is in the $F=1$ ground state. This point will be essential to allow simultaneous and continuous operation of the trap and QND experiments. The trap's absorption in the $F=1$ level is monitored using a weak probe beam. The trap fluorescence, mostly induced by the residual percentage of atoms in the $F=2$ state that are excited by the trapping beams, is measured by imaging it on a photodiode. The diameter of the trap is measured with a CCD camera, either in fluorescence ($F=2$) or in absorption ($F=1$); both measurements yield a value close to 3.5-mm full width at half maximum. The estimated values of the number N of atoms and density n in the $F=1$ dark state are $N=10^9$ and $n=5\times10^{10}$ atoms/cm^3.

B. Doubly resonant cavity

In order to obtain large effects at the quantum noise level, a vertical optical cavity is, set up inside the UHV chamber around the cold-atom cloud. The cavity mirrors have a 60 mm radius of curvature. Thanks to screws and piezoelectric transducers that can be handled from outside the UHV chamber, the cavity length is adjustable from 64 to 68 mm. The input-output cavity mirror has a 5% transmissivity. The upper mirror has a very low transmissivity (3×10^{-5}), and it is used to monitor the intracavity intensities while the cavity is scanned, thanks to two photomultipliers (see Fig. 8).

The level scheme used for the QND effect is shown in Fig. 7. The signal and the meter beams are tuned on the $D1$ line at 795 nm (whereas, as we already stated, the trapping and repumping beams are tuned on the $D2$ line at 780 nm). The signal is linearly polarized and tuned close to the $5S_{1/2}F=2$ to $5P_{1/2}F'=2$ transition with a typical input power of 15 μW. The meter beam, on the $F=1$ to $F'=2$ transition, is linearly polarized but orthogonally to the signal, and is tuned to the red with respect to the dressed levels due to the signal-atom coupling. Its typical input power is 250 nW. Both beams are emitted by two independent frequency-stabilized titanium-sapphire lasers. We carefully checked that they are shot noise limited both in intensity and phase in the frequency range of interest (2–20 MHz), which corresponds to our noise analysis frequency band since the linewidth of our cavity is $2\kappa/2\pi=18$ MHz. The two beams are carried onto the optical table by optical fibers which ensure

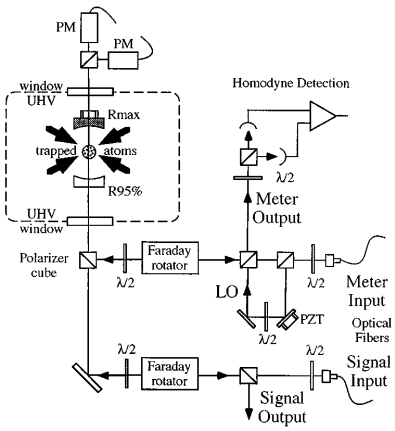

FIG. 8. Schematic view of the experimental setup. The input signal and meter beams are mode matched to an optical cavity surrounding the trapped atoms. Output beams are separated from the input ones using Faraday rotators. The signal beam is directly detected, while the meter beam undergoes a phase-sensitive homodyne detection.

very good spatial mode quality and best mechanical stability. They are mode matched to the optical cavity whose finesse is 125 with an efficiency above 99%. We also measured the optical transmission of the whole system, which is equal to 90% whereas the on-resonance losses of the cavity are negligibly small.

Note that the frequency difference between the signal and meter beam has to be close to the ground-state hyperfine splitting of ^{87}Rb, which is 6.83 GHz. Since both beams also have to be resonant on the cavity, this detuning has to be close to an integer number of the free spectral range (FSR) of the cavity. This is indeed the case when the cavity length is 66 mm, corresponding to a FSR of 2.27 GHz: the two beams are then shifted by three FSR's. As stated above, fine adjustment of the FSR value are still possible while the experiment is running. We note also that the two standing-wave patterns from the signal and meter beams have to be in phase at the atom location, so that the atoms see the appropriate Rabi frequencies from each beam. This is achieved by placing the trapped atoms cloud at one third of the cavity length, i.e., close to 22 mm from one mirror and 44 mm from the other one.

Finally, the output signal is directly detected by a high efficiency photodiode (Centronix BPX-65, quantum efficiency 92%), whereas the meter beam is detected by a phase-sensitive homodyne detection. The fringe visibility (homodyne efficiency) obtained by mode matching the local oscillator onto the meter beam output is 96%.

VI. EXPERIMENTAL RESULTS AND COMPARISON WITH THEORY

A. Mean-field configuration

The configuration we use to perform the QND measurement closely retraces what we have illustrated so far in theory. The strong signal is tuned slightly to the red of its atomic resonance, while the weak meter it is tuned to the red with respect to the lower of the two dressed levels originating from the excited state $|2\rangle$ due to the atom-signal coupling. In the experimental situation and in the notations of our model, the typical input powers of 15 μW for the signal and of 250 nW for the meter correspond to normalized amplitudes of the injected fields equal to $y_2=56$ and $y_1=7$, respectively, while the initial choice of the cavity length for which the two atomic frequencies are almost exactly three FSR's apart corresponds [see Eq. (75)] to $\mathcal{G}\simeq 0$.

After the cavity and input powers have been fixed, the atomic detunings are iteratively adjusted in order to optimize the QND coupling between the fields as follows. A weak intensity modulation at 5 MHz, about 20 dB above shot-noise level (SNL), is applied on the signal beam. When the two fields are coupled in the cavity, it is possible to read the same modulation in the phase of the meter beam by using a phase-sensitive homodyne detection technique. The detunings are adjusted by looking for the maximum transfer of the modulation from the signal onto the meter field and, simultaneously, for the minimum degradation of the signal. This is done while always scanning the cavity about the signal resonance, until a situation similar to the one depicted in Fig. 6 is achieved, where the maximum transfer along the cavity scan occurs in correspondence to the signal resonance. This situation is recovered in fact when both fields resonate at the same time in the cavity at the signal resonance position, as in Fig. 5.

In Fig. 9 we show an example of the mean-field configuration across the cavity scan when the parameters were optimized for the QND experiment. The experimental curves were taken, for the signal and meter intensities, both with and without the trapping beams, thus ''switching on'' and ''switching off'' the nonlinearity. The solid line, superimposed on the ''noisy'' experimental curves, shows the *theoretical* curves obtained for $y_2=42.120$, $y_1=8.768$, $\Delta_2=2$, $\Delta_1=41.3$, $\theta_{01}=0.169$, $\theta_{01}=11.207$, $C_2=135$, $C_1=90$, $\kappa_1=\kappa_2=9.034$, and $\mathcal{G}=-2.01$. The signal curves are shown upside down, and each curved is normalized to the corresponding intensity at resonance in the empty cavity. In Fig. 10 we again show the meter field in the presence of the atoms (intensity and phase across the cavity scan) to point out that the ''nonlinear'' meter peak at the signal resonance position $\delta\theta_1=0$ is actually an extra resonance for the meter field. This very point is the working point for the experiment. Here the cavity scan is stopped and the QND coefficients are measured.

B. QND coefficients

Typical experimental results for the QND coupling between the fields in the case of the mean-field configuration in Fig. 9 are shown in Fig. 11. The lower trace (a) shows the SNL, and the modulation of the output signal beam, taken off cavity resonance without the atoms; the width of the modulation peak is 100 kHz. Over this trace are also shown as dots the SNL and modulation of the output signal beam, taken while the cavity is stopped at resonance in the presence of the atoms (operating conditions). There is clearly neither attenuation nor a change in the noise of the signal beam. The measured nondemolition coefficient T_s is therefore limited

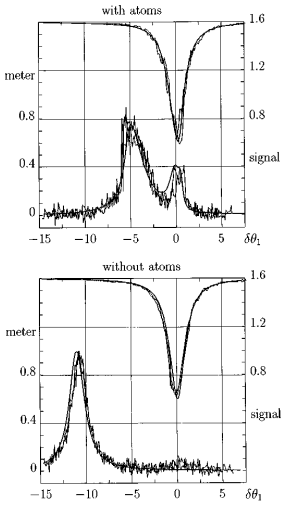

FIG. 9. Normalized intensities of the meter and signal (up side down) as functions of the cavity detuning. The curves were taken both in presence and in absence of the atomic medium. The thin continuous line is the theoretical curve, while the noisy lines are experimental curves. The little bump which appears on the meter curve without the atoms at the signal position is due to a small imperfection in the optics separating the two beams in the monitoring channel. The parameters for the theoretical curves are $y_1=8.768$, $y_2=42.120$, $\Delta_1=41.3$, $\Delta_2=2$, $C_1=135$, $C_2=90$ ($C_1=C_2=0$ for the curves without atoms), $\kappa_1=\kappa_2=3.01\gamma_w$, $\theta_{01}=11.207$, $\theta_{02}=0.169$, and $\mathcal{G}=-2.01$.

only by the passive optical transmission of the system, which relates the output signal without atoms to the input one, i.e., $T_s^{(\mathrm{meas})}=0.90(-0.5\ \mathrm{dB})$. From T_s and from the lower trace in Fig. 11, one obtains the input beam signal to noise ratio, which is 23.8 dB. The upper trace (b) is the phase-dependent noise and modulation of the output meter beam, taken in operating conditions while scanning the phase of the homodyne detection. The SNL of the meter beam was electronically set at the same level as the one of the signal beam. The upper envelope of the fringes gives the meter phase information, and yields the output meter signal-to-noise ratio, which is equal to 21.9 dB. The measurement transfer coefficient is thus -1.9 dB, or $T_m^{(\mathrm{meas})}=0.65$. Finally, the conditional variance is obtained by recombining the output signal and meter

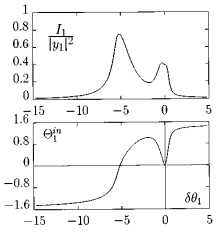

FIG. 10. Meter intensity (top) and phase (bottom) as a function of the cavity detuning, in presence of the atoms. The parameters are as in Fig. 9.

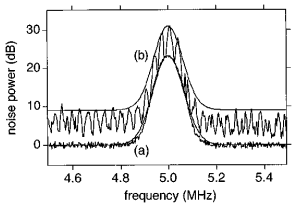

FIG. 11. Measurement of the transfer coefficient T_m. Curve (a), normalized to the SNL, corresponds to the output signal, modeled by a Gaussian peak (dash-dotted line). Two curves are actually displayed, and show no observable difference: one taken off resonance without the atoms (line) and one taken on operating conditions (dots). Curve (b) is the outcoming meter, also taken on operating conditions, and modulated by scanning the phase of the homodyne detection. The upper envelope is fitted by a Gaussian peak of same width as in curve (a). The signal-to-noise ratios are obtained as the differences (in dB) between the fitted peaks and the flat backgrounds.

photocurrents while scanning the phase of the homodyne detection. We show the results in Fig. 12. In correspondence to the right phase of the local oscillator picking up the *phase quadrature* of the meter field, the recombined noise reaches a minimum value 3.5 dB below the SNL, which gives a conditional variance $V_{s|m}^{(\mathrm{meas})}=0.45$. Estimated uncertainties on $T_s^{(\mathrm{meas})}$, $T_m^{(\mathrm{meas})}$, and $V_{s|m}^{(\mathrm{meas})}$ are ± 0.05.

In order to compare the experimentally measured values of the QND coefficients with the theory, it is necessary to take into account some small corrections due to optical losses and nonunity efficiencies. The quantum efficiencies on the two channels are

$$\eta_s=\alpha_s^{\mathrm{res}}\beta_s^{\mathrm{prop}} \tag{77}$$

for the signal beam, and

$$\eta_m=\alpha_m^{\mathrm{res}}\beta_m^{\mathrm{prop}}\mathcal{V}^2\epsilon_m^{\mathrm{det}} \tag{78}$$

for the meter beam, where α_s^{res} and α_m^{res} are the cavity losses at resonance for the signal beam and the meter beam, respectively; β_s^{prop} and β_m^{prop} are the optical losses on propagation for the signal beam and the meter beam, respectively, $\mathcal{V}$ is

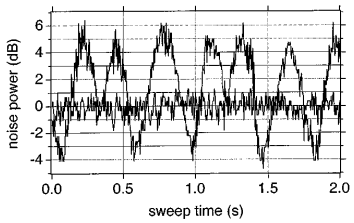

FIG. 12. Measurement of the conditional variance. The dotted line is the signal beam shot noise level at a noise analysis frequency of 4.6 MHz. The full line is the noise from the recombined signal and meter photocurrents, recorded as the phase of the homodyne detection is scanned. The conditional variance appears as the minimum noise level of this curve.

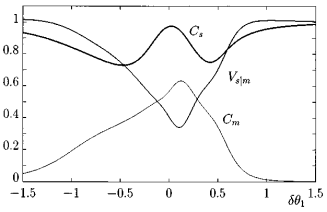

FIG. 13. QND coefficients for $\omega = 1.533\gamma_w$ as a function of the cavity detuning in the region of the double-resonance position ($\delta\theta_1 = 0$). The parameters are as in Fig. 9.

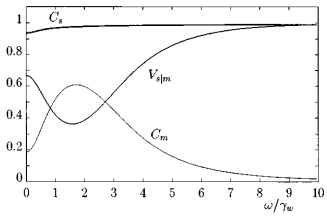

FIG. 14. QND coefficients in the best point of the scan ($\delta\theta_1 = 0.11$) as a function of the frequency of analysis. The parameters are as in Fig. 9.

the fringe visibility of the homodyne detection, and $\epsilon_m^{\rm det}$ is the meter detector quantum efficiency.

With our setup (Sec. V), we have

$$\alpha_s^{\rm res} = \alpha_m^{\rm res} = 1, \quad \beta_s^{\rm prop} = \beta_m^{\rm prop} = 0.90, \quad \mathcal{V} = 0.96, \quad \epsilon_m^{\rm det} = 0.92, \tag{79}$$

which implies $\eta_s = 0.9$ and $\eta_m = 0.76$. The QND coefficients, due *only* to the interaction with the nonlinear medium which are used in the theoretical model (where experimental imperfections are not taken into account), are then related to the measured ones through η_s and η_m. For the coefficient T_s one has simply

$$T_s^{(\rm meas)} = \eta_s T_s . \tag{80}$$

To evaluate T_m, one has to take into account the fact that, after the interaction, the meter has a strong phase noise $\langle \delta\tilde{Y}_m^{\rm out}(\omega)^2 \rangle$. In the limit of high gains, one can show that [14]

$$T_m^{(\rm meas)} = B_m T_m \quad \text{where} \quad B_m = \frac{\eta_m \langle \delta\tilde{Y}_m^{\rm out}(\omega)^2 \rangle}{\eta_m \langle \delta\tilde{Y}_m^{\rm out}(\omega)^2 \rangle + 1 - \eta_m}. \tag{81}$$

For $\langle \delta\tilde{Y}_m^{\rm out}(\omega)^2 \rangle \gg 1$ [like in our case in which $\langle \delta\tilde{Y}_m^{\rm out}(\omega)^2 \rangle = 7.9$], one obtains

$$B_m = 1 - \frac{1 - \eta_m}{\eta_m \langle \delta\tilde{Y}_m^{\rm out}(\omega)^2 \rangle}. \tag{82}$$

For the conditional variance, one can deduce

$$1 - V_{s|m}^{(\rm meas)} = B_m \eta_s (1 - V_{s|m}). \tag{83}$$

By using Eqs. (80)–(83), where we substitute the numerical values (79) for our setup and the measured values for the QND coefficients, we can work out the experimental values for the QND coefficients, corrected for the optical losses. One obtains $T_m = 0.67$, $T_s = 1$, and $V_{s|m} = 0.37$, again with an uncertainty estimated to be about ± 0.05 on each coefficient.

We can directly compare these results with the theoretical prediction, in Fig. 13, for the QND coefficients calculated at $\omega/2\pi = 4.6$ MHz along the cavity scan in the region of the double-resonant point. At the best point of the scan one has $T_m = 0.60$, $T_s = 0.97$, and $V_{s|m} = 0.36$, which is in good agreement with the experiment. In Fig. 14 we finally show the frequency dependence of the QND coefficients at the best point of the scan. As confirmed by the experiment, the quantum correlations display a significant frequency dependence within the frequency band selected by the cavity. The best values are reached around 5 MHz, once more corresponding to the experimental observations.

C. Remarks

As we have shown, the agreement found between the experimental results and the theoretical analysis performed with a three-level model for the atoms is remarkable. The model is able to reproduce and interpret the main experimental results which concern, on the one hand, the steady-state curves of the field intensities across the cavity scan, and, on the other hand, the quantum correlations between the fields in the best configuration for QND identified as the point of the cavity scan where the two fields resonate simultaneously. Nevertheless it is needless to remark that the distance between the three-level model presented in this paper (Sec. III) and the complex situation of a real experiment remains very large. At least two major omissions in the model can be identified.

The first of these is that the restriction to a purely three-level system does not take into account the actual multilevel structure of the transitions used for the two-beam coupling. A schematic view of the involved Zeeman sublevels is represented in the inset of Fig. 7, where we also show the relative importance of the Clebsch-Gordan coefficients for the different transitions. The chance to represent this complicated situation successfully as a simple lambda scheme comes from the fact that most of the contribution to the coupling is given by the lambda schemes (the outermost in the figure) which have the largest Clebsch-Gordon coefficients, and it is indeed by considering these most contributing transitions that we have chosen to set the ratio $C_1/C_2 = 1.5$ in our model to fit the experimental curves.

The second major fault of the model is that, by describing the fields in the cavity as plane waves, it neglects the Gaussian transverse shape of the beams as well as their standing-wave longitudinal structure in the cavity. These spatial gradients in the intensity profile of the waves, and especially the standing-wave structure in the cavity, give rise to optical potentials whose depth can easily be of the same order of magnitude of the small kinetic energy of the cold atoms, thus sizably affecting their external degrees of freedom. Preliminary experiments performed with our setup on one-photon optical bistability showed with some evidence that optical forces due to a strong standing wave in the cavity can have

macroscopic effects on the nonlinearity of the cold atoms, changing the effective cooperativeness of the system in a detuning and intensity-dependent way. The major practical conclusion of this preliminary study was that it is preferable to use red (positive) detuning for the fields, a condition in which the effective cooperatively of the system can be increased sizably with respect to the opposite case of blue (negative) detuning. An attempt at an explanation for this was made on the basis of a very simple model based on the dipole force that would attract cold atoms in the high-intensity regions of the field for red detuning, and repulse them for blue detuning [24]. A more complex situation involving two different light fields was analyzed theoretically very recently [25].

In this view, a too-strict correspondence between the parameters introduced in the model (especially the cooperativity parameters and the input fields amplitudes) and their experimental counterparts loses sense. Instead we are naturally led to consider the parameters of our theoretical model as ''averages'' over more complex phenomena that take place in the real experiment. The very fact that such effective parameters can be defined, and used to obtain a very good description of the results, is actually a good proof of the robustness of the three-level model in our experimental configuration.

VII. CONCLUSIONS

We presented the results of a recent QND experiment performed with cold trapped rubidium atoms [10], and their interpretation on the basis of a theoretical model for three-level atoms in a cavity. By studying in detail the steady-state configurations allowed by the system and the quantum behavior of the fields, we showed by theory and experiment, how a ghost transition configuration for performing QND measurements with atomic $\chi^{(3)}$ nonlinearity can be successfully implemented and optimized using cold atoms. The experimental results are the best obtained so far for a single back-action-evading measurement, and the agreement between theory and experiment is remarkable.

ACKNOWLEDGMENTS

This work was carried out with the support of the European HCM network ''Non-Classical Light.'' One of us, A. S., would like to thank Professor L. Lugiato and Professor G. Strini for fruitful discussions and quite useful advice. One of us, K. W., acknowledges financial support from ICTP Programme, Trieste, Italy and the National Natural Science Foundation of China.

APPENDIX

Here we report the elements of the diffusion matrix D_N, expressed in terms of the normalized variables:

$$[x_1,x_1^*,x_2,x_2^*,v,v^*,w,w^*,z,z^*,m,n,]:$$

$$(D_N)_{6,6}=-\frac{2\gamma_w}{N}x_1v^*,$$

$$(D_N)_{6,8}=-\frac{\gamma_w}{N}(x_1\omega^*+x_2v^*),$$

$$(D_N)_{6,10}=-\frac{\gamma_w}{N}x_1z^*,$$

$$(D_N)_{8,8}=-\frac{2\gamma_w}{N}x_2w^*,$$

$$(D_N)_{8,10}=\frac{\gamma_w}{N}[x_2z^*+x_1(n-m)],$$

$$(D_N)_{8,11}=\frac{\gamma_w}{N}x_1z,$$

$$(D_N)_{8,12}=-\frac{\gamma_w}{N}x_1z,$$

$$(D_N)_{9,10}=\frac{\gamma_w/2}{N}[x_1(v+v^*)]+\frac{\gamma_1}{N}[1/3\eta(1-m-n)],$$

$$(D_N)_{10,11}=-\frac{\gamma_w/2}{N}\eta(x_1w+x_2v^*),$$

$$(D_N)_{10,12}=-\frac{\gamma_w}{N}(x_1w+x_2v^*),$$

$$(D_N)_{11,11}=\frac{2\gamma_w}{N}\left[x_1(v+v^*)+\frac{x_2}{4}(w+w^*)\right]+\frac{\gamma_1}{N}\left[\frac{4}{3}(1+\eta/4)(1-m-n)\right],$$

$$(D_N)_{11,12}=\frac{\gamma_w}{N}[x_1(v+v^*)+x_2(w+w^*)]+\frac{\gamma_1}{N}\left[\frac{2}{3}(1+\eta)(1-m-n)\right],$$

$$(D_N)_{12,12}=\frac{2\gamma_w}{N}\left[\frac{x_1}{4}(v+v^*)+x_2(w+w^*)\right]+\frac{\gamma_1}{N}\left[\frac{4}{3}\left(\frac{1}{4}+\eta\right)(1-m-n)\right],$$

plus the ones obtained by conjugation and index permutation from the terms above (we recall that D_N is symmetrical).

[1] V. B. Braginsky and Yu. I. Vorontsov, Usp. Fiz. Nauk. **114**, 41 (1974) [Sov. Phys. Usp. **17**, 644 (1975)]; V. B. Braginsky, Yu. I. Vorontsov, and F. Ya. Khalili, Zh. Eksp. Teor. Fiz. **73**, 1340 (1975) [Sov. Phys. JETP **46**, 705 (1977)].

[2] K. S. Thorne, R. W. P. Drever, C. M. Caves, M. Zimmerman, and V. D. Sandberg, Phys. Rev. Lett. **40**, 667 (1978).

[3] G. J. Milburn and D. F. Walls, Phys. Rev. A **28**, 2065 (1983); N. Imoto, H. A. Haus, and Y. Yamamoto, *ibid.* **32**, 2287 (1985); B. Yurke, J. Opt. Soc. Am. B **2**, 732 (1985).

[4] M. D. Levenson, R. M. Shelby, M. Reid, and D. F. Walls, Phys. Rev. Lett. **57**, 2473 (1986).

[5] A. LaPorta, R. E. Slusher, and B. Yurke, Phys. Rev. Lett. **62**, 28 (1989).

[6] P. Grangier, J. F. Roch, and G. Roger, Phys. Rev. Lett. **66**, 1418 (1991).

[7] S. R. Friberg, S. Machida, and Y. Yamamoto, Phys. Rev. Lett. **69**, 3165 (1992).

[8] J. Ph. Poizat and P. Grangier, Phys. Rev. Lett. **70**, 271 (1993).

[9] K. Bencheikh, J. A. Levenson, Ph. Grangier, and O. Lopez, Phys. Rev. Lett. **75**, 3422 (1995).

[10] J.-F. Roch, K. Vigneron, P. Grelu, A. Sinatra, J-P. Poizat, and P. Grangier, Phys. Rev. Lett. **78**, 634 (1997).

[11] M. D. Levenson, M. J. Holland, D. F. Walls, P. J. Manson, P. T. H. Fisk, and H. A. Bachor, Phys. Rev. A **44**, 2023 (1991).

[12] K. Gheri, P. Grangier, J. P. Poizat, and D. Walls, Phys. Rev. A **46**, 4276 (1992).

[13] A. Lambrecht, T. Coudreau, A. M. Steinberg, and E. Giacobino, Europhys. Lett. **36**, 93 (1996).

[14] J.-Ph. Poizat and P. Grangier, in *ICONO '95; Coherent Phenomena and Amplification Without Inversion*, edited by A. V. Andreev, O. Kocharovskaya, and P. Mandel [Proc. SPIE **2798**, 260 (1996)].

[15] W. Ketterle, K. Davis, M. Joffe, A. Martin, and D. Pritchard, Phys. Rev. Lett. **70**, 2253 (1993).

[16] M. J. Holland, M. J. Collett, D. F. Walls, and M. D. Levenson, Phys. Rev. A **42**, 2995 (1990).

[17] J. P. Poizat, J. F. Roch, and P. Grangier, Ann. Phys. (Paris) **19**, 256 (1994).

[18] L. A. Lugiato, *Progress in Optics XXI*, edited by E. Wolf (North-Holland, Amsterdam, 1977), p. 71.

[19] C. W. Gardiner and M. J. Collett, Phys. Rev. A **31**, 3761 (1985).

[20] A. Sinatra, Ph.D. thesis, Università di Milano, 1997 (unpublished).

[21] J. M. Courty, P. Grangier, L. Hilico, and S. Reynaud, Opt. Commun. **83**, 251 (1991).

[22] B. Sheehy, S. Q. Shang, R. Watts, S. Hatamian, and H. Metcalf, J. Opt. Soc. Am. B **6**, 2165 (1989).

[23] E. Raab, M. Prentiss, A. Cable, S. Chu, and D. Pritchard, Phys. Rev. Lett. **59**, 2631 (1987).

[24] A. Sinatra, K. Vigneron, P. Grelu, J.-Ph. Poizat, J.-F. Roch, and P. Grangier, 1996 European Quantum Electronic Conference, Hamburg (1996), IEEE Catalog No. 96TH8162, Library of Congress: 95-82410.

[25] W. Alge, K. Ellinger, H. Stecher, K. M. Gheri, and H. Ritsch, Europhys. Lett. **39**, 491 (1997).

3.3 Au voisinage des conditions de piégeage cohérent de population

Dans mon mémoire de thèse, j'ai aussi considéré une autre configuration des champs qui utilise la partie dispersive de la réponse atomique au voisinage des conditions de piégeage cohérent de population (Fig. 3.6).

On injecte dans la cavité deux faisceaux cohérents de même intensité légerement désacordés de façon symétrique par rapport à la résonance.

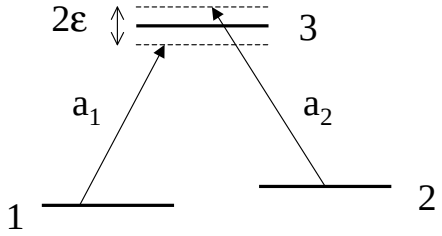

FIG. 3.6 – Système en Λ au voisinage du piégeage cohérent de population.

Dans ces conditions, nous avons montré l'existence d'un courbe de bistabilité optique "universelle" (pour l'intensité intracavité des champs en fonction de l'intensité des champs injectés) qui partage l'espace des paramètre en deux parties. Pour des intensités supérieures à une intensité de seuil Y_s, les champs dans la cavité ont la même intensité. Pour un désaccord de cavité nul et près de $Y = Y_s$, les deux faisceaux sortants sont alors indépendants et comprimés. Pour des intensités des champs injectés inférieures à Y_s, les deux champs en cavité n'ont jamais la même intensité. Les valeurs moyennes des l'intensités intracavité ont alors un comportement de "switching" entre une courbe à forte intensité et une courbe à faible intensité en fonction du désaccord de cavité supposé être le même pour les deux modes. Pour ce qui concerne les fluctuations quantiques, les deux champs présentent des corrélations permettant une mesure QND de l'intensité de l'un des deux faisceaux.

Nous avons obtenu des expressions analytiques simples pour ces effets de réduction du bruit et de QND, permettant de les comprendre et de les optimiser.

Je n'avais pas eu l'occasions de publier ce travail. À l'occasion de la rédaction de ce mémoire, j'ai écrit un article et je l'ai soumis tout récemment [25]. Un article récent considère l'intérêt de cette même configuration pour la production d'états comprimés de spin mais en se limitant aux cas d'égale intensité des champs en cavité. Il serait intéressant d'étudier les corrélations atomiques dans le régime $Y < Y_s$.

3.3.1 Preprint joint

Quantum correlations of two optical fields close to electromagnetically induced transparency

A. Sinatra
Laboratoire Kastler Brossel, ENS, 24 Rue Lhomond, 75231 Paris Cedex 05, France

We show that three-level atoms excited by two cavity modes in a Λ configuration close to electromagnetically induced transparency can produce strongly squeezed bright beams or correlated beams which can be used for quantum non demolition measurements. The input intensity is the experimental "knob" for tuning the system into a squeezer or a quantum non demolition device. The quantum correlations become ideal at a critical point characterized by the appearance of a switching behavior in the mean fields intensities. Our predictions, based on a realistic fully quantum 3-level model including cavity losses and spontaneous emission, allow direct comparison with future experiments.

PACS numbers: 42.50.Dv,42.50.Gy,42.65.Pc

Using optical nonlinearities it is possible to manipulate optical beams to the level of quantum fluctuations, producing squeezed states [1] that are important resources for quantum information with continuous variables [2]. Related to the field of squeezing is that of quantum non demolition (QND) measurements on an optical field, where quantum correlations between two different modes of the electromagnetic field are exploited to overcome the back-action noise of a quantum measurement [3]. Besides the fundamental interest in the theory of measurement, it was shown that QND correlations of propagating beams have direct application in quantum communication protocols as teleportation [4]. The best single back-action-evading measurement on optical beams was performed using cold atoms inside a doubly resonant cavity [5]. We suggest that these performances could be significantly improved by tuning the system close to the electromagnetically induced transparency (EIT) conditions [6].

Already in the nineties, theoretical studies showed that a lambda three-level medium close to EIT conditions in a cavity can be used to obtain squeezing [7]. Contrarily to previous proposals, here we assume that two different modes are resonant in the cavity. For small and symmetrical detunings from the upper level of Λ three-level atoms (see Fig.1), absorption is suppressed and the dispersive non linear response gives rise to a rich scenario where either self correlations (squeezing) or cross QND correlations can be established in the output beams. The correlations become ideal at a critical point that we characterize analytically. The technique we propose is experimentally accessible, and first experimental steps in this directions were done in atomic vapors without a cavity [8]. Here we show that the presence of the cavity is a crucial advantage especially if one can reach the good cavity limit.

We consider N atoms in a cavity excited by two modes symmetrically detuned from the upper level of a Λ three-level scheme as in Fig.1. For $j = 1, 2$ let ω_j be the frequency of field j and $\hbar\omega_{aj}$ the energy of the corresponding

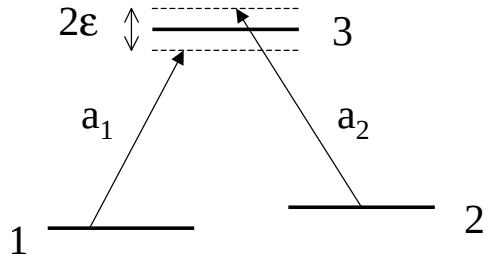

FIG. 1: Two cavity modes interact with the atoms in a Λ configuration close to EIT conditions.

atomic transition. We define $\Delta_j = \frac{\omega_{aj}-\omega_j}{\gamma_w/2}$ the atomic detunings normalized to the decay rate of the optical coherences $\gamma_w = (\gamma_1+\gamma_2)/2$ where $\gamma_1+\gamma_2$ is the total population decay rate of the upper level; $\theta_j = \frac{\omega_{cj}-\omega_j}{\kappa_j}$ the cavity detunings normalized to the cavity decay rates κ_j, and $C_j = \frac{g_j^2 N}{\gamma_w \kappa_j}$ the cooperativities where g_j are the coupling constants for the two considered transitions. We use normalized variables proportional to the intracavity and input fields $x_j = \frac{\sqrt{2}g_j}{\gamma_w}\langle a_j\rangle$ and $y_j = \frac{\sqrt{2}g_j}{\gamma_w}\frac{2}{\sqrt{T_j}}E_j^{in}$ respectively, where T_j is the (input-output) mirror transmissivity for the field j. We name v and w the normalized polarizations between levels 1-3 and 2-3 $v = -(\sqrt{2}/N)\langle R^-\rangle$, $w = -(\sqrt{2}/N)\langle S^-\rangle$ where R and S are collective operators constructed from the single atom operators $|1\rangle\langle 3|$ and $|2\rangle\langle 3|$ as in [9]. The master equation and the semiclassical equations describing the Λ system with two cavity fields, with the same notations introduced here, are given and discussed in detail in [10] where this model was successful to reproduce the experimental results of [5].

Let us consider a set of parameters symmetric for the two transitions: $|y_j| = |y|$, $C_j = C$, $\gamma_j = \gamma$, $\kappa_j = \kappa$, $\theta_j = 0$ (empty cavity resonance for both fields), and let $\Delta_1 = -\Delta_2 = \epsilon$ be small and positive. In Fig. 2 we show in rescaled units the stationary intensities of the intracavity fields $I_j = |x_j|^2/4C\epsilon$ as a function of the common intensity of the input fields $Y = |y|^2/4C\epsilon$. With a solid

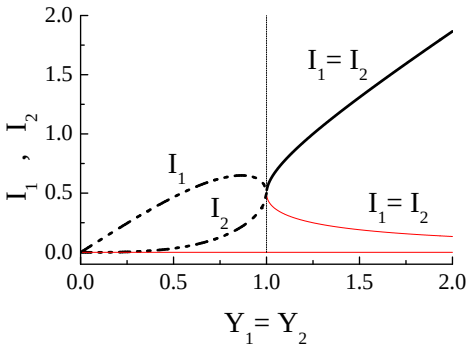

FIG. 2: Stationary intensities of the intracavity fields I_1, and I_2 as a function of the common intensity of the input fields $Y_1 = Y_2 = Y$. In solid line the solution $I_1 = I_2$. The thick (red thin) line correspond to stable (unstable) solutions. In dashed-dotted line one of the two stable solutions with $I_1 \neq I_2$. Parameters: $2\epsilon = 0.125$ and $C_1 = C_2 = 250$, $\gamma_1 = \gamma_2 = 10\kappa_1$, $\kappa_2 = \kappa_1$, $\theta_1 = \theta_2 = 0$.

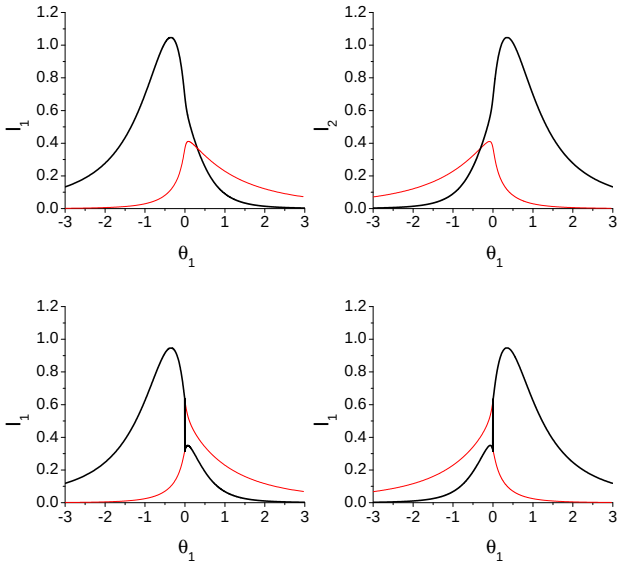

FIG. 3: Intracavity field intensities I_1 (left half), I_2 (right half) across the cavity scan. Upper half: $Y = 1.05$. Lower half: $Y = 0.95$. The thick (red thin) lines correspond to stable (unstable) solutions. The other parameters are as in Fig. 2.

line we have plotted an S-shaped solution with $I_1 = I_2$. A stable branch of this solution appears for $Y > 1$. The negative slope branch and the lower branch very close to zero intensity are both instable and play no role in the following. For $Y < 1$, apart from the solution $I_1 = I_2$, we get two other solutions with $I_1 \neq I_2$. In the figure we show one of them with $I_1 > I_2$. The second one is obtained by exchanging I_1 and I_2. Both solutions are stable in the considered case $\theta_1 = \theta_2 = 0$.

We choose now two values of the input intensity, in turn above and below the turning point $Y = 1$, and show the stationary solutions for intracavity fields intensities as the cavity detunings vary in Fig. 3. The stable branches of these curves (thick lines) can be easily obtained experimentally by sweeping the cavity length [10]. We vary θ_1 and θ_2 keeping them always equal which would imply the use of two driving fields of close optical frequencies $\Delta\lambda/\lambda \ll 1$ (and for example different polarizations). For $Y = 1.05$ i.e. 5% *above* the turning point (upper half of Fig. 3) the stable solutions for the intracavity intensities are Lorentzian-looking curves symmetrically shifted by a small amount from their empty-cavity positions for both fields. Only for $\theta_1 = \theta_2 = 0$ the two fields have the same stationary amplitude in the cavity corresponding to the stable high-transmission branch of the S-shaped curve in Fig.2. For $Y = 0.95$ i.e. 5% *below* the turning point (lower half of Fig. 3) the situation is rather different: the stable solution for the two fields *switches* between a high-intensity and a low-intensity curve being always $I_1 \neq I_2$ although $|y_1| = |y_2|$. In contrast with the previous case this situation is very far from the independent-fields EIT solution and the fields are in fact strongly coupled.

Let us now introduce the usefull correlations to caracterize the quantum fluctuation properties of the system. For a given quadrature of the j^{th} field: $X_j^\phi = a_j e^{-i\phi} + ia_j^\dagger e^{i\phi}$, the squeezing spectrum is defined as

$$S_j^\phi(\omega) = 1 + 2\kappa_j \int_{-\infty}^{\infty} e^{-i\omega t} \langle : \delta X_j^\phi(t)\, \delta X_j^\phi(0) : \rangle \, dt \quad (1)$$

where δX_j^ϕ denotes the time dependent fluctuation of the operator X_j^ϕ around a steady state point. The column indicates normal and time ordering for the product inside the mean. $S_j^\phi = 1$ is the shot noise and $S_j^\phi = 0$ means total suppression of fluctuations in the quadrature X_j^ϕ. The crossed correlations between the two fields are described by the coefficients C_s, C_m and $V_{s|m}$ [11] characterizing a QND measure of the amplitude quadrature X^{in} of one field, the *signal*, performing a direct measurement on the phase quadrature Y^{out} of the other field, the *meter*. Among the tree coefficients C_s quantifies the non-destructive character of the measurement, C_m its accuracy and $V_{s|m}$ refers to the to the "quantum state preparation" capabilities of the system.

$$C_s = C(X^{in}, X^{out}), \quad C_m = C(X^{in}, Y^{out}), \quad (2)$$

$$V_{s|m} = \langle X^{out}, X^{out} \rangle \left(1 - C(X^{out}, Y^{out})\right) \quad (3)$$

where for two operators A and B we define

$$C(A,B) = \frac{|\langle A, B\rangle|^2}{\langle A, A\rangle \langle B, B\rangle} \quad \text{with} \quad (4)$$

$$\langle A, B\rangle = \int_{-\infty}^{+\infty} e^{-i\omega t} \frac{1}{2} \langle A(t)B + BA(t)\rangle \, dt\,. \quad (5)$$

The superscripts *in* and *out* refer to the input and output fields from the cavity. By calling ϕ_j^{in} and ϕ_j^{out} the

phases of the input and output fields in steady state, and choosing field 1 as the *meter* and field 2 as the *signal*, we define $X^{out(in)} = X_2^{\phi_2^{out(in)}}$ and $Y^{out} = Y_1^{\phi_1^{out}+\pi/2}$. For an ideal QND measurement $C_m = C_s = 1$, and $V_{s|m} = 0$.

The quantum fluctuations counterpart of Fig. 3 (top) is shown in Fig. 4 (top) where squeezing of the output fields optimized with respect to the quadrature $S_j^{best}(\omega = 0)$ is plotted as a function of the cavity detuning. A large amount of squeezing is present in both fields close to $\theta_1 = 0$. As one can see from Fig. 3 (top) the two fields are well transmitted by the cavity for $\theta_1 = 0$, and the system efficiently converts the input coherent beams into bright squeezed beams.

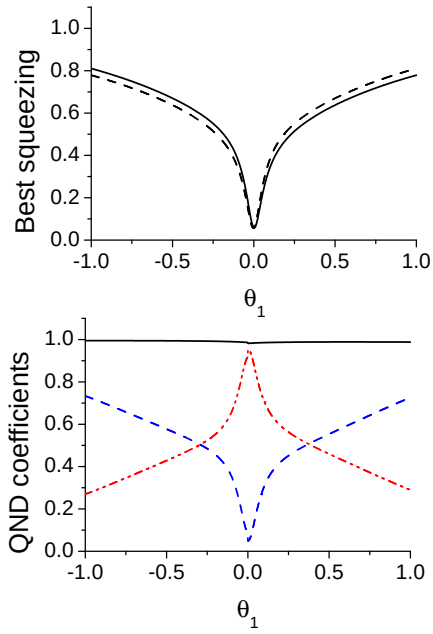

FIG. 4: Top: Best squeezing of the fields across the cavity scan for $Y = 1.05$ and $\omega = 0$. Squeezing of field 1 (2) is plotted with a solid (dashed) line. Bottom: QND coefficients across the cavity scan for $Y = 0.95$ and $\omega = 0$. C_m (red dashed-dotted line), C_s (solid line), $V_{s|m}$ (blue dashed line). Parameters as in Fig.3.

Correspondingly to Fig. 3 (bottom) for $Y = 0.95$, in Fig.4 (bottom) we plot the coefficients C_s, C_m and $V_{s|m}$ across the cavity scan. The useful quantum correlations are calculated by a linearized treatment of quantum fluctuations around the stable stationary solution as in [10]. Despite the fact that the two fields have different intracavity intensities at $\theta_1 = 0$, they play here symmetrical roles for the QND scheme; the figure corresponding to the reversed scheme $1 \leftrightarrow 2$ being obtained by reflection of the plots $\theta_1 \leftrightarrow -\theta_1$.

We show in Fig. 5 the frequency dependence of the quantum correlations both below and above the turning point $Y = 1$, for a fixed value of the cavity detuning close to zero. For values of the cooperativity parameters currently obtained in experiments, QND coefficients such as

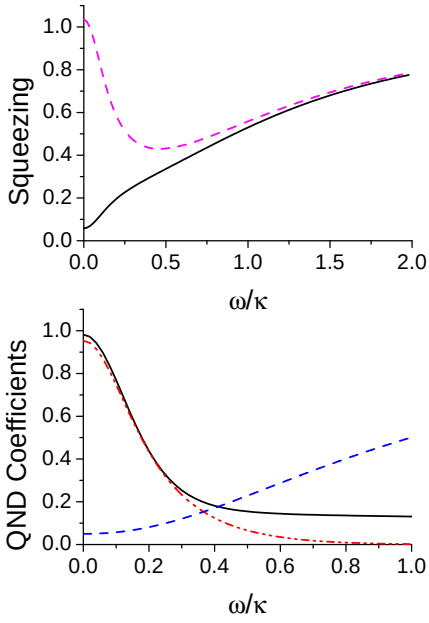

FIG. 5: Top: Squeezing spectra of field 1, for $Y = 1.05$ in the center of the cavity scan ($\theta_1 = 0.0013$). Best squeezing in solid line and amplitude squeezing $S_1^{\phi_1^{out}}$ in purple dashed line. Bottom: QND spectra for $Y = 0.95$ and $\theta_1 = 0.0018$. C_m (red dashed-dotted line), C_s (solid line), $V_{s|m}$ (blue dashed line). The other parameters are as in Fig.2.

$C_s = 0.98$, $C_m = 0.95$, $V_{s|m} = 0.05$ can be acheived in this regime, representing a significant improvement with respect to previously obtained results [5] based on the so called "ghost transition" scheme [12], [10]. Although we concentrate here on the good cavity limit, in which as we will show the quantum correlations become ideal approaching the turining point $Y = 1$, some QND correlations between the two modes persist also in the bad cavity limit. For example for $\epsilon = 0.25$, $C = 25$, $\kappa = 3\gamma$, $\theta_1 = 6 \times 10^{-3}$, $Y = 0.9$ and $\omega = 0.1\gamma$ we get $C_s = C_m = 0.72$, $V_{s|m} = 0.26$.

In the limit of weak atomic detunings, useful analytical results can be obtained. The analytical solution of the semiclassical equations of the system at steady state is given in [10]. By expanding the steady state polarizations v and w to the first order in ϵ we obtain

$$v = i\frac{4\epsilon\, x_1|x_2|^2}{(|x_1|^2+|x_2|^2)^2} \qquad w = -i\frac{4\epsilon\, x_2|x_1|^2}{(|x_1|^2+|x_2|^2)^2}\,. \tag{6}$$

By inserting (6) in the equations for the intracavity fields amplitudes, with $|y_j| = |y|$, $\theta_j = 0$ and $C_j = C$, we obtain at steady state a "universal solution" for rescaled field intensities. For $Y < 1$ there are two stable solutions

$$I_1 = \frac{Y}{2}(1 \pm \eta)\;; \quad I_2 = \frac{Y}{2}(1 \mp \eta) \tag{7}$$

where $\eta = \sqrt{1-Y^2}$. For $Y > 1$, out of two solutions

$$I_1 = I_2 = I \ ; \ I = \frac{Y}{2}\left(1 \pm \sqrt{1-\frac{1}{Y^2}}\right) \qquad (8)$$

the one with the plus sign is stable and the other one unstable. Solutions (7)-(8) are indistinguishable from those of the full three-level model in Fig. 2. The phases of the input fields with respect to intracavity fields (which are taken real at steady state) are $\phi_1^{in} = \text{atan}\left[\sqrt{I_2/I_1}\right]$, $\phi_2^{in} = -\text{atan}\left[\sqrt{I_1/I_2}\right]$ for $Y < 1$, and $\phi_1^{in} = \text{atan}\,[1/2I] = -\phi_2^{in}$ for $Y > 1$. For the output fields $\phi_1^{out} = -\phi_1^{in}$, $\phi_2^{out} = -\phi_2^{in}$ in both cases.

In order to study the quantum properties of the system analytically we further assume that (i) $\gamma \gg \kappa$ so that the atomic fluctuations follow adiabatically the field fluctuations, and (ii) the noise from spontaneous emission is negligible, which we found true when the cooperativity is large enough. In this limit, using the steady state polarizations (6), we can solve analytically the equations for the field fluctuations and obtain the correlation functions.

For $Y > 1$ and $I_1 = I_2 = I$ and taking κ^{-1} as the unit of time, we obtain

$$\delta\dot{x}_j = -\delta x_j + i\,\frac{(-1)^{3-j}}{2I}\delta x_j^* \qquad j = 1, 2\,. \qquad (9)$$

These equations describe two independent two-photon processes for which instabilities and squeezing have been studied extensively [13]. The best squeezing spectrum for each field is

$$S_j^{best}(\omega) = 1 - \frac{4a}{(1+a)^2 + \omega/\kappa^2}\,, \qquad a = \frac{1}{2I}\,, \quad (10)$$

yielding perfect squeezing at zero frequency at the turning point where $Y = 1$, $I = 0.5$ and $a = 1$.

For $Y < 1$ and $I_1 \neq I_2$ the fluctuations of the two fields are coupled. For $I_1 > I_2$ we get

$$\delta X_1 = -\delta X_1 - i\,\frac{1-\eta}{Y}\,\delta Y_1 \qquad (11)$$

$$\delta Y_1 = -\delta Y_1 + i\frac{1+\eta}{Y}\,\delta X_1 - 2i\,\eta\delta X_2\,. \qquad (12)$$

The equations for field 2 are obtained from (11) and (12) by changing the sign in front of η and of i. Simple analytical expressions can be obtained for the squeezing and the conditional variance $V_{s|m}$ of the fields at $\omega = 0$

$$S_j^{int} = S_j^{best} = 1 \ ; \ S_j^{phase} = -3 + \frac{4}{\eta^2} \qquad (13)$$

$$V_{s|m} = \frac{\eta^2}{4 - 3\eta^2} \qquad (14)$$

showing that the fields have diverging phase noise and become perfectly correlated at the turning point. We checked that the spectra in Fig. 5 are well reproduced by the analytical results.

In conclusion, in a symmetrically detuned EIT scheme, and for equal input intensities Y of the two fields we have shown the existence of a universal S-shaped steady state curve (Fig.2) which divides the parameter space into two parts: for input intensities higher than the upper turning point of the curve, the quantum fluctuations of the fields become quadrature dependent and can be reduced in a quadrature, while for input intensities lower than the turning point, crossed phase-intensity quantum correlations build up between the two fields. The system becomes a perfect "squeezer" or an ideal QND device at the turning point. The "universal" point $Y = 1$, can be identified experimentally by the appearance of the switching behavior described in Fig.3, and can be used as a reference in the parameter space to choose either the squeezing or the QND effect and to optimize it. An implementation using either a vapor [8], or a trapped cold atoms in an optical cavity [5],[14],[15] seems within the reach of present technology.

I thank L. Lugiato and P. Grangier for useful discussions, M. Guerzoni for her contribution to this work and Y. Castin for comments on the manuscript. LKB is UMR 8552 du CNRS de l'ENS et de l'UPMC; support from IFRAF is acknowledged.

[1] For a recent review on squeezing see e.g. H. Bachor, "A Guide to Experiments in Quantum Optics", Wiley-VCH (2004).

[2] S.L. Braunstein, P. van Loock, Rev. of Mod. Phys. **77**, 513 (2005).

[3] P. Grangier, A. Levenson, J.-Ph. Poizat, Nature **396**, 537 (1998).

[4] D. B.Horoshko, S.Ya. Kilin, Phys. Rev. A **61**, 032304 (2000).

[5] J-F. Roch, K. Vigneron, P. Grelu, A. Sinatra, J-P. Poizat, P. Grangier, Phys. Rev. Lett.**78**, 634 (1997).

[6] For a review on EIT see e.g. M. Fleischhauer, A. Imamoglu, J.P. Marangos, Rev. Mod. Phys. **77**, 633 (2005);

[7] K.M. Gheri, D.F. Walls, M.A. Marte, Phys. Rev. A **50**, 1871 (1994).

[8] V.A. Sautenkov, Y.V. Rostovstev, M.O. Scully, Phys. Rev. A **72**, 065801 (2005), C.L. Garrido Alzar, L.S. Cruz, J.G. Aguirre Gómez, Europhys. Lett. **61**, 485 (2003).

[9] L.A.Lugiato *Progess in Optics XXI*, edited by E. Wolf (North-Holland, Amsterdam, 1977), p. 71.

[10] A. Sinatra, J-F. Roch, K. Vigneron, P. Grelu, J-P. Poizat, K. Wang, P. Grangier, Phys. Rev. A **57**, 2980 (1998).

[11] M. Holland, M. Collett, D.F. Walls, M.D. Levenson, Phys. Rev. A **42**, 2995 (1990); J.Ph. Poizat, J.-F. Roch and P. Grangier, Ann. Phys. (Paris) **19**, 265 (1994).

[12] K.M. Gheri, P. Grangier, J.-Ph. Poizat, D. Walls, Phys. Rev. A **46**, 4276 (1992).

[13] L. Lugiato, P. Galatola, L. Narducci, Opt. Comm. **76**, 276 (1990).

5

[14] V. Josse, A. Dantan, A. Bramati, M. Pinard, E. Giacobino, Phys. Rev. Lett. **92**, 123601 (2004);
[15] J.K. Thompson, J. Simon, H. Loh, V. Vuletić, Science **313**, 74 (2006).

3.4 Mémoire quantique avec les spins nucléaires de l'^{3}He

Les très longs temps de cohérence des spins nucléaires de l'hélium 3 dans son état fondamental (spin 1/2 purement nucléaire) en font un système potentiellement intéressant pour l'information quantique et en particulier pour le stockage de l'information. La difficulté pour l'application à l'hélium des schémas proposés dans la littérature pour des alcalins, est due au fait que le fondamental, isolé de 20 eV des autres états excités, n'est pas accessible par laser directement.

Avec Gaël Reinaudi en stage de DEA en 2004, nous avons décidé de voir si les collisions d'échange de métastabilité, couramment utilisées pour transférer de l'orientation de l'état métastable à l'état fondamental (voir le chapitre 5 de ce mémoire), pouvaient être utilisées aussi pour transférer des corrélations quantiques. En collaboration avec Franck Laloë et le groupe d'optique quantique du LKB Jussieu spécialiste des mémoires quantiques, nous avons proposé un schéma original qui permet de stocker un état comprimé de la lumière dans le spin nucléaire de l'hélium 3 dans son état fondamental, tout en pouvant le retransférer ensuite au champ électromagnétique. Pour cela, on utilise le couplage dipôlaire électrique entre la lumière et les atomes dans l'état métastable 2^3S, puis le couplage entre l'état métastable et l'état fondamental via les collisions d'échange de métastabilité.

Le schéma utilise un champ de pompage dans un états cohérent et un champ dans un état vide comprimé, en configuration Raman. Selon le rapport entre le taux de pompage (ajustable en variant l'intensité du champ cohérent) et le taux d'échange de métastabilité pour un atome métastable, les fluctuations du vide comprimé sont transférées soit aux spin métastables soit aux spins de l'état fondamental [23].

La mise en œuvre dans le cas de l'hélium dans des conditions réalistes demande quelques astuces mais semble faisable [23]-[24]. Le schéma se généralise à la production d'ensembles intriqués de longue durée de vie.

Pour continuer sur cette voie, le premier pas serait une mise en œvre expérimentale où l'on pourrait par exemple transférer du bruit dépendant de la phase du champ aux spins nucléaires et inversement. Un autre volet serait la recherche d'un schéma de mesure (par exemple par résonance magnétique nucléaire) des fluctuations quantiques des spins directement dans l'état fondamental.

3.4.1 Publications jointes

PRL 95, 123002 (2005) PHYSICAL REVIEW LETTERS week ending 16 SEPTEMBER 2005

Long-Lived Quantum Memory with Nuclear Atomic Spins

A. Dantan,[1] G. Reinaudi,[2] A. Sinatra,[2,*] F. Laloë,[2] E. Giacobino,[1] and M. Pinard[1]
[1]*LKB, UPMC, case 74, place Jussieu, 75252 Paris Cedex 05, France*
[2]*LKB, ENS, 24 Rue Lhomond, 75231 Paris Cedex 05, France*
(Received 20 April 2005; published 15 September 2005)

We propose to store nonclassical states of light into the macroscopic collective nuclear spin (10^{18} atoms) of a ^{3}He vapor, using metastability exchange collisions. These collisions, commonly used to transfer orientation from the metastable state $2\,^3S_1$ to the ground state of ^{3}He, can also transfer quantum correlations. This gives a possible experimental scheme to map a squeezed vacuum field state onto a nuclear spin state with very long storage times (hours).

DOI: 10.1103/PhysRevLett.95.123002 PACS numbers: 32.30.Dx, 03.67.Hk, 03.67.Pp, 42.50.Dv

If great progress has been made in the generation of nonclassical states of light, a major challenge of quantum information and communication lies in the ability to manipulate and reversibly store such quantum states [1,2]. Several proposals have been made to achieve storage of nonclassical light states either in trapped cold atoms or atomic vapors [3,4]. The first successful experiments of quantum memories for coherent states and squeezed states were achieved using atoms as a storage medium [5,6]. In all the proposed schemes, as well as in the experiments realized so far, the information is encoded in the ground state of alkali atoms; the obtained storage times are at most several milliseconds, limited by collisions, magnetic field inhomogeneities, transit time, etc. Nuclear spins have also been proposed as quantum memories for mesoscopic systems, due to their long relaxation time [7]. In this Letter we show how to reversibly map a nonclassical state of light into a squeezed state, encoded in the purely nuclear spin of the ground state of ^{3}He, which interacts very little with the environment. The quantum state can then survive for times as long as *hours*. To access the ground state of ^{3}He, which is 20 eV apart from the nearest excited state, we propose to use metastability exchange (ME) collisions, during which an atom in the ground state and an atom in the metastable triplet state $2\,^3S_1$ exchange their electronic variables. ME collisions are used in optical pumping of ^{3}He to create nuclear polarization in gas samples for nuclear physics experiments as well as in nuclear magnetic resonance imaging applications [8]. When the helium vapor is in a sealed cell, a weak radio-frequency discharge excited by a pair of external electrodes maintains a tiny fraction of the atoms in the metastable state, which has a finite lifetime due to its interactions with the cell walls. A transition is accessible from the metastable state to couple the metastable atoms with light. This, together with ME collisions, provides an effective coupling between the ground state atoms and light. We show that, with such a mechanism, quantum fluctuations can be reversibly transferred from the field to the atoms. Interacting with squeezed light in appropriate conditions, the macroscopic nuclear spin (1.6×10^{18} atoms of ^{3}He at 1 torr in a 50 cm^3 cell, at 300 K) of the polarized ground state gas becomes squeezed. The nuclear coherence relaxation time in absence of discharge and in an homogeneous field can be several hours. By switching on the discharge and repopulating the metastable state, the squeezing can be transferred back to the electromagnetic field and measured. In addition to its interest for quantum information, the scheme offers the exciting possibility to create a long-lived nonclassical state for spins.

We consider a system composed by N atoms in the ground state, and n atoms in the metastable state. These atoms interact with a coherent driving field with Rabi frequency Ω and frequency ω_1 that we treat classically, and a cavity field described by creation and annihilation operators A and $A^\dagger$ [Fig. 1(a)]. The field injected into the ring cavity, A_{in} with frequency ω_2, is in an amplitude-squeezed vacuum state: $\langle A_{in}\rangle = 0$ and $\Delta X_{in}^2 = e^{-2r}$, $\Delta Y_{in}^2 = e^{2r}$, where $X = A + A^\dagger$ and $Y = i(A^\dagger - A)$ are the standard field amplitude and phase quadrature operators, satisfying $[X, Y] = 2i$. The Hamiltonian of the atom-field system is:

$$H = H_0 + \hbar\{\Omega S_{31} e^{-i\omega_1 t} + gAS_{32} + \text{H.c.}\}, \qquad (1)$$

where H_0 describes the free evolution of the atoms and the field, $g = d(2\pi\omega_2/\hbar V)^{1/2}$ is the coupling constant between the atoms and the cavity field, V being the volume

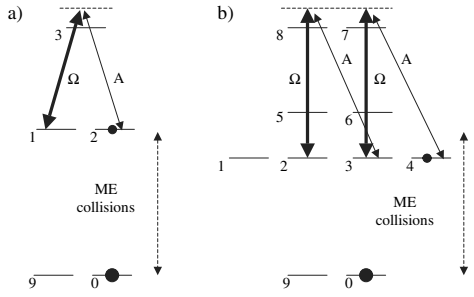

FIG. 1. (a) Sublevels 1 and 2 are metastable, level 3 is the excited state, 9 and 0 are the ground state sublevels. (b) Relevant energy levels in ^{3}He.

 © 2005 The American Physical Society

of the cavity mode, d the atomic dipole. $S_{kl} = \Sigma_{i=1}^{n} |k\rangle_i\langle l|_i$ for $k, l = 1, 2, 3$ are collective atomic operators in the metastable and excited state [9]. The coupling to the ground state collective spin $I_{kl} = \Sigma_{i=1}^{N} |k\rangle_i\langle l|_i$ for $k, l = 9, 0$ is provided by ME collisions.

We start with a simplified picture, in which both the metastable and ground state atoms have a spin $1/2$, which are simply exchanged during each ME collision. The exchange collisions rate for a metastable and a ground state atom are denoted by γ_m and γ_f, respectively. Their ratio γ_m/γ_f is equal to the ratio N/n. We assume that the system is initially prepared using optical pumping in the fully polarized state $\langle I_{00}\rangle = N$ and $\langle S_{22}\rangle = n$. Both the metastable and ground state collective spins are polarized along the z axis of the Bloch sphere. The transverse spin components $S_x = (S_{21} + S_{21}^{\dagger})/2$, $S_y = i(S_{21}^{\dagger} - S_{21})/2$ then play a similar role to field quadratures and, for such a coherent spin state, have equal variances: $\Delta S_x^2 = \Delta S_y^2 = n/4$ and $\Delta I_x^2 = \Delta I_y^2 = N/4$. By definition [10] the metastable (ground state) spin is squeezed if one of the transverse spin variance ΔS_x^2 or ΔS_y^2 (ΔI_x^2 or ΔI_y^2) is smaller than its coherent spin state value. As usual in quantum optics, we study the quantum fluctuations of operators around a ''classical steady state'' of the system (the fully polarized state). We then linearize the equations, and obtain in the rotating frame the following closed set of equations:

$$\dot{S}_{21} = -(\gamma_m - i\delta)S_{21} + \gamma_f I_{09} - i\Omega S_{23} + f_{21} \quad (2)$$

$$\dot{S}_{23} = -(\gamma + i\Delta)S_{23} - i\Omega S_{21} - igAn + f_{23} \quad (3)$$

$$\dot{I}_{09} = -(\gamma_f - i\delta_I)I_{09} + \gamma_m S_{21} + f_{09} \quad (4)$$

$$\dot{A} = -(\kappa + i\Delta_c)A - igS_{23} + \sqrt{2\kappa}A_{in}. \quad (5)$$

We have introduced the detunings $\delta = \omega_S - \delta_{las}$, $\delta_I = \omega_I - \delta_{las}$, $\Delta = (E_3 - E_2)/\hbar - \omega_2$ with E_i the energy of level i, $\omega_I = (E_0 - E_9)/\hbar$, $\omega_S = (E_2 - E_1)/\hbar$, $\delta_{las} = \omega_1 - \omega_2$, and the cavity detuning $\Delta_c = \omega_c - \omega_2$. Ω is assumed to be real. The stochastic part of the evolution (quantum noise) of each operator is described by a time-dependent Langevin operator. If α and β denote two system operators, $\langle f_\alpha(t) f_\beta(t')\rangle = D_{\alpha\beta}\delta(t - t')$ where $D_{\alpha,\beta}$ is the corresponding coefficient of the diffusion matrix. Contributions to D come from polarization decay with a rate γ, ME collisions for metastable and ground state atoms, and cavity losses with a rate κ for the cavity field. The nonzero coefficients of the atomic part of the diffusion matrix are $D_{21,12} = D_{09,90} = 2n\gamma_m$, $D_{21,90} = D_{09,12} = -2n\gamma_m$, $D_{23,32} = 2n\gamma$, calculated using the generalized Einstein relation [11] for an ensemble of uncorrelated atoms. The Langevin forces for ME collisions are necessary for the model to be consistent. Otherwise the non-Hamiltonian character of the exchange terms leads to violation of the Heisenberg uncertainty relations. Physically these forces originate from the fluctuating character of the ME collisions. Their correlation time is the collision time, much shorter than all the time scales we are interested in.

By adiabatic elimination of the polarization S_{23} and the cavity field assuming $\gamma, \kappa \gg \gamma_m, \gamma_f$, one obtains

$$\dot{S}_{21} + (\gamma_m + \Gamma - i\tilde{\delta})S_{21} = \gamma_f I_{09} + f_{21} - \frac{\Omega}{\Delta} f_{23} + i\frac{\Omega g n}{\Delta}\sqrt{\frac{2}{\kappa}}A_{in}, \quad (6)$$

where we introduced the optical pumping parameter $\Gamma = \gamma\Omega^2(1 + C)/\Delta^2$, and the cooperativity $C = g^2 n/(\kappa\gamma)$, and we redefined the two-photon detuning $\tilde{\delta} = \delta + \Omega^2/\Delta$ to account for the light-shift of level 1. In deriving (6) we assumed a Raman configuration $\Delta \gg \gamma$, $(C\gamma/\Delta) \ll 1$ and that the cavity detuning exactly compensates the cavity field dephasing due to the atoms: $\Delta_C = C\kappa\gamma/\Delta$. Optimal coupling between the squeezed field and the metastable coherence is achieved under resonant conditions $\tilde{\delta} = 0$, or

$$\omega_S(B) + \Omega^2/\Delta = \omega_1 - \omega_2, \quad (7)$$

where the Larmor frequency ω_S can be adjusted using a magnetic field. A second resonance condition is $\delta_I = 0$, or

$$\omega_I(B) = \omega_1 - \omega_2, \quad (8)$$

meaning that the natural evolution frequency of the ground state coherence I_{09} should match that of the metastable-state coherence. The Larmor frequency in the metastable and ground states are very different due to the difference between the nucleon and the electron mass. In low field, $\hbar\omega_\alpha = \mu_\alpha B$ ($\alpha = I, S$) with $\mu_I/h = 3.24$ kHz/G and $\mu_S/h = 1.87$ MHz/G. However, the light shift in the metastable state allows us to simultaneously fulfill (7) and (8) for a nonzero magnetic field. Physically, these conditions ensure that both spin coherences are resonantly excited with the same tunable frequency $\omega_I(B)$, thus ensuring the efficiency of the squeezing transfer from the field to ground state. From Eq. (6) and the corresponding equation for I_{09} with $\tilde{\delta} = \delta_I = 0$, we can calculate the variances of the metastable and ground state spins. In the limit $\gamma_f \ll \Gamma$, γ_m one obtains:

$$\Delta I_y^2 = \frac{N}{4}\left\{1 - \frac{\gamma_m}{\Gamma + \gamma_m}\frac{C}{C + 1}(1 - e^{-2r})\right\} \quad (9)$$

$$\Delta S_y^2 = \frac{n}{4}\left\{1 - \frac{\Gamma}{\Gamma + \gamma_m}\frac{C}{C + 1}(1 - e^{-2r})\right\}. \quad (10)$$

In the limit $C \gg 1$, the squeezing can be completely transferred to the atoms. If $\Gamma \gg \gamma_m$, correlations are established among the metastable-state spins, the leakage of correlation towards the ground state being negligible. The metastable collective spin is squeezed while the ground state spin remains unsqueezed. In the opposite limit $\Gamma \ll \gamma_m$, spin exchange is the dominant process for metastable

atoms; they transfer their correlations to the ground state which then becomes squeezed. In all regimes the metastable and the fundamental state share the amount of noise reduction in the field.

In usual optical pumping experiments, the relevant atomic observables are the level orientations, i.e., one-body observables. ME collisions constantly tend to equal the degree of polarization of the two levels. By contrast, squeezing a spin component amounts to giving a negative value to the two-spin correlation function $\langle s_y(1)s_y(2)\rangle$. ME collisions constantly tend to equal the spin correlation functions in the two levels but not the degree of squeezing. This is because, to create maximum squeezing, a much smaller (absolute) value of the correlation function is needed in the fundamental than in the metastable state, due to the large population difference in the two levels [12]. Somehow paradoxically, the squeezed field then maintains a strong squeezing in the ground state via a weakly squeezed metastable state.

If one switches on the discharge and the coherent field in the same configuration as for the ''writing'' phase [4], the nuclear spin memory can be ''read,'' the squeezing being transferred back to the electromagnetic field where it can be measured. During this process, the metastable level acquires only a weak degree of squeezing under the effect of ME collisions. But, because of the optical coupling, this squeezing progressively transits back to the quantum field stored in the cavity, so that, in the end, a strong squeezing is accumulated in the field without ever being large in the metastable state.

One important issue is the writing (or ''reading'') time of the quantum memory, which is the ground state effective response time. The adiabatic elimination of the metastable state in Eq. (4) shows that this time is the inverse of $\Gamma_F = \frac{\gamma_f \Gamma}{\gamma_m + \Gamma}$, which is also the width of the squeezing spectrum in the ground state.

We now apply our scheme to ^{3}He atoms in realistic conditions [Fig. 1(b)]. The coherent field (π polarized) and the squeezed vacuum (σ^- polarized) are tuned to the blue side of the so-called C_9 transition ($\lambda = 1.08\ \mu$m) from the $F = 3/2$ level of the $2\,^3S_1$ metastable state to the $^3P_0$ state, the highest in energy of the $2\,^3P$ multiplicity [13]. The system is initially prepared in the fully polarized state, $\langle I_{00}\rangle = N$ and $\langle S_{44}\rangle = n$, by preliminary optical pumping. The metastable state now has two sublevels $F = 3/2$ and the $F = 1/2$. The effect of ME collisions on the metastable and ground state density matrices ρ_m and ρ_f can be written as [14]:

$$\dot{\rho_f} = \gamma_f(-\rho_f + \mathrm{Tr}_e\rho_m)$$
$$\dot{\rho_m} = \gamma_m(-\rho_m + \rho_f \otimes \mathrm{Tr}_n\rho_m),$$

where Tr_e and Tr_n represent trace operations over the electronic and nuclear variables. After elimination of hyperfine coherences and linearization around the initially prepared state, we obtain a set of 11 closed equations involving the ground state coherence, the cavity field, 4 optical coherences, the excited state coherence, and 4 $\Delta m_F = 1$ coherences in the metastable state. To account for the fact that metastable atoms are destroyed as they reach the cell walls, we introduce a damping rate γ_0 of the metastable-state coherences. Despite the more complicated level structure, in the fully polarized limit considered here, the squeezing transfer to the ground state comes exclusively from the coherence S_{34} which should be excited resonantly. By adiabatic elimination of the field and optical coherences, for optimal squeezing transfer conditions and in the limit $\gamma_f \ll \Gamma, \gamma_m$ we worked out the same analytical expressions (9) and (10) for the ground state and metastable spin variances, within a scaling factor in the optical pumping parameter

$$\Gamma = \gamma 3\Omega^2(1 + C)/\Delta^2, \tag{11}$$

with now $\Delta = (E_7 - E_4)/\hbar - \omega_2$. In Fig. 2 we show the analytical predictions (9) and (10) and a full numerical calculation for realistic experimental parameters: a 1 torr vapor at 300 K, with $\gamma_m = 5 \times 10^6\ \mathrm{s}^{-1}$, and $\gamma = 2 \times 10^7\ \mathrm{s}^{-1}$, and a metastable atom density of $3.2 \times 10^{10}\ \mathrm{atoms/cm}^3$ corresponding to a ratio $n/N = 10^{-6}$. The relaxation rate γ_0 is inversely proportional to the gas pressure (at 1 torr $\gamma_0 = 10^3\ \mathrm{s}^{-1}$). Deviations from the analytical formulas are due to nonadiabaticity of the optical coherence with respect to metastable variables, which affects the squeezing of metastable spin, and to a finite relaxation rate in the metastable state γ_0, which affects the ground state spin squeezing in the region $\Gamma \ll \gamma_m$. In this figure the one-photon detuning Δ is kept fixed while the magnetic field and δ_{las} are chosen to satisfy simultaneously (7) and (8) with now $\omega_S = (E_4 - E_3)/\hbar$. The energy positions of atomic levels in the metastable and

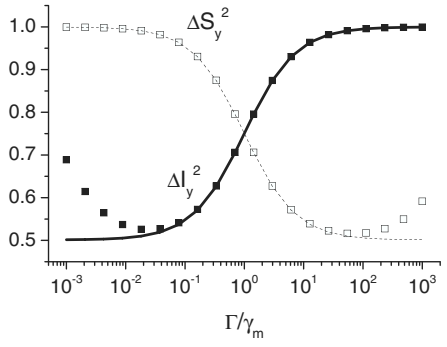

FIG. 2. Analytical predictions (lines) and numerical calculations for spin variances in ground state (full symbols) and metastable state (open symbols), as a function of the ratio Γ/γ_m. Numerical values of parameters are $e^{-2r} = 0.5$, $C = 500$, $\kappa = 100\gamma$, $\Delta = -2000\gamma$, $\gamma = 2 \times 10^7\ \mathrm{s}^{-1}$, $\gamma_m = 5 \times 10^6\ \mathrm{s}^{-1}$, $\gamma_0 = 10^3\ \mathrm{s}^{-1}$.

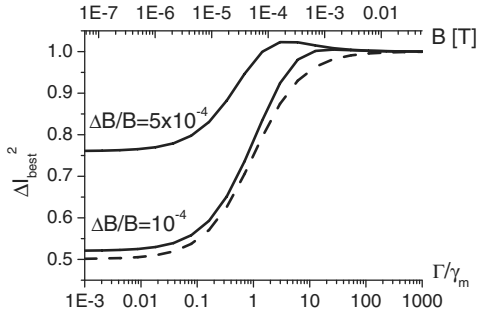

FIG. 3. Ground state spin quadrature optimized (best) variance as a function of the ratio Γ/γ_m (lower x axis), for two relative changes of the magnetic field with respect to its optimal value (upper x axis). $\Delta B/B = 0$ for the dashed curve. $\gamma_0 = 0$ and other parameters are as in Fig. 2.

excited state depending on the field were computed including the effect of hyperfine interactions [15].

We calculated by simulation the effect of a frequency mismatch in (7) or (8), on spin squeezing in the ground state. A frequency mismatch of the order of $\Gamma/3$ in the metastable state or of the order of Γ_F in the ground state affects the efficiency of the squeezing transfer. The condition for the ground state frequency matching (8) imposes stringent requirements on the homogeneity of the magnetic field [16]. Physically, if a significant dephasing between the squeezed field and the ground state coherence builds up during the squeezing transfer time, the atoms will see an average between the squeezed and the antisqueezed quadrature of the field, always above the standard quantum noise limit. Let ΔB be the maximum field difference with respect to the optimal value in the cell volume. For low field, the condition on ΔB to preserve the transfer efficiency reads $\mu_I \Delta B < h\Gamma_F$. Since $\Omega^2/\Delta \simeq \Gamma \frac{\Delta}{3\gamma C} \simeq \frac{\mu_S}{h} B$ we get $\frac{\Gamma}{\Gamma_F} \frac{\mu_I}{\mu_S} \frac{\Delta}{3\gamma C} \frac{\Delta B}{B} < 1$ or, in the regime $\Gamma \ll \gamma_m$, $600 \frac{\Delta}{\gamma C} \frac{\Delta B}{B} < 1$. In Fig. 3 we show the effect of a relative change of the magnetic field with respect to the optimal calculated value. An homogeneity of 100 ppm is sufficient for the chosen parameters to guarantee that all atoms are squeezed. The optimal calculated value for the field is shown as a second x axis in the figure. In realistic conditions, choosing $\Gamma = 0.1\gamma_m$, the required field is about $B = 57$ mG, corresponding to $\omega_I = 184$ Hz. Squeezed vacuum states that can be generated for analysis frequencies as low as 200 Hz [17] could thus be efficiently transferred to the nuclear spins. The readout time is as long as the writing time: $\Gamma_F^{-1} = 2$ s for $\Gamma = 0.1\gamma_m$, limited by the metastable atoms density in the sample.

The possibility to manipulate the spins using nuclear magnetic resonance techniques, and to optically readout the spin state after a long storage time makes this system particularly promising for quantum information [18].

We thank Jacques Dupont-Roc, Nicolas Treps, Yvan Castin, Pierre-Jean Nacher, and Xavier Maître for useful discussions. Laboratoire Kastler Brossel is UMR 8552 du CNRS de l'ENS et de l'UPMC. This work was supported by the COVAQIAL European Project No. FP6-511004.

*Electronic address: alice.sinatra@lkb.ens.fr

[1] L. M. Duan *et al.*, Nature (London) **414**, 413 (2001).
[2] M. D. Lukin, Rev. Mod. Phys. **75**, 457 (2003).
[3] M. Fleischhauer and M. D. Lukin, Phys. Rev. Lett. **84**, 5094 (2000); A. E. Kozhekin, K. Mølmer, and E. Polzik, Phys. Rev. A **62**, 33809 (2000).
[4] A. Dantan and M. Pinard, Phys. Rev. A **69**, 43810 (2004); A. Dantan, A. Bramati, and M. Pinard, Europhys. Lett. **67**, 881 (2004).
[5] B. Julsgaard *et al.*, Nature (London) **432**, 482 (2004).
[6] C. H. van der Wal *et al.*, Science **301**, 196 (2003); C. Schori *et al.*, Phys. Rev. Lett. **89**, 57903 (2002).
[7] J. M. Taylor *et al.*, Phys. Rev. Lett. **90**, 206803 (2003).
[8] J. Becker *et al.*, Nucl. Instrum. Methods Phys. Res., Sect. A **402**, 327 (1998); H. Moller *et al.*, Magn. Reson. Med. **47**, 1029 (2002).
[9] Position dependent phase factors due to field propagation are ignored since we assume that the fields are copropagating, far from resonance, and with very small frequency difference in the working conditions of the memory.
[10] M. Kitagawa and M. Ueda, Phys. Rev. A **47**, 5138 (1993).
[11] C. Cohen-Tannoudji, J. Dupont-Roc, and G. Grynberg *Atom-Photon Interactions* (Wiley-VCH, Berlin, 1998), Chap. V.
[12] The two-spin correlation function is subject to an absolute lower limit that is proportional to the inverse total number of spins in the level, due to a simple positivity condition. When this limit is reached, the corresponding component of the total spin is completely squeezed. In our calculation, the spin correlation functions in the two levels become both equal to $[\exp(-2r) - 1]/4(n + N)$ in the extreme limit $\Gamma \leq \gamma_f$.
[13] We have assumed above that the squeezed field and the coherent field are copropagating. The squeezed field should thus be σ polarized, with a σ^+ component; we checked that this component plays no role here.
[14] R. B. Partridge and G. W. Series, Proc. Phys. Soc. London **88**, 983 (1966); J. Dupont-Roc *et al.*, J. Physique **34**, 961 (1973); **34**, 977 (1973).
[15] E. Courtade *et al.*, Eur. Phys. J. D **21**, 25 (2002).
[16] Although the Larmor precession in the metastable state is $\sim 10^3$ times faster than in the ground state, the effective transfer time (interaction with the field and metastability exchange) is $\sim 10^6$ times shorter for the metastable state, so that the most stringent condition on B comes from the ground state.
[17] K. Mc Kenzie *et al.*, Phys. Rev. Lett. **93**, 161105 (2004); J. Laurat *et al.*, Phys. Rev. A **70**, 42315 (2004).
[18] A. Kuzmich and E. S. Polzik, Phys. Rev. Lett. **85**, 5639 (2000); A. Dantan *et al.*, Phys. Rev. Lett. **94**, 50502 (2005).

To appear in Jour. of Mod. Optics.

Squeezing and entangling nuclear spins in helium 3

G. Reinaudi, A. Sinatra
LKB, ENS, 24 Rue Lhomond, 75231 Paris Cedex 05, France

A. Dantan, M. Pinard
LKB, UPMC, case 74, place Jussieu, 75252 Paris Cedex 05, France

We present a realistic model for transferring the squeezing or the entanglement of optical field modes to the collective ground state nuclear spin of ^{3}He using metastability exchange collisions. We discuss in detail the requirements for obtaining good quantum state transfer efficiency and study the possibility to readout the nuclear spin state optically.

PACS numbers: 03.67.-a, 03.67.Hk, 42.50.Dv, 67.65.+z

I. INTRODUCTION

Helium 3 atoms in their ground state possess a purely nuclear spin $I = 1/2$. Such spins are well-isolated from the environment and show extremely long coherence times. Longitudinal coherence times T_1 of several days are measured in room temperature samples [1]. The transverse coherence time T_2, which would be as long as T_1 in zero magnetic field, is usually limited by magnetic field inhomogeneity if no special precaution is taken. Transverse coherence times of several hours are observed in a very low field [2]. These very long coherence times originate from the weakness of magnetic coupling on the one hand, and from the absence of electrical coupling on the other hand, as there is no electric quadrupole coupling within the ground state for spins 1/2. It is tempting to exploit such long-lived coherence for quantum information purposes. In a previous letter [3] we studied the possibility to transfer the squeezing of a cavity mode to ^{3}He nuclear spins. We showed that the squeezeing could be stored and retrieved from the atoms, thus realizing a quantum memory [4–9]. For the sake of simplicity we presented in our letter a simplified model involving only two sublevels in the metastable state and gave numerical results for the more complicated case of ^{3}He. In this paper we concentrate on ^{3}He and treat in detail this more realistic case.

Section II is devoted to metastability exchange collisions. We derive linearized Heisenberg-Langevin equations describing the exchange collisions from the standpoint of quantum fluctuations. In section III we describe the model for squeezing transfer from a squeezed vacuum mode of the electromagnetic field to the atoms. Numerical results are shown and discussed in section IV. In section V we obtain analytical results in the adiabatic elimination limit for the optical coherences and the cavity field. Section VI is devoted to the readout scheme of the quantum memory. In section VII, as a straightforward application of our scheme, we consider the possibility of creating long-lived quantum correlations between two macroscopic spins, in the move of the successful experiment in Copenhagen [10], in which two macroscopic spins were entangled for 0.5 ms, but on a completely different timescale. Finally, in section VIII, we use a toy model to explore the consequences of an imperfect polarization of the atoms on our squeezing transfer scheme.

II. METASTABILITY EXCHANGE COLLISIONS IN HELIUM 3

Over forty years ago, Colegrove, Schearer and Walters [11] demonstrated a technique to polarize ^{3}He relying on (*i*) an optical interaction on an infrared transition from the metastable 2^3S triplet state to the 2^3P triplet state, and (*ii*) *metastability exchange collisions* between atoms in the ground state and in the metastable state. During such a collision, two atoms exchange their electronic degrees of freedom so that the metastable atom, oriented by optical pumping and with a nuclear polarization due to hyperfine coupling in the metastable state, becomes a polarized ground state atom [12]. This technique called *metastability exchange optical pumping* is currently used to prepare polarized samples for nuclear physics experiments as well as in nuclear magnetic resonance imaging applications [13].

In what follows we suggest that metastability exchange collisions can also be used to transfer quantum correlations to the ground state nuclear spin of ^{3}He.

A. Equations for the one-body density matrix elements

Partridge and Series [12] describe a metastability exchange (ME) collision in terms of the one-body density matrices representing the internal states of two colliding atoms that we name $\rho_{\rm g}^{\rm at}$ and $\rho_{\rm m}^{\rm at}$ for the ground and metastable state,

2

respectively. The density matrices after the collision, $\rho_{\rm g}^{\rm at\prime}$ and $\rho_{\rm m}^{\rm at\prime}$, are given by

$$\left\{ \begin{array}{lcl} \rho_{\rm g}^{\rm at\prime} & = & {\rm Tr}_e\ \rho_{\rm m}^{\rm at} \\ \rho_{\rm m}^{\rm at\prime} & = & \rho_{\rm g}^{\rm at} \otimes {\rm Tr}_n\ \rho_{\rm m}^{\rm at} \end{array} \right. \tag{1}$$

where ${\rm Tr}_e$ and ${\rm Tr}_n$ are trace operators over the electronic and nuclear variables.

Let us consider n metastable and N ground state independent atoms. We introduce $\rho_{\rm g} = N\rho_{\rm g}^{\rm at}$, $\rho_{\rm m} = n\rho_{\rm m}^{\rm at}$, and the same for $\rho'_{\rm g}$ and $\rho'_{\rm m}$.

To represent the state of the system, we will use the density matrix ρ defined by:

$$\rho = \left(\begin{array}{cc} \rho_{\rm m} & 0 \\ 0 & \rho_{\rm g} \end{array} \right) \tag{2}$$

Note that $Tr\rho = n + N$ and that we neglect all coherences between the ground and the metastable states. The matrices $\rho_{\rm g}$ and $\rho_{\rm m}$ evolve according to

$$\left\{ \begin{array}{lcl} \frac{d}{dt}\rho_{\rm g} & = & -\gamma_f \rho_{\rm g} + \gamma_f \rho'_{\rm g} \\ \frac{d}{dt}\rho_{\rm m} & = & -\gamma_m \rho_{\rm m} + \gamma_m\ \rho'_{\rm m} \end{array} \right. \tag{3}$$

where γ_f and γ_m are the metastability exchange collision rates in the ground and metastable states respectively

$$\gamma_m = N\gamma_{exc} \qquad \gamma_f = n\gamma_{exc} \tag{4}$$

with γ_{exc} a rate depending on the metastability exchange cross section, the relative velocity of the atoms and the volume explored by the atoms.

The calculation of $d\rho/dt$ is performed by expressing ρ in the decoupled spin basis of the nuclear spin $I = \frac{1}{2}$ and the total electronic spin $J = S = 1$ in the metastable state, followed by a projection onto the hyperfine states (eigenstates of the total momentum operator F and F_z) which we name from 1 to 6 as in figure 1. The explicit evolution equations for the density matrix elements are given in the Appendix. The fully polarized state in which all the atoms are in the sublevel with highest angular momentum projection along z is stationary for equations (3).

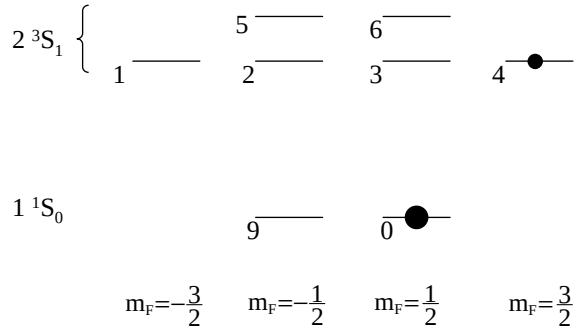

FIG. 1: Sublevels 1 to 6 are metastable; 9 and 0 are the ground state sublevels. The fully polarized stationary state is shown.

Starting from equations (3) we proceed in two steps which will be detailed in the following:

1. We linearize these equations around the fully polarized steady state in which the only non-zero elements of ρ are $\rho_{44} = n$ and $\rho_{00} = N$.
2. From the linearized classical equations, interpreted as semiclassical equations for the mean values of the collective operators, we derive the corresponding Heisenberg-Langevin equations.

B. Linearized Heisenberg-Langevin equations

By linearization around the fully polarized solution we obtain equations for the "fluctuations" or deviations of the ρ_{ij} from their steady-state values. Such linear equations coincide with the linearized semiclassical equations for the collective atomic operators operators mean values:

$$\rho_{kl} = \langle S_{lk} \rangle \qquad k,l = 1,\ldots,6 \tag{5}$$

$$\rho_{kl} = \langle I_{lk} \rangle \qquad k,l = 9,0 \tag{6}$$

where $S_{kl} = \sum_{i=1}^{n} |k\rangle_i\langle l|_i$ for $k,l = 1,\ldots,6$ and $I_{kl} = \sum_{i=1}^{N} |k\rangle_i\langle l|_i$ for $k,l = 9,0$ are the collective atomic operators in the metastable and ground state, respectively. The corresponding linearized Heisenberg-Langevin equation for the operators are obtained by adding zero-mean valued fluctuating terms which are the Langevin forces. Denoting by f_α the Langevin force for the operator α we get a closed set of equations:

$$\dot{S}_{21} = -\gamma_m S_{21} + f_{21} \tag{7}$$

$$\dot{S}_{32} = \frac{2}{9}\gamma_m\left(-\frac{7}{2}S_{32} + \sqrt{3}S_{21} + S_{65}\right) + f_{32} \tag{8}$$

$$\dot{S}_{65} = -\frac{7}{9}\gamma_m\left(S_{65} - \frac{2}{7}\sqrt{3}S_{21} - \frac{2}{7}S_{32}\right) + f_{65} \tag{9}$$

$$\dot{S}_{43} = \gamma_m\left(-\frac{1}{3}S_{43} + \frac{2\sqrt{3}}{9}(S_{32} + S_{65})\right) + \frac{\sqrt{3}}{3}\gamma_f I_{09} + f_{43} \tag{10}$$

$$\dot{I}_{09} = \frac{1}{3}\left[-3\gamma_f I_{09} + 2\gamma_m\left(S_{32} - \frac{1}{2}S_{65} + \frac{\sqrt{3}}{2}S_{43} + \frac{\sqrt{3}}{2}S_{21}\right)\right] + f_{09} \tag{11}$$

If α and β denote two system operators, $\langle f_\alpha(t) f_\beta(t')\rangle = D_{\alpha\beta}\delta(t-t')$ where $D_{\alpha,\beta}$ is the corresponding coefficient of the diffusion matrix which can be calculated using the generalized Einstein relations [14] for an ensemble of uncorrelated atoms. The non-zero coefficients are

$$D_{43,34} = \tfrac{2}{3}\gamma_m n, \quad D_{09,34} = D_{43,90} = -\tfrac{2\sqrt{3}}{3}\gamma_m n, \quad D_{09,90} = 2\gamma_m n. \tag{12}$$

Langevin forces are necessary to the consistency of the model. Otherwise, the non-Hamiltonian character of the exchange terms leads to a violation of the Heisenberg uncertainty relations. Physically, these forces originate from the fluctuating character of the ME collisions and their correlation time is the collision time, much shorter ($\sim 10^{-13}$ s) than all the times scales we are interested in.

C. Consequences of the Heisenberg-Langevin equations for ME collisions

We notice that Eqs. (7)-(9) for S_{21}, S_{32}, S_{65} form a closed subset of equations. This means that in the frequency domain each of these variables can be expressed as a linear combination of the Langevin forces f_{21}, f_{32}, f_{65}. However, in the fully polarized limit we consider here, these Langevin forces do not contribute to the diffusion matrix. It follows that these variables do not contribute to the spin noise and can be neglected. One is then left with only two equations

$$\dot{S}_{43} = -\frac{\gamma_m}{3}S_{43} + \frac{\sqrt{3}}{3}\gamma_f I_{09} + f_{43} \tag{13}$$

$$\dot{I}_{09} = -\gamma_f I_{09} + \gamma_m\frac{\sqrt{3}}{3}S_{43} + f_{09}\,. \tag{14}$$

Let us introduce the transverse spin quadratures S_x, S_y

$$S_x = (S_{34} + S_{43})/2, \qquad S_y = i(S_{34} - S_{43})/2 \tag{15}$$

(and similarly for the ground state spin transverse components I_x, I_y) and let us assume that the ground state is initially squeezed, while the metastable atoms are in a coherent spin state. Integrating (13)-(14) with the initial conditions $\overline{\Delta I_y^2}(0) = \Delta I_y^2(0)/(N/4) = e^{-2r}$ and $\overline{\Delta S_y^2}(0) = \Delta S_y^2(0)/(n/4) = 1$ one finds the normalized steady state variances to be

$$\overline{\Delta S_y^2} = 1 - [1 - e^{-2r}]\frac{3nN}{(3n+N)^2} \tag{16}$$

$$\overline{\Delta I_y^2} = 1 - [1 - e^{-2r}]\frac{N^2}{(3n+N)^2} \tag{17}$$

Since $n \ll N$ (typically $n/N \sim 10^{-6}$), the ground state spin is still squeezed by approximately the same factor e^{-2r}, whereas the metastable atoms squeezing is negligible (in n/N). By introducing the correlation functions $\mathcal{C}_S$ and $\mathcal{C}_I$ of two individual spins in the metastable and ground state respectively:

$$\mathcal{C}_S = \frac{\overline{\Delta S_y^2} - 1}{4n} \qquad \text{and} \qquad \mathcal{C}_I = \frac{\overline{\Delta I_y^2} - 1}{4N} \tag{18}$$

this simple calculation shows that ME collisions tend to equalize the correlation function (up to some numerical constant): $C_S = 3C_I$. If the ground state spin is squeezed, C_I has a negative value of order $1/N$, corresponding to significant collective correlations for the N-particle ensemble. However, as $n \ll N$, this negative value of the correlation function in the metastable state is by far too small to induce squeezing into the n-particle metastable state, which would require $\mathcal{C}_S \sim -1/n$. For $e^{-2r} = 1$ we recover the coherent spin state with no correlation between the ground state and the metastable spins.

Noise spectra can also be derived in a similar fashion. By defining the noise spectrum as

$$\mathcal{S}_{x_i x_j}(\omega) = \int d\tau \; e^{-i\omega\tau} \langle x_i(0) x_j(\tau) \rangle \tag{19}$$

where x_i, x_j are fluctuations of system operators and for the same initial conditions $\overline{\Delta I_y^2}(0) = \Delta I_y^2(0)/(N/4) = e^{-2r}$ and $\overline{\Delta S_y^2}(0) = \Delta S_y^2(0)/(n/4) = 1$ we get:

$$\mathcal{S}_{I_y,I_y}(\omega) = \frac{\pi(Ne^{-2r} + 3n)N^2\delta(\omega)}{2(N+3n)^2} + \frac{9\gamma_{\rm exc} nN}{18\omega^2 + 2(N+3n)^2\gamma_{\rm exc}^2} \tag{20}$$

$$\mathcal{S}_{S_y,S_y}(\omega) = \frac{3\pi(Ne^{-2r} + 3n)n^2\delta(\omega)}{2(N+3n)^2} + \frac{3\gamma_{\rm exc} nN}{18\omega^2 + 2(N+3n)^2\gamma_{\rm exc}^2} \tag{21}$$

The equal time correlations (16) and (17) can be recovered from these formulas by integration:

$$\langle x_i x_j \rangle = \frac{1}{2\pi} \int d\omega \; \mathcal{S}_{x_i x_j}(\omega) \, . \tag{22}$$

For an initial coherent spin state ($e^{-2r} = 1$), the ME collision process does not change the collective spin variances, but it affects the noise spectra. The δ-shaped atomic spectra of the two spins in absence of ME collisions acquire a width of order $\gamma_{\rm exc}(N+3n)$, that is, of order γ_m. The contribution to the total variance of the "broad" part of the spectrum which is not sensitive to initial squeezing in the system, is large for the metastable state and small for the ground state.

III. THE MODEL FOR SQUEEZING TRANSFER

In figure 2 are represented the ^{3}He energy levels which are relevant for our squeezing transfer scheme. The atoms interact with a coherent control field of Rabi frequency Ω and frequency ω_1 that we treat classically, and a cavity field described by operators A and $A^\dagger$. The field injected into the cavity, A_{in} with frequency ω_2, is in an amplitude-squeezed vacuum state: $\langle A_{in} \rangle = 0$ and $\Delta X_{in}^2 = e^{-2r}$, $\Delta Y_{in}^2 = e^{2r}$, where we have introduced the field quadratures

$$X = A + A^\dagger \qquad\qquad Y = i(A^\dagger - A) \, . \tag{23}$$

The coherent field (π-polarized) and the squeezed vacuum (σ^--polarized) are tuned to the blue side of the so-called C_9 transition ($\lambda = 1.08$ μm) from the $F = 3/2$ level of the 2^3S metastable state to the 2^3P_0 state, the highest in energy of the 2^3P multiplicity [15]. The atom-field Hamiltonian of the system is:

$$H = H_0 + \hbar \left\{ \Omega e^{-i\omega_1 t}(S_{73} + S_{82}) + A(g_A S_{74} + g_B S_{83}) + h.c. \right\} \tag{24}$$

where H_0 describes the atom-field free evolution, $g_{A,(B)} = d_{A,(B)}\sqrt{2\pi\omega_2/\hbar V}$ are the coupling constants between the atoms and the cavity field, V being the volume of the cavity mode and $d_{A,(B)}$ the atomic dipoles of the transitions $7 \leftrightarrow 4$, $(8 \leftrightarrow 3)$. The system is initially prepared in the fully polarized state $\langle I_{00} \rangle = N$ and $\langle S_{44} \rangle = n$ by preliminary optical pumping.

Non-Hamiltonian contributions to the evolution of the system operators describe damping of the cavity mode, spontaneous emission from the excited state and the ME collisions described in detail in the previous section. Linearizing the equations in the rotating frame around the fully polarized state solution we obtain the following closed set of equations:

$$\dot{S}_{21} = -(\gamma_m - i\delta_{12})S_{21} + i\Omega S_{81} + f_{21} \tag{25}$$

$$\dot{S}_{81} = -(\gamma - i(\Delta_{18} - 2\delta_{las}))S_{81} + i\Omega S_{21} + f_{81} \tag{26}$$

$$\dot{S}_{32} = \frac{2}{9}\gamma_m \left(-\frac{7}{2} S_{32} + \sqrt{3} S_{21} + S_{65} \right) + i\delta_{23} S_{32} - i\Omega(S_{38} - S_{72}) + f_{32} \tag{27}$$

5

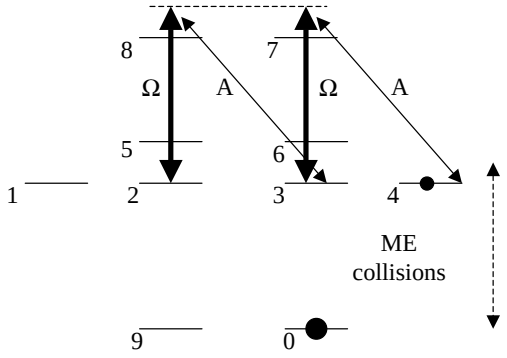

FIG. 2: a) Metastable and excited sublevels of ^{3}He. Three coupling constants to the light are introduced. b) Squeezing transfer scheme using a control field Ω, a squeezed vacuum field A and metastability exchange collisions. 9 and 0 are the ground state sublevels.

$$\dot{S}_{72} = -(\gamma - i(\Delta_{27} - 2\delta_{las}))S_{72} - i\Omega(S_{78} - S_{32}) + f_{72} \quad (28)$$

$$\dot{S}_{43} = \gamma_m \left(-\frac{1}{3}S_{43} + \frac{2\sqrt{3}}{9}(S_{32} + S_{65})\right) + \frac{\sqrt{3}}{3}\gamma_f I_{09} + i\delta_{34}S_{43} - i\Omega S_{47} + f_{43} \quad (29)$$

$$\dot{S}_{65} = -\frac{7}{9}\gamma_m \left(S_{65} - \frac{2}{7}\sqrt{3}S_{21} - \frac{2}{7}S_{32}\right) + i\delta_{56}S_{65} + f_{65} \quad (30)$$

$$\dot{S}_{47} = -(\gamma + i\Delta_{47})S_{47} - ig_A nA - i\Omega S_{43} + f_{47} \quad (31)$$

$$\dot{S}_{38} = -(\gamma + i\Delta_{38})S_{38} - i\Omega(S_{32} - S_{78}) + f_{38} \quad (32)$$

$$\dot{S}_{78} = -(2\gamma - i\delta_{87})S_{78} - i\Omega(S_{72} - S_{38}) + f_{78} \quad (33)$$

$$\dot{I}_{09} = \frac{1}{3}\left[-3\gamma_f I_{09} + 2\gamma_m \left(S_{32} - \frac{1}{2}S_{65} + \frac{\sqrt{3}}{2}S_{43} + \frac{\sqrt{3}}{2}S_{21}\right)\right] + i\delta_{90}I_{09} + f_{09} \quad (34)$$

$$\dot{A} = -(\kappa + i\Delta_C)A - ig_B S_{38} - ig_A S_{47} + \sqrt{2\kappa}A_{in} \quad (35)$$

where

$$\Delta_{ij} = (E_j - E_i) - \omega_2 \quad (36)$$

$$\delta_{ij} = (E_j - E_i) - \delta_{las} \quad (37)$$

$$\delta_{las} = \omega_1 - \omega_2\,, \quad (38)$$

γ is the coherence decay rate due to spontaneous emission from the excited state and collisions and we supposed Ω to be real. The non-zero atomic diffusion coefficients are

$$D_{43,34} = \frac{2}{3}\gamma_m n, \;\; D_{43,90} = D_{09,34} = -\frac{2\sqrt{3}}{3}\gamma_m n, \;\; D_{47,74} = 2\gamma n, \;\; D_{09,09} = 2\gamma_m n \quad (39)$$

We notice that metastable variables S_{21}, S_{81}, S_{32}, S_{72}, S_{65}, S_{38} and S_{78} form a closed subset of equations involving Langevin forces which do not give rise to non-zero diffusion coefficients in the fully polarized limit we consider here. Using the same argument as in section II, we deduce that these variables do not contribute to the spin noise and can be neglected. One is then left with only four relevant equations

$$\dot{S}_{43} = -\frac{\gamma_m}{3}S_{43} + \frac{\sqrt{3}}{3}\gamma_f I_{09} + i\delta_{34}S_{43} - i\Omega S_{47} + f_{43} \quad (40)$$

$$\dot{S}_{47} = -(\gamma + i\Delta)S_{47} - ig_A nA - i\Omega S_{43} + f_{47} \quad (41)$$

$$\dot{I}_{09} = \frac{1}{3}\left(-3\gamma_f I_{09} + \gamma_m\sqrt{3}S_{43}\right) + i\delta_I I_{09} + f_{09} \quad (42)$$

$$\dot{A} = -(\kappa + i\Delta_C)A - ig_A S_{47} + \sqrt{2\kappa}A_{in} \quad (43)$$

with $\Delta = \Delta_{47}$ and $\delta_I = \delta_{90}$.

IV. NUMERICAL RESULTS

Equations (40)-(43) can be used to find the variances of the metastable and ground state spin numerically. A typical result is displayed in figure 3, for which we assume that a squeezed vacuum field with $\Delta X_{in}^2 = 0.5$ is injected into the cavity with the coherent control field in the squeezing-transfer configuration. In this figure $\overline{\Delta S_y^2}$ and $\overline{\Delta I_y^2}$ represent

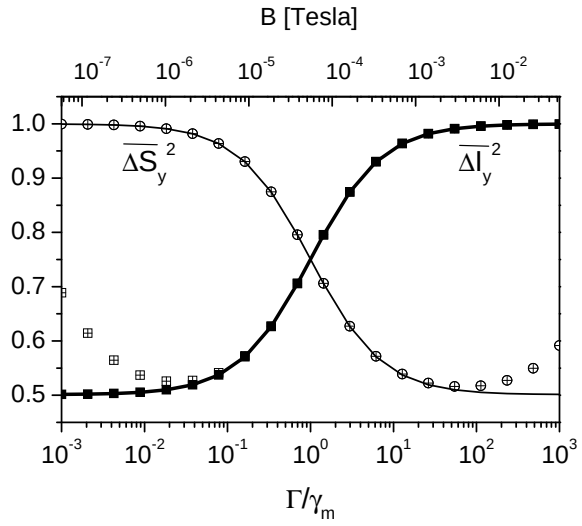

FIG. 3: Symbols: numerical calculations for spin variances in ground state (squares) and metastable state (circles), as a function of the ratio Γ/γ_m (lower x-axis). The corresponding magnetic field needed to satisfy the resonance conditions (46) and (47) is shown in the upper x-axis. Numerical values of parameters are $e^{-2r} = 0.5$, $C = 500$, $\kappa = 100\gamma$, $\Delta = -2000\gamma$, $\gamma = 2 \times 10^7$ s^{-1}, $\gamma_m = 5 \times 10^6$ s^{-1}. The crossed squares correspond to a calculation including an extra relaxation rate $\gamma_0 = 10^3$ s^{-1} for the metastable variables. The lines correspond to the analytical predictions (50) and (51).

the variances of S_y and I_y, both normalized to their coherent spin state values. They are plotted as a function of the ratio Γ/γ_m, where Γ is the pumping parameter

$$\Gamma = \gamma 3\Omega^2(1+C)/\Delta^2\,, \tag{44}$$

and $C = g^2 n/(\kappa\gamma)$ the cooperativity. It is precisely this ratio Γ/γ_m which acts as a control parameter to decide how the available squeezing of the field is shared between the metastable and the ground state spin. If $\Gamma \gg \gamma_m$, correlations are established among the metastable-state spins, the leakage of correlation towards the ground state being negligible. The metastable collective spin is squeezed while the ground state spin remains unsqueezed. In the opposite limit $\Gamma \ll \gamma_m$, spin exchange is the dominant process for metastable atoms; they transfer their correlations to the ground state which then becomes squeezed, while the metastable state remains unsqueezed.

In this plot we have chosen the best conditions for squeezing transfer:

1. The metastable coherence S_{43} is resonantly excited by the two fields in a Raman configuration. By introducing the effective two-photon detuning for this coherence

$$\tilde{\delta} = \delta_{34} + \Omega^2/\Delta \tag{45}$$

accounting for the light-shift of level 3, this condition reads $\tilde{\delta} = 0$, or

$$(E_4 - E_3)/\hbar + \Omega^2/\Delta = \omega_1 - \omega_2\,. \tag{46}$$

2. The ground state coherence I_{09} should be resonantly excited by the metastable coherence ($\delta_I = 0$), i.e.

$$(E_0 - E_9)/\hbar = \omega_1 - \omega_2\ . \tag{47}$$

In practice a magnetic field (shown as the upper x-axis) can be used to simultaneously fulfill (46) and (47). When the resonance conditions are fulfilled the difference in the Larmor frequencies in the metastable and in the ground

state is exactly compensated by the light-shift induced by the coherent control field. Choosing $\Gamma = 0.1\gamma_m$ as a working point, the required field is about $B = 57$ mG, corresponding to $\omega_I = 184$ Hz.

The vapor parameters in the figure correspond to a 1 torr sample at 300 K, with $\gamma_m = 5 \times 10^6$ s^{-1} and $\gamma = 2 \times 10^7$ s^{-1}, and a metastable atom density of 3.2×10^{10} atoms/cm^3 which gives $n/N = 10^{-6}$. The symbols with a cross are a second calculation in which we added a finite relaxation rate in the metastable state γ_0, to account for the fact that metastable atoms are destroyed as they reach the cell walls. We notice that only the ground state spin squeezing in the region $\Gamma \ll \gamma_m$ is affected.

V. ANALYTICAL RESULTS

In order to have a better physical insight it is possible to find simple analytical results within some reasonable approximation. By adiabatic elimination of the polarization S_{47} and the cavity field assuming $\gamma, \kappa \gg \gamma_m, \gamma_f$, one obtains

$$\dot{S}_{43} + (\frac{\gamma_m}{3} + \frac{\Gamma}{3} - i\tilde{\delta})S_{43} = \frac{\gamma_f}{\sqrt{3}} I_{09} + f_{43} - \frac{\Omega}{\Delta} f_{47} + i\frac{\Omega g n}{\Delta}\sqrt{\frac{2}{\kappa}} A_{in} \tag{48}$$

$$\dot{I}_{09} + (\gamma_f - i\delta_I) I_{09} = \frac{\gamma_m}{\sqrt{3}} S_{43} + f_{09} \tag{49}$$

In deriving (48) we assumed a Raman configuration $\Delta \gg \gamma$, $\frac{C\gamma}{\Delta} \ll 1$ and that the cavity detuning exactly compensates the cavity field dephasing due to the atoms: $\Delta_C = C\kappa\gamma/\Delta$. From equation (48) we see that $(\gamma_m + \Gamma)/3$ is the inverse of the characteristic time constant for the metastable coherence evolution.

A. Resonant case

If the resonance conditions (46) and (47) are satisfied ($\tilde{\delta} = \delta_I = 0$) and in the limit $\gamma_f \ll \Gamma, \gamma_m$, we can calculate the variances of the metastable and ground state spins

$$\Delta I_y^2 = \frac{N}{4}\left\{1 - \frac{\gamma_m}{\Gamma + \gamma_m}\frac{C}{C+1}(1 - e^{-2r})\right\} \tag{50}$$

$$\Delta S_y^2 = \frac{n}{4}\left\{1 - \frac{\Gamma}{\Gamma + \gamma_m}\frac{C}{C+1}(1 - e^{-2r})\right\} \tag{51}$$

which are plotted as full lines in figure 3.

B. Non-perfectly resonant case

In order to test the robustness of our scheme, let us now concentrate on what happens if the resonance conditions (46) and (47) are only approximatively satisfied. We will focus on the variance of the ground state spin coherence I_{09}.

By adiabatically eliminating the metastable coherence S_{43} one obtains

$$\dot{I}_{09} + [\Gamma_F + ib]\, I_{09} = f_{09} + \frac{\gamma_m\sqrt{3}}{\gamma_m + \Gamma - i3\tilde{\delta}}\left(f_{43} - \frac{\Omega}{\Delta} f_{47} + i\frac{\Omega g n}{\Delta}\sqrt{\frac{2}{\kappa}} A_{in}\right) \tag{52}$$

The real part in the brackets

$$\Gamma_F = \gamma_f \frac{\Gamma(\gamma_m + \Gamma) + (3\tilde{\delta})^2}{(\gamma_m + \Gamma)^2 + (3\tilde{\delta})^2} \tag{53}$$

is the inverse of the effective time constant for the ground state coherence evolution which would also be the "writing" (or "reading") time of the quantum memory. $\Gamma_F^{-1} = 2s$ in the example of figure 3 for $\Gamma = 0.1\gamma_m$. It would be proportionally shortened by increasing the metastable atoms density although Penning collisions prevent in practice metastable atoms densities exceeding 10^{10}-10^{11} at/cm^2. The imaginary part in the brackets

$$b = -\left(\gamma_f \frac{3\tilde{\delta}\gamma_m}{(\gamma_m + \Gamma)^2 + (3\tilde{\delta})^2} + \delta_I\right) \tag{54}$$

is a light-shift "brought back" to the ground state, which is zero in the resonant case. Equation (52) can be used to calculate the best squeezing (optimized with respect to the transverse spin quadrature) of the ground state coherence: $\Delta I^2_{best} = \min_\theta \Delta I^2_\theta$ with $I_\theta = I_x \cos\theta + I_y \sin\theta$. We obtain

$$\Delta I^2_{best} = \frac{N}{4}\left\{1 - \frac{\gamma_m}{\Gamma + \gamma_m + (3\tilde{\delta})^2/\Gamma}\,\frac{C}{C+1}\,\left[1 - (e^{-2r} + m\sinh(2r))\right]\right\} \tag{55}$$

where

$$m = 1 - \sqrt{\frac{1}{1 + (b/\Gamma_F)^2}} \tag{56}$$

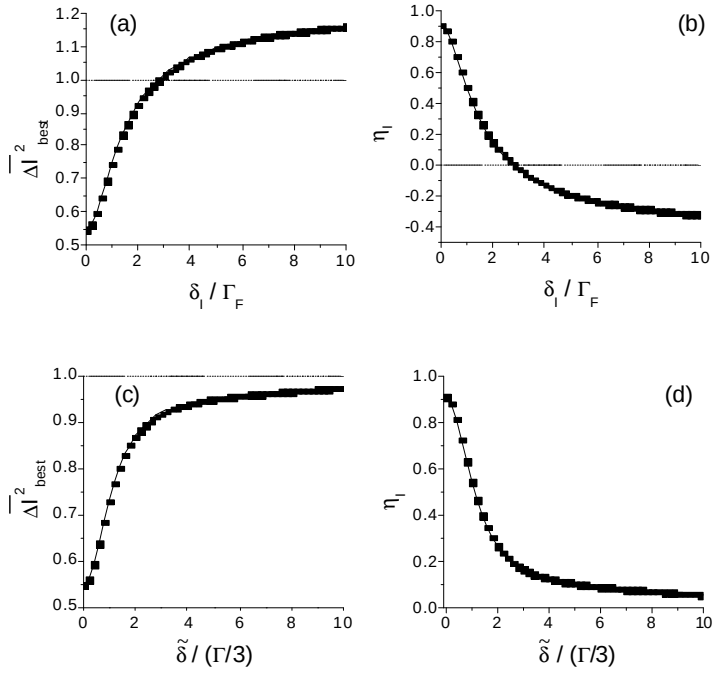

FIG. 4: Normalized ground state spin variance corresponding quantum transfer efficiency η_I as a function of δ_I/Γ_F (while $\tilde{\delta} = 0$) (plots (a) and (b)), or $\tilde{\delta}/(\Gamma/3)$ (while $\delta_I = 0$) (plots (c) and (d). Symbols: numerical integration of equations (25)-(35). Lines: analytical expression (55). Parameters are the same as in figure 3 and $\Gamma = 0.1\gamma_m$.

We show in figure 4 the effect of a frequency mismatch in on the normalized spin variance, $\overline{\Delta I_y^2}$ and the corresponding squeezing transfer efficiency η_I

$$\eta_I = \frac{1 - \overline{\Delta I_y^2}}{1 - e^{-2r}}\,. \tag{57}$$

In this example, a frequency mismatch of the order of $\Gamma/3$ in the metastable state or of the order of Γ_F in the ground state affects the efficiency of the squeezing transfer. The condition for the ground state frequency matching (47) imposes stringent requirements on the homogeneity of the magnetic field. Because of the $\sinh(2r)$ in equation (55), the larger the squeezing the worse are the consequences of a mismatch in the condition on $\delta_I = 0$ on the ground state atoms. Physically, if a significant dephasing between the squeezed field and the ground state coherence builds up during the squeezing transfer time, the atoms will see an average between the squeezed and the anti-squeezed quadrature of the field noise. We can easily estimate the required magnetic field homogeneity as follows. Let us introduce the Larmor evolution frequencies in the metastable and ground states: in low field, $\hbar\omega_\alpha = \mu_\alpha B$ (α=I,S) with $\mu_I/h = 3.24$kHz/G and $\mu_S/h = 1.87$MHz/G, and let ΔB be the maximum field difference with respect to the optimal value in the cell volume. For low field, the condition on ΔB to preserve the transfer efficiency reads $\mu_I \Delta B \ll h\Gamma_F$. Since $\Omega^2/\Delta \simeq \Gamma\frac{\Delta}{3\gamma C} \simeq \frac{\mu_S}{h}B$ we get $\frac{\Gamma}{\Gamma_F}\frac{\mu_I}{\mu_S}\frac{\Delta}{3\gamma C}\frac{\Delta B}{B} < 1$ or, in the regime $\Gamma \ll \gamma_m$, $600\frac{\Delta}{\gamma C}\frac{\Delta B}{B} \ll 1$.

With the parameters of figure 3 this gives a condition on the magnetic field inhomogeneity: $\Delta B/B \ll 4 \times 10^{-4}$. In figure 5 we calculated the variance of the ground state spin as a function of Γ/γ_m for an increasing inhomogeneity $\Delta B/B$ from zero (thick line) to 6×10^{-4}. In practice a homogeneity of 100 ppm should be sufficient for the chosen parameters to guarantee that all atoms will be squeezed.

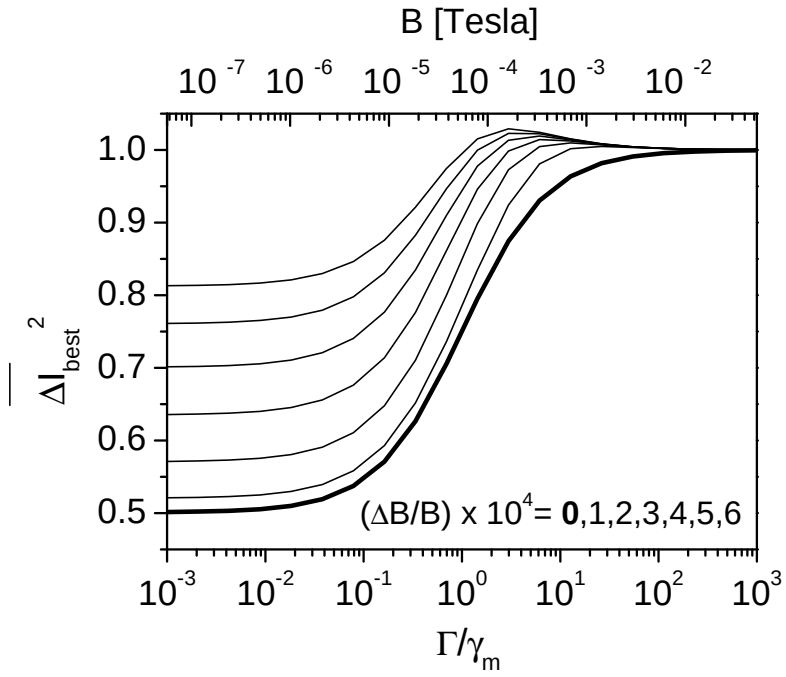

FIG. 5: Normalized "best" variance of the ground state spin as a function of Γ/γ_m (lower x-axis) for an increasing inhomogeneity $\Delta B/B$ from zero to 6×10^{-4} by steps of 1×10^{-4}. On the upper x-axis we show the corresponding homogeneous magnetic field needed to satisfy resonance conditions (46) and (47). Numerical values of parameters are $e^{-2r} = 0.5$, $C = 500$, $\kappa = 100\gamma$, $\Delta = -2000\gamma$, $\gamma = 2 \times 10^7$ s^{-1}, $\gamma_m = 5 \times 10^6$ s^{-1}, $\gamma_0 = 0$.

VI. OPTICAL READOUT

A. Outgoing field squeezing

As briefly stressed in [3] the squeezed fluctuations which are stored into the nuclear spins can be retrieved optically in the field exiting the cavity by using the reverse transfer process. Indeed, once the write sequence of the quantum memory has been completed, both the fields and the discharge can be switched off, leaving the atoms in the fundamental state in a spin-squeezed state. After a variable storage time, switching back on the discharge and only the control field in the same configuration as for the writing phase ($\Gamma \ll \gamma_m$), will rapidly put a small fraction of atoms in the metastable state and start the reverse transfer process from the fundamental atoms to the field. The correlations in the ground state will slowly transfer via the metastable state to the intracavity field. This will then result in squeezed fluctuations for the field exiting the cavity, which can be measured by homodyne detection.

More quantitatively, if we still assume that the metastable spin observables and the intra-cavity field adiabatically follow the ground state spin observables and the evolution equations for the fluctuations of the squeezed component are in the resonant situation, we have

$$\dot{I}_y(t) = -\Gamma_F I_y(t) + \beta X_{in}(t) + \tilde{f}_y(t) \tag{58}$$

$$X_{out}(t) = \sqrt{2\kappa} X(t) - X_{in}(t) \tag{59}$$

with

$$\beta = \frac{\gamma_m}{\gamma_m + \Gamma} \frac{g_A n \Omega \sqrt{3}}{2\Delta} \sqrt{\frac{2}{\kappa}} \tag{60}$$

10

$$\tilde{f}_y = \frac{\gamma_m\sqrt{3}}{\gamma_m+\Gamma}\left[\frac{f_{43}-f_{34}}{2i} - \frac{\Omega}{\Delta}\frac{f_{74}-f_{47}}{2i}\right] + \frac{f_{09}-f_{90}}{2i} \tag{61}$$

Denoting by $t=0$ the start of the readout sequence and by $e^{-2r} = \Delta I_y^2(0)/(N/4)$ the initial squeezing of the ground state nuclear spin, the two-time correlation function of the outgoing field amplitude quadrature can be obtained via (59) after integration of (58)

$$\mathcal{C}(t,t') \equiv \langle X^{out}(t)X^{out}(t')\rangle = \delta(t-t') - 2\Gamma_F\eta_I[1-e^{-2r}]e^{-\Gamma_F(t+t')} \tag{62}$$

The δ-correlated term corresponds to the vacuum fluctuations contribution, whereas the second term corresponds to a transient squeezing for the outgoing field which is proportional to the initial atomic squeezing. In (62), η_I designates the optimal quantum transfer efficiency in the ground state

$$\eta_I = \frac{\gamma_m}{\gamma_m+\Gamma}\frac{C}{C+1} \tag{63}$$

The ground state squeezing can be adequately measured by homodyne detection using a temporally matched local oscillator as shown in Refs. [6, 16]. Using a local oscillator with envelope $\mathcal{E}(t)$ the normalized power measured by a Fourier-limited spectrum analyzer integrating over a time T is given by

$$P(t) = \frac{1}{\mathcal{E}(t)^2}\int_{-\pi/T}^{\pi/T}\frac{d\omega}{2\pi}\int_t^{t+T}d\tau\int_t^{t+T}d\tau' e^{-i\omega(\tau-\tau')}\mathcal{E}(\tau)\mathcal{E}(\tau')\mathcal{C}(\tau,\tau') \tag{64}$$

In order to measure the atomic squeezing one has to maximize the temporal overlap between the local oscillator and the field radiated by the atoms: $\mathcal{E}(t) \propto e^{-\Gamma_F t}$. For such a local oscillator and for an integration time longer than the readout time Γ_F^{-1} the measured power can be written as the sum of a shot-noise term $\mathcal{N}$ and a time-dependent signal term $\mathcal{S}$ proportional to the initial squeezing:

$$P(t) = \mathcal{N} - \mathcal{S}[1-e^{-2r}]e^{-2\Gamma_F t} \tag{65}$$

with $\mathcal{S} \simeq \eta_I\mathcal{N}$. The ground state nuclear spin fluctuations can therefore be measured optically with the same efficiency η_I as in the write sequence. However, because of the slow character of the correlation transfer process in the ground state the readout time is as long as the write time. As expected it is not possible to access the quantum memory faster during the readout than during the write phase. One could think of a faster readout method by transferring the fundamental atoms fluctuations to the metastable atoms and perform the optical readout in the regime $\Gamma \gg \gamma_m$. However, as we showed in section II, starting with a squeezed fundamental spin and first switching on the discharge (without the fields) will transfer very few correlations from the fundamental to the metastable atoms and almost no squeezing will be retrieved in the field.

VII. ENTANGLING TWO SEPARATE SAMPLES

A direct and important extension of the previous results is that it is possible to transfer quantum correlations between different light beams to two spatially separated nuclear spins. If one disposes of EPR fields this allows to entangle two separate ensembles [18]. Such EPR atomic states are very useful for quantum information protocols involving the manipulation of continuous variable entanglement, such as atomic teleportation for instance [19].

Let us consider two identical ensembles 1 and 2 illuminated by EPR-correlated vacuum fields $A_{in}^{(i)}$ and coherent control fields Ω_i $(i=1,2)$. Without loss of generality we assume symmetrical field correlations of the form

$$\Delta^2 X_{in}^{(i)} = \Delta^2 Y_{in}^{(i)} = \cosh(2r) \quad (i=1,2) \tag{66}$$

$$\langle X_{in}^{(i)} X_{in}^{(j)}\rangle = -\langle Y_{in}^{(i)} Y_{in}^{(j)}\rangle = \sinh(2r) \quad (i\neq j), \tag{67}$$

i.e. that the amplitude quadratures are correlated and the phase quadratures anti-correlated: $\Delta^2(X_{in}^{(1)} - X_{in}^{(2)}) = \Delta^2(Y_{in}^{(1)} + Y_{in}^{(2)}) = 2e^{-2r}$. For perfect entanglement ($r=\infty$) these EPR variances vanish. Both spins are initially prepared in a coherent spin state and we assume an equal incident power on both samples ($\Omega_1 = \Omega_2$). Under the same adiabatic approximations as before, the fluctuations of the transverse spin components satisfy equation of the form (58)

$$\dot{I}_{xi} = -\Gamma_F I_{xi} - \beta Y_{in}^{(i)} + \tilde{f}_{xi}, \tag{68}$$

$$\dot{I}_{yi} = -\Gamma_F I_{yi} + \beta X_{in}^{(i)} + \tilde{f}_{yi}, \tag{69}$$

$(i = 1, 2)$. Because of the linearity of the coupling in this regime, the EPR atomic nuclear spin operators, $I_{x1} + I_{x2}$ and $I_{y1} - I_{y2}$, are clearly coupled to the EPR field operators

$$\frac{d}{dt}(I_{x1} + I_{x2}) = -\Gamma_F(I_{x1} + I_{x2}) - \beta(Y_{in}^{(1)} + Y_{in}^{(2)}) + \tilde{f}_{x1} + \tilde{f}_{x2} \tag{70}$$

$$\frac{d}{dt}(I_{y1} - I_{y2}) = -\Gamma_F(I_{y1} - I_{y2}) + \beta(X_{in}^{(1)} - X_{in}^{(2)}) + \tilde{f}_{y1} - \tilde{f}_{y2} \tag{71}$$

The amount of EPR-type correlations between the incident fields is given by the half-sum of the EPR variances

$$\mathcal{E}_f = \frac{1}{2}\left[\Delta^2(X_{in}^{(1)} - X_{in}^{(2)}) + \Delta^2(Y_{in}^{(1)} + Y_{in}^{(2)})\right] = 2e^{-2r} \tag{72}$$

In the Gaussian approximation the entanglement between the nuclear spins can be evaluated using the same quantity (also normalized to 2)

$$\mathcal{E}_I = \frac{2}{N}\left[\Delta^2(I_{x1} + I_{x2}) + \Delta^2(I_{y1} - I_{y2})\right] \tag{73}$$

It follows from (70-71) that the last two quantities are simply related by

$$\mathcal{E}_I = \eta_I \mathcal{E}_f + 2(1 - \eta_I). \tag{74}$$

Like squeezing entanglement can also be in principle perfectly mapped onto the nuclear spins with an efficiency η_I (63), close to unity in the regime $\Gamma \gg \gamma_m$ and $C \gg 1$. Let us introduce the correlation functions $\mathcal{C}_I^{(i,i)}$ of individual spins *inside* the ensemble i (i=1,2):

$$\mathcal{C}_I^{(i,i)} = \frac{\overline{\Delta I_{xi}^2} - 1}{4N} \qquad (i = 1, 2) \tag{75}$$

and the correlation function $\mathcal{C}_I^{(i,j)}$ of two individual spins belonging to the *different* ensembles i and j:

$$\mathcal{C}_I^{(i,j)} = \frac{\overline{\langle I_{xi} I_{xj}\rangle}}{4N} \qquad (i \neq j = 1, 2) \tag{76}$$

where the overline indicates the normalization of the correlation functions to $N/4$. In our case for $\eta_I \simeq 1$ we get:

$$\mathcal{C}_I^{(1,1)} = \mathcal{C}_I^{(2,2)} \simeq \frac{\cosh(2r) - 1}{4N} \tag{77}$$

$$\mathcal{C}_I^{(1,2)} = \mathcal{C}_I^{(2,1)} \simeq \frac{\sinh(2r)}{4N}\,. \tag{78}$$

It is interesting to note that the two correlation functions $\mathcal{C}_I^{(1,1)}$ and $\mathcal{C}_I^{(1,2)}$ become approximately equal for a large entanglement $e^{2r} \gg 1$ so that an individual spin is about as much correlated with the other spins in its own ensemble as with the spins of the other ensemble.

VIII. THE IMPERFECT POLARIZATION CASE

The nuclear polarization of the sample is defined as

$$P = \frac{\langle I_{00}\rangle - \langle I_{99}\rangle}{\langle I_{00}\rangle + \langle I_{99}\rangle} \tag{79}$$

In practice polarization between 80% and 85% are currently achieved by optical pumping in dilute ^{3}He samples [20]. If the atoms are prepared in a state which is not fully polarized - $P \neq 1$ - the situation is clearly more complicated than we described in [3] and in the present paper. In particular, equations (25)-(35) and (39) obtained by linearization around the fully polarized state are no longer valid. We did not perform a complete analysis in the $P \neq 1$ case. However, one can have a good idea of the result by using the simplified model of [3] which involves only two metastable sublevels

12

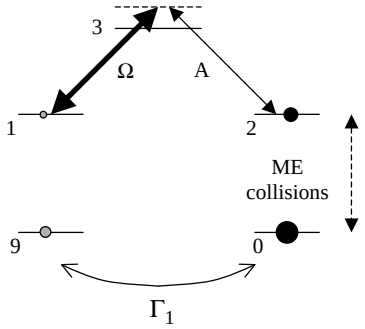

FIG. 6: Sublevels 1 and 2 are metastable, level 3 is the excited state, 9 and 0 are the ground state sublevels. We include a relaxation process in the ground state so that $P \neq 1$ in steady state.

(see figure 6). As in section III, a Raman transition is driven by a coherent control field of Rabi frequency Ω and a squeezed vacuum cavity field:

$$H = H_0 + \hbar \left\{ \Omega \, \tilde{S}_{31} e^{-i\omega_1 t} + g \, A \, \tilde{S}_{32} + \text{h.c.} \right\} . \tag{80}$$

In this toy-model the control field Ω also acts as an optical pumping beam (able to transfer the atoms from sublevel 9 to sublevel 0) and we introduce explicitly a relaxation in the ground state, so that $P \neq 1$ in steady state. Let us introduce for this model the rescaled coupling constant $\tilde{g}$, the atomic one-photon detunings Δ_1 and Δ, the two-photon detunings $\tilde{\delta}$ and δ_I, and two pumping parameters Γ_p and Γ:

$$\Delta_1 = (E_3 - E_1)/\hbar - \omega_1, \qquad \Delta = (E_3 - E_2)/\hbar - \omega_2, \tag{81}$$

$$\tilde{\delta} = \Delta_1 - \Delta + \frac{\Omega^2}{\Delta}, \qquad \delta_I = (E_0 - E_9)/\hbar - (\omega_1 - \omega_2), \tag{82}$$

$$\Gamma_P = \gamma \frac{\Omega^2}{\Delta^2}, \qquad \Gamma = \Gamma_p (1 + C), \tag{83}$$

where γ is the optical coherence decay rate and C is the cooperativity parameter defined by equation (44). For the atomic operators we introduce $\tilde{S}_+ = \tilde{S}_{21}$, $\tilde{S}_- = \tilde{S}_{12}$

$$\tilde{S}_x = (\tilde{S}_- + \tilde{S}_+)/2, \qquad \tilde{S}_y = i(\tilde{S}_- - \tilde{S}_+)/2, \qquad \tilde{S}_z = (\tilde{S}_{22} - \tilde{S}_{11})/2, \tag{84}$$

and similarly for the ground state operators. In the limit of large one photon detunings the excited state and the optical coherences can be adiabatically eliminated, yielding a set of equations similar to those of Ref. [17] with the addition of metastability exchange. By adiabatically eliminating the field (assumed to be resonant in the cavity) and for $\tilde{\delta} = 0$, $\delta_I = 0$, we obtain:

$$\dot{\tilde{S}}_+ = -(\Gamma_p + \gamma_m)\tilde{S}_+ + \gamma_f I_+ + 2i\tilde{g} A \tilde{S}_z + + f_{\tilde{S}_+} \tag{85}$$

$$\dot{\tilde{S}}_z = -(\Gamma_p + \gamma_m)\tilde{S}_z + \gamma_f I_z + \frac{n\Gamma_p}{2} + i\tilde{g}[A^\dagger \tilde{S}_+ - A\tilde{S}_-] + f_{\tilde{S}_z} \tag{86}$$

$$\dot{A} = -(\kappa + i\Delta_C)A + i\tilde{g}\tilde{S}_+ + \sqrt{2\kappa} A_{in} \tag{87}$$

$$\dot{I}_+ = -(\gamma_f + \Gamma_1) I_+ + \gamma_m \tilde{S}_+ + f_{I_+} \tag{88}$$

$$\dot{I}_z = -(\gamma_f + \Gamma_1) I_z + \gamma_m \tilde{S}_z + f_{I_z} \tag{89}$$

The semiclassical version of equations (85)-(89) has a stationary solution $\langle \tilde{S}_+ \rangle = \langle I_+ \rangle = \langle A_{in} \rangle = 0$ and with

$$\langle \tilde{S}_z \rangle = \frac{\gamma_f + \Gamma_1}{\gamma_m} \langle I_z \rangle \qquad P = \frac{1}{1 + \Gamma_1 (\Gamma_p + \gamma_m)/(\Gamma_p \gamma_f)} \tag{90}$$

We will have in practice $\Gamma_1 \ll \gamma_f$, meaning that the nuclear polarization in the metastable state $P^* = \langle \tilde{S}_z \rangle / (n/2)$ and the nuclear polarization in the ground state $P = \langle I_z \rangle / (N/2)$ are almost equal. In this toy-model the stationary

P is determined by the balance between the decay Γ_1 and the pumping Γ_p. In reality, the atoms will be previously pumped more efficiently with resonant light. When we linearize the equations around the steady state we obtain

$$\dot{\tilde{S}}_+ = -(\tilde{\Gamma}+\gamma_m)\tilde{S}_+ + \frac{ig\Omega n}{\kappa\Delta}P^*\sqrt{2\kappa}A_{in} + \gamma_f I_+ + f_{\tilde{S}_+} \quad (91)$$

$$\dot{I}_+ = -(\gamma_f+\Gamma_1)I_+ + \gamma_m\tilde{S}_+ + f_{I_+} \quad (92)$$

with

$$\tilde{\Gamma} = \Gamma_p(1+CP^*) \quad (93)$$

Starting from equations (91)-(92) one can proceed as in section V to obtain

$$\overline{\Delta I_y^2} = \frac{\Delta I_y^2}{NP/4} = \frac{1}{P} + (P^*e^{-2r}-1)\eta_I' + \frac{\eta_I'}{2\tilde{C}}\frac{P^*-1}{P} \quad (94)$$

where

$$\tilde{C} = CP^* \qquad \text{and} \qquad \tilde{\Gamma}_f = \frac{\gamma_f\tilde{\Gamma}}{\tilde{\Gamma}+\gamma_m} \quad (95)$$

$$\eta_I' = \frac{\tilde{C}}{\tilde{C}+1}\,\frac{\gamma_m}{\tilde{\Gamma}+\gamma_m}\,\frac{\tilde{\Gamma}_f}{\tilde{\Gamma}_f+\Gamma_1} \quad (96)$$

For $P^* \simeq P$ and $\tilde{C} \gg 1$, we have finally

$$\overline{\Delta I_y^2} = \eta_I' e^{-2r} + (1-\eta_I')/P \quad (97)$$

Equation (97) shows that the main consequence of having $P \neq 1$ is a rescaling of the cooperativity and the pumping parameter $\tilde{\Gamma}$ and the quantum transfer efficiency η_I', which are reduced by a factor P. Let us note that, for $P \neq 1$, when no squeezing enters the cavity, the atoms are no longer in a coherent spin state. This shows, however, that strong squeezing transfer is still possible with a non-ideal polarization.

Acknowledgments

Laboratoire Kastler Brossel is UMR 8552 du CNRS, de l'ENS et de l'UPMC. This work was supported by the COVAQIAL European project No. FP6-511004.

IX. APPENDIX

Evolution equations of the density matrix elements under ME collisions are:

$$\begin{aligned}
\frac{d}{dt}\rho_{11} &= \gamma_{\text{exc}}\left(-N\rho_{11} + \frac{1}{3}\rho_{99}\left(\rho_{22}+3\rho_{11}+2\rho_{55}\right)\right)\\
\frac{d}{dt}\rho_{12} &= \gamma_{\text{exc}}\left(-N\rho_{12} + \frac{2}{9}\rho_{99}\left(\left(\rho_{23}+\rho_{56}\right)\sqrt{3}+3\rho_{12}\right) + \frac{\sqrt{3}}{9}\rho_{90}\left(\rho_{22}+3\rho_{11}+2\rho_{55}\right)\right)\\
\frac{d}{dt}\rho_{13} &= \gamma_{\text{exc}}\left(-N\rho_{13} + \frac{1}{3}\rho_{99}\left(\rho_{13}+\rho_{24}\right) + \frac{2}{9}\rho_{90}\left(\left(\rho_{23}+\rho_{56}\right)\sqrt{3}+3\rho_{12}\right)\right)\\
\frac{d}{dt}\rho_{14} &= \gamma_{\text{exc}}\left(-N\rho_{14} + \frac{\sqrt{3}}{3}\rho_{90}\left(\rho_{13}+\rho_{24}\right)\right)\\
\frac{d}{dt}\rho_{22} &= \gamma_{\text{exc}}\left(-N\rho_{22} + \frac{2}{9}\rho_{99}\left(2\rho_{22}+\rho_{55}+\rho_{66}+2\rho_{33}\right) + \frac{2}{9}\rho_{90}\left(\sqrt{3}\rho_{21}+\rho_{65}+\rho_{32}\right)\right.\\
&\qquad \left. + \frac{2}{9}\rho_{09}\left(\sqrt{3}\rho_{12}+\rho_{23}+\rho_{56}\right) + \frac{1}{9}\rho_{00}\left(\rho_{22}+3\rho_{11}+2\rho_{55}\right)\right)
\end{aligned}$$

$$
\begin{aligned}
\frac{d}{dt}\rho_{23} = \gamma_{\text{exc}} & \left(-N\rho_{23} + \frac{2}{9}\rho_{99}\left(\sqrt{3}\rho_{34} + \rho_{56} + \rho_{23}\right) + \frac{2}{9}\rho_{90}\left(2\rho_{22} + \rho_{55} + \rho_{66} + 2\rho_{33}\right)\right. \\
& \left. + \frac{\sqrt{3}}{9}\rho_{09}\left(\rho_{13} + \rho_{24}\right) + \frac{2}{9}\rho_{00}\left(\sqrt{3}\rho_{12} + \rho_{23} + \rho_{56}\right)\right) \\
\frac{d}{dt}\rho_{24} = \gamma_{\text{exc}} & \left(-N\rho_{24} + \frac{2}{9}\rho_{90}\left(\sqrt{3}\left(\rho_{23} + \rho_{56}\right) + 3\rho_{34}\right) + \frac{1}{3}\rho_{00}\left(\rho_{13} + \rho_{24}\right)\right) \\
\frac{d}{dt}\rho_{33} = \gamma_{\text{exc}} & \left(-N\rho_{33} + \frac{1}{9}\rho_{99}\left(2\rho_{66} + \rho_{33} + 3\rho_{44}\right) + \frac{2}{9}\rho_{90}\left(\sqrt{3}\rho_{43} + \rho_{65} + \rho_{32}\right)\right. \\
& \left. + \frac{2}{9}\rho_{09}\left(\sqrt{3}\rho_{34} + \rho_{56} + \rho_{23}\right) + \frac{2}{9}\rho_{00}\left(2\rho_{22} + \rho_{55} + \rho_{66} + 2\rho_{33}\right)\right) \\
\frac{d}{dt}\rho_{34} = \gamma_{\text{exc}} & \left(-N\rho_{34} + \frac{\sqrt{3}}{9}\rho_{90}\left(2\rho_{66} + \rho_{33} + 3\rho_{44}\right) + \frac{2}{9}\rho_{00}\left(\sqrt{3}\left(\rho_{23} + \rho_{56}\right) + 3\rho_{34}\right)\right) \\
\frac{d}{dt}\rho_{44} = \gamma_{\text{exc}} & \left(-N\rho_{44} + \frac{1}{3}\rho_{00}\left(2\rho_{66} + \rho_{33} + 3\rho_{44}\right)\right) \\
\frac{d}{dt}\rho_{55} = \gamma_{\text{exc}} & \left(-N\rho_{55} + \frac{1}{9}\rho_{99}\left(2\rho_{22} + \rho_{55} + \rho_{66} + 2\rho_{33}\right) - \frac{2}{9}\rho_{90}\left(\sqrt{3}\rho_{21} + \rho_{65} + \rho_{32}\right)\right. \\
& \left. - \frac{2}{9}\rho_{09}\left(\sqrt{3}\rho_{12} + \rho_{23} + \rho_{56}\right) + \frac{2}{9}\rho_{00}\left(\rho_{22} + 3\rho_{11} + 2\rho_{55}\right)\right) \\
\frac{d}{dt}\rho_{56} = \gamma_{\text{exc}} & \left(-N\rho_{56} + \frac{2}{9}\rho_{99}\left(\sqrt{3}\rho_{34} + \rho_{56} + \rho_{23}\right) - \frac{1}{9}\rho_{90}\left(2\rho_{22} + \rho_{55} + \rho_{66} + 2\rho_{33}\right)\right. \\
& \left. - \frac{2\sqrt{3}}{9}\rho_{09}\left(\rho_{13} + \rho_{24}\right) + \frac{2}{9}\rho_{00}\left(\sqrt{3}\rho_{12} + \rho_{23} + \rho_{56}\right)\right) \\
\frac{d}{dt}\rho_{66} = \gamma_{\text{exc}} & \left(-N\rho_{66} + \frac{2}{9}\rho_{99}\left(2\rho_{66} + \rho_{33} + 3\rho_{44}\right) - \frac{2}{9}\rho_{90}\left(\sqrt{3}\rho_{43} + \rho_{65} + \rho_{32}\right)\right. \\
& \left. - \frac{2}{9}\rho_{09}\left(\sqrt{3}\rho_{34} + \rho_{56} + \rho_{23}\right) + \frac{1}{9}\rho_{00}\left(2\rho_{22} + \rho_{55} + \rho_{66} + 2\rho_{33}\right)\right) \\
\frac{d}{dt}\rho_{00} = \gamma_{\text{exc}} & \left(-n\rho_{00} + \frac{1}{3}\left(3\rho_{44} + \rho_{66} + \rho_{22} + 2\rho_{55} + 2\rho_{33}\right)N\right) \\
\frac{d}{dt}\rho_{09} = \gamma_{\text{exc}} & \left(-n\rho_{09} + \frac{1}{3}N\left(\left(\rho_{43} + \rho_{21}\right)\sqrt{3} + 2\rho_{32} - \rho_{65}\right)\right) \\
\frac{d}{dt}\rho_{99} = \gamma_{\text{exc}} & \left(-n\rho_{99} + \frac{1}{3}\left(\rho_{33} + 2\rho_{22} + 3\rho_{11} + \rho_{55} + 2\rho_{66}\right)N\right)
\end{aligned}
$$

---

[1] W. Heil, H. Humblota, E. Otten, M. Schafera, R. Sarkaua and M. Leduc, Phys. Lett A, **201**, 337 (1995)
[2] C.Cohen-Tannoudji, J. Dupont-Roc, S. Haroche and F. Laloë, Phys. Rev. Lett. **22**, 758 (1969)
[3] A. Dantan, G. Reinaudi, A. Sinatra, F. Laloë, E. Giacobino, M. Pinard, Phys. Rev. Lett. **95**, 123002 (2005)
[4] M. Fleischhauer and M.D. Lukin, Phys. Rev. Lett. **84**, 5094 (2000)
[5] A.E. Kozhekin, K. Mølmer and E. Polzik, Phys. Rev. A **62**, 033809 (2000)
[6] A. Dantan and M. Pinard, Phys. Rev. A **69**, 43810 (2004)
[7] C.H. van der Wal *et al.*, Science **301**, 196 (2003)
[8] C. Schori, B. Julsgaard, J.L. Sørensen, E.S. Polzik, Phys. Rev. Lett. **89**, 57903 (2002)
[9] B. Julsgaard, J. Sherson, J.I. Cirac, J. Fiurášek, E.S. Polzik, Nature (London) **432**, 482 (2004)
[10] B. Julsgaard, A. Khozekin, E.S. Polzik, Nature (London) **413**, 400 (2001)
[11] F.D. Colegrove , L.D. Schearer and G.K. Walters, Phys. Rev. **132**, 2561 (1963)
[12] R.B. Partridge and G.W. Series, Proc. Phys. Soc. **88**, 983 (1966)
[13] J. Becker *et al.*, Nucl. Instrum. Methods Phys. Res. A **402**, 327 (1998); H. Moller *et al.*, Magn. Reson. Med. **47**, 1029 (2002)
[14] C. Cohen-Tannoudji, J. Dupont-Roc, G. Grynberg "Atom-Photon Interactions", Wiley-VCH, Berlin (1998), ch. V.

15

[15] In practice one wants the squeezed field and the coherent field to be copropagating. The squeezed field should thus be σ-polarized, with a σ^+ component; we checked that this component plays no role here.
[16] A. Dantan, J. Cviklinski, M. Pinard, Ph. Grangier, quant-ph/0512175.
[17] A. Dantan, M. Pinard, V. Josse, N. Nayak, P.R. Berman, Phys. Rev A **67**, 045801 (2003)
[18] A. Dantan, A. Bramati and M. Pinard, Europhys. Lett. **67**, 881 (2004)
[19] A. Dantan, N. Treps, A. Bramati, M. Pinard, Phys. Rev. Lett. **95**, 050520 (2005)
[20] P.-J. Nacher, M. Leduc, J. Physique **46**, 2057 (1985).

Chapitre 4

Gaz dégénérés

Les numéros entre crochets font référence à la liste de mes publications, disponible en fin de document.

4.1 Condensats de Bose-Einstein atomiques gazeux

L'obtention de condensats de Bose-Einstein atomiques gazeux a réellement secoué la communauté de la physique atomique et dans une certaine mesure celle de l'optique quantique, ouvrant des nouvelles voies de recherche fascinantes. Le condensat est potentiellement un outil en optique atomique, en optique non linéaire, en métrologie, en information quantique, ainsi qu'un "mini-laboratoire" où l'on voit en œuvre la physique quantique. En exploitant l'extrême souplesse et le haut degré de contrôle des systèmes d'atomes piégés, on peut non seulement porter les atomes (fermions ou bosons) à la dégénérescence quantique, mais aussi réaliser des modèles de la physique statistiques ou de la matière condensée. L'exemple le plus marquant est la possibilité de changer à loisir la force des interactions, en passant d'un régime de gaz parfait au régime d'interaction forte caractéristique des systèmes fortement corrélés.

Dans notre travail, souvent motivé par des expériences ou par des projets d'expérience, nous nous sommes essentiellement intéressé à deux aspects. Le premier lié à la cohérence de phase du condensat qui dérive du fait que, comme pour les photons issus d'un laser, presque toutes les particules occupent un seul mode décrit par la fonction d'onde du condensat. Le deuxième lié aux caractère multimode du champ atomique lorsque la température du système est non nulle.

4.1.1 Rappels : équation de Gross-Pitaevskii et approches de champ classique

Considérons un gaz de N atomes bosoniques en interaction faible et à très basse température ($T \ll T_c$ où T_c est la température critique) dans un potentiel externe de piégeage U. Comme le système forme alors un condensat de Bose-Einstein presque pur, on utilise un Ansatz de Hartree pour l'état à N corps : $|\psi\rangle = |N : \phi\rangle$. En modélisant les interactions entre atomes par un potentiel de contact

$$V(|\vec{r} - \vec{r}'|) \to V_\delta = g\delta(\vec{r} - \vec{r}') \qquad\qquad g = \frac{4\pi\hbar^2}{m}\, a \tag{4.1}$$

où la constante g est liée à la longueur de diffusion a du vrai potentiel d'interaction, qui caractérise les collisions à très basse énergie, on déduit, par le principe variationnel,

l'équation de Gross-Pitaevskii [1] :

$$i\hbar\partial_t\phi(\vec{r},t) = \left[-\frac{\hbar^2}{2m}\Delta + U(\vec{r}) + gN|\phi(\vec{r},t)|^2\right]\phi(\vec{r},t)\,. \tag{4.2}$$

Dans ce contexte, l'équation (4.2) décrit l'évolution de la fonction d'onde ϕ du condensat pur.

Il existe néanmois différentes lectures de cette équation. On remarque que l'équation de Heisenberg pour l'opérateur champ $\hat{\psi}(\vec{r})$, obtenue à partir du Hamiltonien en deuxième quantification :

$$H = \int d^3\vec{r}\,\hat{\psi}^\dagger(\vec{r})h_1\hat{\psi}(\vec{r}) + \frac{1}{2}\int d^3\vec{r}\int d^3\vec{r}'\,\hat{\psi}^\dagger(\vec{r})\hat{\psi}^\dagger(\vec{r}')V(\vec{r}-\vec{r}')\hat{\psi}(\vec{r})\hat{\psi}(\vec{r}')\,, \tag{4.3}$$

où h_1 est la partie à 1 corps du Hamiltonien, suivie du remplacement

$$\hat{\psi} \to \psi = \sqrt{N}\phi\,, \tag{4.4}$$

redonne l'équation (4.2). Dans ce contexte, la solution de (4.2) donne la solution exacte d'un modèle de champ classique. Cette fois, ψ représente tout le champ atomique, partie non condensée incluse. Il est intéressant de remarquer que si, pendant son évolution, le système passe par une phase turbulente suite à une instabilité dynamique, le point de vue "condensat pur" ne peut plus être maintenu. On peut en effet commencer l'évolution avec un condensat pur à température nulle, et se retrouver avec un champ thermalisé à une température non nulle.

Une troisième clé de lecture de l'équation (4.2) est donnée par la représentation de Wigner de l'opérateur densité du système. Comme nous l'expliquerons plus tard dans le manuscrit, si l'on choisit un ensemble de champs $\{\psi(\vec{r},t=0)\}$ qui échantillonnent la distribution de Wigner W du gaz à $t=0$, faire évoluer chaque ψ avec l'équation (4.2) correspond à négliger les dérivés d'ordre trois dans l'équation d'évolution de W (approximation dite de "Wigner tronquée") [2]. Les valeurs moyennes quantiques sont alors remplacées par des moyennes sur les réalisations $\{\psi\}$, et les fluctuations thermiques *et quantiques* seront prises en compte bien que de façon approximée.

4.2 Brouillage et résurgence de phase : influence des pertes de particules

La phase relative de deux condensats évolue d'une façon non triviale à cause des interactions entre les atomes. Il a été prédit théoriquement que cette phase, lors qu'elle est bien définie initialement, subit une alternance de brouillages complets et de résurgences dues au caractère discret du nombre d'atomes. Un problème important qui restait à étudier

[1] La méthode variationnelle ici brièvement décrite, qui néglige les corrélations à courte distance entre les atomes, est valable pour un système dilué ($nr_0^3 \ll 1$, n étant la densité et r_0 étant la portée du potentiel), où les atomes sont la plupart du temps loin les uns des autres. Dans ce régime, c'est alors le comportement asymptotique des fonctions d'onde qui est important pour décrire leurs interactions et on peut remplacer le vrai potentiel d'interaction par un potentiel d'interaction modèle. De plus, on impose la condition $n|a|^3 \ll 1$, ce qui permet de traiter le potentiel d'interaction modèle dans l'approximation de Born.

[2] Pour un seul mode avec une non linéarité de type Kerr et un nombre d'occupation $\mathcal{N}$, les termes négligés sont $1/\mathcal{N}^2$ plus petits que les termes de champ classique.

en vue d'une observation expérimentale de ces phénomènes était l'influence des pertes de particules. Ces pertes, inévitables dans une expérience réelle, sont dues par exemple à des collisions avec le gaz résiduel dans l'enceinte à vide, ou à des collisions entre trois atomes du condensat formant une molécule et un atome rapide éjecté du piège.

Nous avons développé un modèle pour décrire la dynamique de phase en présence de pertes de particules. Nous avons obtenu une solution analytique approchée de ce modèle à l'aide du formalisme des fonctions d'onde Monte-Carlo. Nous avons démontré que l'amplitude des résurgences de phase est amortie exponentiellement avec un taux donné par le nombre d'événements de perte par unité de temps. Ainsi, l'occurrence d'un seul événement de perte en moyenne entre l'instant initial et la première résurgence réduit l'amplitude de cette résurgence d'un facteur $1/e$. Cette sensibilité extrême aux phénomènes de pertes est la marque d'un état quantique fortement intriqué. En effet, entre deux résurgences de phase, le système se trouve dans un état de type chat de Schrödinger superposition de deux état mésoscopiques avec une phase relative bien définie entre les deux condensats. Nous avons cependant identifié des régimes à faible nombre d'atomes dans lesquels les résurgences seraient observables [8].

Si notre étude paraissait un peu académique en 1997, elle est d'extrême d'actualité aujourd'hui où un projet de réalisation d'un chat de Schrödinger par cette méthode est en cours dans l'équipe de Fabrice Gerbier et Jean Dalibard.

4.2.1 Publication jointe

Eur. Phys. J. D **4**, 247–260 (1998)

THE EUROPEAN PHYSICAL JOURNAL D

© EDP Sciences
Springer-Verlag 1998

Phase dynamics of Bose-Einstein condensates: Losses versus revivals

A. Sinatra[a] and Y. Castin

Laboratoire Kastler Brossel[b], 24 rue Lhomond, 75231 Paris Cedex 5, France

Received: 23 February 1998 / Revised: 21 July 1998 / Accepted: 23 July 1998

Abstract. In the absence of losses the phase of a Bose-Einstein condensate undergoes collapses and revivals in time due to elastic atomic interactions. As experiments necessarily involve inelastic collisions, we develop a model to describe the phase dynamics of the condensates in presence of collisional losses. We find that *a few inelastic processes* are sufficient to damp the revivals of the phase. For this reason the observability of phase revivals for present experimental conditions is limited to condensates with a few hundreds of atoms.

PACS. 03.75.Fi Phase coherent atomic ensemble (Bose condensation) – 05.30.Jp Boson systems

1 Introduction

Since the recent experimental observations of Bose-Einstein condensation in dilute atomic gases [1–5], much interest has been raised about the characteristic features of the condensate [6–8], and about its coherence properties in particular. Considerable attention has been devoted to the matter of the relative phase between two Bose-Einstein Condensates (BECs): how the phase manifests itself in an interference experiment (such as the one performed recently at MIT [9]), how the phase can be established by measurement, and how it evolves in presence of the elastic atomic interactions (see *e.g.* [10] and references therein). In this paper, in view of a possible experimental investigation of these problems, we complete the theoretical work already done on this subject by studying the dynamics of the relative phase in presence of loss processes occurring in the two condensates. Such loss processes, unavoidable in a real experiment, are due for example to collisions of condensed atoms with the background gas, or to three-body collisions between condensed atoms followed by recombination of two atoms to form a molecule [11,12].

We consider two mutually non interacting and spatially non overlapping BECs in two trapping potentials. We suppose that the experimentalist has at hand a device, such as the one depicted in Figure 1, allowing both the measurement of the relative phase between the condensates and the preparation of a state with a well-defined relative phase [13]. Starting from an initial state with a well-defined relative phase, we imagine that the two condensates evolve independently, under the influence of the atomic interactions, during a given time interval t at the end of which a measurement of the relative phase is performed. By repeating this procedure many times, one accesses the probability distribution of the relative phase [13].

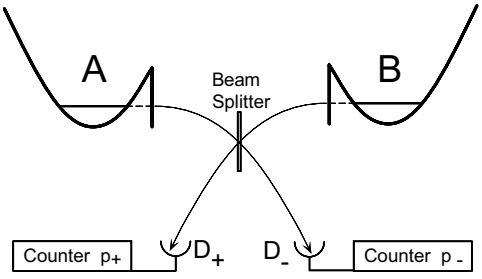

Fig. 1. Two BECs **A** and **B** in two non overlapping trapping potentials. Some atoms can be let out of the condensates towards a 50–50 atomic beam splitter. The detection of the atoms in the output channels of the beam-splitter realizes a measurement of the relative phase between the condensates.

In the lossless case, the relative phase shows *collapses* and *revivals* periodically in time due to the presence of elastic atomic interactions. In presence of losses, we find that *a few inelastic processes* are sufficient to dramatically damp the revivals of the phase. In practice, for typical experimental configurations, the observability of the revivals is limited to condensates with a small number of atoms, of the order of a few hundreds, for which the revival time is of the order of 0.1 to 1 second.

In Section 2 we present the theoretical model describing the evolution of the system in presence of losses. An interesting feature of the model is that it can be solved almost exactly analytically within the Monte-Carlo wave

[a] e-mail: `alice.sinatra@physique.ens.fr`

[b] Unité de recherche de l'École Normale Supérieure et de l'université Pierre et Marie Curie, associée au CNRS.

function approach recently put forward by several authors [14–17]. We take advantage of this circumstance in the following sections, to deduce analytical expressions for the interesting phase-dependent measurable quantities, and to a give a simple picture of the phase dynamics in presence of losses.

In Section 3 we find an approximate analytical expression for the evolution of a single stochastic wave function, and we give a simple physical interpretation of the result pointing out separately the role of the elastic atomic interactions and of the losses in the dynamics of the relative phase of the condensates. In Sections 4 and 5 we concentrate on the case in which the two condensates are placed in two identical traps and have initially the same average number of atoms, and we use the analytical results of Section 3 to calculate the time dependence of some relative phase dependent quantities. In particular in Section 4 we consider an interference experiment where one counts the atoms detected in the two output channels of the beamsplitter of Figure 1, and we analyze the two different physical situations in which the condensates' relative phase is initially sharply defined or is described by a "broad" relative phase distribution with a width $\gg 1/\sqrt{N}$. In Section 5 we imagine instead an experiment in which the time evolution of the whole relative phase probability distribution is measured. Sections 6 and 7 are dedicated to the analysis of additional features that would appear in an experiment; the effect of asymmetries in the parameters of the two condensates and in the initial average number of atoms is considered in Section 6, and the effect of fluctuations in the initial total number of atoms is considered in Section 7. Some concluding remarks are presented in Section 8.

2 Model

2.1 Master equation

Let us consider two mutually non-interacting and spatially non-overlapping BECs **A** and **B** in two harmonic potentials. Our starting point to describe the evolution of this system in presence of m-body losses is a master equation for the density matrix ρ describing the atoms in the traps:

$$\frac{d\rho}{dt} = \frac{1}{i\hbar}[H,\rho] + \int d^3\mathbf{r}\,\kappa\big[[\hat{\psi}(\mathbf{r})]^m\,\rho\,[\hat{\psi}^\dagger(\mathbf{r})]^m - \frac{1}{2}\{[\hat{\psi}^\dagger(\mathbf{r})]^m[\hat{\psi}(\mathbf{r})]^m,\rho\}\big], \quad (1)$$

where $\{X,Y\}$ denotes the anticommutator, and $[\hat{\psi}(\mathbf{r})]^m$ is the field operator raised to the power m which suppresses m particles in $\mathbf{r}$. In second quantized form the Hamiltonian H reads:

$$H = \int d^3\mathbf{r}\left[\hat{\psi}^\dagger(\mathbf{r})H_0\hat{\psi}(\mathbf{r}) + \frac{g}{2}\hat{\psi}^\dagger(\mathbf{r})\hat{\psi}^\dagger(\mathbf{r})\hat{\psi}(\mathbf{r})\hat{\psi}(\mathbf{r})\right], \quad (2)$$

where H_0 is the one-particle Hamiltonian including the trapping potential and the kinetic energy, and $g = 4\pi\hbar^2 a/M$ where M is the mass of the atoms and a is the s-wave scattering length.

The loss terms in equation (1) are parameterized by the number m of particles lost per collisional event and by the collisional constant κ. Physically the case $m = 1$ corresponds to collisions of atoms in the condensate with atoms of background gas in the cell; the case $m = 2$ corresponds to spin-flip collisions between condensed atoms in magnetic traps, as only specific spin components are trapped; the case $m = 3$ corresponds to three-body collisions between condensed atoms, leading to the formation of an excited molecule and a hot atom supposed to leave the condensate. The collisional constant κ for the processes $m = 1$ and $m = 3$ has been measured for ^{87}Rb atoms at JILA [11] and for ^{23}Na atoms at MIT [12]. The collisional constant for the $m = 2$ process has not been accurately measured for these atoms yet, as the two-body losses seem to give a smaller contribution to the total decay rate.

We assume that at any time the state of the condensate **A** (resp. **B**) can be described in terms of a single occupied mode, neglecting the excitations out of this mode due to a non-zero temperature or to the loss processes. We assume furthermore that these modes are the single particle ground state wave functions ϕ_a, ϕ_b given self-consistently as functions of the number of particles by the Gross-Pitaevskii equation:

$$\left[H_0 + gN_\epsilon|\phi_\epsilon(\mathbf{r};N_\epsilon)|^2\right]\phi_\epsilon(\mathbf{r};N_\epsilon) = \mu_\epsilon(N_\epsilon)\phi_\epsilon(\mathbf{r};N_\epsilon), \quad (3)$$

where the $\mu_\epsilon(N_\epsilon)$'s are the chemical potentials for the condensates with N_ϵ particles, and where the wave functions ϕ_ϵ are normalized to unity. In more mathematical words we approximate the atomic field operator by:

$$\hat{\psi}(\mathbf{r}) = \sum_{\epsilon=a,b} c_\epsilon\phi_\epsilon(\mathbf{r};\hat{N}_\epsilon) \quad (4)$$

where the operators $c_a^\dagger$ ($c_b^\dagger$) and c_a (c_b) create and annihilate a particle in the condensate **A** (**B**) respectively, and where $\hat{N}_\epsilon = c_\epsilon^\dagger c_\epsilon$ are the operators giving the number of particles in each condensate. Note that we keep in equation (4) the dependence of the mode on the number of particles in the condensate.

By substituting equation (4) into equation (2) we get

$$H = E_a(\hat{N}_a) + E_b(\hat{N}_b) \quad (5)$$

with

$$E_\epsilon(N_\epsilon) = N_\epsilon\left[\int d^3\mathbf{r}\phi_\epsilon^*(\mathbf{r};N_\epsilon)H_0\phi_\epsilon(\mathbf{r};N_\epsilon) + \frac{gN_\epsilon}{2}|\phi_\epsilon(\mathbf{r};N_\epsilon)|^4\right] \quad (6)$$

(we have used $N_\epsilon - 1 \simeq N_\epsilon$).

By assuming that in the considered time interval the atom number distributions in the two condensates remain peaked around the initial average values:

$$\bar{N}_\epsilon = Tr[\rho(0)c_\epsilon^\dagger c_\epsilon], \quad (7)$$

we expand the condensates' Hamiltonian around $\bar{N}_a$, $\bar{N}_b$ keeping up to the quadratic terms:

$$H(\hat{N}_a,\hat{N}_b) \simeq H^q(\hat{N}_a,\hat{N}_b) \equiv \sum_{\epsilon=a,b} E(\bar{N}_\epsilon) + (\hat{N}_\epsilon - \bar{N}_\epsilon) \times \mu_\epsilon(\bar{N}_\epsilon) + \frac{1}{2}(\hat{N}_\epsilon - \bar{N}_\epsilon)^2 \mu'_\epsilon(\bar{N}_\epsilon). \quad (8)$$

In our model we will use this quadratic version of the Hamiltonian, where the chemical potentials μ_a and μ_b and their derivatives can be calculated by solving numerically the Gross-Pitaevskii equation (3).

We now substitute our ansatz equation (4) in the loss part of the master equation; since the condensates do not overlap this amounts to the substitution

$$[\hat{\psi}(\mathbf{r})]^m \to \sum_{\epsilon=a,b} [c_\epsilon \phi_\epsilon(\mathbf{r};\hat{N}_\epsilon)]^m \quad (9)$$

in equation (1). In contrast to the Hamiltonian part which required a careful quadratization in $\hat{N}_\epsilon - \bar{N}_\epsilon$ to get the correct phase dynamics, the dissipative part will be treated to lowest order by replacing $\hat{N}_\epsilon$ by $\bar{N}_\epsilon$ in equation (9). This allows us finally to obtain a master equation of the form:

$$\frac{d\rho}{dt} = \frac{1}{i\hbar}[H^q(\hat{N}_a,\hat{N}_b),\rho] + \sum_{\epsilon=a,b} \gamma_\epsilon [c_\epsilon]^m \rho [c_\epsilon^\dagger]^m - \frac{\gamma_\epsilon}{2}\{[c_\epsilon^\dagger]^m [c_\epsilon]^m, \rho\}, \quad (10)$$

where (for $\epsilon = a, b$) we have introduced the rates for the m-body collisions:

$$\gamma_\epsilon = \kappa \int d^3\mathbf{r} |\phi_\epsilon(\mathbf{r};\bar{N}_\epsilon)|^{2m}. \quad (11)$$

2.2 Stochastic formulation

To study the evolution of the system we adopt the Monte-Carlo wave function point of view [14] which provides us with a stochastic formulation of the master equation (10). To this aim we introduce the jump operators:

$$S_\epsilon = \sqrt{\gamma_\epsilon}[c_\epsilon]^m \qquad \epsilon = a, b \quad (12)$$

and an effective Hamiltonian:

$$H_{eff} = H^q - \frac{i\hbar}{2}\sum_{\epsilon=a,b} S_\epsilon^\dagger S_\epsilon \,. \quad (13)$$

The Monte-Carlo wave function $|\psi(t)\rangle$ undergoes a non hermitian Hamiltonian evolution ruled by H_{eff} (plus a continuous renormalization) interrupted by random quantum jumps occurring at a rate $\langle\psi(t)|\sum_{\epsilon=a,b}(S_\epsilon^\dagger S_\epsilon)|\psi(t)\rangle$, where $|\psi(t)\rangle$ is normalized to unity. The effect of a quantum jump is to replace $|\psi\rangle$ by $S_\epsilon|\psi\rangle$ up to a normalization factor. Physically this corresponds to the loss of m particles in the condensate ϵ *via* the m-body collisional processes described above. The two kinds of jumps $\epsilon = a, b$ occur with relative probabilities:

$$\frac{P_a}{P_b} = \frac{\langle\psi(t)|S_a^\dagger S_a|\psi(t)\rangle}{\langle\psi(t)|S_b^\dagger S_b|\psi(t)\rangle}\,. \quad (14)$$

Starting with a state with a fixed total number of particles N, we can expand at each time the state vector on the Fock basis

$$|\psi(t)\rangle = \sum_{N_a=0,\tilde{N}} d_{N_a}|N_a, \tilde{N}-N_a\rangle, \quad (15)$$

where $\tilde{N}$ is the total number of atoms at time t in the two condensates, and we can carry out the evolution numerically. The mean value of an observable $\hat{O}$ is obtained by averaging the expectation value $\langle\psi(t)|\hat{O}|\psi(t)\rangle$ over all possible stochastic realizations for the evolution of $|\psi(t)\rangle$.

Usually the Monte-Carlo wave function technique is carried out purely numerically. It turns out that for the present problem it is possible to treat analytically the evolution of a Monte-Carlo wave function and, after a minor approximation, average analytically over all the possible stochastic realizations. This leads to a simple interpretation of the dynamics and allows the derivation of analytical formulas for observables' mean values. As it will appear in the figures the analytical results are in good agreement with the numerical results.

3 Evolution of a single wave function

In this section we derive an approximate formula for the evolution of a single stochastic wave function, and we discuss its physical interpretation. We first consider the simple case in which the condensates are initially in a *phase state*, introduced in the beginning of the section, and subsequently the general case in which the initial state is characterized by a given relative phase distribution.

For the following it will be useful to introduce the operators

$$\hat{N} = \hat{N}_b + \hat{N}_a, \quad \hat{n} = \hat{N}_b - \hat{N}_a \quad (16)$$

corresponding to the sum and difference of the number of atoms in **A** and in **B**.

3.1 Phase states

A very useful class of states of two condensates is represented by the *phase states* [18]:

$$|\phi\rangle_N = \frac{1}{\sqrt{2^N N!}}\,(c_a^\dagger e^{i\phi} + c_b^\dagger e^{-i\phi})^N\,|0\rangle \quad (17)$$

having a fixed total number of particles N and leading to a well-defined relative phase 2ϕ between the condensates **A** and **B**. These states have the remarkable properties:

$$c_\epsilon|\phi\rangle_N = \sqrt{\frac{N}{2}} e^{i\phi\,(\delta_{\epsilon,a}-\delta_{\epsilon,b})}\,|\phi\rangle_{N-1} \quad \epsilon = a,b \tag{18}$$

$$e^{-i\alpha\hat{n}}|\phi\rangle_N = |\phi+\alpha\rangle_N \qquad \forall\alpha, \tag{19}$$

where the $\delta_{\epsilon,\epsilon'}$ for $\epsilon,\epsilon' = a,b$ are Kronecker deltas. The first property reflects the fact that in a phase state, all the particles are in the same state (see Eq. (17)), and the second one shows that n and ϕ are to some extent conjugate variables like the momentum and position of a particle. Note that the phase states are not orthogonal:

$${}_N\langle\phi'|\phi\rangle_N = [\cos(\phi-\phi')]^N, \tag{20}$$

though the function $[\cos(\phi-\phi')]^N$ in equation (20) becomes very peaked around zero when $N\to\infty$ with a width scaling as $1/\sqrt{N}$. Any state with a total number N of particles can be expanded on the overcomplete set of phase states:

$$|\psi\rangle = \mathcal{A}\int_{-\pi/2}^{\pi/2}\frac{d\phi}{\pi}\,c(\phi)\,|\phi\rangle_N, \tag{21}$$

where $c(\phi)$ can be obtained from the expansion of the state vector on the Fock state basis:

$$c(\phi) = \mathcal{A}^{-1}\sum_{N_a=0,N} 2^{N/2}\left(\frac{N_a!(N-N_a)!}{N!}\right)^{1/2} \times e^{i(N-2N_a)\phi}\,\langle N_a, N-N_a|\psi\rangle. \tag{22}$$

The quantity $|c(\phi)|^2$ can be interpreted as the relative phase probability distribution [13]. This distribution, flat for a Fock state and very peaked for a phase state, is normalized in such a way that:

$$\int_{-\pi/2}^{\pi/2}\frac{d\phi}{\pi}\,|c(\phi)|^2 = 1. \tag{23}$$

The factor $\mathcal{A}$ in equation (21) ensures that $|\psi\rangle$ is normalized to unity. For $N\gg 1$ and for a $c(\phi)$ varying slowly at the scale $1/\sqrt{N}$, we can replace the scalar product ${}_N\langle\phi'|\phi\rangle_N$ by the delta distribution $\sqrt{2\pi/N}\delta(\phi-\phi')$ to obtain $\mathcal{A} = (\pi N/2)^{1/4}$.

3.2 Approximate expression for $|\psi(\mathbf{t})\rangle$

Consider the evolution of the state vector $|\psi(t)\rangle$, from a time $t_0 = 0$ to a time t, for *a particular stochastic realization*. We imagine that k quantum jumps, each corresponding to the loss of m particles, occur at times $t_1,...,t_k$ separated by time intervals $\tau_j = t_j - t_{j-1}$ with $j = 1,...,k$; the kth jump takes place in the condensate ϵ_k with $\epsilon_k = a,b$. We have:

$$|\psi(t)\rangle = \mathcal{N}e^{-\frac{i}{\hbar}H_{eff}(t-t_k)}S_{\epsilon_k}e^{-\frac{i}{\hbar}H_{eff}\tau_k}S_{\epsilon_{k-1}} \times e^{-\frac{i}{\hbar}H_{eff}\tau_{k-1}}...\,S_{\epsilon_1}e^{-\frac{i}{\hbar}H_{eff}\tau_1}|\psi(0)\rangle \tag{24}$$

where $\mathcal{N}$ is a normalization factor. By using the identity:

$$[c_\epsilon]^m f(\hat{N}_a,\hat{N}_b) = f(\hat{N}_a+m\delta_{\epsilon,a},\hat{N}_b+m\delta_{\epsilon,a})\,[c_\epsilon]^m \quad \epsilon = a,b, \tag{25}$$

we shift all the jump operators in equation (24) to the right by letting them "pass through" the exponentials and we obtain:

$$\begin{aligned}|\psi(t)\rangle = \mathcal{N}&\exp[-iH_{eff}(\{\hat{N}_\epsilon\})(t-t_k)/\hbar]\\ &\times\exp[-iH_{eff}(\{\hat{N}_\epsilon+m\delta_{\epsilon,\epsilon_k}\})\tau_k/\hbar]\\ &\times\exp[-iH_{eff}(\{\hat{N}_\epsilon+m(\delta_{\epsilon,\epsilon_k}+\delta_{\epsilon,\epsilon_{k-1}}\})\tau_{k-1}/\hbar]...\\ &\times\prod_{j=1,k}S_{\epsilon_j}|\psi(0)\rangle.\end{aligned} \tag{26}$$

We introduce now the major approximation in our calculations by replacing $[c_\epsilon^\dagger]^m[c_\epsilon]^m$ by $\bar{N_\epsilon}^m$ in the expression for the effective Hamiltonian equation (13), supposing that the fraction of lost particles is small. The resulting effective Hamiltonian then takes the form:

$$H_{eff} = H^q - \frac{i\hbar}{2}\lambda\,, \tag{27}$$

quadratic in $\hat{N}_a$ and $\hat{N}_b$, where λ is a constant representing the mean total number of collisional events per unit of time:

$$\lambda = \lambda_a+\lambda_b \quad\text{with}\quad \lambda_a = \gamma_a\bar{N_a}^m, \quad \lambda_b = \gamma_b\bar{N_b}^m. \tag{28}$$

In this approximation the statistics of the quantum jumps is simply Poissonian with a parameter λ and $\delta_{b,\epsilon_j} = 1-\delta_{a,\epsilon_j}$ takes the values 1 and 0 with probabilities λ_b/λ and λ_a/λ respectively, according to equation (14).

We then expand the effective Hamiltonians in each exponential in equation (26) around $\hat{N}_a$, $\hat{N}_b$ in powers of $m\delta_{\epsilon,\epsilon_k}$, $m(\delta_{\epsilon,\epsilon_k}+\delta_{\epsilon,\epsilon_{k-1}})$, *etc.* Due to the quadratic dependence of equation (27) on $\hat{N}_a$ and $\hat{N}_b$ we limit the expansion at the first order, the subsequent terms being constants or zero. By using equation (27) we then obtain the following result for the state vector at time t:

$$|\psi(t)\rangle = \mathcal{N}e^{-\lambda t/2}U_0(t)U_1(t)\prod_{j=1,k}S_{\epsilon_j}|\psi(0)\rangle. \tag{29}$$

In equation (29) we have introduced the unitary operators

$$U_0(t) = \exp[-iH^q(\{\hat{N}_\epsilon\})t/\hbar] \tag{30}$$

$$U_1(t) = \exp\left[-i\left(\frac{\partial H^q}{\partial N_a}(\{\hat{N}_\epsilon\})\Delta_a+\frac{\partial H^q}{\partial N_b}(\{\hat{N}_\epsilon\})\Delta_b\right)/\hbar\right] \tag{31}$$

where for $\epsilon = a,b$:

$$\Delta_\epsilon = m\sum_{j=1,k}\sum_{l=j,k}\delta_{\epsilon,\epsilon_l}\tau_j = m\sum_{l=1,k}\delta_{\epsilon,\epsilon_l}t_l \tag{32}$$

are random quantities that depend on the particular realization.

We sketch out briefly the physical interpretation of the result equation (29), considering the action of the successive factors in equation (29) on a *phase state* defined in equation (17).

- The factor $U_0(t)$ in equation (29) accounts for the evolution in absence of losses. Expressed in terms of the operators $\hat{N}$ and $\hat{n}$ of equation (16) it involves:

$$H^q(\{N_\epsilon\}) = f_0(\hat{N}) + \hat{n}v(\hat{N}) + \hat{n}^2(\mu'_b + \mu'_a)/8. \quad (33)$$

We have used equation (8) and we have defined

$$v(\hat{N}) = \frac{1}{2\hbar}\{\mu_b - \mu_a + \frac{\mu'_b - \mu'_a}{2}(\hat{N} - \bar{N}) - \frac{\mu'_b + \mu'_a}{2}(\bar{N}_b - \bar{N}_a)\}, \quad (34)$$

where $\bar{N} = \bar{N}_a + \bar{N}_b$ and where μ_ϵ stands for $\mu_\epsilon(\bar{N}_\epsilon)$. From the properties of the phase state we find that the terms in $\hat{n}$ and $\hat{n}^2$ in equation (33), when exponentiated in U_0, (i) shift the relative phase at the N-dependent constant speed $v(\hat{N})$ and (ii) spread the relative phase (in a way analogous to the spreading of a wave packet of a massive particle under free evolution), respectively. The term $f_0(\hat{N})$ in equation (33) is a function of the total number of atoms N only and plays no role, since it amounts in $U_0(t)$ to adding a global phase factor to the wave function. The phase-spreading will eventually lead to a *collapse* of the relative phase [6]. On the other hand due to the discreteness of the spectrum of the operator $\hat{n}$ (the spectrum of $\hat{n}$ consists of even integers for an even N, and of odd integers for an odd N), there are special times at which the exponential operator equation (33) reduces to a mere translation of the relative phase, yielding the well-known result that *revivals* should follow the collapses of the relative phase. More precisely if one uses the expansion equation (15) for the phase state defined in equation (17), one realizes that a relative phase distribution initially peaked around ϕ_0 displays revivals at the times:

$$t_R = q\pi/\chi, \quad q \text{ integer} \quad (35)$$

where we have introduced:

$$\chi = \frac{\mu'_a + \mu'_b}{2\hbar}\,. \quad (36)$$

At these times, for N even:

$$e^{-i\chi\hat{n}^2 t_R/4}|\phi\rangle_N = |\phi + q\pi/2\rangle_N \quad (37)$$

and for N odd:

$$e^{-i\chi\hat{n}^2 t_R/4}|\phi\rangle_N = e^{-iq\pi/4}|\phi\rangle_N. \quad (38)$$

The initial relative phase distribution is then reconstructed around $(\phi_0 + v(N)t_R + q\pi/2)$ for N even and around $(\phi_0 + v(N)t_R)$ for N odd.
- The factor $U_1(t)$ in equation (29) accounts for the presence of losses. Expressed in terms of the operators $\hat{n}$ and $\hat{N}$, it involves:

$$\frac{\partial H^q}{\partial N_a}(\{N_\epsilon\})\,\Delta_a/\hbar + \frac{\partial H^q}{\partial N_b}(\{N_\epsilon\})\,\Delta_b/\hbar = f_1(\hat{N}) + \hat{n}D \quad (39)$$

where global phase factors are included in $f_1(\hat{N})$. The translation operator $\hat{n}$ appears in equation (39) multiplied by a random quantity D defined as:

$$D = m\sum_{l=1,k} t_l\left[\chi\delta_{b,\epsilon_l} - \frac{\mu'_a}{2\hbar}\right]. \quad (40)$$

Equations (19, 39) show that the relative phase in a single stochastic realization is shifted by the random amount D due to the loss processes. This effect will turn out to have a dramatic influence on the coherence properties of the condensates.
- Finally in equation (29) the action of the jump operators on a phase state is simply:

$$\prod_{j=1,k} S_{\epsilon_j}|\phi\rangle_N = \left[\frac{N}{2}\frac{N-1}{2}\cdots\frac{N-mk+1}{2}\right]^{1/2} \times e^{-i\phi\alpha}|\phi\rangle_{N-mk} \quad (41)$$

where we have introduced the quantity

$$\alpha = m\sum_{j=1,k}\left[2\delta_{b,\epsilon_j} - 1\right]. \quad (42)$$

Apart from numerical factors that will be absorbed in the normalization and the phase factor involving α, equation (41) amounts to reducing by a random amount the total number of particles.

In the general case, an initial state with N particles can be expanded on the phase states set (see Eq. (21)). By using equations (33, 39, 41), and getting rid of the global phase factors we then obtain the wave function:

$$|\psi(t)\rangle = \mathcal{B}(t)\int_{-\pi/2}^{\pi/2}\frac{d\phi}{\pi}c(\phi,0)e^{-i\chi\hat{n}^2 t/4} \times e^{-i\phi\alpha}|\phi + D + v(N-mk)t\rangle_{N-mk}, \quad (43)$$

where $\mathcal{B}(t)$ is a normalization factor.

4 Mean beating intensity of the condensates

To monitor the evolution of the relative phase between the condensates, a possible choice is to determine the relative phase dependent quantity $\langle c_a^\dagger c_b\rangle$ after some time during which the two condensates, initially prepared in a state with a defined relative phase, evolve independently. As the relative phase between the condensates is affected by the elastic atomic interactions, the average $\langle c_a^\dagger c_b\rangle$ undergoes collapses and revivals in time.

In the situation described in Figure 1 the measure of $\langle c_a^\dagger c_b\rangle$ would correspond to the following measurement scheme: Prepare a state in which **A** and **B** have a well-defined relative phase [13]; let the condensates evolve during a time interval t; then let $p \ll N$ atoms escape from the condensates and beat them on the beam-splitter. The

counts registered in the two output channels of the beam-splitter will be fluctuating variables whose averages over many realizations of the whole procedure are [13]:

$$I_{\pm} = \langle \frac{p}{\hat{N}} \frac{(c_a^\dagger \pm c_b^\dagger)(c_a \pm c_b)}{2} \rangle \simeq \frac{p}{N} \frac{1}{2} \left(\langle c_a^\dagger c_a \rangle + \langle c_b^\dagger c_b \rangle \pm 2Re\langle c_a^\dagger c_b \rangle \right), \quad (44)$$

the difference between I_+ and I_- gives then the real part of $\langle c_a^\dagger c_b \rangle$.

We shall now use the approximated formulas (29, 43) to calculate the time dependence of $\langle c_a^\dagger c_b \rangle$. The main result of this section is that the revivals in this quantity are damped in time with a simple exponential law $e^{-\lambda t}$ where the constant λ, defined in equation (28), is the mean number of loss processes per unit of time.

In the present and in the following section we restrict for simplicity to the perfectly *symmetric* case where the two trapping potentials are identical and the two condensates have initially the same mean number of particles:

$$\bar{N}_a = \bar{N}_b, \quad (45)$$
$$\gamma_a = \gamma_b, \quad (46)$$
$$\mu_a = \mu_b. \quad (47)$$

Moreover we consider an initial state having a *fixed* total number of particles equal to N; and as a reminder of this choice (when it is the case) we will attach a superscript $\langle ... \rangle^{fix}$ to the averages. The *non symmetric* case for the condensates will be considered in Section 6; while the effect of fluctuations in the initial total number of atoms (requiring a further averaging over N) will be analyzed in Section 7.

We calculate $\langle c_a^\dagger c_b \rangle^{fix}$ in two different physical situations. The first one refers to a sharply defined initial relative phase ($\Delta\phi \simeq 1/\sqrt{N}$) for which we choose a *phase state* as the initial state; the second one, probably more realistic from the experimental point of view, makes use of an initial phase distribution much broader than $1/\sqrt{N}$. In each case we first calculate the expectation value of the operator $\hat{O} = c_a^\dagger c_b$ for a single stochastic realization using the results of Section 3, and then take the average over the stochastic realizations. In the whole paper we will denote with $\langle \psi(t)|\hat{O}|\psi(t)\rangle$ the single realization expectation value and with $\langle \hat{O} \rangle$ the quantum mechanical average.

4.1 Case of an initial phase state

Let us assume $|\psi(0)\rangle = |\phi\rangle_N$; by using equations (29) and (33, 39, 41), for a single realization, we find:

$$\langle \psi(t)|c_a^\dagger c_b|\psi(t)\rangle = {}_{N-mk}\langle \phi + D|e^{i\frac{\chi}{4}\hat{n}^2 t} c_a^\dagger c_b \times e^{-i\frac{\chi}{4}\hat{n}^2 t}|\phi + D\rangle_{N-mk} \quad (48)$$

where χ and D are defined in equation (36) and equation (40) respectively. Note that the contribution involving the drift velocity of equation (34) vanishes as we are considering here the *symmetric* case. The quadratic dependence on $\hat{n}$ in equation (48) can be eliminated by shifting $c_a^\dagger c_b$ through the exponential $e^{-i\frac{\chi}{4}\hat{n}^2 t}$ using equation (25):

$$e^{i\frac{\chi}{4}\hat{n}^2 t} c_a^\dagger c_b e^{-i\frac{\chi}{4}\hat{n}^2 t} = e^{-i\chi(\hat{n}+1)t} c_a^\dagger c_b \quad (49)$$

so that

$$\langle \psi(t)|c_a^\dagger c_b|\psi(t)\rangle = {}_{N-mk}\langle \phi + D|e^{-i\chi(\hat{n}+1)t} \times c_a^\dagger c_b|\phi + D\rangle_{N-mk}; \quad (50)$$

by using the properties (18, 19, 20) we then have:

$$\langle \psi(t)|c_a^\dagger c_b|\psi(t)\rangle = \frac{N-mk}{2}\, e^{-2i\phi} e^{-2iD} \times [\cos(\chi t)]^{N-mk-1}. \quad (51)$$

The next step is to take the average of the result equation (51) over the stochastic realizations which amounts to averaging over the random variables k, τ_j and δ_{b,ϵ_j} (the last two variables appearing in the random quantity D). We show the calculation of the average in detail in the Appendix A. The result for $\langle c_a^\dagger c_b \rangle^{fix}$ reads:

$$\langle c_a^\dagger c_b \rangle^{fix} = e^{-2i\phi} e^{-\lambda t} \sum_{k=0,N/m-1} \frac{N-mk}{2} \frac{1}{k!} \times [\lambda t\, u(t)]^k [\cos(\chi t)]^{N-mk-1}, \quad (52)$$

where the function $u(t)$ is given by:

$$u(t) = \frac{\sin(m\chi t)}{m\chi t}\,. \quad (53)$$

By identifying the factor $N - mk$ with N under the assumption of a small fraction of lost particles, and by extending the sum over k up to ∞, we are able to express the result in a compact way[1]:

$$\langle c_a^\dagger c_b \rangle^{fix} = e^{-2i\phi} e^{-\lambda t[1-u(t)/\cos^m(\chi t)]} \frac{N}{2} [\cos(\chi t)]^{N-1}. \quad (54)$$

The factor $[\cos(\chi t)]^{N-1}$ in equation (54), already obtained in [19] in the absence of losses, is responsible for the collapses of the average value $\langle c_a^\dagger c_b \rangle^{fix}$ and for revivals at times $t_R = q\pi/\chi$ with q integer. The collapses and revivals of $\langle c_a^\dagger c_b \rangle^{fix}$ are shown in Figure 2 both (a) in absence and (b) in presence of three-body losses. We see immediately that the losses have a dramatic effect reducing exponentially in time the average with the rate λ given by equation (28). In fact at a revival times $t = t_R$, $u(t)$ vanishes so that the average value of $\langle c_a^\dagger c_b \rangle^{fix}$ is simply attenuated with respect to the lossless case:

$$\langle c_a^\dagger c_b \rangle^{fix}_{t=t_R} = (-1)^{q(N-1)} \langle c_a^\dagger c_b \rangle^{fix}_{t=0}\, e^{-\lambda t_R}, \quad (55)$$

[1] It should be noted however that the compact formula (54) diverges for $\chi t = \pi/2 + q\pi$, where the explicit sum equation (52) should be used instead. At such points $\langle c_a^\dagger c_b \rangle^{fix} = 0$ anyway.

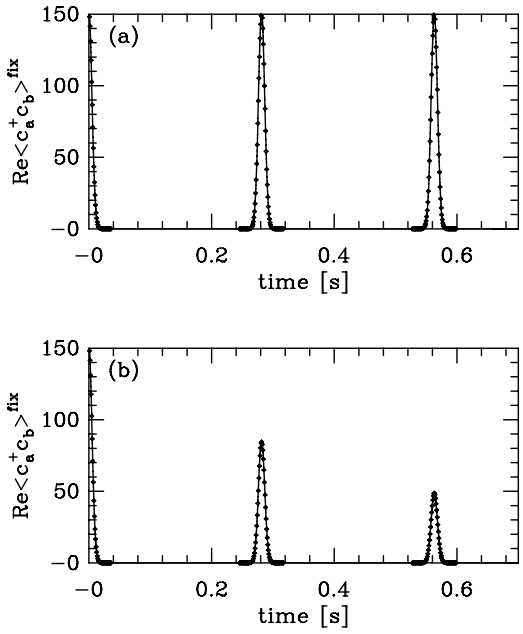

Fig. 2. Collapses and revivals of $\langle c_a^\dagger c_b\rangle^{fix}$ for an initial phase state (a) without losses and (b) in presence of 3-body losses. The calculation is performed for ^{87}Rb atoms in the $F = 1, m_F = -1$ state and for isotropic harmonic traps. The 3-body loss rate is inferred from the experimental data of JILA. The initial total number of atoms is $N = 301$, and the harmonic frequencies are $\Omega_a/2\pi = \Omega_b/2\pi = 500$ Hz. Diamonds: numerical result with 2.5×10^4 Monte-Carlo wave functions. Solid line: analytical result.

by an exponential factor which is exactly the probability that no particles are lost up to time t. The effect of losses on the revivals, already significative when $\lambda t_R \simeq 1$ (that is *one* loss process has occurred on average at the revival time), can be understood by the fact that in each single Monte-Carlo realization experiencing a quantum jump at a time $t \sim t_R$ the relative phase is shifted by an amount $D \gtrsim \pi$. This point will be further exemplified in Section 5.

4.2 Case of an initial relative phase distribution broader than that of a phase state

Since it may be difficult to prepare experimentally the condensates in a phase state we now consider the more realistic case in which the initial relative phase distribution $|c(\phi,0)|^2$ for the condensates is broad as compared to $1/\sqrt{N}$. To be specific we assume that the initial relative phase distribution is a Gaussian centered at $\phi = 0$:

$$c(\phi,0) = \mathcal{G}_0 \exp\left(-\phi^2/(4\Delta\phi^2)\right) \quad \frac{1}{\sqrt{N}} \ll \Delta\phi \ll 1\,, \quad (56)$$

where ϕ ranges between $-\pi/2$ and $\pi/2$. This choice corresponds to a Gaussian distribution for the number of particles in the condensates:

$$\langle N_a, N - N_a|\psi(0)\rangle = \mathcal{G} e^{-(N-2N_a)^2/4\Delta n^2} \quad (57)$$

with $\Delta n\,\Delta\phi = 1/2$.

For a single realization, we use equation (43) and we proceed along the lines of the previous calculation to get:

$$\langle\psi(t)|c_a^\dagger c_b|\psi(t)\rangle = \left[\frac{\pi\tilde{N}}{2}\right]^{1/2} \int_{-\pi/2}^{\pi/2} \frac{d\phi}{\pi}\frac{d\phi'}{\pi} \times c(\phi,0)c^*(\phi',0)\frac{\tilde{N}}{2}e^{-i\alpha(\phi-\phi')} \times e^{-i(\phi+\phi'+2D)}\,{}_{\tilde{N}-1}\langle\phi' - \chi t|\phi\rangle_{\tilde{N}-1} \quad (58)$$

where $\tilde{N} = N - mk$ with k equal to the number of quantum jumps experienced by the Monte-Carlo wave function up to time t. Now by using the fact that the scalar product between the phase states for $N \gg 1$ is a very peaked function of $\phi - \phi'$ with respect to the other functions in the integral, we perform the substitution:

$${}_{\tilde{N}-1}\langle\phi' - \chi t|\phi\rangle_{\tilde{N}-1} \to \cos^{\tilde{N}-1}(q_0\pi)\sqrt{\frac{2\pi}{\tilde{N}}} \times \delta(\phi' + q_0\pi - \chi t - \phi) \quad (59)$$

where the integer q_0 is chosen such that $-\pi/2 < (\chi t + \phi - q_0\pi) \leq \pi/2$. As the factor $c(\phi,0)$ defined in equation (56) is peaked around $\phi = 0$, we neglect the dependence of q_0 on ϕ so that the integer q_0 is finally chosen such that $-\pi/2 < (\chi t - q_0\pi) \leq \pi/2$. In this way we obtain

$$\langle\psi(t)|c_a^\dagger c_b|\psi(t)\rangle = (-1)^{q_0(N-1)}\frac{\tilde{N}}{2}e^{i(\chi\alpha t - 2D)} \times \int_{-\pi/2}^{\pi/2}\frac{d\phi}{\pi}c(\phi,0)c^*(\phi + \chi t - q_0\pi, 0)\, e^{-i(2\phi + \chi t - q_0\pi)}. \quad (60)$$

The next step is to average the factor $e^{i(\chi\alpha t - 2D)}$over the stochastic realizations. The procedure closely follows the one in the Appendix A. By identifying $\tilde{N}$ with N, as in the previous case, and by extending the boundaries of integration in equation (60) to $\pm\infty$ we can express the result in the compact form[2]:

$$\langle c_a^\dagger c_b\rangle^{fix} = \frac{N}{2}e^{-\lambda t[1-u(t)]}\sum_{q=0}^{+\infty} \times e^{-[(\chi t - q\pi)/2]^2/2\Delta\phi^2}(-1)^{q(N-1)} \quad (62)$$

[2] To obtain equation (62) we use the condition $\Delta\phi \ll 1$ to set:

$$\langle c_a c_b^\dagger\rangle_{t=0}^{fix} = \frac{N}{2}\left(\int_{-\pi/2}^{\pi/2}\frac{d\phi}{\pi}c^2(\phi,0)\,e^{-2i\phi}\right) \simeq \frac{N}{2}\,. \quad (61)$$

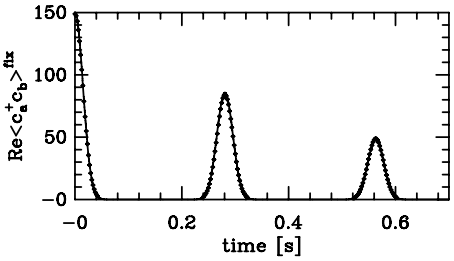

Fig. 3. Collapses and revivals of $\langle c_a^\dagger c_b\rangle^{fix}$ for an initial phase distribution broader than that of the phase state. The initial total number of atoms is $N = 301$. The initial distribution for the difference in the number of particles in the two condensates is Gaussian with a standard deviation $\Delta n = 6$ and a vanishing mean (so that $\bar{N}_a = \bar{N}_b$). The other parameters are as in Figure 2b. Diamonds: numerical result with 2.5×10^4 Monte-Carlo wave functions. Solid line: analytical result.

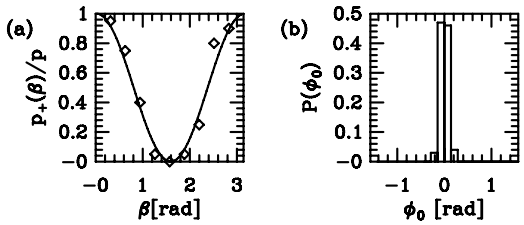

Fig. 4. Monte-Carlo simulation of a multichannel detection experiment using the device in Figure 1 to sample the relative phase distribution corresponding to the initial state of Figure 3. (a) Single realization of the multichannel detection: For each dephasing $\beta_i = i\pi/10, i = 0\ldots9$ added to one of the input channels of the beam splitter, $p_+(\beta_i)$ (resp. $p_-(\beta_i)$) particles are detected in the + (resp. −) output channel of the beam splitter with $p_+(\beta_i) + p_-(\beta_i) = p = 20$. The obtained integers $p_+(\beta_i)$ (diamonds) are fitted with the function $p\cos^2(\phi_0 - \beta)$ (solid line) where $-\pi/2 < \phi_0 \leq \pi/2$ is the adjustable parameter, varying from one realization to the other. (b) After 100 realizations of the multichannel detection (each starting with new condensates): histogram for the obtained values of ϕ_0.

where $u(t)$ is defined in equation (53). The factor involving the sum over q in equation (62) plays the role of the factor $[\cos(\chi t)]^{N-1}$ in equation (54) which was obtained for an initial phase state. At each time $t_R = q\pi/\chi$ there is a revival of the quantity $\langle c_a^\dagger c_b\rangle^{fix}$ and equation (62) reduces to the very simple expression:

$$\langle c_a^\dagger c_b\rangle^{fix}_{t=t_R} = (-1)^{q(N-1)}\langle c_a^\dagger c_b\rangle^{fix}_{t=0}\, e^{-\lambda t_R}. \qquad (63)$$

This formula does not depend on the initial width $\Delta\phi$ and coincides with the one equation (55) obtained for a phase state. There is therefore no possible way of reducing the damping of the revivals by adjusting the initial width of the phase distribution. Only the temporal width of the revivals is larger for a distribution broader than that for a phase state, as it clearly appears from a comparison between Figure 3 and the previous Figure 2b.

Remark: Formula (62) can also be used to study the collapse of the phase around $t = 0$. For short times ($t \ll t_R$) we expand $u(t)$ to second order in t obtaining:

$$\langle c_a^\dagger c_b\rangle^{fix} \simeq \frac{N}{2}\exp\left\{-\frac{(\chi t)^2}{8\Delta\phi^2}\left[1 + \frac{4}{3}m^2\Delta\phi^2\lambda t\right]\right\}. \qquad (64)$$

In the absence of losses we recover the collapse time $t_c = 2\Delta\phi/\chi$ [10] as the half temporal width at the relative height $e^{-1/2}$ of the mean signal $\langle c_a^\dagger c_b\rangle^{fix}$. Losses start *accelerating* the collapse significantly when $\lambda t_c > 1/m^2\Delta\phi^2$. As this last quantity is much larger than 1 the subsequent revivals cannot then be observed.

5 Evolution of the relative phase distribution

We turn now our attention to the phase distribution $|c(\phi)|^2$ which could be reconstructed in an experiment for example *via* a series of multichannel measurements. We show an example of the procedure in Figure 4 [13,20].

In the frame of our model, the evolution of $c(\phi)$ can be obtained numerically from the evolution of the state vector $|\psi(t)\rangle$ expanded on the Fock state basis by using equation (22); however, as we show in the following, the approximated analytical treatment allows us also in this case to find some simple results at the revival times.

Let the initial state of the condensate, with a total number N of atoms, be characterized by a given relative phase distribution amplitude $c(\phi, 0)$; the state vector at time t is then given by our approximated formula equation (43). One can easily check that the integrand in equation (43) is periodic of period π so that we can shift the interval of integration to obtain[3]:

$$|\psi(t)\rangle = \mathcal{B}(t)e^{-i\chi\hat{n}^2 t/4}\int_{-\pi/2}^{\pi/2}\frac{d\phi}{\pi}\,\tilde{c}(\phi - D - v(\tilde{N})t, 0)|\phi\rangle_{\tilde{N}} \qquad (65)$$

where $\tilde{c}(\phi) = e^{-i\alpha\phi}c(\phi)$ and $\tilde{N} = N - mk$. This result has a very suggestive interpretation: the loss processes in a single realization *shift* the relative phase distribution by a random amount D, and the overall evolution can be separated in a random shift plus the Hamiltonian evolution. To make clearer this interpretation, we have plotted in Figure 5 the phase distribution at the second revival time (given by Eq. (35) with $q = 2$) for different realizations. For $\lambda t_R \simeq 1$, as in the figure, there is an important fraction of realizations in which the relative phase is shifted considerably. This is the reason why the relative phase distribution at the revival time will be smeared out by the losses when we take the average over the stochastic realization, which we do now.

[3] When $\phi \to \phi+\pi$, $c(\phi, 0)$ is multiplied by $(-1)^N$, $\exp(-i\alpha\phi)$ is multiplied by $(-1)^{mk}$, and the phase state $|\phi + D + vt\rangle_{\tilde{N}}$ is multiplied by $(-1)^{N-mk}$.

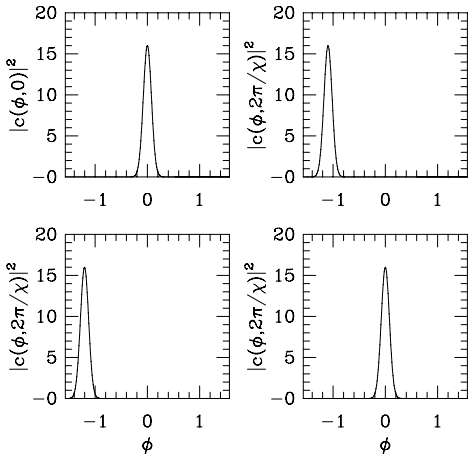

Fig. 5. Single realization relative phase probability distribution at $t = 0$ and at the 2nd revival time $t = 2\pi/\chi$ for three different Monte-Carlo wave functions. The parameters are as in Figure 3. From upper left to lower right the wave functions have experienced 0, 3, 1 and 0 quantum jumps respectively.

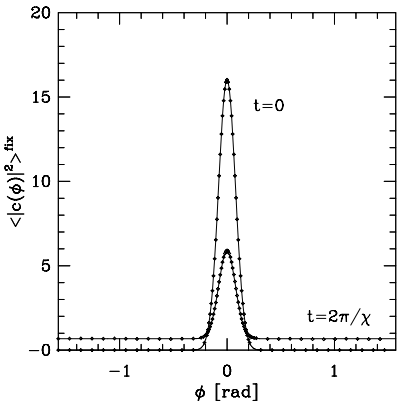

Fig. 6. Relative phase probability distribution at $t = 0$ and at the 2nd revival time. The parameters are as in Figure 3. Solid line: analytical prediction. Diamonds: average of 2.5×10^4 Monte-Carlo wave functions.

As in Section 4 we consider the symmetric case defined by the equations (45, 46, 47). Furthermore we restrict ourselves to the revival times $t = t_R = q\pi/\chi$, q integer (see Eq. (35)). In this case the Hamiltonian evolution operator in equation (65) takes a simple numerical form (see Eqs. (37, 38)) and by comparing equation (65) to equation (21) we can simply read out the phase distribution amplitude $c(\phi, t)$:

$$c(\phi, t_R) = \tilde{c}(\phi_{\tilde{N}} - D, 0), \tag{66}$$

where:

$$\phi_{\tilde{N}} = \phi - q\pi/2 \quad \text{for } \tilde{N} \text{ even} \tag{67}$$

$$\phi_{\tilde{N}} = \phi \quad \text{for } \tilde{N} \text{ odd.} \tag{68}$$

From equation (66) we see again that a single loss event (which can lead to $D \gtrsim \pi$) has a dramatic effect on the phase distribution.

As shown in the Appendix B the phase distribution at the revival times averaged over the stochastic realizations takes the very simple form:

$$\langle |c(\phi, t_R)|^2 \rangle^{fix} = (1 - e^{\lambda t_R}) + e^{-\lambda t_R} |c(\phi_N, 0)|^2. \tag{69}$$

At the revival time the relative phase distribution is "damped" by the factor $e^{-\lambda t_R}$ while a flat background component appears. This effect is clearly shown in Figure 6, where we have plot the averaged relative phase distribution at $t = 0$ and at the second revival time.

6 Effect of an asymmetry between the two condensates

In the previous sections we have investigated the relative phase dynamics in the *symmetric* case for the two condensates. In this section we extend the analysis to account for a small imbalance in the initial average number of particles

$$|\bar{N}_b - \bar{N}_a| \ll \bar{N}, \tag{70}$$

where $\bar{N}$ is the average of the total initial number of particles, and for arbitrary values of the parameters μ_a, μ_b, γ_a, γ_b. We restrict the calculation to the contrast of the interference fringes between the two condensates averaged over many experimental realizations, assuming an initial phase distribution broader than the phase state.

Our initial Monte-Carlo wave function has a fixed total number of particles equal to N, and a Gaussian distribution for number of particles in each condensate. The calculation of $\langle c_a^\dagger c_b \rangle^{fix}$ is now slightly more involved than in the symmetric case, as the phase distribution amplitude $c(\phi, 0)$ acquires a phase factor varying rapidly with ϕ at the scale $1/\sqrt{N}$. All the calculations are therefore put in the Appendix C, and we give here the result only at the revival time $t = t_R$:

$$\langle c_a^\dagger c_b \rangle^{fix}_{t=t_R} = (-1)^{q(N-1)} \frac{N}{2} e^{-2iv(N)t_R} e^{-\lambda t_R[1-U(t_R)]}, \tag{71}$$

where $v(N)$ is defined by equation (34) and $U(t)$ is a function of time (see Eq. (C.11) in Appendix C). In Figure 7 we show an example of the time evolution of $\langle c_a^\dagger c_b \rangle^{fix}$ in the case of a 10% asymmetry in the initial number of particles $\bar{N}_a$ and $\bar{N}_b$. As far as the *damping* of the revivals is concerned, no significant difference appears with respect

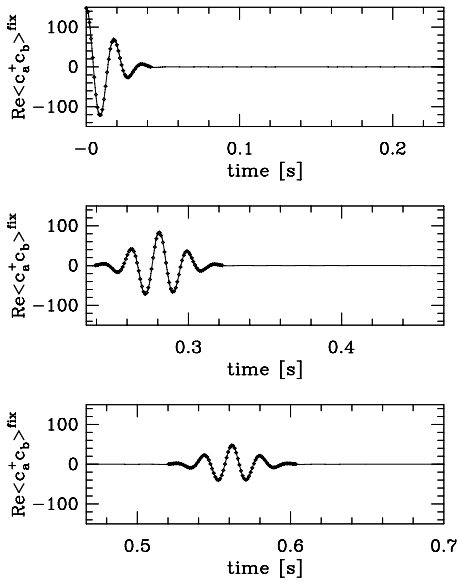

Fig. 7. Collapses and revivals of $\langle c_a^\dagger c_b\rangle^{fix}$ for a 10% asymmetry in the initial number of particles $\bar{N}_a$ and $\bar{N}_b$ in the condensates $\bar{N}_a = 135.5$ and $\bar{N}_b = 165.5$, leading to $\gamma_a \neq \gamma_b$, $\mu_a \neq \mu_b$. The initial total number of atoms is $N = 301$. The initial distribution for the difference in the numbers of particles n in the condensates is Gaussian with a standard deviation $\Delta n = 6$, and a non-vanishing mean value equal to 30. The other parameters are as in Figure 2b. Diamonds: numerical result with 2.5×10^4 Monte-Carlo wave functions. Solid line: analytical result.

to the symmetric case. The damping of the revivals is in this case ruled by the exponent:

$$-\lambda t_R[1 - \mathrm{Re}U(t_R)] \tag{72}$$

where:

$$\mathrm{Re}U(t_R) = \frac{1}{\lambda}\left(\lambda_b\,\mathrm{sinc}(m\mu_b' t_R/\hbar) + \lambda_a\,\mathrm{sinc}(m\mu_a' t_R/\hbar)\right), \tag{73}$$

where $\mathrm{sinc}(x) = \sin(x)/x$. Obviously $|\mathrm{Re}U(t_R)| \leq 1$, meaning that an asymmetry between the condensates cannot *amplify* the revivals with respect to the lossless case. From equation (73) we notice, just as a curiosity, that a complete suppression of the effect of the losses ($\mathrm{Re}U(t_R) = 1$) would occur only in the case in which there are no losses in the condensate **A** ($\lambda_a = 0$) and no elastic interactions in the condensate **B** ($\mu_b' = 0$) (or *vice versa*).

A trivial effect of the asymmetry, evident in Figure 7, is the appearance of *oscillations* of the mean value $\langle c_a^\dagger c_b\rangle^{fix}$ due to the non zero drift velocity of the relative phase of the condensates. We will see in the next section that this effect, harmless at first sight, can have dramatic consequences when we consider the effect of the dispersion in the initial total number of particles N.

7 Effect of fluctuations in the total number of particles

Through all the previous sections in this paper we have chosen an initial state, represented by our initial Monte-Carlo wave function, with a fixed total number of particles in the condensates. The averages that we calculated $\langle ...\rangle^{fix}$ then correspond to the real quantum mechanical averages supposing that the initial total number of atoms is fixed to a value N for any realization of the experiment. In practice it is probably difficult to produce a Fock state for the condensates and the total number of atoms should be governed by some probability distribution $P(N)$. Since we have analytical formulas for the quantities of interest (such as the average $\langle c_a^\dagger c_b\rangle^{fix}$), it is very simple to add a further averaging over N for a given $P(N)$. Suppose for example that the distribution for the initial total number of atoms is a Poissonian distribution of parameter $\bar{N}$. By averaging the result equation (71), valid at the revival times t_R for slightly asymmetric condensates, we get:

$$|\langle c_a^\dagger c_b\rangle_{t=t_R}^{Poiss}| = \frac{\bar{N}}{2} e^{-\lambda t_R[1-\mathrm{Re}U(t_R)]} \times e^{-\bar{N}\left\{\sin^2(\mu_a' t_R/2\hbar)+\sin^2(\mu_b' t_R/2\hbar)\right\}}. \tag{74}$$

The result equation (74) shows that a slight asymmetry between the condensates kills the revivals of $\langle c_a^\dagger c_b\rangle$: the quantity in curly brackets, multiplied by the large number $\bar{N}$, does not vanish in general when $\mu_a' \neq \mu_b'$. This is due to the fact that the drift velocity of the relative phase $v(N)$ in equation (71) depends on the initial total number of particles, giving to $\langle c_a^\dagger c_b\rangle_{t=t_R}^{fix}$ a phase factor of the form:

$$\exp[-2iv(N)t_R] \propto \exp\left[i\,(N-\bar{N})\,\frac{\mu_b' - \mu_a'}{2\hbar}\,t_R\right] = \exp\left[i\,(N-\bar{N})\,\frac{\mu_b' - \mu_a'}{\mu_b' + \mu_a'}\,q\pi\right]. \tag{75}$$

To be able to observe the revivals it is then necessary to be as close as possible to the symmetric conditions in order to satisfy:

$$\frac{\mu_b' - \mu_a'}{\mu_b' + \mu_a'}\Delta N \ll 1, \tag{76}$$

where ΔN is the width of the distribution $P(N)$.

If the *symmetry* between the condensates is perfectly realized, the atom number fluctuations have the simple effect of doubling the revival time. We show an example in Figure 8 where we averaged the result for $\langle c_a^\dagger c_b\rangle^{fix}$ for an initial phase state (Fig. 2) using a Poissonian distribution for $P(N)$. The main effect is the disappearance of the "odd" revivals; this is due to the fact that the amplitude of these odd revivals for N particles is proportional to $[\cos(q\pi)]^{(N-1)} = (-1)^{(N-1)}$ which alternates its sign depending on the parity of N.

In fact it is possible to show that a Poissonian ensemble of phase states is equivalent to a *coherent state* for the two condensates, as long as one calculates the mean values of

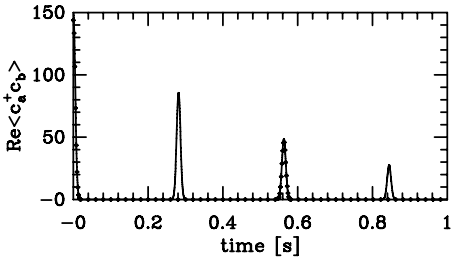

Fig. 8. Collapses and revivals of $\langle c_a^\dagger c_b \rangle^{fix}$ for an initial phase state with $N = 301$ particles (solid line) and after an average over N with a Poisson distribution of parameter $\bar{N} = 301$ (diamonds). The effect of the average is mainly to suppress the odd revivals. The parameters are as in Figure 2b and the results are obtained from the analytical predictions.

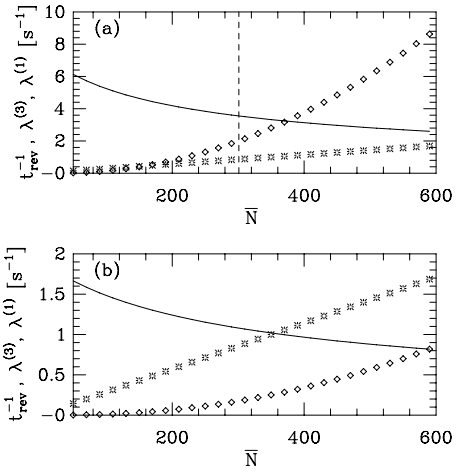

Fig. 9. Collision fluxes $\lambda^{(1)}$ (stars) and $\lambda^{(3)}$ (diamonds), due to one-body and three-body collisions respectively, calculated as in Figure 2, and inverse of the first revival time $1/t_{rev} = \chi/\pi$ (solid line) as a function of the total number of atoms. The trap frequency is $\Omega = 2\pi \times 500$ Hz in (a) and $\Omega = 2\pi \times 200$ Hz in (b). The vertical dashed line for $\bar{N} = 301$ in (a) represents the conditions of Figure 2b. $\lambda^{(1)}$ corresponds to a lifetime due to background gas collisions of 350 seconds.

operators commuting with the total number of particles in the condensates. For the perfectly symmetric case in Figure 8 we then recover the result obtained in [19] (in the absence of losses) *i.e.* the doubling of the revival period for a coherent state of the condensates as compared to the phase state.

Within the coherent states pictures we can also reinterpret the result equation (74) for the asymmetric case in the following way: in order to observe a revival of the relative phase between two condensates it is necessary that *both* condensates display a phase revival at the same time *i.e.* $\mu_a'/2\hbar t_R = q\pi$ and $\mu_b'/2\hbar t_R = q'\pi$, with q, q' integers.

8 Conclusion

We have studied the dynamics of the relative phase between two Bose-Einstein condensates in presence of m-body loss processes in order to question the observability of the *collapses* and *revivals* of the phase predicted by purely Hamiltonian models.

We have shown that the losses damp exponentially in time the phase dependent quantity $\langle c_a^\dagger c_b \rangle$ (see Eq. (55) for an initial phase state and Eq. (63) for an initially broader phase distribution). The decay rate λ of $\langle c_a^\dagger c_b \rangle$ coincides (up to the factor m) with the mean total number of particles lost per unit of time, and it is therefore approximately N times larger than the inverse lifetime of a particle in the condensates, where N is the total number of particles initially in the condensates.

The dramatic effect of the losses on the relative phase has been suggestively interpreted within the Monte-Carlo wave function approach. In a single realization each single loss event occurring at a time of the order of the revival time shifts the relative phase by a random amount of the order of π. A few loss processes are then sufficient to smear out the relative phase completely at the revival time when the average over the stochastic realizations is taken. For this reason the experimental observation of the revivals is limited to condensates with a small number of atoms where the condition $\lambda t_R < 1$ (where t_R is the revival time Eq. (35)) can be satisfied for all the relevant loss processes in the system.

In order to give an idea of the possible scenarios and of the order of magnitudes in different experimental conditions, we have shown in Figure 9 the loss rates due to one-body and three-body collisions and the inverse revival time as functions of the total number of atoms, for two different values of the trap frequencies. For higher trap frequencies (Fig. 9a) the revivals occur on a shorter time scale and one is confronted mainly to three-body losses, while for less confining traps (Fig. 9b) collisions with the residual gas should be taken into account due to longer revival times. Figure 9 shows that phase revivals in presence of losses are in principle observable in condensates with some hundreds of atoms.

By studying the general case of two asymmetric condensates, and the effects of fluctuations in the initial total number of atoms in the condensates, we have finally pointed out a practical difficulty which should be overcome in order to observe phase revivals. The difficulty comes from the fact that in the case of two non perfectly symmetric condensates their relative phase drifts with a velocity *depending* on the initial total number of atoms. For this reason random fluctuations in the initial number of atoms turn out to destroy the relative phase revivals when the asymmetry is too large. A possible way to overcome this problem is of course to use two almost symmetric condensates. Another possibility, which we have not examined in detail, would be to use a condensate **A** which has a collapse time longer than the duration of the

experiment ($\bar{N}(\mu'_a t_R/\hbar)^2 \ll 1$) as a *phase reference* to measure the evolving phase of the other condensate **B**.

We wish to thank Jean Dalibard for useful discussions, and Christopher Herzog for comments on the manuscript. Y.C. wishes to thank Keith Burnett for pointing out the problem of the influence of losses on the revivals at several conferences. A.S. acknowledges financial support from the Atomic Coherence TMR network ERB FMRX-CT96-0002 of the European Community.

Appendix A: Average of the phase factor e^{-2iD}

In this appendix we derive the average over the stochastic realizations of the quantity $e^{-2iD}S(k)$ where D is defined in equation (40) and where $S(k)$ is an arbitrary function of the number of jumps k. We perform the average over the variables δ_{b,ϵ_j} first, using their probability distribution given after equation (28); we have:

$$\begin{aligned}\langle e^{-2iD}\rangle_{\delta_{b,\epsilon_j}} &= \prod_{j=1,k}\frac{1}{\lambda}(\lambda_b e^{-\frac{i}{\hbar}m\mu'_b t_j}+\lambda_a e^{\frac{i}{\hbar}m\mu'_a t_j})\\ &\equiv \prod_{j=1,k} f(t_j). \end{aligned} \tag{A.1}$$

In order to perform the average over the variables k and τ_j, we need the probability distribution $P_t(k,t_1,t_2,...t_k)$ of having in the time interval $(0,t)$ exactly k jumps separated by time intervals $\tau_j = t_j - t_{j-1}$. Since we assume that the loss processes occur randomly with a constant rate λ, corresponding to a waiting-time distribution of the form $w(\tau) = \lambda e^{-\lambda\tau}$, the probability distribution $P_t(k,t_1,t_2,...t_k)$ is simply [17]:

$$P_t(k,t_1,t_2,....t_k) = \lambda^k e^{-\lambda t}. \tag{A.2}$$

Using this result we are led to the calculation of a multiple integral of the form:

$$I = \int_{0<t_1<t_2...<t_k<t} f(t_1)f(t_2)...f(t_k)\; dt_1 dt_2...dt_k \tag{A.3}$$

where $f(t)$ is the argument of the product in equation (A.1). Since I is equal to I_σ calculated for any permutation $t_{\sigma(1)},...t_{\sigma(k)}$ of the integration variables, we can write it as:

$$\begin{aligned} I &= \frac{1}{k!}\left[\sum_\sigma \int_{0<t_{\sigma(1)}<...<t_{\sigma(k)}<t} f(t_1)f(t_2)...f(t_k)dt_1dt_2...dt_k\right]\\ &= \frac{1}{k!}\left[\int_0^t f(t)dt\right]^k. \end{aligned} \tag{A.4}$$

We then obtain

$$\langle S(k)e^{-2iD}\rangle_{k,\tau_j,\delta_{b,\epsilon_j}} = \sum_{k\geq 0} S(k)\frac{\lambda^k}{k!}\left[\int_0^t f(t)\;dt\right]^k e^{-\lambda t}. \tag{A.5}$$

In this last equation we may have to introduce by hand a cut-off $N/m-1$ over the index k if $S(k)$ has divergences for $k \geq N/m$ (*i.e.* when no particles are left in the condensates).

Appendix B: Phase distribution at revival times

We are interested in calculating the phase distribution at the revival time averaged over the realizations that is $\langle|c(\phi,t_R)|^2\rangle_{k,\tau_j,\delta_{b,\epsilon_j}}$. We restrict to the symmetric case between the condensates and we start from equation (66). By using equation (22) for $t=0$ we have:

$$\begin{aligned}\langle|c(\phi,t_R)|^2\rangle_{k,\tau_j,\delta_{b,\epsilon_j}} &= |\mathcal{A}(0)|^{-2}\sum_{N_a=0,N}\sum_{N'_a=0,N}\mathrm{fac}(N_a)\\ &\times \mathrm{fac}^*(N'_a)\langle e^{2i(N'_a-N_a)(\phi_{\tilde{N}}-D)}\rangle_{k,\tau_j,\delta_{b,\epsilon_j}}\end{aligned} \tag{B.1}$$

where we have introduced the notation

$$\mathrm{fac}(N_a) = 2^{N/2}\left(\frac{N_a!(N-N_a)!}{N!}\right)^{1/2}\langle N_a, N-N_a|\psi(0)\rangle. \tag{B.2}$$

The calculation of the average over the stochastic realizations closely resembles the previous one equation (A.1) that we have explained in the Appendix A; we have:

$$\begin{aligned}\langle e^{2i(N'_a-N_a)(\phi_{\tilde{N}}-D)}\rangle_{k,\tau_j,\delta_{b,\epsilon_j}} &= \sum_{k\geq 0} e^{-\lambda t_R}\frac{(\lambda t_R)^k}{k!}\\ &\times\left[\frac{\sin[(N'_a-N_a)m\chi t_R]}{(N'_a-N_a)m\chi t_R}\right]^k e^{2i(N'_a-N_a)\phi_{\tilde{N}}}.\end{aligned} \tag{B.3}$$

We note that the terms in the sum in equation (B.3) for $k\neq 0$ are equal to zero unless $(N'_a-N_a)=0$ in which case the average in equation (B.3) is equal to one. We can then rewrite the result (B.1) as:

$$\begin{aligned}\langle|c(\phi,t_R)|^2\rangle^{fix} = |\mathcal{A}(0)|^{-2}&\left[\sum_{N_a=0,N}\sum_{N'_a=0,N}\delta_{N'_a,N_a}|\mathrm{fac}(N_a)|^2\right.\\ &\left.\times(1-\delta_{N'_a,N_a})\left(\mathrm{fac}(N_a)[\mathrm{fac}(N'_a)]^* e^{2i(N'_a-N_a)\phi_N}e^{-\lambda t_R}\right)\right].\end{aligned} \tag{B.4}$$

Now by using the property:

$$\sum_{N_a=0,N}|\mathrm{fac}(N_a)|^2|\mathcal{A}(0)|^{-2} = 1 \tag{B.5}$$

coming from the normalization condition equation (23) and from equation (22), we find the suggestive result equation (69).

Appendix C: Asymmetric condensates

In this appendix we show the explicit calculation of the mean contrast of the interference fringes $\langle c_a^\dagger c_b\rangle^{fix}$ for asymmetric condensates. We consider an initial Monte-Carlo wave function for which the total number of particles N is fixed and the number of particles in condensate **A** has a Gaussian probability distribution:

$$\langle N_a, N-N_a|\psi(0)\rangle = \mathcal{G}e^{-(N_a-x_aN)^2/\Delta n^2} \tag{C.1}$$

where $\mathcal{G}$ is a normalization factor and Δn is the standard deviation for the difference n in the number of particles in the two condensates. The quantities $x_a = \bar{N}_a/(\bar{N}_a+\bar{N}_b)$ and $x_b = \bar{N}_b/(\bar{N}_a+\bar{N}_b)$ are the average fractions of particles initially in the condensate **A** and **B** respectively, which are supposed to be fixed from one realization to the other even in presence of fluctuations of the initial total number of atoms.

We suppose in what follows that

$$1 \ll \Delta n \ll \sqrt{N}, \tag{C.2}$$

and

$$|x_aN - x_bN| \ll N. \tag{C.3}$$

We first derive the phase distribution amplitude corresponding to the initial state equation (C.1) by using equation (22). We evaluate the factorials in equation (22) using the Stirling's formula, and we use a local approximation valid for $|N_a - x_aN| \ll \sqrt{N}$:

$$\frac{N_a!(N-N_a)!}{N!} \simeq \frac{(x_aN)!(x_bN)!}{N!} e^{(N_a-x_aN)\ln(x_a/x_b)}. \tag{C.4}$$

By approximating the discrete sum in equation (22) with an integral over N_a ranging from $-\infty$ to $+\infty$ we obtain:

$$c(\phi,0) = \mathcal{N}e^{-\phi^2\Delta n^2}e^{i\kappa\phi} \tag{C.5}$$

where:

$$\kappa = (x_b-x_a)N - \frac{1}{2}\Delta n^2\ln(x_a/x_b) \tag{C.6}$$

and where $\mathcal{N}$ is a normalization factor obtained from equation (23). We note that in the symmetric case $\bar{N}_a = \bar{N}_b$, we recover the Gaussian dependence for $c(\phi)$ of equation (56) with $\Delta n\Delta\phi = 1/2$.

We are now ready to calculate $\langle c_a^\dagger c_b\rangle^{fix}$ starting from equation (43). The calculation closely follows the one in Section 4. In particular we use the key property equation (49) to obtain:

$$\begin{aligned}\langle\psi(t)|c_a^\dagger c_b|\psi(t)\rangle = \frac{1}{\pi^2}|\mathcal{B}(t)|^2|\mathcal{N}|^2\int_{-\pi/2}^{\pi/2}d\phi\int_{-\pi/2}^{\pi/2}d\phi' \\ \times e^{-(\phi^2+\phi'^2)\Delta n^2}e^{i(\kappa-\alpha)(\phi-\phi')}\frac{\tilde{N}}{2} \\ \times e^{-i[\phi+\phi'+2(D+v(\tilde{N})t)]}{}_{\tilde{N}-1}\langle\phi'-\chi t|\phi\rangle_{\tilde{N}-1}.\end{aligned} \tag{C.7}$$

The phase factor $e^{i\kappa(\phi-\phi')}$ in the integrand varies rapidly with $\phi-\phi'$ at the scale $1/\sqrt{N}$ when $\bar{N}_b-\bar{N}_a$ is larger than $\sqrt{N}$. For this reason we approximate the scalar product between the phase states $|\phi\rangle_{\tilde{N}}$ and $|\phi'\rangle_{\tilde{N}}$ by a Gaussian $\exp(-\tilde{N}(\phi-\phi')^2/2)$ rather than by the δ distribution of Section 4. This leads to the approximation

$${}_{\tilde{N}-1}\langle\phi'-\chi t|\phi\rangle_{\tilde{N}-1} \simeq (-1)^{q_0(\tilde{N}-1)}e^{-(\tilde{N}-1)(\phi'-\phi-\chi t+q_0\pi)^2/2} \tag{C.8}$$

where the integer q_0 is chosen such that $-\pi/2 < (\chi t - q_0\pi) \leq \pi/2$. By extending the limits of integration over ϕ,ϕ' to $\pm\infty$ in equation (C.7) we are then left with a double Gaussian integral that can be calculated exactly. The result is quite involved but it can be simplified by using the condition (C.3) and equation (C.2). We take the average over the stochastic realizations and we use again equation (C.2) to simplify the result. We calculate the normalization factor $\mathcal{B}(t)$:

$$\begin{aligned}1 \simeq \frac{1}{\pi^2}|\mathcal{N}|^2|\mathcal{B}|^2(t)\left(\frac{2\pi}{4}\Delta n^2\right)^{1/2}\left(\frac{2\pi}{\tilde{N}+\Delta n^2}\right)^{1/2} \\ \times e^{-\frac{1}{2}(\kappa-\alpha)^2/(\tilde{N}+\Delta n^2)}.\end{aligned} \tag{C.9}$$

We finally obtain for the mean contrast of the interference fringes between **A** and **B** as:

$$\begin{aligned}\langle c_a^\dagger c_b\rangle^{fix} \simeq e^{-\lambda t}e^{-2iv(N)t}\sum_{q=0}^{+\infty}e^{-\frac{1}{2}\Delta n^2[(\chi t-q\pi)]^2}(-1)^{q(N-1)} \\ \times \sum_{k=0}^{N/m-1}\frac{\tilde{N}}{2}e^{-i\kappa(\chi t-q\pi)\frac{\tilde{N}-1}{\Delta n^2+\tilde{N}-1}}\frac{1}{k!}[\lambda tU(t)]^k\end{aligned} \tag{C.10}$$

where the function $U(t)$ is given by:

$$U(t) = \frac{1}{\lambda}\left(\lambda_b\frac{e^{im\mu_b't/\hbar}-1}{im\mu_b't/\hbar} + \lambda_a\frac{e^{-im\mu_a't/\hbar}-1}{-im\mu_a't/\hbar}\right). \tag{C.11}$$

References

1. M.H. Anderson, J.R. Ensher, M.R. Matthews, C.E. Wieman, E.A. Cornell, Science **269**, 198 (1995).
2. K.B. Davis, M.-O. Mewes, M.R. Andrews, N.J. van Druten, D.S. Durfee, D.M. Kurn, W. Ketterle, Phys. Rev. Lett. **75**, 3969 (1995).
3. C.C. Bradley, C.A. Sackett, R. Hulett, Phys. Rev. Lett. **78**, 985 (1997).
4. Since the first experimental achievements of BEC with alkali atoms at JILA, MIT, and Rice, condensation has been observed by other groups. See for example [5] and the WEB server `http://amo.phy.gasou.edu/bec.html/`.
5. U. Ernst, A. Marte, F. Schreck, J. Schuster, G. Rempe, Europhys. Lett. **41**, 1 (1998).
6. A.S. Parkins, D. Walls, preprint submitted to Elsevier Science (1997).

7. F. Dalfovo, S. Giorgini, L. Pitaevskii, S. Stringari, preprint, May 1998, for publication in Review of Modern Physics.
8. Y. Castin, in *Nuclear matter in different phases and transitions*, edited by J.-P. Blaizot, H. Campi, M. Ploszajczak, series "Fundamental Theories in Physics" (Kluwer Academic Publisher, to appear).
9. M.R. Andrews, C.G. Townsend, H.-J. Miesner, D.S. Durfee, D.M. Kurn, W. Ketterle, Science **275**, 637 (1997).
10. P. Villain, M. Lewenstein, R. Dum, Y. Castin, L. You, A. Imamoglu, T.A.B. Kennedy, J. Mod. Opt. **44**, 1775 (1997).
11. E.A. Burt, R.W. Ghrist, C.J. Myatt, M.J. Holland, E.A. Cornell, C.E. Wieman, Phys. Rev. Lett. **79**, 337 (1997).
12. D.M. Stamper-Kurn, M.R. Andrews, A.P. Chikkatur, S. Inouye, H.-J. Miesner, J. Stenger, W. Ketterle, Phys. Rev. Lett. **80**, 2027 (1998).
13. Y. Castin, J. Dalibard, Phys. Rev. A, **55**, 4330 (1997).
14. K. Mølmer, Y. Castin, J. Dalibard, J. Opt. Soc. Am. B **10**, 524 (1993); for a review see *e.g.* K. Mølmer, Y. Castin, Quantum Semiclass. Opt. **8**, 49 (1996).
15. R. Dum, P. Zoller, H. Ritsch, Phys. Rev. A **45**, 315 (1992).
16. N. Gisin, I. Percival, Phys. Lett. A **167**, 315 (1992); J. Phys. A **25**, 5677 (1992)
17. H.J. Carmichael, *An Open Systems Approach to Quantum Optics*, LNIP m18, edited by W. Beiglböck (Springer 1993).
18. A.J. Leggett, F. Sols, Found. Phys. **21**, 353 (1991).
19. T. Wong, M.J. Collett, S.M. Tan, D.F. Walls, 1996, preprint (cond-mat # 9611101).
20. J. Javanainen, Sung Mi Yoo, Phys. Rev. Lett. **76**, 161 (1996).

4.3 Étude des expériences du JILA sur les mélanges de deux condensats

4.3.1 Dynamique turbulente d'un mélange

Par transfert cohérent d'une partie des atomes du condensat de l'état atomique interne $|a\rangle$ vers un autre état interne $|b\rangle$, le groupe du JILA a réussi en 1998 à préparer deux condensats avec une phase relative initialement bien définie. Le dispositif du JILA a ouvert ainsi des perspectives passionnantes, puisqu'il permet aussi de mesurer l'évolution de la phase relative en fonction du temps. Il a été ainsi mesuré une durée de cohérence de phase de 150 ms.

Cependant, les deux condensats dans l'expérience du JILA se recouvrent spatialement et interagissent entre eux de façon répulsive, ce qui doit être pris en compte dans l'étude de la dynamique de phase. Effectivement, les premiers résultats obtenus au JILA sur les mélanges portaient sur leur dynamique de séparation spatiale. Il a été observé qu'un petit déplacement du piège pour l'un des deux états internes met les condensats en oscillation l'un par rapport à l'autre, et que ces oscillations sont rapidement amorties. L'origine de l'amortissement était inexpliquée.

Nous avons donc attaqué ce problème en résolvant deux équations de Schrödinger non linéaires couplées (équations de Gross-Pitaevskii) qui décrivent bien les condensats en l'absence de nuage thermique. Ceci nous a permis de prouver l'origine hamiltonienne de l'amortissement observé au JILA. En effet, même pour des déplacements du piège petits par rapport à la taille des condensats, la dynamique du système peut devenir turbulente. De cette façon, l'énergie initialement localisée dans un mode d'oscillation relative des centres de masse des condensats est rapidement dissipée vers des modes très excités par couplage entre les modes dû à la non linéarité [9].

4.3.2 Dynamique de phase

Nous avons ensuite poursuivi notre travail sur la cohérence de phase en étudiant la dynamique de phase dans un mélange de condensats en interaction mutuelle, ce qui nous a conduit à généraliser les traitements existants qui se limitaient à des condensats spatialement séparés et dans un état stationnaire. Notre traitement permet également de prendre en compte simplement l'effet des fluctuations du nombre total de particules d'une réalisation expérimentale à l'autre [11].

Nous avons obtenu des solutions analytiques au problème dans (1) le cas où il existe une solution approchée par changement d'échelle des équations de Gross-Pitaevskii couplées, et (2) le cas où une linéarisation des équations de Gross-Pitaevskii autour de l'état initial peut être effectuée. Dans les deux cas nous prédisons une augmentation notable du temps de cohérence de la phase lorsque les longueurs de diffusion a_{12}, a_{11} et a_{22} décrivant les collisions élastiques entre atomes des condensats 1 ou 2 ont des valeurs proches les unes des autres.

Les interactions mutuelles entre condensats peuvent donc aider à préserver la cohérence de phase ! Il est possible de comprendre ce résultat surprenant assez simplement. La différence de phase entre le condensat 1 avec N_1 particules et le condensat 2 avec N_2 particules évolue à la fréquence $\omega = \mu_1(N_1, N_2) - \mu_2(N_1, N_2)$ où μ_1 et μ_2 sont les potentiels chimiques des deux condensats. Initialement les deux condensats sont dans un état de phase relative bien défini, il y a donc une dispersion sur la variable conjuguée $n = N_1 - N_2$, avec un écart type $\Delta n \simeq \sqrt{N}$ où $N = N_1 + N_2$. Ceci entraîne une dispersion sur les

fréquences d'oscillation de la phase relative, $\Delta\omega \simeq \chi\Delta n$ avec $\chi = \partial_n[\mu_1 - \mu_2]$, ce qui conduit à un brouillage de la phase au bout d'un temps $t_c \simeq 1/\Delta\omega$. Physiquement χ représente le changement de différence de potentiel chimique lorsqu'on transfère un atome du condensat 2 au condensat 1. L'on conçoit alors que χ puisse être très faible lorsque $a_{11} \simeq a_{12} \simeq a_{22}$ pour des condensats voyant le même potentiel de piégeage, l'atome transféré dans 2 interagissant presque de la même façon avec les $N-1$ autres atomes que lorsqu'il était dans 1.

Pour les paramètres du JILA les trois longueurs de diffusion diffèrent de quelques pour cent seulement. On s'attend donc à un allongement de la durée de vie de la phase par rapport au cas de condensats séparés. En fait la situation du JILA ne rentre pas exactement dans le domaine de validité des cas limites traitables analytiquement, nous avons donc eu recours à un traitement numérique. Le résultat clé auquel nous sommes parvenus est que le temps de cohérence observé (de 150 ms) n'était certainement pas limité par le phénomène de brouillage de phase dû aux interactions, et qu'il pouvait seulement en partie être expliqué par des fluctuations du nombre total de particules dans l'expérience.

4.3.3 Publications jointes

VOLUME 82, NUMBER 2 PHYSICAL REVIEW LETTERS 11 JANUARY 1999

Dynamics of Two Interacting Bose-Einstein Condensates

A. Sinatra,[1] P. O. Fedichev,[2,3] Y. Castin,[1] J. Dalibard,[1] and G. V. Shlyapnikov[1,2,3]
[1]*Laboratoire Kastler Brossel, 24 Rue Lhomond, F-75231 Paris Cedex 05, France*
[2]*FOM—Institute for Atomic and Molecular Physics, Kruislaan 407, 1098 SJ Amsterdam, The Netherlands*
[3]*Russian Research Center, Kurchatov Institute, Kurchatov Square, 123182 Moscow, Russia*
(Received 2 September 1998)

We analyze the dynamics of two trapped interacting Bose-Einstein condensates in the absence of thermal cloud and identify two regimes for the evolution: a regime of slow periodic oscillations and a regime of strong nonlinear mixing leading to the damping of the relative motion of the condensates. We compare our predictions with an experiment recently performed at JILA. [S0031-9007(98)08104-6]

PACS numbers: 03.75.Fi, 05.30.Jp

The experimental evidence for Bose-Einstein condensation in trapped atomic gases [1] has attracted a lot of attention, as the presence of a macroscopically occupied quantum state makes the behavior of these gases drastically different from that of ordinary gas samples. Trapped Bose-Einstein condensates are well isolated from the environment and, at the same time, can be excited by deforming the trap or changing the interparticle interaction. The question of how the gas sample, being initially a pure condensate, subsequently reaches a new equilibrium state is directly related to the fundamental problem of the appearance of irreversibility in a quantum system with a large number of particles. Thus far the time dependent dynamics of trapped condensates has mainly been analyzed for a single condensate [2–6] on the basis of the Gross-Pitaevskii equation for the condensate wave function. Remarkably, already in this mean-field approach the stochastization in the condensate evolution has been found [3], and the damping of the condensate oscillations has been observed numerically [5]. However, the question of the formation of a thermal component, addressed in [3], has not been investigated.

In this paper we study the evolution of a richer system, a mixture of two interacting condensates (a and b), in the situation where initially the thermal cloud is absent. The properties of a static two-component trapped condensate, including the issue of spatial separation of the a and b components due to interparticle interaction [7,8], were investigated in [9]. The response of the system to small modulations of the trap frequency has also been studied numerically [10]. In our case the a and b condensates have initially the same density profile and are set into motion mostly by an abrupt displacement of the trap centers. The main goal of our work is to study the dynamics of spatial separation of the two condensates and analyze how the system can acquire statistical properties and reach a new equilibrium state. From a general point of view, we are facing the problem raised by Fermi, Pasta, and Ulam [11]. They considered classical vibrations of a chain of coupled nonlinear oscillators to analyze the emergence of statistical properties in a system with a large number of degrees of freedom. As was revealed later, the appearance of statistical properties requires a sufficiently strong nonlinearity leading to stochastization of motion [12], whereas for small nonlinearity the motion remains quasiperiodic (see, e.g., [13]).

We consider a situation in which the two condensates a and b see harmonic trapping potentials of exactly the same shape, and the interparticle interactions characterized by the scattering lengths a_{aa}, a_{ab}, and a_{bb} are close to each other. The control parameter, determining the possibilities of nonlinear mixing and stochastization, is the relative displacement z_0 of the trap centers. We identify two regimes for the evolution. In the first one the relative motion of the condensates exhibits oscillations at a frequency much lower than the trap frequency ω. In the other regime there is a strong nonlinear mixing leading to the damping of the relative motion, and the system has a tendency to approach a new equilibrium state. We compare our predictions with the results of the Joint Institute for Laboratory Astrophysics (JILA) experiments [14,15] on a two-component condensate of ^{87}Rb atoms in the $F = 1, m = -1$ and $F = 2, m = 1$ states. In these experiments the double condensate was prepared from a single condensate in the state $F = 1, m = -1$ (a) by driving a two-photon transition which coherently transfers half of the atoms to the state $F = 2, m = 1$ (b).

We mostly perform our analysis in the mean-field approach relying on the Gross-Pitaevskii equations for the wave functions ϕ_a and ϕ_b of the a and b condensates. This approach corresponds to the classical limit of the evolution of a quantum field, the subsequent corrections being proportional to a small parameter $(na^3_{\varepsilon\varepsilon'})^{1/2}$ (n is the gas density) and, hence, manifesting themselves only on a rather large time scale. The two coupled Gross-Pitaevskii equations for ϕ_a and ϕ_b normalized to unity read

$$i\hbar\partial_t\phi_\varepsilon = \left[-\frac{\hbar^2\Delta}{2m} + U_\varepsilon - \mu + \sum_{\varepsilon'=a,b} g_{\varepsilon\varepsilon'} N_{\varepsilon'} |\phi_{\varepsilon'}|^2 \right] \phi_\varepsilon . \qquad (1)$$

Here $g_{\varepsilon\varepsilon'} = 4\pi\hbar^2 a_{\varepsilon\varepsilon'}/m$ are the coupling constants for elastic interaction between atoms in the states ε and ε', m

 © 1999 The American Physical Society

is the atom mass, and N_ε, U_ε are the number of atoms and trapping potential for the ε condensate. As in the JILA experiment, we choose the initial condition $\phi_{a,b}(0) = \phi_0$, where the (real) wave function ϕ_0 corresponds to the ground state of Eq. (1) with all atoms in the a state and no trap displacement. The chemical potential of this ground state is denoted as μ.

We consider the a and b condensates in the Thomas-Fermi regime ($\hbar\omega \ll \mu$) and assume the number of condensate atoms $N_a = N_b = N/2$ [16]. The first set of our calculations is performed for the evolution of the condensates in a spherically symmetric trapping potential $U_0(r) = m\omega^2 r^2/2$ which at $t = 0$ is displaced along the z axis by a distance $z_0/2$ for the a atoms and by $-z_0/2$ for the b atoms. We present the results for the time dependence of the mean separation between the condensates,

$$u(t) = \int d^3r\, z(|\phi_a(\mathbf{r},t)|^2 - |\phi_b(\mathbf{r},t)|^2)\,. \qquad (2)$$

For the curves in Fig. 1 the coupling constants are $g_{aa} = g_{ab} = g_{bb}$, and for $z_0 = 0$ our initial state is an equilibrium state at $t \geq 0$. In this state the Thomas-Fermi radius of the condensate $R_0 = (2\mu/m\omega^2)^{1/2}$ serves as unit of length, and the shape of ϕ_0 is determined by $\mu/\hbar\omega$. Hence, for $z_0 \neq 0$ the dependence of the quantity u/R_0 on ωt is governed by the parameters $\mu/\hbar\omega$ and z_0/R_0.

Our results reveal two key features of the evolution dynamics. The first one, for a tiny displacement z_0, is a periodic motion with slow frequencies which turn out to be sensitive to small variations in the values of the coupling constants. The other feature, for much larger z_0, but still $z_0 \ll R_0$, is a strong damping in the relative motion of the two condensates, as observed at JILA [14].

In order to understand the physics behind the evolution pattern, we first perform a linear analysis of Eq. (1). For the case where $g_{aa} = g_{ab} = g_{bb} = g$, and the displacement z_0 is sufficiently small, we linearize Eq. (1) with respect to small quantities $\delta\phi_{a,b} = (\phi_{a,b} - \phi_0)$ and z_0. Then, for the quantity $\delta\phi_- = \delta\phi_a - \delta\phi_b$, describing the relative motion of the condensates, we obtain the equation

$$i\hbar\partial_t\delta\phi_- = \left[-\frac{\hbar^2\Delta}{2m} + U_0 - \mu + Ng\phi_0^2\right]\delta\phi_- + S_-\,, \qquad (3)$$

with the source term $S_- = m\omega^2 z_0 z\phi_0$. For the quantity $\delta\phi_+ = \delta\phi_a + \delta\phi_b$ we find an equation decoupled from $\delta\phi_-$ and without source terms. Hence, the initial condition $\delta\phi_+(\mathbf{r},0) = 0$ allows us to put $\delta\phi_+(\mathbf{r},t) = 0$ for $t \geq 0$.

For $S_- = 0$ Eq. (3) is the equation for the wave function of a particle moving in the potential $V = U_0 - \mu + Ng\phi_0^2$. Stationary solutions of this equation provide us with the eigenmodes of oscillations of the condensates with respect to each other. In the Thomas-Fermi limit the potential V, originating from the kinetic energy of the condensate, is a smooth function of r inside the condensate spatial region $r < R_0$: $V = \hbar^2(\Delta\phi_0)/2m\phi_0 \ll \hbar\omega$. For $r > R_0$ this potential is close to $U_0 - \mu$ and is much steeper. Replacing V by an infinite square well of radius R_0 we obtain the energy spectrum of eigenmodes with large quantum numbers n: $E_{nl} = (\pi\hbar\omega)^2(2n + l)^2/16\mu$, where l is the orbital angular momentum. This explains the appearance of oscillations at a frequency much smaller than ω in our numerical calculations (see Fig. 1a), since the energy scale in the spectrum is $(\hbar\omega)^2/\mu \ll \hbar\omega$. For the latter reason we call these eigenmodes soft modes. Note that the soft modes for the relative motion of the two condensates also exist in the spatially homogeneous case where they have a free-particle spectrum [7].

As in our linear approach we have $\delta\phi_+(\mathbf{r},t) = 0$, Eq. (2) for the mean separation between the condensates reduces to $u(t) = 2\int d^3r\, z\phi_0\,\mathrm{Re}\{\delta\phi_-\}$, and the contribution to $u(t)$ comes from the components of $\delta\phi_-$ with $l = 1, m_l = 0$. Solving Eq. (3) with the initial condition $\delta\phi_-(\mathbf{r},0) = 0$, we obtain $u(t)$ as a superposition of components, each of them oscillating at an eigenfrequency of a soft mode:

$$u(t) = z_0 \sum_{n\geq 1} \frac{2m\omega^2}{E_{n1}} \left| \int d^3r\, \varphi_{n1} z\phi_0 \right|^2 \times \left[1 - \cos\left(\frac{E_{n1}t}{\hbar}\right)\right], \qquad (4)$$

where φ_{n1} is the wave function of the soft mode with $l = 1, m_l = 0$ and main quantum number n. Damping of oscillations of $u(t)$ could, in principle, originate from the interference between the components with different n in Eq. (4). However, the source S_- basically populates only the lowest soft mode, irrespective of the value of z_0: the amplitude of oscillations at the lowest eigenfrequency in Eq. (4) (the term with $n = 1$) greatly exceeds the sum of the amplitudes of other terms. Hence,

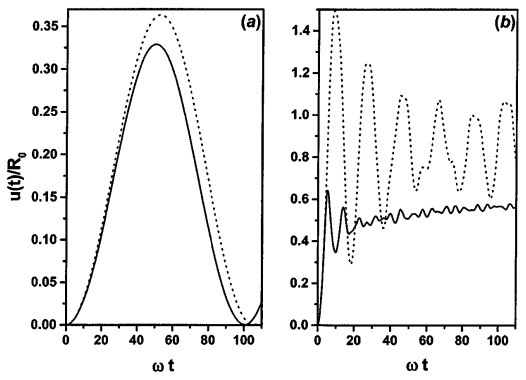

FIG. 1. Mean separation between the condensates versus time in isotropic traps for $g_{aa} = g_{ab} = g_{bb}$ and $\mu/\hbar\omega = 29.2$. Relative displacement: $z_0 = 6.66 \times 10^{-4} R_0$ (a), and $z_0 = 7.17 \times 10^{-2} R_0$ (b). Solid curves: Numerical integration of Eq. (1). Dotted curves: Analytical prediction for (a) (see text), and the linear model relying on Eq. (6) for (b).

these oscillations remain undamped. For the same reason their frequency and amplitude can be found with φ_{n1} replaced by the function $z\phi_0$ normalized to unity. Using the Thomas-Fermi approximation for the condensate wave function [17]: $\phi_0^2(r) = 15(1 - r^2/R_0^2)/8\pi R_0^3$ for $r < R_0$, and $\phi_0 = 0$ for $r > R_0$, we obtain $E_{11} \equiv \hbar\Omega = (7/4)(\hbar\omega)^2/\mu$ which is very close to $E_{11} = 1.62(\hbar\omega)^2/\mu$ calculated numerically. Then, retaining only the leading term ($n = 1$) in Eq. (4), we find $u(t) \approx z_0(4\mu/7\hbar\omega)^2[1 - \cos(\Omega t)]$ shown in the dotted line in Fig. 1a. As one can see, the condition of the linear regime $u \ll R_0$ requires a very small displacement

$$z_0 \ll (\hbar\omega/\mu)^2 R_0\,, \tag{5}$$

and already a moderate z_0 as in Fig. 1b is sufficient to drive the system out of the linear regime.

We have performed a similar linear analysis for the case where $g_{aa} \neq g_{ab} \neq g_{bb}$, but the relative difference between the coupling constants is small. Also in this case the source S_- mostly generates oscillations of the condensates relative to each other at a single frequency $\Omega' \ll \omega$. For a relative difference between the coupling constants much smaller than $(\hbar\omega/\mu)^2$, the frequency Ω' coincides with the soft-mode frequency Ω found above. Otherwise the sign of $g_- = g_{aa} + g_{bb} - 2g_{ab}$ becomes important. In particular, for positive $g_- \gg |g_{aa} - g_{bb}|$ already a moderate difference between the coupling constants strongly increases the frequency Ω' compared to Ω. In this case we obtain undamped oscillations at $\Omega' \approx (g_-/g_{aa})^{1/2}\omega$. For $g_- < 0$, already in the $z_0 = 0$ case, a breathing mode in which the two condensates oscillate out of phase becomes unstable, and the system evolves far from the initial state. Note that for a small difference between the coupling constants the condition $g_- < 0$ is equivalent to the criterion of spatial separation of the condensates in the homogeneous case, $g_{aa}g_{bb} < g_{ab}^2$ [7,8].

We now turn to the large z_0 regime (Fig. 1b) where we find a strong damping of the oscillations of the mean separation between the condensates, $u(t)$. In order to prove the key role of nonlinearity in this regime, we first attempt a linear model assuming that the densities $|\phi_{\varepsilon'}|^2$ inside the square brackets of Eq. (1) are not evolving:

$$\sum_{\varepsilon'} N_{\varepsilon'} g_{\varepsilon\varepsilon'} |\phi_{\varepsilon'}|^2 \to N g |\phi_0|^2. \tag{6}$$

In contrast to the analysis which led to Eq. (4), the displacement z_0 is now explicitly included in the Hamiltonian through the terms $\pm m\omega^2 z z_0/2$ in $U_{a,b}$, and the number of populated oscillation modes depends on z_0. However, for the parameters in Fig. 1b we find that only a few modes are populated, and the interference between them cannot account for the damping found numerically (dotted versus solid curve in Fig. 1b).

We argue that the damping in our calculations mostly originates from nonlinearity of the system, which increases the number and amplitude of populated oscillation modes and provides an interaction between them. As a result, the evolution of the condensate wave functions ϕ_a and ϕ_b becomes chaotic. This can be seen from Fig. 2 where we compare the spectral density $R_n(\nu) = |T^{-1}\int_0^T dt\, n(\mathbf{0}, t)\exp(i\nu t)|^2$ of the density at the origin $n(\mathbf{0}, t)$ with an identically defined spectral density $R_u(\nu)$ of $u(t)$ for the parameters in Fig. 1b and $T = 110/\omega$. The function $R_n(\nu)$ has a smooth envelope at large ν, with peaks corresponding to the islands of regular motion. On the contrary, $R_u(\nu)$ exhibits pronounced peaks at ν of order ω, without any smooth background. This picture provides a clear signature of stochastization in the system [13] and prompts us to represent each of the condensate wave functions in Eq. (1) as a superposition of two constituents: (i) a slowly oscillating regular part conserving the phase coherence properties and (ii) a composition of high-energy excitations characterized by stochastic motion. Only the slow constituent contributes to such macroscopic quantities as $u(t)$, since the contribution of the fast stochastic part is averaged out.

Our analysis is consistent with the general statement that for a large population of various oscillation modes the nonlinear interaction between them leads to stochastization in the motion of excitations with sufficiently high energy [13]. This allows us to employ the mechanism of stochastic heating [13] for explaining the damping of oscillations of $u(t)$: The mean-field interaction between the fast stochastic and the slowly oscillating parts leads to energy transfer from the slow to the fast part.

The evolution of the occupation numbers of the modes of the fast stochastic part is governed by kinetic equations [13] and eventually slows down. The rate of energy and particle exchange between the two constituents then reduces. After a sufficiently long time only small linear oscillations of the condensates survive, mostly at the lowest eigenfrequency and the gas sample as a whole could be thought of as being close to a steady state. However, the damping of the remaining oscillations and the ultimate evolution of the fast stochastic part towards the thermal equilibrium require an analysis beyond the mean-field approach. For the parameters in Fig. 1b, using

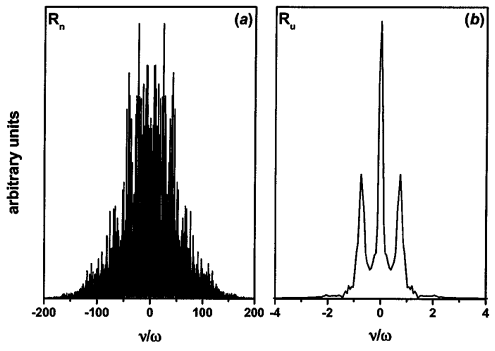

FIG. 2. Spectral densities $R_n(\nu)$ (a) and $R_u(\nu)$ (b) for the parameters in Fig. 1b and $T = 110/\omega$ (see text).

the semiclassical Bogolyubov approach [18] and relying on the conservation of energy and number of particles, we find an equilibrium temperature $T_{\rm eq} \approx 0.6\mu$ and a condensed fraction $\gamma_{a,b} \approx 0.9$, for $N = 5 \times 10^5$.

The last set of our calculations relates to the recent JILA experiment [14] where the evolution of a two-component ^{87}Rb condensate has been investigated. In the conditions of this experiment we solved numerically Eq. (1) by taking $a_{ab} = 55$ Å and the ratio g_{aa}:g_{ab}:$g_{bb} = 1.03$:1:0.97. We also explicitly included in these equations the 22 ms expansion of the clouds after switching off the trapping potential. The results of our calculations are presented in Fig. 3. As in Fig. 1b, we find a strong damping of the oscillations of the mean separation between the condensates, $u(t)$. Our numerical results are in fair agreement with the experimental data, although the damping in the experiment is somewhat larger. We extended the calculations to twice the maximum experimental time and found small oscillations which remain undamped on this time scale.

Our data for the JILA experiment [14] can be analyzed along the same lines as the results in Fig. 1b, with a damping originating from stochastization in the evolution of the condensate wave functions. The equilibrium temperature is close to μ, corresponding to condensed fractions $\gamma_a \approx \gamma_b \approx 0.9$. The large value of the condensed fraction explains why phase coherence between the a and b components could be observed even after the damping of the motion of $u(t)$ [15]. The damping time of the small remaining oscillations, estimated along the lines of [19], will be of order 1 s.

We believe that the stochastic regime identified from our calculations is promising for investigating the loss of phase coherence and the formation of a new thermal component in initially purely Bose-condensed gas samples. An interesting possibility concerns the observation of a continuous change in the phase coherence between the a and b components with increasing the trap displacement and, hence, decreasing the final Bose-condensed fraction.

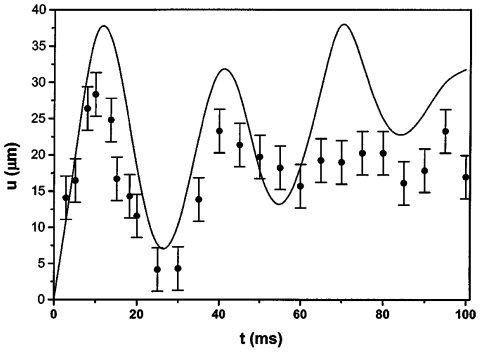

FIG. 3. Mean separation between the condensates in the JILA experiment versus evolution time in the traps, after a 22 ms free expansion. Dots with error bars: JILA experiment. Solid curve: Our numerical calculation.

This work was partially funded by EC (TMR network ERB FMRX-CT96-0002), by the Stichting voor Fundamenteel Onderzoek der Materie (FOM), by the Russian Foundation for Basic Studies, by INTAS, and by NSF under Grant No. PHY94-07194. Laboratoire Kastler Brossel is a unité de recherche de l'Ecole Normale Supérieure et de l'Université Pierre et Marie Curie, associée au CNRS.

[1] M. H. Anderson, J. R. Ensher, M. R. Matthews, C. E. Wieman, and E. A. Cornell, Science **269**, 198 (1995); K. Davis, M.-O. Mewes, M. R. Andrews, N. J. van Druten, D. S. Durfee, D. M. Kurn, and W. Ketterle, Phys. Rev. Lett. **75**, 3969 (1995); C. C. Bradley, C. A. Sackett, and R. G. Hulet, Phys. Rev. Lett. **78**, 985 (1997).

[2] P. A. Ruprecht, M. J. Holland, K. Burnett, and M. Edwards, Phys. Rev. A **51**, 4704 (1995).

[3] Y. Kagan, E. L. Surkov, and G. Shlyapnikov, Phys. Rev. A **54**, R1753 (1996); **55**, R18 (1997).

[4] Y. Castin and R. Dum, Phys. Rev. Lett. **77**, 5315 (1996).

[5] A. Smerzi and S. Fantoni, Phys. Rev. Lett. **78**, 3589 (1997).

[6] M. J. Holland, D. S. Jin, M. L. Chiofalo, and J. Cooper, Phys. Rev. Lett. **78**, 3801 (1997).

[7] W. B. Colson and A. Fetter, J. Low Temp. Phys. **33**, 231 (1978).

[8] E. Goldstein and P. Meystre, Phys. Rev. A **55**, 2935 (1997).

[9] T.-L. Ho and V. B. Shenoy, Phys. Rev. Lett. **77**, 3276 (1996); B. D. Esry, C. H. Greene, J. P. Burke, and J. L. Bohn, Phys. Rev. Lett. **78**, 3594 (1997); C. K. Law, H. Pu, N. P. Bigelow, and J. H. Eberly, Phys. Rev. Lett. **79**, 3105 (1997); H. Pu and N. P. Bigelow, Phys. Rev. Lett. **80**, 1130 (1998).

[10] H. Pu and N. P. Bigelow, Phys. Rev. Lett. **80**, 1134 (1998).

[11] E. Fermi, J. Pasta, and S. Ulam, in *Collected Papers of Enrico Fermi* (Accademia Nazionale dei Lincei and University of Chicago, Roma, 1965), Vol. II, p. 978.

[12] F. M. Izrailev and B. V. Chirikov, Soviet Phys. Dokl. **11**, 30 (1966).

[13] R. Z. Sagdeev, D. A. Usikov, and G. M. Zaslavsky, *Nonlinear Physics: From the Pendulum to Turbulence and Chaos*, in Contemporary Concepts in Physics (Harwood Academic, Chur, New York, 1988).

[14] D. S. Hall, M. R. Matthews, J. R. Ensher, C. E. Wieman, and E. A. Cornell, Phys. Rev. Lett. **81**, 1539 (1998).

[15] D. S. Hall, M. R. Matthews, C. E. Wieman, and E. A. Cornell, Phys. Rev. Lett. **81**, 1543 (1998).

[16] We solve Eq. (1) numerically, using cylindrical symmetry, on a finite grid with a splitting technique. Numerical accuracy is tested by changing the grid size and checking energy conservation ($\delta E/E \leq 10^{-5}$ for $\omega t = 100$).

[17] V. V. Goldman, I. F. Silvera, and A. J. Leggett, Phys. Rev. B **24**, 2870 (1981); D. A. Huse and E. D. Siggia, J. Low Temp. Phys. **46**, 137 (1982).

[18] F. Dalfovo, S. Giorgini, L. Pitaevskii, and S. Stringari, Rev. Mod. Phys. (to be published).

[19] P. O. Fedichev, G. V. Shlyapnikov, and J. T. M. Walraven, Phys. Rev. Lett. **80**, 2269 (1998), and references therein.

Eur. Phys. J. D **8**, 319–332 (2000)

THE EUROPEAN PHYSICAL JOURNAL D

EDP Sciences
© Società Italiana di Fisica
Springer-Verlag 2000

Binary mixtures of Bose-Einstein condensates: Phase dynamics and spatial dynamics

A. Sinatra and Y. Castin[a]

Laboratoire Kastler Brossel[b], 24 rue Lhomond, 75231 Paris Cedex 5, France

Received 23 April 1999 and Received in final form 21 September 1999

Abstract. We investigate the relative phase coherence properties and the occurrence of demixing instabilities for two mutually interacting and time evolving Bose-Einstein condensates in traps. Our treatment naturally includes the additional decoherence effect due to fluctuations in the total number of particles. Analytical results are presented for the breathe-together solution, an extension of previously known scaling solution to the case of a binary mixture of condensates. When the three coupling constants describing the elastic interactions among the atoms in the two states are close to each other, a dramatic increase of the phase coherence time is predicted. Numerical results are presented for the parameters of the recent JILA experiments.

PACS. 03.75.Fi Phase coherent atomic ensembles; quantum condensation phenomena – 05.30.Jp Boson systems

1 Introduction

Since the recent experimental observation of Bose-Einstein condensation in dilute atomic gases [1], much interest has been raised about the coherence properties of the condensates. Considerable attention has been devoted to the matter of the relative phase between two condensates: how this phase manifests itself in an interference experiment [2,3], how it can be established by measurement [4,5], and how it evolves in presence of atomic interactions [5–7] and in presence of particle losses [8].

As it was proved in recent experiments performed at JILA, binary mixtures of condensates represent an ideal system to study the phase coherence properties of Bose-Einstein condensates [9]. In these experiments two condensates in two different internal atomic states are created with a well-defined relative phase. After a time τ during which the condensates evolve in the trapping potentials, one mixes coherently the two internal atomic states which makes the two condensates interfere; from the spatial interference pattern one gets the relative phase of the two condensates. By repeating the whole experimental process, one has access to the distribution of the relative phase after an evolution time τ, so that one can investigate phase decoherence as function of time.

The interaction between the two condensates in the JILA experiment gives rise to a rich spatial separation dynamics between the two condensates [10], which complicates the theoretical study of the relative phase dynamics. As a consequence previous theoretical treatments of the phase decoherence processes, dealing essentially with steady state condensates, as in [11], cannot *a priori* be applied to the experimental situation.

A treatment of the phase coherence of two interacting, non stationary, condensates can be found in [12], with two important differences as compared to the present situation of interest: (1) in [12] the condensates are subject to a continuous coherent coupling of amplitude Λ; results are obtained from a perturbative expansion in powers of $1/\Lambda$ and cannot be simply extended to the present $\Lambda = 0$ case; (2) in [12] all the coupling constants $g_{\rm aa}, g_{\rm ab}, g_{\rm bb}$ between the two internal atomic states a and b are assumed to be equal.

In this paper we propose a formalism to study the relative phase dynamics of interacting and dynamically evolving Bose-Einstein condensates initially at zero temperature.

We present the general method in Section 2. It consists in expanding the initial state on Fock states, and in evolving each Fock state in the Hartree-Fock approximation. We determine the time dependence of the phase collapse for a binary mixture of condensates, due to (1) fluctuations in the relative number of particles between the condensates, intrinsic to the initial state with well-defined relative phase, and (2) fluctuations in the total number of particles. In the next two sections we apply this general formalism to two limiting cases that can be treated analytically.

The first case, in Section 3, considers a particular solution of the non-linear Schrödinger equations for the condensates wavefunctions; in this solution the

[a] e-mail: yvan.castin@lkb.ens.fr
[b] Unité de recherche de l'École Normale Supérieure et de l'Université Pierre et Marie Curie, associée au CNRS.

two condensates remain spatially superimposed as they breathe in phase, provided that dynamical stability conditions (that we determine) are satisfied. We find that phase decoherence can be highly reduced with respect to non mutually interacting condensates when the three coupling constants g_{aa}, g_{ab}, g_{bb} between atoms in the two internal states a, b are close to each other.

In Section 4, we therefore study in a more general case (not restricted to the breathe-together solution) the dynamics of the relative phase for a mixture of condensates for close coupling constants. Our treatment requires also in this case the absence of demixing instability, a point that we discuss in detail.

Finally we discuss the case of the JILA experiment in Section 5. This case, that corresponds to close coupling constants in a regime of demixing instability, is more difficult to analyze. The predicted phase collapse time depends on the fluctuations of the total number of particles; it is on the order of 0.4 s for Gaussian fluctuations of 8%.

2 General method

In this section, we introduce a gedanken experiment to characterize phase coherence between two condensates: the relevant quantity is the interference term $\langle \hat{\psi_b}^\dagger(\mathbf{r},t)\hat{\psi}_a(\mathbf{r},t)\rangle$ between the atomic fields of the two condensates a and b. Subsequently we express this interference term in the Hartree-Fock approximation, assuming an initially well-defined relative phase between the condensates. After a further approximation on the modulus and the phase of the condensate wavefunctions, we determine the decay with time of the interference term due to atomic interactions; we arrive at the simple results equation (18) for a fixed total number of particles and equation (22) for Gaussian fluctuations in the total number of particles.

2.1 Considered gedanken experiment

The experimental procedure we consider to measure the phase coherence is inspired by recent experiments at JILA [9]. A condensate is first created in a trap in some internal atomic state a; the corresponding condensate wavefunction in the zero temperature mean-field approximation is ϕ_0, a stationary solution of the Gross-Pitaevskii equation:

$$\mu\phi_0 = -\frac{\hbar^2}{2m}\Delta\phi_0 + [U_a(\mathbf{r}) + N g_{aa}|\phi_0|^2]\phi_0. \qquad (1)$$

In this equation N is the number of particles, g_{aa} is the coupling constant between the atoms in the internal state a, related to the scattering length a_{aa} by $g_{aa} = 4\pi\hbar^2 a_{aa}/m$; U_a is the trapping potential seen by the atoms in a and μ is the chemical potential. Note that we have normalized ϕ_0 to unity.

At time $t = 0$ a resonant electromagnetic pulse transfers in a coherent way part of the atoms to a second internal state b. The state of the system is then given in the Hartree-Fock approximation by

$$|\Psi(0)\rangle = [c_a|a,\phi_0\rangle + c_b|b,\phi_0\rangle]^N \qquad (2)$$

with $|c_a|^2 + |c_b|^2 = 1$. As we assume a Rabi coupling between a and b much more intense than $\mu/\hbar$ the atomic interactions have a negligible effect during the transfer so that the amplitudes $c_{a,b}$ depend only on the pulse parameters, not on the number N of particles. In the N-particle state equation (2) the condensate in state a and the condensate in state b have a well-defined relative phase; we therefore call this state *a phase state*, in analogy with [13].

The two condensates evolve freely in their trapping potentials during the time τ. During this evolution we assume that there is no coherent coupling between a and b to lock the relative phase of the condensates; in particular the only considered interactions between the particles are elastic, of the type $a+a \to a+a$ (coupling constant $g_{aa} > 0$), $a+b \to a+b$ (coupling constant $g_{ab} > 0$), $b+b \to b+b$ (coupling constant $g_{bb} > 0$). We therefore expect a collapse of the relative phase for sufficiently long times, due to atomic interactions.

To test the phase coherence at time τ, a second electromagnetic pulse is applied to mix the internal states a and b. We assume that this second pulse is a $\pi/2$ pulse, so that the atomic field operators in the Heisenberg picture are transformed according to

$$\hat{\psi}_a(\tau^+) = \frac{e^{-i\delta}}{\sqrt{2}}\hat{\psi}_a(\tau^-) + \frac{e^{i\delta}}{\sqrt{2}}\hat{\psi}_b(\tau^-), \qquad (3)$$

$$\hat{\psi}_b(\tau^+) = -\frac{e^{-i\delta}}{\sqrt{2}}\hat{\psi}_a(\tau^-) + \frac{e^{i\delta}}{\sqrt{2}}\hat{\psi}_b(\tau^-), \qquad (4)$$

δ being an adjustable phase. One then measures the mean spatial density ρ_a in the internal state a, averaging over many realizations of the whole experiment:

$$\rho_a = \langle \hat{\psi}_a^\dagger(\tau^+)\hat{\psi}_a(\tau^+)\rangle. \qquad (5)$$

The signature of a phase coherence between the two condensates at time τ is the dependence of the mean density ρ_a on the adjustable phase δ. More precisely we define the contrast

$$C = \frac{\max_\delta \rho_a - \min_\delta \rho_a}{\max_\delta \rho_a + \min_\delta \rho_a} = \frac{2|\langle \hat{\psi}_b^\dagger(\tau^-)\hat{\psi}_a(\tau^-)\rangle|}{\sum_{\varepsilon=a,b}\langle \hat{\psi}_\varepsilon^\dagger(\tau^-)\hat{\psi}_\varepsilon(\tau^-)\rangle}\cdot \qquad (6)$$

The contrast involves the interference term $\langle \hat{\psi}_b^\dagger(\tau^-)\hat{\psi}_a(\tau^-)\rangle$ which carries the information about the relative phase between the two condensates.

2.2 Approximate evolution of an initial phase state

The time evolution in the phase state representation is not simple, as an initial phase state is mapped onto a superposition of phase states. It is more convenient to introduce Fock states, that is states with a well-defined number of particles in a and in b, these numbers being preserved by the time evolution.

We therefore expand the initial phase state over the Fock states:

$$|\Psi(0)\rangle = \sum_{N_\mathrm{a}=0}^{N} \left(\frac{N!}{N_\mathrm{a}!N_\mathrm{b}!}\right)^{1/2} c_\mathrm{a}^{N_\mathrm{a}} c_\mathrm{b}^{N_\mathrm{b}} |N_\mathrm{a}:\phi_0, N_\mathrm{b}:\phi_0\rangle \quad (7)$$

where we set $N_\mathrm{b} = N - N_\mathrm{a}$.

By calculating the evolution of each Fock state in the simplest Hartree-Fock approximation, we get the following mapping:

$$|N_\mathrm{a}:\phi_0, N_\mathrm{b}:\phi_0\rangle \rightarrow \mathrm{e}^{-\mathrm{i}A(N_\mathrm{a},N_\mathrm{b};t)/\hbar} |N_\mathrm{a}:\phi_\mathrm{a}(N_\mathrm{a},N_\mathrm{b};t), N_\mathrm{b}:\phi_\mathrm{b}(N_\mathrm{a},N_\mathrm{b};t)\rangle \quad (8)$$

where the condensates wavefunctions evolve according to the coupled Gross-Pitaevskii equations:

$$\mathrm{i}\hbar\partial_t\phi_\varepsilon = \Big[-\frac{\hbar^2}{2m}\Delta + U_\varepsilon(\mathbf{r}) + N_\varepsilon g_{\varepsilon\varepsilon}|\phi_\varepsilon|^2 + N_{\varepsilon'} g_{\varepsilon\varepsilon'}|\phi_{\varepsilon'}|^2\Big]\phi_\varepsilon \quad (9)$$

(where $\varepsilon' \neq \varepsilon$) with the initial conditions

$$\phi_\mathrm{a}(0) = \phi_\mathrm{b}(0) = \phi_0 \quad (10)$$

and where the time dependent phase factor A solves:

$$\frac{\mathrm{d}}{\mathrm{d}t}A(N_\mathrm{a},N_\mathrm{b};t) = -\frac{1}{2}N_\mathrm{a}^2 g_\mathrm{aa}\int \mathrm{d}\mathbf{r}\ |\phi_\mathrm{a}|^4 - \frac{1}{2}N_\mathrm{b}^2 g_\mathrm{bb}\int \mathrm{d}\mathbf{r}\ |\phi_\mathrm{b}|^4 - N_\mathrm{a}N_\mathrm{b}g_\mathrm{ab}\int \mathrm{d}\mathbf{r}\ |\phi_\mathrm{a}|^2|\phi_\mathrm{b}|^2. \quad (11)$$

Equation (11) is derived in Appendix A. Physically $\mathrm{d}A/\mathrm{d}t$ is simply the opposite of the mean interaction energy between the particles in the Fock state. In the case where the Fock state is a steady state, the need for the phase factor A additional to the Gross-Pitaevskii equation is obvious; the exact phase factor is indeed $\mathrm{e}^{-\mathrm{i}Et/\hbar}$, where E is the energy of the Fock state, whereas the phase factor obtained from the Gross-Pitaevskii evolution is $\mathrm{e}^{-\mathrm{i}(N_\mathrm{a}\mu_\mathrm{a}+N_\mathrm{b}\mu_\mathrm{b})t/\hbar}$, where $\mu_\mathrm{a,b}$ is the chemical potential in a, b.

Using the evolution of the Fock states, and other approximations valid in the limit of large numbers of particles (as detailed in the Appendix B) we obtain for the interference term between the condensates with a well-defined total number N of particles:

$$\langle\hat\psi_\mathrm{b}^\dagger\hat\psi_\mathrm{a}\rangle_N = c_\mathrm{a}c_\mathrm{b}^* \sum_{N_\mathrm{a}=1}^{N} \frac{N!}{(N_\mathrm{a}-1)!N_\mathrm{b}!}|c_\mathrm{a}|^{2(N_\mathrm{a}-1)}|c_\mathrm{b}|^{2N_\mathrm{b}} \times \phi_\mathrm{a}(N_\mathrm{a},N_\mathrm{b})\phi_\mathrm{b}^*(N_\mathrm{a}-1,N_\mathrm{b}+1) \quad (12)$$

where $N_\mathrm{b} = N - N_\mathrm{a}$. The exact computation of this sum remains a formidable task, since it involves in principle the solution of N different sets of two coupled Gross-Pitaevskii equations. We introduce some simplifying approximations in the next subsection.

2.3 Phase collapse for a mixture

In the present experiments the total number of particles fluctuates from one realization to the other, so that equation (12) has to be averaged over N. We assume that the fluctuations of the total number of particles have a standard deviation ΔN much smaller than the mean total particle number $\bar N$. As the distributions of the number of particles in a and b in a phase state have also a width much smaller than $\bar N$ (typically on the order of $\bar N^{1/2}$) we can assume than the number of particles in a and in b are very close to their average values $\bar N_\varepsilon = |c_\varepsilon|^2\bar N$. We now take advantage of this property to simplify equation (12).

We split the condensate wavefunctions in a modulus and a phase θ_ε; we assume that the variation of the modulus can be neglected over the distribution of $N_\mathrm{a,b}$, and that the variation of the phase can be approximated by a linear expansion around $\bar N_\varepsilon$. We thus get the approximate form for the condensate wavefunctions:

$$\phi_\varepsilon(N_\mathrm{a},N_\mathrm{b}) \simeq \bar\phi_\varepsilon \exp\left[\mathrm{i}\sum_{\varepsilon'=\mathrm{a,b}} (N_{\varepsilon'} - \bar N_{\varepsilon'})(\partial_{N_{\varepsilon'}}\theta_\varepsilon)(\bar N_\mathrm{a},\bar N_b)\right] \quad (13)$$

where $\bar\phi_\varepsilon = \phi_\varepsilon(N_\mathrm{a} = \bar N_\mathrm{a}, N_\mathrm{b} = \bar N_\mathrm{b})$.

To this level of approximation the mean densities in the internal states a, b are simply given by

$$\langle\hat\psi_\varepsilon^\dagger\hat\psi_\varepsilon\rangle_N \simeq \bar N_\varepsilon|\bar\phi_\varepsilon|^2 \quad (14)$$

whereas the interference term between the condensates is:

$$\langle\hat\psi_\mathrm{b}^\dagger\hat\psi_\mathrm{a}\rangle_N \simeq \bar N c_\mathrm{a}c_\mathrm{b}^*\bar\phi_\mathrm{a}\bar\phi_\mathrm{b}{}^* \exp\big\{\mathrm{i}[(N-\bar N)\chi_\mathrm{s} - \bar N(|c_\mathrm{a}|^2 - |c_\mathrm{b}|^2)\chi_\mathrm{d}]\big\}\, e^{\mathrm{i}\chi_0} \times \left[|c_\mathrm{a}|^2\mathrm{e}^{\mathrm{i}\chi_\mathrm{d}} + |c_\mathrm{b}|^2\mathrm{e}^{-\mathrm{i}\chi_\mathrm{d}}\right]^{N-1}. \quad (15)$$

In this last expression we have introduced the time and position dependent quantities

$$\chi_\mathrm{s} = \frac{1}{2}\left[(\partial_{N_\mathrm{a}} + \partial_{N_\mathrm{b}})(\theta_\mathrm{a} - \theta_\mathrm{b})\right](\bar N_\mathrm{a},\bar N_\mathrm{b}) \quad (16)$$

$$\chi_\mathrm{d} = \frac{1}{2}\left[(\partial_{N_\mathrm{a}} - \partial_{N_\mathrm{b}})(\theta_\mathrm{a} - \theta_\mathrm{b})\right](\bar N_\mathrm{a},\bar N_\mathrm{b}). \quad (17)$$

The phase $\chi_0 = (1/2)(\partial_{N_\mathrm{a}} - \partial_{N_\mathrm{b}})(\theta_\mathrm{a} + \theta_\mathrm{b})(\bar N_\mathrm{a},\bar N_\mathrm{b})$ in equation (15) is less important as contrarily to $\chi_\mathrm{s,d}$ it is not multiplied by N. At time $t = 0$ all the χ's vanish. In the large N limit, the χ's are expected to be on the order of $\bar\mu t/\hbar\bar N$.

The factor responsible for the collapse of the contrast at a fixed value of N is the last line of equation (15), the exponential factors in the first two lines being of modulus one. As N is large a small variation of χ_d from its initial value $\chi_\mathrm{d}(t = 0) = 0$ is sufficient to destroy the interference term. Over the range of the collapse we can therefore expand the exponential of $\pm\mathrm{i}\chi_\mathrm{d}$ to second order in χ_d, obtaining:

$$\langle\hat\psi_\mathrm{b}^\dagger\hat\psi_\mathrm{a}\rangle_N \simeq \bar N c_\mathrm{a}c_\mathrm{b}^*\bar\phi_\mathrm{a}\bar\phi_\mathrm{b}{}^* \exp\big\{\mathrm{i}(N-\bar N) \times[\chi_\mathrm{s} + (|c_\mathrm{a}|^2 - |c_\mathrm{b}|^2)\chi_\mathrm{d}]\big\}\ \exp\left[-2N\chi_\mathrm{d}^2|c_\mathrm{a}|^2|c_\mathrm{b}|^2\right]. \quad (18)$$

The second exponential factor in this expression allows to determine the collapse time $t_\mathrm{c}^\mathrm{fix}$ for a fixed number of particles, through the condition

$$4N|c_\mathrm{a}|^2|c_\mathrm{b}|^2\chi_\mathrm{d}^2(t_\mathrm{c}^\mathrm{fix}) \simeq 1 \quad (19)$$

such that the modulus of the interference term is reduced by a factor $\mathrm{e}^{-1/2}$ from its initial value. The first exponential factor in equation (18) accounts for the phase difference of the interference term for N particles and $\bar{N}$ particles, as shown by the identity:

$$\chi_{\mathrm{s}} + (|c_{\mathrm{a}}|^2 - |c_{\mathrm{b}}|^2)\chi_{\mathrm{d}} = \frac{\mathrm{d}}{\mathrm{d}N}\left[(\theta_{\mathrm{a}} - \theta_{\mathrm{b}})(N|c_{\mathrm{a}}|^2, N|c_{\mathrm{b}}|^2)\right]_{N=\bar{N}}. \quad (20)$$

This phase factor can also be understood as a consequence of a drift of the relative phase between two condensates at a velocity $v(N)$ depending on the total number of particles:

$$v(N) = \partial_t(\bar{\theta_{\mathrm{a}}} - \bar{\theta_{\mathrm{b}}}) + (N - \bar{N})\partial_t\left[\chi_{\mathrm{s}} + (|c_{\mathrm{a}}|^2 - |c_{\mathrm{b}}|^2)\chi_{\mathrm{d}}\right]. \quad (21)$$

As we shall see in the next subsection fluctuations in the total number of particles N result in fluctuations of this phase factor, providing an additional source of smearing of the phase, as already emphasized in [8].

2.4 Effect of fluctuations in the total number of particles

The effect on the phase collapse of fluctuations in the total number of particles is obtained by averaging equation (18) over the probability distribution of N. To be specific we assume a Gaussian distribution for N. The average can be calculated by replacing the discrete sum over N by an integral; we neglect a term proportional to $(\Delta N \chi_{\mathrm{d}}^2)^2$ scaling as $(\Delta N/\bar{N})^2$ at the collapse time $t_{\mathrm{c}}^{\mathrm{fix}}$; the resulting modulus of the interference term reads:

$$|\langle\hat{\psi}_{\mathrm{b}}^\dagger\hat{\psi}_{\mathrm{a}}\rangle^{\mathrm{Gauss}}| \simeq \bar{N}|c_{\mathrm{a}}c_{\mathrm{b}}^*\bar{\phi}_{\mathrm{a}}\bar{\phi_{\mathrm{b}}}^*| \exp\left\{-\frac{1}{2}(\Delta N)^2 \times \left[\frac{\mathrm{d}}{\mathrm{d}N}(\theta_{\mathrm{a}} - \theta_{\mathrm{b}})\right]_{N=\bar{N}}^2\right\} \exp\left[-2\bar{N}\chi_{\mathrm{d}}^2|c_{\mathrm{a}}|^2|c_{\mathrm{b}}|^2\right]. \quad (22)$$

The first exponential factor in this expression represents the damping of the interference term due to fluctuations in the total number of particles; the second exponential factor, already present in equation (18), gives the damping due to fluctuations in the relative number of particles between a and b, as can be seen in equation (17).

2.5 The steady state case and comparison with previous treatments

Our treatment can be easily adapted to the case of two initially different condensate wavefunctions $\phi_{\mathrm{a}}(t=0)$ and $\phi_{\mathrm{b}}(t=0)$. In the particular case of condensates in stationary states, the formulas for the interference term $\langle\hat{\psi_{\mathrm{b}}}^\dagger\hat{\psi}_{\mathrm{a}}\rangle$ remain the same, and one has $\theta_\varepsilon = -\mu_\varepsilon(N_{\mathrm{a}}, N_{\mathrm{b}})t/\hbar$. We can give in this case the explicit expression for the collapse time $t_{\mathrm{c}}^{\mathrm{fix}}$ defined in equation (19), assuming a fixed total number of atoms $N = \bar{N}$:

$$t_{\mathrm{c}}^{\mathrm{fix}} = \hbar\left[\bar{N}^{1/2}|c_{\mathrm{a}}c_{\mathrm{b}}||(\partial_{N_{\mathrm{a}}} - \partial_{N_{\mathrm{b}}})(\mu_{\mathrm{a}} - \mu_{\mathrm{b}})|\right]^{-1}. \quad (23)$$

For the particular case of non mutually interacting steady state condensates μ_ε depends on N_ε only, so that the partial derivatives in the denominator of equation (23) reduce to $\mathrm{d}\mu_{\mathrm{a}}/\mathrm{d}N_{\mathrm{a}} + \mathrm{d}\mu_{\mathrm{b}}/\mathrm{d}N_{\mathrm{b}}$, and we recover the results of [5,8].

From equation (23) we see that what matters physically is the change in the *difference* between the chemical potentials of the two condensates when one transfers one particle from one condensate to the other. For this reason the case of mutually interacting condensates with close coupling constants can lead to much larger t_{c}'s as compared to the case of non-mutually interacting condensates. For example, in the case of the JILA experiment [9], assuming that the condensates are in steady state, one finds $t_{\mathrm{c}}^{\mathrm{fix}} \simeq 3.1$ s; by ignoring the interaction between the condensates (setting by hand $g_{\mathrm{ab}} = 0$) one obtains the much shorter time $\simeq 0.25$ s. The JILA case is analyzed in more detail in our section 5.

A similar prediction on the reduction of decoherence due to mutual interactions between the two condensates, in trapping potentials with different curvatures, was obtained numerically in [11].

The treatment in [7] considers the absolute phase dynamics of a single condensate (in our formalism $c_{\mathrm{b}} = 0$) in a coherent state. When the condensate wavefunction is stationary one has simply $\theta_{\mathrm{a}} = -\mu_{\mathrm{a}}t/\hbar$. From equation (22) with $\Delta N = \bar{N}^{1/2}$ (as the coherent state has a Poisson distribution for N) we then find that the phase of the condensate order parameter is damped as $\exp[-\bar{N}(\mathrm{d}\mu_{\mathrm{a}}/\mathrm{d}N)^2t^2/2\hbar^2]$ as in [7].

3 Application to the breathe-together solution

In this section we consider a particular solution of the coupled Gross-Pitaevskii equations for which an approximate scaling solution is available when the chemical potential is much larger than the energy spacing between trap levels, the so-called Thomas-Fermi regime. We first give the set of parameters for which this solution, that we call the breathe-together solution, exists. We then linearize the Gross-Pitaevskii equations around this solution to determine its stability with respect to demixing and to obtain the phase coherence dynamics.

3.1 Description of the breathe-together solution

We now determine the set of parameters such that the coupled Gross-Pitaevskii equations (Eq. (9)) for

$$N_\varepsilon = \bar{N}_\varepsilon \equiv \bar{N}|c_\varepsilon|^2 \quad (24)$$

have a solution with $\bar{\phi}_{\rm a}(\mathbf{r},t) = \bar{\phi}_{\rm b}(\mathbf{r},t) \equiv \bar{\phi}(\mathbf{r},t)$. The general condition is that the effective potential, that is the trapping potential plus the mean field potential, seen by the atoms in a and in b should be the same. This condition is satisfied when:

$$U_{\rm a}(\mathbf{r}) = U_b(\mathbf{r}) \equiv U(\mathbf{r}) \tag{25}$$

$$\bar{N}_{\rm a} g_{\rm aa} + \bar{N}_{\rm b} g_{\rm ab} = \bar{N}_{\rm b} g_{\rm bb} + \bar{N}_{\rm a} g_{\rm ab} \equiv \bar{N} g. \tag{26}$$

The resulting Gross-Pitaevskii equation for the condensate wavefunction $\bar{\phi}$ common to a and b is then:

$$\mathrm{i}\hbar\partial_t \bar{\phi} = \left[-\frac{\hbar^2}{2m}\Delta + U(\mathbf{r}) + \bar{N} g |\bar{\phi}|^2 \right] \bar{\phi} \tag{27}$$

with the initial condition $\bar{\phi}(\mathbf{r},0) = \phi_0[N=\bar{N}](\mathbf{r}) \equiv \bar{\phi}_0$, where ϕ_0 is defined in equation (1).

By rewriting equation (26) as $\bar{N}_{\rm a}/\bar{N}_{\rm b} = (g_{\rm bb} - g_{\rm ab})/(g_{\rm aa} - g_{\rm ab})$ we see that this equality can be satisfied by choosing properly the mixing angle between a and b provided that

$$g_{\rm ab} < g_{\rm aa}, g_{\rm bb} \quad \text{or} \quad g_{\rm ab} > g_{\rm aa}, g_{\rm bb}. \tag{28}$$

As we shall see below, only the first case is relevant here, since the second case corresponds to an unstable solution with respect to demixing between a and b.

3.2 Linearization around the breathe-together solution

The strategy to obtain the quantities $\chi_{\rm s,d}$ relevant for the phase dynamics is to calculate in the linear approximation the deviations $\delta\phi_\varepsilon$ between the breathe-together solution $\bar{\phi}$ and neighboring solutions ϕ_ε for N_ε slightly different from $\bar{N}_\varepsilon$:

$$\delta\phi_\varepsilon \equiv \phi_\varepsilon(\bar{N}_{\rm a} + \delta N_{\rm a}, \bar{N}_{\rm b} + \delta N_{\rm b}) - \phi_\varepsilon(\bar{N}_{\rm a}, \bar{N}_{\rm b}). \tag{29}$$

From the definitions equations (16, 17) one indeed realizes that in the limit of small $\delta N_{\rm a}$:

$$\chi_{\rm s} = \left[\frac{\delta\theta_{\rm a} - \delta\theta_{\rm b}}{2\delta N_{\rm a}} \right]_{\delta N_{\rm b} = \delta N_{\rm a}} \tag{30}$$

$$\chi_{\rm d} = \left[\frac{\delta\theta_{\rm a} - \delta\theta_{\rm b}}{2\delta N_{\rm a}} \right]_{\delta N_{\rm b} = -\delta N_{\rm a}} \tag{31}$$

where $\delta\theta_{\rm a,b}$ are the deviations of the phase of the neighboring solutions ϕ_ε from the phase of the breathe-together solution:

$$\delta\theta_{\rm a} - \delta\theta_{\rm b} = \mathrm{Im}\left[\frac{\delta\phi_{\rm a}}{\bar{\phi}} - \frac{\delta\phi_{\rm b}}{\bar{\phi}} \right]. \tag{32}$$

It turns out that homogeneous rather than inhomogeneous linear equations can be obtained for the deviations $\delta\phi_\epsilon$ by introducing the quantities:

$$\delta\varphi_\varepsilon \equiv \frac{\delta[\sqrt{N_\varepsilon}\phi_\varepsilon]}{\sqrt{\bar{N}_\varepsilon}} = \frac{\delta N_\varepsilon}{2\bar{N}_\varepsilon}\bar{\phi} + \delta\phi_\varepsilon. \tag{33}$$

Furthermore a partial decoupling occurs for the linear combinations

$$\delta\varphi_{\rm s} \equiv \delta\varphi_{\rm a} + \delta\varphi_{\rm b} \tag{34}$$

$$\delta\varphi_{\rm d} \equiv \delta\varphi_{\rm a} - \delta\varphi_{\rm b}. \tag{35}$$

The sum $\delta\varphi_{\rm s}$ obeys a linear equation involving $\delta\varphi_{\rm d}$ as a source term:

$$\mathrm{i}\hbar\partial_t\delta\varphi_{\rm s} = \left[-\frac{\hbar^2}{2m}\Delta + U + 2\bar{N} g |\bar{\phi}|^2 \right] \delta\varphi_{\rm s} + \bar{N} g \bar{\phi}^2 \delta\varphi_{\rm s}^* + (\bar{N}_{\rm a} g_{\rm aa} - \bar{N}_{\rm b} g_{\rm bb})(|\bar{\phi}|^2 \delta\varphi_{\rm d} + \bar{\phi}^2 \delta\varphi_{\rm d}^*). \tag{36}$$

The part of this equation involving $\delta\varphi_{\rm s}$ is identical to the one obtained for a single condensate with $\bar{N}$ particles and a coupling constant g. The corresponding modes have minimal frequencies on the order of the trap frequency ω for an isotropic harmonic trap [14].

The difference $\delta\varphi_{\rm d}$ obeys the closed equation:

$$\mathrm{i}\hbar\partial_t\delta\varphi_{\rm d} = \left[-\frac{\hbar^2}{2m}\Delta + U + \bar{N} g |\bar{\phi}|^2 \right] \delta\varphi_{\rm d} + \frac{\bar{N}_{\rm a}\bar{N}_{\rm b}}{\bar{N}} (g_{\rm aa} + g_{\rm bb} - 2g_{\rm ab})(|\bar{\phi}|^2 \delta\varphi_{\rm d} + \bar{\phi}^2 \delta\varphi_{\rm d}^*) \tag{37}$$

where we have used the identity:

$$\bar{N}_{\rm b}(g_{\rm bb} - g_{\rm ab}) = \bar{N}_{\rm a}(g_{\rm aa} - g_{\rm ab}) = \frac{\bar{N}_{\rm a}\bar{N}_{\rm b}}{\bar{N}}(g_{\rm aa} + g_{\rm bb} - 2g_{\rm ab}). \tag{38}$$

As shown in [15] minimal eigenfrequencies of this equation can be much smaller than ω; *e.g.* when all the coupling constants are equal, the minimal eigenfrequencies in a harmonic isotropic trap of frequency ω scale as $\hbar\omega^2/\mu \ll \omega$ in the Thomas-Fermi limit.

For the derivation of the χ's it is sufficient to calculate $\delta\varphi_{\rm d}$. The relative phase between the two condensates for the considered neighboring solution with $N_\varepsilon = \bar{N}_\varepsilon + \delta N_\varepsilon$ particles in the state ε is in fact given by:

$$\delta\theta_{\rm a} - \delta\theta_{\rm b} = \frac{1}{2\mathrm{i}}\left[\frac{\delta\varphi_{\rm d}}{\bar{\phi}} - \frac{\delta\varphi_{\rm d}^*}{\bar{\phi}^*} \right]. \tag{39}$$

as can be checked from the definition equation (32).

3.3 Approximate equations of evolution in the Thomas-Fermi limit

In the remaining part of this section we assume an isotropic harmonic trapping potential $U(\mathbf{r}) = m\omega^2 r^2/2$ and we restrict to the Thomas-Fermi limit $\mu \gg \hbar\omega$.

In the Thomas-Fermi limit it is known [16,17] that most of the time dependence of the wavefunction $\bar{\phi}$ can be absorbed by a time dependent gauge and scaling transform; here we apply this transform to both $\bar{\phi}$ and $\delta\varphi_{\rm d}$:

$$\bar{\phi}(\mathbf{r},t) \equiv \frac{\mathrm{e}^{-\mathrm{i}\eta(t)}}{\lambda^{3/2}(t)} \mathrm{e}^{\mathrm{i}mr^2\dot{\lambda}(t)/2\hbar\lambda(t)} \tilde{\bar{\phi}}(\mathbf{r}/\lambda(t), t) \tag{40}$$

$$\delta\varphi_{\rm d}(\mathbf{r},t) = \frac{\mathrm{e}^{-\mathrm{i}\eta(t)}}{\lambda^{3/2}(t)} \mathrm{e}^{\mathrm{i}mr^2\dot{\lambda}(t)/2\hbar\lambda(t)} \delta\tilde{\varphi}_{\rm d}(\mathbf{r}/\lambda(t), t). \tag{41}$$

The scaling factor $\lambda(t)$ solves the second order Newton-type differential equation

$$\ddot{\lambda} = \frac{g}{g_{\rm aa}}\frac{\omega^2}{\lambda^4} - \omega^2\lambda \tag{42}$$

with the initial condition $\lambda(0) = 1, \dot{\lambda}(0) = 0$. The "force" seen by λ in equation (42) derives from the sum of an expelling $1/\lambda^3$ potential due to repulsive interactions between atoms and an attractive λ^2 potential due to the harmonic confinement of the atoms. It leads to periodic oscillations of λ, that is to a periodic breathing of the condensates. We have also introduced a phase factor involving the time dependent function η such that $\dot{\eta} = \bar{\mu}g/(g_{\rm aa}\lambda^3\hbar)$.

In the Appendix C we derive approximate evolution equations for $\tilde{\bar{\phi}}$ and $\delta\tilde{\varphi}_{\rm d}$; we give here only the result. To lowest order in the Thomas-Fermi approximation $\tilde{\bar{\phi}}$ does not evolve and can be approximated by the Thomas-Fermi approximation for $\bar{\phi}_0$:

$$\tilde{\bar{\phi}}(\mathbf{r},t) \simeq \bar{\phi}_0(\mathbf{r}) \simeq \left(\frac{15}{8\pi R_0^3}\right)^{1/2}\left[1 - \frac{r^2}{R_0^2}\right]^{1/2} \tag{43}$$

with a Thomas-Fermi radius $R_0 = \sqrt{2\bar{\mu}/m\omega^2}$. The approximate evolution for $\delta\tilde{\varphi}_{\rm d}$ is conveniently expressed in terms of the real function α and the purely imaginary function β:

$$\alpha = \tilde{\bar{\phi}}^*\,\delta\tilde{\varphi}_{\rm d} + \tilde{\bar{\phi}}\delta\tilde{\varphi}_{\rm d}^* \tag{44}$$

$$\beta = \frac{1}{2}\left[\frac{\delta\tilde{\varphi}_{\rm d}}{\tilde{\bar{\phi}}} - \frac{\delta\tilde{\varphi}_{\rm d}^*}{\tilde{\bar{\phi}}^*}\right]. \tag{45}$$

These functions have a clear physical meaning. The first one α corresponds to the deviation $\delta\rho_{\rm a}/\bar{N}_{\rm a} - \delta\rho_{\rm b}/\bar{N}_{\rm b}$ written in the rescaled frame, $\delta\rho_\varepsilon$ being the deviation of spatial density in the condensate ε from the breathe-together solution. Apart from a factor i the second function β is the deviation of the relative phase equation (39) written in the rescaled frame:

$$(\delta\theta_{\rm a} - \delta\theta_{\rm b})(\mathbf{r},t) = -{\rm i}\beta(\mathbf{r}/\lambda, t). \tag{46}$$

The equations of evolution for α, β are:

$${\rm i}\hbar\partial_t\begin{pmatrix}\alpha\\ \beta\end{pmatrix} = L(t)\begin{pmatrix}\alpha\\ \beta\end{pmatrix} \tag{47}$$

where the operator $L(t)$ in the Thomas-Fermi approximation reads:

$$L(t) = \begin{pmatrix} 0 & -\frac{\hbar^2}{m\lambda^2}\,{\rm div}\left[\bar{\phi_0}^2\,\mathbf{grad}(\cdot)\right] \\ \frac{1}{\lambda^3}\frac{\bar{N}_{\rm a}\bar{N}_{\rm b}}{\bar{N}}(g_{\rm aa}+g_{\rm bb}-2g_{\rm ab}) & 0\end{pmatrix}. \tag{48}$$

The initial conditions for α, β at time $t = 0$ obtained from equations (33, 10) are:

$$\alpha(0) = \left(\frac{\delta N_{\rm a}}{\bar{N}_{\rm a}} - \frac{\delta N_{\rm b}}{\bar{N}_{\rm b}}\right)\bar{\phi_0}^2 \tag{49}$$

$$\beta(0) = 0. \tag{50}$$

3.4 Solution of the Thomas-Fermi evolution equations: stability against demixing

The strategy to determine the time evolution of α, β is (1) to expand the vector $(\alpha(0), \beta(0))$ on eigenmodes of the operator $L(0)$, and (2) to calculate the time evolution of each eigenmode.

3.4.1 Expansion on modes of L(0)

Consider an eigenvector (α, β) of the operator $L(0)$ with the eigenvalue $\hbar\Omega$. For $\Omega \neq 0$ one can express the component β as function of α:

$$\beta = \frac{\alpha}{\hbar\Omega}\frac{\bar{N}_{\rm a}\bar{N}_{\rm b}}{\bar{N}}(g_{\rm aa}+g_{\rm bb}-2g_{\rm ab}) \tag{51}$$

and obtain the eigenvalue problem for α:

$$\Omega^2\alpha = \left(\frac{\bar{N}_{\rm a}\bar{N}_{\rm b}}{\bar{N}^2}\frac{(g_{\rm aa}+g_{\rm bb}-2g_{\rm ab})}{g_{\rm aa}}\right)S[\alpha] \tag{52}$$

where we have introduced the Stringari operator:

$$S[\alpha] \equiv -\frac{\bar{N}g_{\rm aa}}{m}\,{\rm div}[\bar{\phi_0}^2\,\mathbf{grad}\,\alpha]. \tag{53}$$

This operator has been studied in [14]. It is an Hermitian and positive operator, with a spectrum $q\omega^2$, q non negative integer; q is given by

$$q = 2n^2 + 2nl + 3n + l \tag{54}$$

as function of the radial quantum number n and the angular momentum l. This allows the determination of the eigenfrequencies Ω:

$$\Omega_q = \pm\left(\frac{\bar{N}_{\rm a}\bar{N}_{\rm b}}{\bar{N}^2}\frac{(g_{\rm aa}+g_{\rm bb}-2g_{\rm ab})}{g_{\rm aa}}\right)^{1/2} q^{1/2}\omega, \tag{55}$$

with $q > 0$ as we have assumed $\Omega \neq 0$. The case of a vanishing Ω corresponds to the zero energy mode $\alpha_0 = 0, \beta_0 = 1$ of the operator $L(0)$, as it can be checked from a direct calculation.

All the eigenmodes of $L(0)$ have been identified. They do not form a complete family of vectors however. The vector $(\alpha = 1, \beta = 0)$ cannot be expanded on the eigenmodes of $L(0)$. Its first component α is indeed in the kernel of the operator S (as $S[\alpha] = 0$) whereas none of the α_q is in the kernel of S ($S[\alpha_q] = q\omega^2\alpha_q$ is not identically zero) except when α_q is identically zero (for $q = 0$). The family of eigenvectors of $L(0)$ completed by the additional vector $(\alpha = 1, \beta = 0)$ forms a basis. The additional vector is called an anomalous mode, and we set $\alpha_{\rm anom} = 1$, $\beta_{\rm anom} = 0$; the action of $L(0)$ on the anomalous mode gives the zero energy mode times the constant factor $\bar{N}_{\rm a}(g_{\rm aa} - g_{\rm ab})$ [18].

The mode functions α_q of the operator S are given in [14]. It turns out that in the expansion of the initial conditions for α, β equations (49, 50), only the isotropic

eigenmodes of $L(0)$ with $q = 5$ and the anomalous mode are involved:

$$\begin{pmatrix} \alpha(0) \\ \beta(0) \end{pmatrix} = C_5 \left[\begin{pmatrix} \alpha_{q=5} \\ \beta_{q=5} \end{pmatrix} + \begin{pmatrix} \alpha_{q=5} \\ -\beta_{q=5} \end{pmatrix} \right] + C_{\rm anom} \begin{pmatrix} 1 \\ 0 \end{pmatrix}. \tag{56}$$

The isotropic eigenmode of S with $q = 5$, the so-called breathing mode, reads

$$\alpha_{q=5}(\mathbf{r}) = \left[\frac{r^2}{R_0^2} - \frac{3}{5} \right]. \tag{57}$$

By equation (51) we have $\beta_{q=5} = \alpha_{q=5} \bar{N}_{\rm a} \bar{N}_{\rm b} (g_{\rm aa} + g_{\rm bb} - 2g_{\rm ab})/\bar{N}\hbar\Omega_{q=5}$. For the coefficients of the modal expansion of $(\alpha(0), \beta(0))$, we obtain

$$C_{\rm anom} = \frac{3}{4\pi R_0^3} \left(\frac{\delta N_{\rm a}}{\bar{N}_{\rm a}} - \frac{\delta N_{\rm b}}{\bar{N}_{\rm b}} \right) \tag{58}$$

$$C_5 = -\frac{5}{4} C_{\rm anom}. \tag{59}$$

3.4.2 Evolution of the modes and stability against demixing

As a second step we determine the time evolution of the modes of the operator $L(0)$. If we consider an eigenstate $(\alpha_q(0), \beta_q(0))$ of $L(0)$ with the eigenenergy $\hbar\Omega_q$ and evolve it according to equation (47), we find that the evolution reduces to multiplication by purely time dependent factors $A_q(t), B_q(t)$:

$$\alpha_q(\mathbf{r}, t) = A_q(t)\alpha(\mathbf{r}, 0) \tag{60}$$

$$\beta_q(\mathbf{r}, t) = B_q(t)\beta(\mathbf{r}, 0) \tag{61}$$

where the factors satisfy the differential equations:

$$\mathrm{i}\dot{A}_q = \frac{\Omega_q}{\lambda^2} B_q \tag{62}$$

$$\mathrm{i}\dot{B}_q = \frac{\Omega_q}{\lambda^3} A_q \tag{63}$$

with the initial conditions $A_q(0) = B_q(0) = 1$. Note that the zero energy eigenmode does not evolve, as $\Omega_q = 0$. The anomalous mode has to be integrated separately, leading to

$$\alpha_{\rm anom}(\mathbf{r}, t) = 1 \tag{64}$$

$$\beta_{\rm anom}(\mathbf{r}, t) = \frac{\bar{N}_{\rm a}\bar{N}_{\rm b}}{\bar{N}} \frac{(g_{\rm aa} + g_{\rm bb} - 2g_{\rm ab})}{\mathrm{i}\hbar} \int_0^t \frac{\mathrm{d}t'}{\lambda^3(t')}. \tag{65}$$

We are now able to address the problem of dynamical stability of the breathe-together solution. Dynamical stability requires that any small deviation of the ϕ_ε's from the breathe-together solution $\bar{\phi}$ should not grow exponentially with time. Here an exponential growth of α may correspond to a demixing of the two condensates a and b.

A first case of instability occurs when $g_{\rm ab} > g_{\rm aa}, g_{\rm bb}$. In this case the eigenfrequencies Ω_q are purely imaginary and A_q, B_q diverge exponentially with time [19]. We have checked by a numerical integration of the Gross-Pitaevskii equations with spherical symmetry that the spatial distribution then acquires a structure of alternating shells of a atoms and b atoms (see Fig. 1).

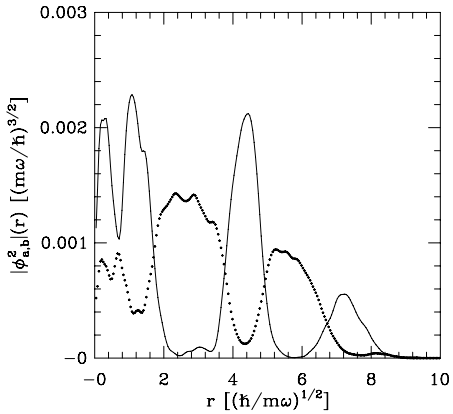

Fig. 1. Modulus squared of the condensate wavefunctions $|\phi^2_{\rm a,b}|(N_{\rm a}, N_{\rm b})$ as function of the distance r to the trap center at a time $\omega t \simeq 29.5$, from a numerical solution of the coupled Gross-Pitaevskii equations in the case of a dynamically unstable breathe-together solution. We have taken $g_{\rm bb}/g_{\rm aa} = 1.2$ and $g_{\rm ab}/g_{\rm aa} = 1.5$. We have applied a deviation $\delta N_{\rm a} = -\delta N_{\rm b} = -0.05\bar{N}_{\rm a}$ from the exact breathe-together condition. The chemical potential is $\bar{\mu} = 28.9\hbar\omega$. The curve in solid line corresponds to $\phi_{\rm a}$, the dotted curve corresponds to $\phi_{\rm b}$.

We suppose from now on that $g_{\rm ab} < g_{\rm aa}, g_{\rm bb}$. Instability may still occur in this case due to the periodic time dependence of the coefficients in the system (63), as shown in [20]. We have studied in more detail the stability of the mode $q = 5$, which is the one populated initially (see Eq. (56)); we have found non-zero instability exponents σ ($C_5(t) \sim \mathrm{e}^{\sigma t}$) in a very limited region of the plane $(g_{\rm ab}/g_{\rm aa}, g_{\rm bb}/g_{\rm aa})$, with very small exponents ($\sigma < 3 \times 10^{-2}\omega$). A direct numerical integration of the Gross-Pitaevskii equations did not show any demixing of a and b even at times $\gg \sigma^{-1}$ [21]. This suggests that the finite instability exponent is an artifact of the Thomas-Fermi approximation.

We assume in what follows the dynamical stability of the breathe-together solution.

3.5 Phase dynamics

In order to calculate the functions $\chi_{\rm d}, \chi_{\rm s}$ relevant for the relative phase dynamics, we calculate the evolution of the deviation $\delta\varphi_{\rm d}$ due to a small change in $N_{\rm a}, N_{\rm b}$ with respect to $\bar{N}_{\rm a}, \bar{N}_{\rm b}$, that is we evolve the initial state (56) according to the results of the previous subsection.

As we assume dynamical stability of the breathe-together solution, the modes with $q = 5$ perform only oscillations in time [22]. The relevant contribution for the phase dynamics therefore comes from the anomalous mode, which from equation (65) has a β diverging linearly with time. Assuming $\beta(\mathbf{r}, t) \sim C_{\rm anom}\beta_{\rm anom}(t)$

and using equations (58, 46) we obtain:

$$(\delta\theta_{\rm a}-\delta\theta_{\rm b})(\mathbf{r},t)\sim-\frac{2\bar{\mu}}{5}\frac{\bar{N}_{\rm a}\bar{N}_{\rm b}}{\bar{N}^2}\frac{(g_{\rm aa}+g_{\rm bb}-2g_{\rm ab})}{g_{\rm aa}}\times\left(\frac{\delta N_{\rm a}}{\bar{N}_{\rm a}}-\frac{\delta N_{\rm b}}{\bar{N}_{\rm b}}\right)\int_0^t\frac{{\rm d}t'}{\lambda^3(t')}\cdot\quad(66)$$

We specialize this formula with $\delta N_{\rm b}=\pm\delta N_{\rm a}$ and we get from equations (30, 31):

$$\chi_{\rm d}\sim-\frac{1}{2\hbar}\left(\frac{{\rm d}\mu}{{\rm d}N}\right)_{N=\bar{N}}\frac{g_{\rm aa}+g_{\rm bb}-2g_{\rm ab}}{g_{\rm aa}}\int_0^t\frac{{\rm d}t'}{\lambda^3(t')}\quad(67)$$

$$\chi_{\rm s}\sim(|c_{\rm b}|^2-|c_{\rm a}|^2)\chi_{\rm d}.\quad(68)$$

We have introduced the derivative of the chemical potential with respect to the total number of particles ($({\rm d}\mu/{\rm d}N)(N=\bar{N})\simeq 2\bar{\mu}/5\bar{N}$ in the Thomas-Fermi limit) in order to recover the characteristic time scale for the phase collapse of steady state non mutually interacting condensates. Our formula reveals the interest of close coupling constants, such that $g_{\rm aa}+g_{\rm bb}-2g_{\rm ab}\ll g_{\rm aa}$. In this case $\chi_{\rm d}$ is strongly reduced with respect to non mutually interacting condensates; λ performs small oscillations around the value $\lambda=1$ so that the integral over t' can be replaced by t. The more general case of close g's not necessarily satisfying the breathe together condition is analyzed in the next section.

We note that the value of $\chi_{\rm s}$ as function of $\chi_{\rm d}$ could be expected *a priori* from equation (20): when equation (26) is satisfied, the condensate wavefunctions form a breathe-together solution and have therefore a vanishing relative phase for $N_{\rm a}=N|c_{\rm a}|^2, N_{\rm b}=N|c_{\rm b}|^2$, whatever the value of N is. An important consequence is that there is no extra damping of the phase coherence due to the fluctuations of the total number of particles (see Eq. (22)).

4 Case of close coupling constants

We consider in this section the case of close coupling constants which leads to a dramatic reduction of the relative phase decoherence with respect to the case of non mutually interacting condensates.

The strategy is to solve approximately the Gross-Pitaevskii equations (Eq. (9)) for $\phi_{\rm a}(N_{\rm a},N_{\rm b})$ and $\phi_{\rm b}(N_{\rm a},N_{\rm b})$ and apply the formulas (16, 17) directly. For all equal g's the initial state is indeed a steady state for the equation (9) and $\chi_{\rm s}=\chi_{\rm d}=0$. For close g's we linearize the Gross-Pitaevskii equations around the initial value in the hydrodynamic point of view.

4.1 Linearization in the classical hydrodynamics approximation

We first rewrite the Gross-Pitaevskii equations (Eq. (9)) in terms of the hydrodynamic variables:

$$\rho_\varepsilon\equiv N_\varepsilon|\phi_\varepsilon(N_{\rm a},N_{\rm b})|^2\quad(69)$$

$$\mathbf{v}_\varepsilon\equiv\frac{\hbar}{m}\,\mathbf{grad}\,\theta_\varepsilon(N_{\rm a},N_{\rm b})\quad(70)$$

that is densities and velocity fields of the two condensates. We further assume the Thomas-Fermi limit $\mu\gg\hbar\omega$ and neglect the quantum pressure terms as in [14] in the time evolution of the velocity fields:

$$\partial_t\rho_\varepsilon+{\rm div}(\rho_\varepsilon\mathbf{v}_\varepsilon)=0\quad(71)$$

$$\partial_t\mathbf{v}_\varepsilon+\frac{1}{2}\,\mathbf{grad}\,v_\varepsilon^2=-\frac{1}{m}\,\mathbf{grad}\,[U(\mathbf{r})+\rho_\varepsilon g_{\varepsilon\varepsilon}+\rho_{\varepsilon'}g_{\varepsilon\varepsilon'}].\quad(72)$$

At this point we introduce the deviations of the densities and velocity fields from their initial values:

$$\rho_\varepsilon(t)=\rho_\varepsilon(0)+\delta\rho_\varepsilon(t)\quad(73)$$

$$\mathbf{v}_\varepsilon(t)=\mathbf{v}_\varepsilon(0)+\delta\mathbf{v}_\varepsilon(t)\quad(74)$$

where the initial values are given by:

$$\rho_\varepsilon(t=0)=N_\varepsilon|\phi_0|^2(N)\quad(75)$$

$$\mathbf{v}_\varepsilon(t=0)=\mathbf{0}.\quad(76)$$

By expanding equations (71, 72) to first order in the small quantities $\delta\rho_\varepsilon,\delta\mathbf{v}_\varepsilon$, we obtain:

$$\partial_t\delta\rho_\varepsilon+{\rm div}[N_\varepsilon|\phi_0|^2\delta\mathbf{v}_\varepsilon]=0\quad(77)$$

$$\partial_t\delta\mathbf{v}_\varepsilon+\frac{1}{m}\,\mathbf{grad}\,[\delta\rho_\varepsilon g_{\varepsilon\varepsilon}+\delta\rho_{\varepsilon'}g_{\varepsilon\varepsilon'}]=-\frac{1}{m}\,\mathbf{grad}\,[|\phi_0|^2](N_\varepsilon g_{\varepsilon\varepsilon}+N_{\varepsilon'}g_{\varepsilon\varepsilon'}-Ng_{\rm aa}).\quad(78)$$

By taking the first time derivative of equation (77) we eliminate the velocity field and we get:

$$\partial_t^2\delta\rho_\varepsilon+\sum_{\varepsilon'}M_{\varepsilon\varepsilon'}S[\delta\rho_{\varepsilon'}]+\sigma_\varepsilon=0.\quad(79)$$

The source terms of these inhomogeneous equations are:

$$\sigma_\varepsilon=-\frac{N_\varepsilon}{m}{\rm div}[|\phi_0|^2\,\mathbf{grad}\,|\phi_0|^2](N_\varepsilon g_{\varepsilon\varepsilon}+N_{\varepsilon'}g_{\varepsilon\varepsilon'}-Ng_{\rm aa}).\quad(80)$$

The homogeneous part of equation (79) involves the 2×2 matrix M:

$$M=\frac{1}{Ng_{\rm aa}}\begin{pmatrix}N_{\rm a}g_{\rm aa} & N_{\rm a}g_{\rm ab}\\ N_{\rm b}g_{\rm ab} & N_{\rm b}g_{\rm bb}\end{pmatrix}\quad(81)$$

and the Stringari operator defined in equation (53). In order to solve equation (79) we introduce the eigenvectors $\mathbf{e}_\pm$ of the matrix M with corresponding eigenvalues $g_\pm$. Consistently with our previous approximations, we calculate, to leading order in the differences between the coupling constants, the eigenvalues:

$$g_+\simeq g_{\rm aa}\quad(82)$$

$$g_-\simeq\frac{N_{\rm a}N_{\rm b}}{N^2}(g_{\rm aa}+g_{\rm bb}-2g_{\rm ab})\quad(83)$$

and the components of $(\delta\rho_{\rm a}, \delta\rho_{\rm b})$ on the eigenvectors of M:

$$\delta\rho_+ \simeq \delta\rho_{\rm a} + \delta\rho_{\rm b} \tag{84}$$

$$\delta\rho_- \simeq \frac{N_{\rm b}}{N}\delta\rho_{\rm a} - \frac{N_{\rm a}}{N}\delta\rho_{\rm b}. \tag{85}$$

For those linear combinations we get the decoupled equations:

$$\partial_t^2 \delta\rho_\pm + \frac{g_\pm}{g_{\rm aa}} S[\delta\rho_\pm] + \sigma_\pm = 0. \tag{86}$$

To study the dynamics of the system we expand $\rho_\pm$ and the source terms $\sigma_\pm$ on the eigenmodes of the Stringari operator. It turns out that the source terms are simply proportional to the breathing mode $\alpha_{q=5}$ already introduced in equation (57). The solution of equation (86) with the initial conditions $\delta\rho_\pm = \partial_t \delta\rho_\pm = 0$ is then:

$$\delta\rho_\pm(\mathbf{r}, t) = N|\phi_0(\mathbf{0})|^2 \mathcal{A}_\pm \frac{g_{\rm aa}}{g_\pm}[1 - \cos\Omega_\pm t]\alpha_{q=5}(r) \tag{87}$$

with eigenfrequencies and amplitudes given by:

$$\Omega_\pm = \left(\frac{5g_\pm}{g_{\rm aa}}\right)^{1/2} \omega \tag{88}$$

$$\mathcal{A}_+ = \frac{N_{\rm a}^2 g_{\rm aa} + N_{\rm b}^2 g_{\rm bb} + 2N_{\rm a}N_{\rm b}g_{\rm ab}}{N^2 g_{\rm aa}} - 1 \tag{89}$$

$$\mathcal{A}_- = \frac{N_{\rm a}N_{\rm b}}{N^2}\left[\frac{N_{\rm a}g_{\rm aa} + N_{\rm b}g_{\rm ab} - N_{\rm b}g_{\rm bb} - N_{\rm a}g_{\rm ab}}{N g_{\rm aa}}\right]. \tag{90}$$

We note that when the numbers of atoms $N_{\rm a,b}$ satisfy the breathe-together condition (Eq. (26)) the amplitude $\mathcal{A}_-$ vanishes as expected, since $\delta\rho_- \equiv 0$ in this case.

4.2 Validity of the linear approximation

In order for our linearized treatment to be valid the deviations $\delta\rho_\pm$ should remain small as compared to the initial densities. A first necessary condition to be satisfied is that the eigenfrequencies $\Omega_\pm$ should be real. This imposes the positivity of the matrix M, ensured by the positivity of its determinant:

$$g_{\rm ab}^2 \leq g_{\rm aa} g_{\rm bb}. \tag{91}$$

This condition is known in the case of homogeneous mixtures of condensates as a stability condition against demixing [23]. To the leading order in the difference between the coupling constants, the condition (91) is equivalent to $g_{\rm aa} + g_{\rm bb} - 2g_{\rm ab} > 0$.

We note at this point that the amplitude $\mathcal{A}_-/g_-$ in the expression for $\delta\rho_-$ is a ratio of two small numbers. When this ratio is large the system can evolve far from its initial state even in the stable case $g_- > 0$: numerical solutions of the Gross-Pitaevskii equations confirm this expectation, showing the formation of a crater at the center of one of the condensates. We therefore have to impose a second condition:

$$\left|\mathcal{A}_\pm \frac{g_{\rm aa}}{g_\pm}\right| \ll 1. \tag{92}$$

Finally the present treatment is based on the classical hydrodynamic approximation; by including the quantum pressure terms in the hydrodynamic equation for the velocity field one can show that this imposes on the eigenfrequencies Ω_-:

$$\frac{\hbar\omega^2}{\mu} \ll \Omega_- \tag{93}$$

(see also Appendix C). This condition can be violated even in the Thomas-Fermi limit, when the g_- eigenvalue almost vanishes. In this case one has to include the quantum pressure terms; the decoupling property of $\delta\rho_\pm$ is unaffected; for the evolution of $\delta\rho_-$ similar results as in equation (87) are obtained; we find *e.g.* $\Omega_- \simeq 63\hbar\omega^2/8\mu$.

4.3 Phase dynamics

We assume that all the conditions for the validity of the linearized treatment are satisfied so that we can proceed to the analysis of the relative phase dynamics. To this aim we write the equation of evolution for the phases θ_ε of the condensate wavefunctions ϕ_ε in the classical hydrodynamic approximation:

$$\partial_t \theta_\varepsilon + \frac{\hbar}{2m}\left(\mathbf{grad}\ \theta_\varepsilon\right)^2 = -[U + g_{\varepsilon\varepsilon}\rho_\varepsilon + g_{\varepsilon\varepsilon'}\rho_{\varepsilon'}]/\hbar. \tag{94}$$

The equations for the velocity fields previously given are simply the gradient of equation (94). By linearizing equation (94) around the initial state $\theta_\varepsilon = 0$ we obtain for the relative phase:

$$\hbar\partial_t(\theta_{\rm a} - \theta_{\rm b}) \simeq -|\phi_0|^2(N_{\rm a}g_{\rm aa} + N_{\rm b}g_{\rm ab} - N_{\rm b}g_{\rm bb} - N_{\rm a}g_{\rm ab}) + (g_{\rm ab} - g_{\rm aa})\delta\rho_{\rm a} + (g_{\rm bb} - g_{\rm ab})\delta\rho_{\rm b}. \tag{95}$$

The right hand side of this equation is a sum of terms constant in time and of oscillatory functions of time. The function $\theta_{\rm a} - \theta_{\rm b}$ then has two components: an oscillating component and a component diverging linearly with time which will dominate for long times. By using the result equation (87) and the Thomas-Fermi approximation for $|\phi(0)|^2$ (Eq. (43)) we can calculate the time diverging component and we obtain to leading order in the g's difference:

$$\theta_{\rm a} - \theta_{\rm b} \sim -\frac{2\mu}{5Ng_{\rm aa}}[N_{\rm a}g_{\rm aa} - N_{\rm b}g_{\rm bb} + (N_{\rm b} - N_{\rm a})g_{\rm ab}]\ t/\hbar. \tag{96}$$

We now use equations (17, 20) to obtain:

$$\chi_{\rm d} \sim -\frac{1}{2}\left(\frac{{\rm d}\mu}{{\rm d}N}\right)_{N=\bar{N}} \frac{g_{\rm aa} + g_{\rm bb} - 2g_{\rm ab}}{g_{\rm aa}}\ t/\hbar \tag{97}$$

$$\chi_{\rm s} + (|c_{\rm a}|^2 - |c_{\rm b}|^2)\chi_{\rm d} \sim -\frac{2}{5g_{\rm aa}}\left(\frac{{\rm d}\mu}{{\rm d}N}\right)_{N=\bar{N}} \times (|c_{\rm a}|^2 g_{\rm aa} + |c_{\rm b}|^2 g_{\rm ab} - |c_{\rm b}|^2 g_{\rm bb} - |c_{\rm a}|^2 g_{\rm ab})\ t/\hbar \tag{98}$$

where we introduced the derivative of the chemical potential with respect to the total number of particle $(\mathrm{d}\mu/\mathrm{d}N)(N = \bar{N}) \simeq (2/5)\bar{\mu}/\bar{N}$ in the Thomas-Fermi limit. As we already found in the particular case of the breathe-together solution the constants χ_d and χ_s governing the relative phase collapse are highly reduced for close g's with respect to the case of non mutually interacting condensates.

4.4 Physical interpretation of the results

We now show that all the previous results of this section can be interpreted in terms of small oscillations of the condensates around the steady state.

Let us introduce the steady state densities $\rho_\varepsilon^\mathrm{st}$ for the condensates with N_a particles in a and N_b particles in b. As we are in the case of quasi complete spatial overlap between the two condensates we can use the Thomas-Fermi approximation to determine these densities:

$$\mu_\mathrm{a} - U = \rho_\mathrm{a}^\mathrm{st} g_\mathrm{aa} + \rho_\mathrm{b}^\mathrm{st} g_\mathrm{ab} \tag{99}$$

$$\mu_\mathrm{b} - U = \rho_\mathrm{a}^\mathrm{st} g_\mathrm{ab} + \rho_\mathrm{b}^\mathrm{st} g_\mathrm{bb} \tag{100}$$

where μ_ε are the chemical potentials in steady state. We rewrite these equations in terms of the deviations $\delta\rho_\varepsilon^\mathrm{st}$ of the steady-state densities from the initial state densities $N_\varepsilon|\phi_0|^2$ and in terms of the deviations $\delta\mu_\varepsilon$ of the chemical potentials from μ defined in equation (1):

$$\delta\mu_\mathrm{a} = (N_\mathrm{a} g_\mathrm{aa} + N_\mathrm{b} g_\mathrm{ab} - N g_\mathrm{aa})|\phi_0|^2 + \delta\rho_\mathrm{a}^\mathrm{st} g_\mathrm{aa} + \delta\rho_\mathrm{b}^\mathrm{st} g_\mathrm{ab} \tag{101}$$

$$\delta\mu_\mathrm{b} = (N_\mathrm{b} g_\mathrm{bb} + N_\mathrm{a} g_\mathrm{ab} - N g_\mathrm{aa})|\phi_0|^2 + \delta\rho_\mathrm{a}^\mathrm{st} g_\mathrm{ab} + \delta\rho_\mathrm{b}^\mathrm{st} g_\mathrm{bb}. \tag{102}$$

Using the fact that the spatial integral of $\delta\rho_\varepsilon$ vanishes, we get from integration of equations (101, 102) over the volume of $|\phi_0|^2$ the approximate relations:

$$\delta\mu_\mathrm{a} = \frac{2\mu}{5N g_\mathrm{aa}}(N_\mathrm{a} g_\mathrm{aa} + N_\mathrm{b} g_\mathrm{ab} - N g_\mathrm{aa}) \tag{103}$$

$$\delta\mu_\mathrm{b} = \frac{2\mu}{5N g_\mathrm{aa}}(N_\mathrm{b} g_\mathrm{bb} + N_\mathrm{a} g_\mathrm{ab} - N g_\mathrm{aa}). \tag{104}$$

We can therefore check that the relative phase of the condensates in steady state, given by $\theta_\mathrm{a}^\mathrm{st} - \theta_\mathrm{b}^\mathrm{st} = -\mathrm{i}(\delta\mu_\mathrm{a} - \delta\mu_\mathrm{b})t/\hbar$, evolves as in equation (96). The phase decoherence properties of the evolving mixture are then essentially the same as in steady state.

Moreover we now show that the average $\langle\delta\rho_\varepsilon\rangle$ of $\delta\rho_\varepsilon$ over the oscillations at frequencies $\Omega_\pm$ coincide with $\delta\rho_\varepsilon^\mathrm{st}$. First, by averaging equation (77) over time we find that the velocity fields have a vanishing time average [24]. Second, we average equation (78) over time; we find equations for the spatial gradient of $\langle\delta\rho_\varepsilon\rangle$, which coincide with the spatial gradient of equations (101, 102), so that $\langle\delta\rho_\varepsilon\rangle = \delta\rho_\varepsilon^\mathrm{st}$ [25].

5 Discussion of the JILA case

In the JILA experiment the values of the three coupling constants between the atoms are known with good precision; they are in the ratio [10]:

$$g_\mathrm{aa} : g_\mathrm{ab} : g_\mathrm{bb} = 1.03 : 1 : 0.97. \tag{105}$$

No breathe-together solution exists in this case, as g_ab lies within g_aa and g_bb. Experimentally half of the particles are in the state a so that $|c_\mathrm{a}|^2 = |c_\mathrm{b}|^2 = 1/2$, and the mean total number of particles is $\bar{N} = 5 \times 10^5$. Although the coupling constants are close, the linearized treatment presented in Section 4 does not apply either, because condition (92) is violated. It is actually found experimentally that the two condensates evolve far from the initial state, with formation of a crater in the a condensate while the b condensate becomes more confined at the center of the trap; eventually the condensates separate in some random direction [10].

To avoid the crater formation and trigger the spatial separation of the two condensates in a reproducible direction a small spatial shift is applied to the trapping potential of one of the two states. The two condensates separate, with a relative motion exhibiting strongly damped oscillations [10]. The system then reaches a steady state that still exhibits phase coherence, up to times on the order of 150 ms after the phase state preparation [9].

5.1 Time dependent calculations

We have already studied in [15] the damping of the relative motion between the condensates, by numerical integration of the coupled Gross-Pitaevskii equations (Eq. (9)). The agreement with the experimental results of [10] is qualitatively good, although the damping in the theory is weaker and incomplete, small oscillations of the condensate wavefunctions remaining undamped even at long times.

We have applied the formalism of Section 2 by numerically integrating the Gross-Pitaevskii equations for the parameters of the JILA experiment. The coefficients $\chi_\mathrm{s}, \chi_\mathrm{d}$, now complicated functions of time and space, are obtained by evolving wavefunctions with slightly different numbers of atoms in a and b. In order to facilitate the comparison with the experiments, in which the x-integrated atomic density $\bar{\rho}_\mathrm{a}(y,z)$ in the internal state a is measured after the $\pi/2$ pulse applied at time τ, we calculated the following contrast:

$$C_\mathrm{JILA}(y,z) = \frac{\max_\delta \bar{\rho}_\mathrm{a} - \min_\delta \bar{\rho}_\mathrm{a}}{\max_\delta \bar{\rho}_\mathrm{a} + \min_\delta \bar{\rho}_\mathrm{a}} = \frac{2|\int \mathrm{d}x\ \langle\hat{\psi}_\mathrm{a}^\dagger(\tau^-)\hat{\psi}_\mathrm{b}(\tau^-)\rangle^\mathrm{Gauss}|}{\sum_{\varepsilon=\mathrm{a,b}} \int \mathrm{d}x\ \bar{N}_\varepsilon |\bar{\phi}_\varepsilon|^2(\tau^-)} \tag{106}$$

where the interference term (15) is averaged over a Gaussian distribution of the total number of particles with a standard deviation ΔN. A direct comparison with the experiment would require the inclusion of the 22 ms ballistic

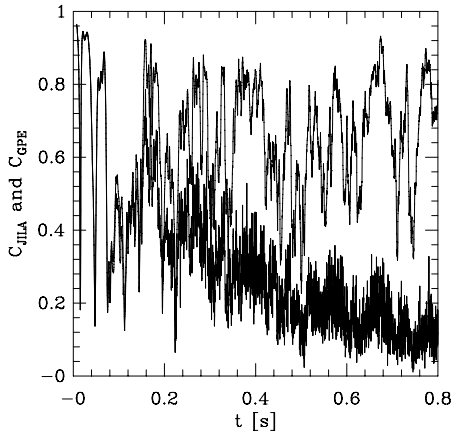

Fig. 2. For the parameters of the JILA experiment (not including the 22 ms ballistic expansion), phase contrasts $C_{\rm JILA}$ (lower curve) and $C_{\rm GPE}$ (upper curve) defined in the text, at $y = z = 0$, as function of time in seconds, for the evolving binary mixture, with $\Delta N = 0.08\bar{N}$.

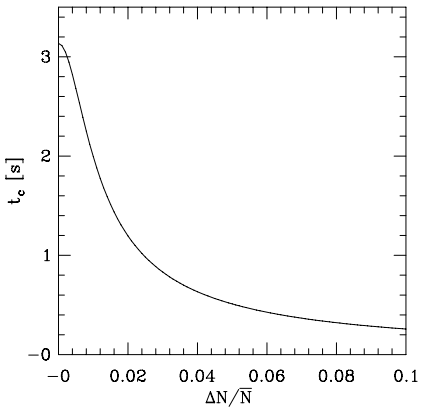

Fig. 3. For the parameters of the JILA experiment (except the 22 ms ballistic expansion), collapse time $t_{\rm c}$ for $C_{\rm JILA}$ at $y = z = 0$ as a function of $\Delta N/\bar{N}$ for zero temperature steady state condensates in the shifted traps.

expansion, not included in the present numerical calculations.

Our numerical result for $C_{\rm JILA}$ at the center of the trap for the species a, $y = z = 0$, is presented in Figure 2, for Gaussian fluctuations in the total number of particles $\Delta N/\bar{N} = 8\%$ corresponding to the JILA experiment [26], together with the pure Gross-Pitaevskii prediction $C_{\rm GPE}$ obtained by setting all the χ's to 0. The Gross-Pitaevskii prediction oscillates around $\langle C_{\rm GPE}\rangle = 0.63$. On the contrary the result of the more complete calculation including fluctuations in the relative and total number of particles exhibits a damping of the contrast, that we have fitted by convenience with the formula $C_{\rm JILA} = C_0 {\rm e}^{-\gamma t}$; we obtain $C_0 \simeq \langle C_{\rm GPE}\rangle$ and $\gamma^{-1} = 0.42$ s.

Note the oscillatory aspect of the curves in Figure 2. More understanding of the structure of the condensate wavefunctions given by equation (9) is required as this point: as detailed in [15] $\bar{\phi}_\varepsilon$ is a sum of a smooth part, performing oscillations with frequencies expected to be close to eigenfrequencies of the steady state condensates [27], and of a noisy quasi-stochastic part. The slow oscillatory structure evident on $C_{\rm GPE}$ comes from this smooth oscillating part of the wavefunctions.

We have also considered the ideal case of a well-defined total number of particles. The numerical prediction for the contrast $C_{\rm JILA}$ in this case corresponds to a very long lived phase coherence: after a time of 1 s, the contrast is still very close to the pure Gross-Pitaevskii prediction.

5.2 Steady state calculations and effect of particle losses

As the wavefunctions at long times perform mainly oscillations around the steady state we have also tried a much simpler steady state calculation (see Sect. 2.5). During the collapse time the contrast $C_{\rm JILA}$ is a Gaussian in time (Eq. (22)), with an initial value 0.958 and with a half-width $t_{\rm c}$ at the relative height ${\rm e}^{-1/2}$. We plot in Figure 3 the variation of $t_{\rm c}$ as function of the standard deviation ΔN. As we find $\chi_{\rm s}/t = -7.7 \times 10^{-5}$ s^{-1} and $\chi_{\rm d}/t = -4.5 \times 10^{-4}$ s^{-1}, one has $|\chi_{\rm s}| \simeq |\chi_{\rm d}|/6$, so that relatively high values of ΔN are required to observe a significant effect of the fluctuations of the total number of particles on phase decoherence. For $\Delta N = 0.08\bar{N}$ the phase decoherence time is $t_{\rm c} = 0.32$ s, close to the result of the time-dependent calculation of Figure 2. Note that for such a high value of $\Delta N/\bar{N}$ the decay of the phase contrast in equation (22) is essentially due to the first exponential factor accounting for the smearing of the phase by fluctuations of the total number of particles, the spreading of the phase for a fixed number of particles being very small ($\bar{N}\chi_{\rm d}^2(t_{\rm c})/2 \simeq 0.005$).

We now briefly consider the issue of losses of particles. An intrinsic source of losses in the JILA experiment are the inelastic collisions between a atoms and b atoms, resulting in the simultaneous loss of two particles. We estimate the mean number $\langle \delta N\rangle$ of lost particles from the rate constant K_2 for binary inelastic collisions between the states $|F = 1, m = -1\rangle$ and $|F = 2, m = 2\rangle$ [28] and from a numerical calculation of the overlap integral $\int {\rm d}^3\mathbf{r}\, |\bar{\phi}_{\rm a}|^2 |\bar{\phi}_{\rm b}|^2$. For the JILA parameters we find $\langle \delta N\rangle/\bar{N} = 0.04$ at time $t_{\rm c} = 0.32$ s. One could then naively expect the effect of losses on phase coherence to be comparable with the effect of fluctuations of N.

To test this naive expectation we use the following simple model, inspired by the two-mode model developed in [8], and focusing on the effect of the losses on the drift velocity $v(N)$ of the relative phase of the two condensates given in equation (21). Imagine that the system has initially $\bar{N}$ condensate atoms and that k binary inelastic collisions have taken place at times $t_1 < \ldots < t_k$ between

time 0 and time t. The shift of the relative phase during t is then given by:

$$\Theta = \int_0^t \mathrm{d}\tau\ v(N(\tau)) = v(\bar{N})t_1 + v(\bar{N}-2)(t_2-t_1) + \ldots + v(\bar{N}-2k)(t-t_k). \quad (107)$$

As we do in [8] we assume a constant mean number of collisions λ per unit of time and we average the phase factor $\mathrm{e}^{\mathrm{i}\Theta}$ multiplying the interference term $\langle\hat{\psi_\mathrm{b}}^\dagger\hat{\psi}_\mathrm{a}\rangle$ over the probability distribution of the times $t_1,\ldots,t_k$ and of the number of loss events k,

$$P_t(t_1,\ldots,t_k;k) = \lambda^k \mathrm{e}^{-\lambda t} \quad (108)$$

to obtain:

$$|\langle\mathrm{e}^{\mathrm{i}\Theta}\rangle| = \exp\{-\langle k\rangle[1-\sin(2\chi_\mathrm{s})/(2\chi_\mathrm{s})]\} \quad (109)$$

$$\simeq \exp\left[-\frac{2}{3}\langle k\rangle\chi_\mathrm{s}^2\right] \quad \text{for } |\chi_\mathrm{s}| \ll 1 \quad (110)$$

where $2\langle k\rangle = 2\lambda t = \langle\delta N\rangle$ is the mean number of lost particles during t. At time $t = t_\mathrm{c} = 0.32$ s the corresponding modulus of the averaged phase factor is on the order of $[1-4\times10^{-6}]$, very close to one: particle losses have a negligible effect on the phase coherence at the considered time t_c, even if $\langle\delta N\rangle$ and ΔN have the same order of magnitude.

Actually an inspection of the χ_s dependent factor in equation (22) and of equation (110) reveals that these equations have the same structure; replacing in equation (22) the variance ΔN^2 of the total number of particles by the variance Δk^2 of the number of loss events ($\Delta k^2 = \langle k\rangle$ as k obeys a Poisson law) one recovers equation (110) up to a numerical factor inside the exponential. For equally large values of ΔN and $\langle k\rangle$ the effect of losses on phase coherence is less important than that of fluctuations of N because $\Delta k^2 = \langle k\rangle \ll \Delta N^2$.

We have also investigated another source of losses, the collisions of condensate atoms with the background gas of the cell. Assuming a lifetime of the particles in the cell of 250 s as in [29] we find as well that this loss mechanism has a negligible effect on the phase coherence for a time $t_\mathrm{c} = 0.32$ s.

6 Conclusion and perspectives

We have extended previous treatments of the phase dynamics of Bose-Einstein condensates at zero temperature to the case of mutually interacting and dynamically evolving binary mixtures of condensates, for a measurement scheme of the phase coherence inspired by the JILA experiment.

We have first applied this extended formalism to the interesting breathe-together solution of the Gross-Pitaevskii equations, in which the two condensates oscillate in phase, remaining always exactly spatially superimposed. The analytical results for the phase show that a dramatic increase of the phase coherence time can be obtained for close coupling constants $g_\mathrm{aa}, g_\mathrm{ab}, g_\mathrm{bb}$ describing the elastic interactions between a atoms and b atoms.

We have also treated analytically the case of close g's, in the absence of demixing instability. Basically the phase collapse is identical to the steady state case for the two mutually interacting condensates.

Finally, we have investigated numerically the more difficult case of JILA. We find a collapse time of the phase on the order of 0.4 s, both by a dynamical and a steady state calculation, in the case of Gaussian fluctuations of the total number of particles, corresponding to $\Delta N/\bar{N} = 8\%$. This result for the collapse time is significantly larger than the experimental results (no phase coherence measured after 150 ms). We have also estimated in a simple way the effect of collisional losses on phase coherence in the JILA experiment.

A possible extension of this work could include the effect of the presence of a thermal component in the experiment.

Part of this work (the breathe-together solution) would have not been possible without the contribution of G. Shlyapnikov, J. Dalibard and P. Fedichev. We thank A. Leggett, Y. Kagan for very useful discussions on the role of fluctuations in the total number of particles. We thank Ralph Dum for help in the numerical calculations. A.S. acknowledges financial support from the European Community (TMR individual research grant).

Appendix A: Phase correction to the Gross-Pitaevskii prediction

We consider the evolution of the Fock state $|N_\mathrm{a}:\phi_\mathrm{a}(0), N_\mathrm{b}:\phi_\mathrm{b}(0)\rangle$ (with $N_\mathrm{a,b}$ particles in the internal state a, b). The model Hamiltonian we consider contains the one-body Hamiltonians $\mathcal{H}_\varepsilon$ and elastic interactions terms:

$$H = \int \mathrm{d}^3\mathbf{r} \sum_{\varepsilon=\mathrm{a,b}} \hat{\psi_\varepsilon}^\dagger \mathcal{H}_\varepsilon \hat{\psi_\varepsilon} + \frac{1}{2}g_\mathrm{aa}\hat{\psi_\mathrm{a}}^\dagger\hat{\psi_\mathrm{a}}^\dagger\hat{\psi}_\mathrm{a}\hat{\psi}_\mathrm{a} + \frac{1}{2}g_\mathrm{bb}\hat{\psi_\mathrm{b}}^\dagger\hat{\psi_\mathrm{b}}^\dagger\hat{\psi}_\mathrm{b}\hat{\psi}_\mathrm{b} + g_\mathrm{ab}\hat{\psi_\mathrm{b}}^\dagger\hat{\psi_\mathrm{a}}^\dagger\hat{\psi}_\mathrm{a}\hat{\psi}_\mathrm{b} \quad (A.1)$$

where $\hat{\psi_\varepsilon}$ is the atomic field operator in the internal state ε.

We use the Hartree-Fock type ansatz for the N-body state vector:

$$|\Psi\rangle = \mathrm{e}^{-\mathrm{i}A(t)/\hbar}|N_\mathrm{a}:\phi_\mathrm{a}(t), N_\mathrm{b}:\phi_\mathrm{b}(t)\rangle. \quad (A.2)$$

A variational formulation of the Hamiltonian equation

$$\mathrm{i}\hbar\frac{\mathrm{d}}{\mathrm{d}t}|\Psi\rangle = H|\Psi\rangle \quad (A.3)$$

leads to the Gross-Pitaevskii equations for $\phi_\varepsilon(t)$, given in equation (9), up to the undetermined phase factor A corresponding formally to a time dependent Lagrange

multiplier ensuring the conservation of the norm of $|\Psi\rangle$. To determine this phase factor A, we multiply equation (A.3) on the left by the bra $\langle\Psi|$; we obtain:

$$\dot{A} + \mathrm{i}\hbar\langle N_\mathrm{a}:\phi_\mathrm{a}(t), N_\mathrm{b}:\phi_\mathrm{b}(t)|\frac{\mathrm{d}}{\mathrm{d}t}|N_\mathrm{a}:\phi_\mathrm{a}(t), N_\mathrm{b}:\phi_\mathrm{b}(t)\rangle = \langle\Psi|H|\Psi\rangle. \quad \text{(A.4)}$$

The scalar products are calculated in second quantized formalism, *e.g.* we find:

$$\langle N_\mathrm{a}:\phi_\mathrm{a}(t), N_\mathrm{b}:\phi_\mathrm{b}(t)|\frac{\mathrm{d}}{\mathrm{d}t}|N_\mathrm{a}:\phi_\mathrm{a}(t), N_\mathrm{b}:\phi_\mathrm{b}(t)\rangle = \sum_\varepsilon N_\varepsilon\langle\phi_\varepsilon|\frac{\mathrm{d}}{\mathrm{d}t}|\phi_\varepsilon\rangle. \quad \text{(A.5)}$$

We finally arrive at equation (11).

Appendix B: Derivation of the interference term

When the N-body state vector is initial a phase state (2) and if one assumes that the Fock states evolve according to equation (8) one gets the following expression for the interference term between the two condensates:

$$\begin{aligned}\langle\hat{\psi}_\mathrm{b}^\dagger\hat{\psi}_\mathrm{a}\rangle_N = c_\mathrm{a}c_\mathrm{b}^* \sum_{N_\mathrm{a}=1}^{N} \frac{N!}{(N_\mathrm{a}-1)!N_\mathrm{b}!}|c_\mathrm{a}|^{2(N_\mathrm{a}-1)}|c_\mathrm{b}|^{2N_\mathrm{b}} \\ \times \phi_\mathrm{a}(N_\mathrm{a},N_\mathrm{b})\phi_\mathrm{b}^*(N_\mathrm{a}-1,N_\mathrm{b}+1) \\ \times \mathrm{e}^{\mathrm{i}[A(N_\mathrm{a}-1,N_\mathrm{b}+1)-A(N_\mathrm{a},N_\mathrm{b})]/\hbar} \\ \times [\langle\phi_\mathrm{a}(N_\mathrm{a}-1,N_\mathrm{b}+1)|\phi_\mathrm{a}(N_\mathrm{a},N_\mathrm{b})\rangle]^{N_\mathrm{a}-1} \\ \times [\langle\phi_\mathrm{b}(N_\mathrm{a}-1,N_\mathrm{b}+1)|\phi_\mathrm{b}(N_\mathrm{a},N_\mathrm{b})\rangle]^{N_\mathrm{b}}\end{aligned} \quad \text{(B.1)}$$

where $N_\mathrm{b} = N - N_\mathrm{a}$. In the large N limit, we expand to first order the effect of shifts of N_ε by unity in the last three lines of the previous equation:

$$\phi_\mathrm{a}(N_\mathrm{a}-1,N_\mathrm{b}+1) \simeq \phi_\mathrm{a}(N_\mathrm{a}-1,N_\mathrm{b}) + \partial_{N_\mathrm{b}}\phi_\mathrm{a}(N_\mathrm{a}-1,N_\mathrm{b}) \quad \text{(B.2)}$$

$$\phi_\mathrm{a}(N_\mathrm{a},N_\mathrm{b}) \simeq \phi_\mathrm{a}(N_\mathrm{a}-1,N_\mathrm{b}) + \partial_{N_\mathrm{a}}\phi_\mathrm{a}(N_\mathrm{a}-1,N_\mathrm{b}) \quad \text{(B.3)}$$

$$A(N_\mathrm{a}-1,N_\mathrm{b}+1) \simeq A(N_\mathrm{a}-1,N_\mathrm{b}) + \partial_{N_\mathrm{b}}A(N_\mathrm{a}-1,N_\mathrm{b}) \quad \text{(B.4)}$$

$$A(N_\mathrm{a},N_\mathrm{b}) \simeq A(N_\mathrm{a}-1,N_\mathrm{b}) + \partial_{N_\mathrm{a}}A(N_\mathrm{a}-1,N_\mathrm{b}). \quad \text{(B.5)}$$

We then get:

$$\begin{aligned}\langle\hat{\psi}_\mathrm{b}^\dagger\hat{\psi}_\mathrm{a}\rangle_N = c_\mathrm{a}c_\mathrm{b}^* \sum_{N_\mathrm{a}=1}^{N} \frac{N!}{(N_\mathrm{a}-1)!N_\mathrm{b}!}|c_\mathrm{a}|^{2(N_\mathrm{a}-1)}|c_\mathrm{b}|^{2N_\mathrm{b}} \\ \times \phi_\mathrm{a}(N_\mathrm{a},N_\mathrm{b})\phi_\mathrm{b}^*(N_\mathrm{a}-1,N_\mathrm{b}+1) \\ \times \mathrm{e}^{\mathrm{i}\Theta(N_\mathrm{a}-1,N_\mathrm{b})}\end{aligned} \quad \text{(B.6)}$$

where we have introduced the real quantity:

$$\Theta(N_\mathrm{a},N_\mathrm{b}) = \frac{1}{\hbar}(\partial_{N_\mathrm{b}} - \partial_{N_\mathrm{a}})A(N_\mathrm{a},N_\mathrm{b}) + \mathrm{i}\sum_\varepsilon N_\varepsilon\langle\phi_\varepsilon(N_\mathrm{a},N_\mathrm{b})|(\partial_{N_\mathrm{b}} - \partial_{N_\mathrm{a}})|\phi_\varepsilon(N_\mathrm{a},N_\mathrm{b})\rangle. \quad \text{(B.7)}$$

We calculate the time derivative of $\Theta(N_\mathrm{a},N_\mathrm{b})$ using the Gross-Pitaevskii equations (Eq. (9)). After lengthy calculations we find

$$\dot{\Theta}(N_\mathrm{a},N_\mathrm{b}) = 0. \quad \text{(B.8)}$$

In the Gedanken experiment considered in this paper, the initial wavefunctions $\phi_\varepsilon(t=0)$ depend only on $N_\mathrm{a}+N_\mathrm{b}$ so that they have a vanishing derivative $\partial_{N_\mathrm{b}} - \partial_{N_\mathrm{a}}$, and we take initially $A = 0$; this leads to $\Theta \equiv 0$. The same conclusion holds if the initial wavefunctions are real.

Appendix C: Approximate evolution in the Thomas-Fermi limit

After the gauge and scale transforms equations (40, 41), the equations of evolution for $\tilde{\bar{\phi}}$ and $\delta\tilde{\varphi}_\mathrm{d}$ read:

$$\mathrm{i}\hbar\partial_t\tilde{\bar{\phi}} = -\frac{\hbar^2}{2m\lambda^2}\Delta\tilde{\bar{\phi}} + \frac{g}{g_\mathrm{aa}\lambda^3}\left[U(\mathbf{r}) + \bar{N}g_\mathrm{aa}|\tilde{\bar{\phi}}|^2 - \bar{\mu}\right]\tilde{\bar{\phi}} \quad \text{(C.1)}$$

$$\begin{aligned}\mathrm{i}\hbar\partial_t\delta\tilde{\varphi}_\mathrm{d} = &-\frac{\hbar^2}{2m\lambda^2}\Delta\delta\tilde{\varphi}_\mathrm{d} \\ &+ \frac{g}{g_\mathrm{aa}\lambda^3}\left[U(\mathbf{r}) + \bar{N}g_\mathrm{aa}|\tilde{\bar{\phi}}|^2 - \bar{\mu}\right]\delta\tilde{\varphi}_\mathrm{d} \\ &+ \frac{1}{\lambda^3}N_\mathrm{b}(g_\mathrm{bb} - g_\mathrm{ab})(|\tilde{\bar{\phi}}|^2\delta\tilde{\varphi}_\mathrm{d} + \tilde{\bar{\phi}}^2\delta\tilde{\varphi}_\mathrm{d}^*).\end{aligned} \quad \text{(C.2)}$$

In the Thomas-Fermi limit the terms involving the Laplacian are small; if we neglect them we get for the time derivatives of the α and β variables defined in equations (44, 45):

$$\mathrm{i}\hbar\partial_t\alpha = 0 \quad \text{(C.3)}$$

$$\mathrm{i}\hbar\partial_t\beta = \frac{1}{\lambda^3}N_\mathrm{a}(g_\mathrm{aa} - g_\mathrm{ab})\alpha. \quad \text{(C.4)}$$

The variable α has actually been defined in a way to obtain zero on the right hand side of equation (C.3).

The first equation (C.3) is not an acceptable approximation for the evolution of α, we therefore include in $\partial_t\alpha$ the contribution of the Laplacian terms:

$$\mathrm{i}\hbar\partial_t\alpha = -\frac{\hbar^2}{2m\lambda^2}\ \mathrm{div}\left\{\alpha\left[\frac{\mathbf{grad}\ \tilde{\bar{\phi}}}{\tilde{\bar{\phi}}} - \frac{\mathbf{grad}\ \tilde{\bar{\phi}}^*}{\tilde{\bar{\phi}}^*}\right] + 2|\tilde{\bar{\phi}}|^2\ \mathbf{grad}\ \beta\right\}. \quad \text{(C.5)}$$

Furthermore, along the lines of reference [17], one can show that $\tilde{\bar{\phi}}$ has a negligible time evolution in the Thomas-Fermi limit; we can then replace $\tilde{\bar{\phi}}$ by its initial value $\bar{\phi}_0$ and we recover the first line of equation (47).

The second equation (C.4) is an acceptable approximation for the evolution of β if the neglected terms, all involving spatial derivatives of α, β or $\tilde{\tilde{\phi}}$, are small as compared to the right hand side of equation (C.4), as they are expected to be in the Thomas-Fermi limit. Neglecting these terms, we recover the second line of equation (47).

In order to estimate the order of magnitude of the neglected terms in the time derivative of β, we calculate the exact derivative:

$$\begin{aligned} \mathrm{i}\hbar\partial_t\beta = & \frac{1}{\lambda^3} N_{\mathrm{a}}(g_{\mathrm{aa}} - g_{\mathrm{ab}}) \\ & - \frac{\hbar^2}{2m\lambda^2}\, \mathbf{grad}\, \beta \cdot \left[\frac{\mathbf{grad}\tilde{\tilde{\phi}}}{\tilde{\tilde{\phi}}} - \frac{\mathbf{grad}\tilde{\tilde{\phi}}^*}{\tilde{\tilde{\phi}}^*} \right] \\ & - \frac{\hbar^2}{2m\lambda^2|\tilde{\tilde{\phi}}|^2} \left\{ \Delta\alpha - \frac{1}{2}\, \mathbf{grad}\, \alpha \cdot \left[\frac{\mathbf{grad}\tilde{\tilde{\phi}}}{\tilde{\tilde{\phi}}} + \frac{\mathbf{grad}\tilde{\tilde{\phi}}^*}{\tilde{\tilde{\phi}}^*} \right] \right. \\ & \left. - \frac{1}{2}\alpha \left[\frac{\Delta\tilde{\tilde{\phi}}}{\tilde{\tilde{\phi}}} + \frac{\Delta\tilde{\tilde{\phi}}^*}{\tilde{\tilde{\phi}}^*} \right] \right\} \cdot \end{aligned} \tag{C.6}$$

We replace $\tilde{\tilde{\phi}}$ by $\overline{\phi_0}$. We consider an eigenmode with frequency Ω_q; from equation (52) we estimate $\Delta\alpha/\alpha \sim q/R_0^2$. Assuming λ on the order of 1 we get the condition

$$\Omega_q \gg q\frac{\hbar\omega^2}{\mu} \tag{C.7}$$

which we can rewrite as

$$1 \leq \sqrt{q} \ll \frac{\Omega_{q=1}}{\hbar\omega^2/\mu}\,. \tag{C.8}$$

References

1. M.H. Anderson, J.R. Ensher, M.R. Matthews, C.E. Wieman, E.A. Cornell, Science **269**, 198 (1995); K.B. Davis, M.-O. Mewes, M.R. Andrews, N.J. van Druten, D.S. Durfee, D.M. Kurn, W. Ketterle, Phys. Rev. Lett **75**, 3969 (1995); C.C. Bradley, C.A. Sackett, R. Hulett, Phys. Rev. Lett **78**, 985 (1997). Since the first experimental achievements of BEC with alkali atoms at JILA, MIT, and Rice, condensation has been observed by other groups. See for example the WEB server `http://amo.phy.gasou.edu/bec.html/`.
2. J. Javanainen, Sung Mi Yoo, Phys. Rev. Lett. **76**, 161 (1996).
3. M.R. Andrews, C.G. Townsend, H.-J. Miesner, D.S. Durfee, D.M. Kurn, W. Ketterle, Science **275**, 637 (1997).
4. J.I. Cirac, C.W. Gardiner, M. Naraschewski, P. Zoller, Phys. Rev. A **54**, R 3714 (1996).
5. Y. Castin, J. Dalibard, Phys. Rev. A **55**, 4330 (1997).
6. E.M. Wright, D.F. Walls, J.C. Garrison, Phys. Rev. Lett. **77**, 2158 (1996).
7. P. Villain, M. Lewenstein, R. Dum, Y. Castin, L. You, A. Imamoglu, T.A.B. Kennedy, J. Mod. Opt. **44**, 1775 (1997).
8. A. Sinatra, Y. Castin, Eur. Phys. D **4**, 247 (1998).
9. D. Hall, M.R. Matthews, C. Wiemann, E.A. Cornell, Phys. Rev. Lett. **81**, 1543 (1998).
10. D. Hall, M.R. Matthews, J.R. Ensher, C. Wiemann, E.A. Cornell, Phys. Rev. Lett. **81**, 1539 (1998).
11. C.K. Law, H. Pu, N.P. Bigelow, J.H. Eberly, Phys. Rev. A **58**, 531 (1998).
12. P. Villain, M. Lewenstein, Phys. Rev. A **59**, 2250 (1999).
13. A.J. Leggett, F. Sols, Found. Phys. **21**, 353 (1991).
14. S. Stringari, Phys. Rev. Lett. **77**, 2360 (1996).
15. A. Sinatra, P. Fedichev, Y. Castin, J. Dalibard, G. Shlyapnikov, Phys. Rev. Lett. **82**, 251 (1998).
16. Y. Kagan, E.L. Surkov, G. Shlyapnikov, Phys. Rev. A. **54**, R1753 (1996); Phys. Rev. A. **55**, R18 (1997).
17. Y. Castin, R. Dum, Phys. Rev. Lett. **77**, 5315 (1996).
18. M. Lewenstein, Li You, Phys. Rev. Lett. **77**, 3489 (1996); Y. Castin, R. Dum, Phys. Rev. A **57**, 3008 (1998); see also [7].
19. Consider the case $\Omega_q = \mathrm{i}\gamma$, where $\gamma > 0$; then A_q, B_q are real positive for all time and one has: $\frac{\mathrm{d}}{\mathrm{d}t}(A_qB_q) = \frac{\gamma}{\lambda^2}B_q^2 + \frac{\gamma}{\lambda^3}A_q^2 \geq \frac{\gamma}{\lambda_{\max}^3}(A_q^2 + B_q^2) \geq \frac{2\gamma}{\lambda_{\max}^3}A_qB_b$ where $\lambda_{\max} = \max_t\lambda(t) \geq 1$.
20. Y. Castin, R. Dum, Phys. Rev. Lett. **79**, 3553 (1997).
21. The calculation was done for $g_{\mathrm{ab}}/g_{\mathrm{aa}} = 0.4596$, $g_{\mathrm{bb}}/g_{\mathrm{aa}} = 0.67$ (leading to $\sigma = 2.6\times10^{-2}\omega$) with a chemical potential $\overline{\mu} \simeq 72.5\hbar\omega$ and a deviation $\delta N_{\mathrm{a}} = -\delta N_{\mathrm{b}} = -0.1\overline{N_{\mathrm{a}}}$.
22. We do not get the linear divergence with time of the quadrupolar mode $q = 5$ predicted in [20] as the equations for $\delta\varphi_{\mathrm{d}}$ differ from the ones obtained for a single condensate, leading to a frequency of the breathing eigenmode Ω_5 very different from the one of a single condensate. The divergence of the quadrupolar mode occurs here for $\delta\varphi_{\mathrm{s}}$.
23. W.B. Colson, A. Fetter, J. Low Temp. Phys. **33**, 231 (1978); E. Goldstein, P. Meystre, Phys. Rev. A **55**, 2935 (1997).
24. More precisely we arrive at $\mathrm{div}[|\phi_0|^2\langle\delta\mathbf{v}_\varepsilon\rangle] = 0$. The velocity fields are of the form $f_\varepsilon(r)\mathbf{r}$ because the condensate wavefunctions are isotropic. Using Gauss formula we find that $f_\varepsilon \equiv 0$.
25. More precisely $\langle\delta\rho_\varepsilon\rangle$ and $\delta\rho_\varepsilon^{\mathrm{st}}$ differ by a constant; on the other hand this constant vanishes as both the density deviations have a vanishing integral over the volume of the condensate, so we conclude $\langle\delta\rho_\varepsilon\rangle = \delta\rho_\varepsilon^{\mathrm{st}}$.
26. E. Cornell (private communication).
27. We have checked numerically this statement for the JILA case by looking at the time dependence of the relative distance between the two condensates; at long times this distance oscillates at a frequency close to an eigenfrequency of the steady state condensates.
28. C.J. Myatt, E.A. Burt, R.W. Ghrist, E.A. Cornell, C.E. Wieman, Phys. Rev. Lett. **78**, 586 (1997); in the JILA experiment the states a and b actually correspond to $|F = 1, m = -1\rangle$ and $|F = 2, m = 1\rangle$, but the rate constant K_2 is close to that of $|F = 1, m = -1\rangle$ and $|F = 2, m = 2\rangle$ inelastic collisions, according to the estimation given by J.P. Burke Jr, J.L. Bohn, B.D. Esry, C.H. Greene, Phys. Rev. A **55**, R2511 (1997).
29. E.A. Burt, R.W. Ghrist, C.J. Myatt, M.J. Holland, E.A. Cornell, C.E. Wieman, Phys. Rev. Lett. **79**, 337 (1997).

4.4 Description d'un condensat à température non nulle

Aux températures expérimentales usuelles (k_BT de l'ordre du potentiel chimique μ) le nuage d'atomes non condensé contient en fait une fraction significative ($\sim 10\%$) des atomes du gaz. Lorsqu'on perturbe le gaz (en modifiant par exemple le potentiel de piégeage) la dynamique du condensat peut être modifiée par interaction avec le nuage non condensé, effet négligé dans l'équation de Gross-Pitaevskii. On s'attend à que cet effet soit important pour décrire par exemple l'amortissement d'oscillations collectives du condensat, le temps de vie d'un vortex ou d'un soliton, la cohérence de phase à température non nulle, ou encore pour déterminer la statistique du nombre de particules dans le condensat.

Le formalisme que nous avons développé est inspiré des méthodes d'optique quantique (distribution de Wigner) : les atomes sont décrits par un champ classique dont la partie lisse spatialement est donnée par la solution de Gross-Pitaevskii et la partie bruitée correspond aux fluctuations thermiques (atomes non condensés) et quantiques. Nous avons démarré ce projet dans le cadre d'une collaboration CNRS-University of Illinois, mettant en jeu du côté d'Urbana le groupe du professeur Anthony Leggett dont Carlos Lobo faisait partie à l'époque en tant que doctorant.

4.4.1 Distribution de Wigner pour un condensat à l'équilibre thermique

Une méthode bien établie pour la description d'un condensat à basse température $T \ll T_c$ est la méthode de Bogoliubov. Néanmoins, la mise en œuvre de cette méthode est très lourde lors qu'il s'agit de systèmes à trois dimensions en l'absence de symétrie particulière (comme dans le cas d'un condensat avec vortex). En outre, dans l'approximation de Bogoliubov, on traite linéairement la dynamique des modes non condensés ce qui en limite la validité aux faibles fractions non condensés et aux temps courts. Nous avons proposé et mis en œuvre une méthode stochastique pour échantillonner la distribution de Wigner d'équilibre d'un condensat de Bose-Einstein à une température $k_BT > \hbar\omega$ (situation habituellement rencontrée dans les expériences) qui, contrairement à l'application directe de la méthode de Bogoliubov, ne nécessite pas la diagonalisation de grosses matrices, et qui peut servir de point de départ pour une évolution dynamique de type champ classique. Nous avons montré analytiquement et numériquement que notre méthode est équivalente à l'approche "Number conserving Bogoliubov" développée en 1997 par Y. Castin et R. Dum, et nous avons été les premiers à calculer la distribution du nombre de particules dans le condensat à 1D et 2D en présence d'interactions.

4.4.2 Méthode de Wigner tronquée pour les condensats de Bose-Einstein

Quitte à introduire des éléments stochastiques dans son évolution, on peut remplacer le champ quantique $\hat{\psi}(r)$ par un champ classique $\psi(r)$ ou de façon équivalente l'opérateur densité $\hat{\sigma}$ du système par une distribution de quasi probabilité classique P, de telle sorte que les moyennes quantiques sont reproduites par des moyennes classiques sur ψ ou sur P. Déterminer l'évolution exacte de la fonction de quasi-probabilité P comporte des difficultés intrinsèques car elle revient à la solution exacte du problème quantique à N corps. Les approches approximées les plus courantes sont celles des distributions de Glauber P,

de la fonction Q et de la fonction de Wigner W. On s'attend en général à que ces approches dites de champ classique soient valables pour décrire des modes dont le nombre d'occupation est élevé (condition nécessaire mais pas toujours suffisante). Il se trouve que dans l'approche de Wigner cette contrainte est moins forte et l'approche est même exacte pour un Hamiltonien quadratique.

Dans l'approche de Wigner tronquée, la composante stochastique venant des fluctuations thermiques et des fluctuations quantiques est contenue dans l'état initial, et l'évolution du champ classique se fait avec une équation formellement identique à l'équation de Gross-Pitaevskii utilisé pour décrire un condensat pur. Dans [17] nous avons montré la supériorité de l'approche de Wigner tronquée sur celle de Bogoliubov pour décrire le brouillage des oscillations d'un condensat à 1D suite à un changement brusque de son potentiel de confinement. Suite à une augmentation importante de la fraction non condensée, l'approche linéarisée de Bogoliubov sort de son domaine de validité. Toutefois un travail de fond nous a permis de mettre en évidence des limites de validité de l'approche de Wigner tronquée pour les condensats dans les systèmes à 3D. Le problème réside dans la relaxation du champ vers l'état d'équilibre thermique d'un champ classique où les nombres d'occupation des modes sont donnés par le théorème d'équipartition. La température à laquelle se thermalise le champ dépend du nombre de modes dans la simulation. Dans le cas de l'approche de Wigner tronquée où chaque mode est initialement "rempli" par le bruit quantique ceci entraîne un "réchauffement" non physique du système ce qui donne une contrainte que nous avons pu quantifier sur le nombre de modes que l'on doit inclure dans sa simulation.

4.4.3 Publication jointe

J.Phys. B : At. Mol. Opt. Phys. **35** (2002) 3599-3631

The truncated Wigner method for Bose condensed gases: limits of validity and applications

Alice Sinatra, Carlos Lobo and Yvan Castin
Laboratoire Kastler Brossel, ENS, 24 rue Lhomond, 75 231 Paris, France Cedex 5

J. Phys. B: At. Mol. Opt. Phys. **35** (2002) 3599-3631

Abstract

We study the truncated Wigner method applied to a weakly interacting spinless Bose condensed gas which is perturbed away from thermal equilibrium by a time-dependent external potential. The principle of the method is to generate an ensemble of classical fields $\psi(r)$ which samples the Wigner quasi-distribution function of the initial thermal equilibrium density operator of the gas, and then to evolve each classical field with the Gross-Pitaevskii equation. In the first part of the paper we improve the sampling technique over our previous work [Jour. of Mod. Opt. **47**, 2629-2644 (2000)] and we test its accuracy against the exactly solvable model of the ideal Bose gas. In the second part of the paper we investigate the conditions of validity of the truncated Wigner method. For short evolution times it is known that the time-dependent Bogoliubov approximation is valid for almost pure condensates. The requirement that the truncated Wigner method reproduces the Bogoliubov prediction leads to the constraint that the number of field modes in the Wigner simulation must be smaller than the number of particles in the gas. For longer evolution times the nonlinear dynamics of the noncondensed modes of the field plays an important role. To demonstrate this we analyse the case of a three dimensional spatially homogeneous Bose condensed gas and we test the ability of the truncated Wigner method to correctly reproduce the Beliaev-Landau damping of an excitation of the condensate. We have identified the mechanism which limits the validity of the truncated Wigner method: the initial ensemble of classical fields, driven by the time-dependent Gross-Pitaevskii equation, thermalises to a classical field distribution at a temperature $T_{\rm class}$ which is larger than the initial temperature T of the quantum gas. When $T_{\rm class}$ significantly exceeds T a spurious damping is observed in the Wigner simulation. This leads to the second validity condition for the truncated Wigner method, $T_{\rm class} - T \ll T$, which requires that the maximum energy $\epsilon_{\rm max}$ of the Bogoliubov modes in the simulation does not exceed a few $k_B T$.

PACS: 03.75.Fi, 05.10.Gg, 42.50.-p

1 Introduction

In Ref. [1] the formalism of the Wigner representation of the density operator, widely used in quantum optics, was proposed as a possible way to study the time evolution of Bose-Einstein condensates in the truncated Wigner approximation [2]. Like other existing approximate methods, such as the time-dependent Bogoliubov approach, it allows us to go beyond the commonly used Gross-Pitaevskii equation, in which the interactions between the condensate and the noncondensed atoms are neglected. Our aim in this paper is to illustrate the advantages and the limits of the truncated Wigner approach.

For reasons of clarity we will address two different situations in two separate parts of the paper: (i) the case of a stationary Bose condensed gas in thermal equilibrium and (ii) a time-dependent case when the gas is brought out of equilibrium by a known external perturbation. Even if the stationary gas is the starting point for both situations, the problems raised by the application of the Wigner method are of a different nature in the two cases.

(i) In the case of a Bose condensed gas in thermal equilibrium, the first step is to calculate the Wigner quasi-distribution function associated with the N-body density operator $\hat{\sigma}$, which is a functional of a complex classical field $\psi(r)$. We showed in [3] that this is possible in the Bogoliubov approximation when the noncondensed fraction of atoms is small. With such an approximation, the Hamiltonian of the system is quadratic in the noncondensed field and its Wigner functional is a Gaussian. After that, we went through some more technical work to calculate the Wigner functional of the whole matter field including the condensate mode. In our derivation we made further approximations in addition to the Bogoliubov approximation. This introduces some artifacts in the Wigner functional as far as the condensate mode is concerned [3]. These artifacts are, however, insignificant when the number of thermally populated

modes is much larger than one, or $k_B T \gg \hbar\omega$ in an isotropic trap of harmonic frequency ω, so that the fluctuations in the number of condensate particles, due to finite temperature, are much larger than one. Once the Wigner functional for the Bose condensed gas in thermal equilibrium is calculated, the goal is to be able to sample it numerically in order to compute averages of observables and probability distributions. In practice, this step consists in generating a set of random atomic fields $\{\psi(r)\}$ according to a probability distribution dictated by the Wigner functional. We have now developed a more efficient algorithm to sample the Wigner functional in the case of spatially inhomogeneous condensates in a trapping potential than the one that we had presented in a previous paper [4], which we will explain here in detail. As far as the equilibrium Bose condensed gases are concerned, our method in its regime of validity, is equivalent to the $U(1)$ symmetry-preserving Bogoliubov approach of [5, 6], up to second order in the small parameter of the theory, which is the square root of the noncondensed fraction. Compared with the traditional Bogoliubov approach, our method presents, however, the practical advantage of avoiding the direct diagonalisation of the Bogoliubov matrix, which is a heavy numerical task in 2D and 3D in the absence of rotational symmetry. Moreover, due to the stochastic formulation we adopt, our method gives us access to single realisations and to the probability distribution of some observables such as the number of condensate particles, not easily accessible by the traditional Bogoliubov method. We show some examples where we compare the probability distribution of the number of condensate particles obtained with our method with an exact calculation in case of the ideal Bose gas.

(ii) Let us now consider the situation of a Bose condensed gas at thermal equilibrium which is brought out of equilibrium by a perturbation. The initial Wigner functional then evolves in time according to a kind of Fokker-Planck equation containing first and third order derivatives with respect to the atomic field. Numerical simulation of the exact evolution equation for the Wigner functional has intrinsic difficulties, as one would expect, since it represents the exact solution of the quantum many-body problem [7]. We are less ambitious here, and we rely on an approximation that consists in neglecting the third order derivatives in the evolution equation. This is known as the truncated Wigner approximation [1]. For a delta interaction potential between a finite number of low energy modes of the atomic field, the third order derivatives are expected to give a contribution which is smaller than that of the first order derivatives when the occupation numbers of the modes are much larger than unity. If we reason in terms of the stochastic fields $\psi(r,t)$ which sample the Wigner distribution at time t, then the truncated Wigner approximation corresponds to evolving the initial set of stochastic fields according to the Gross-Pitaevskii equation [8]:

$$i\hbar\partial_t\psi = \left[-\frac{\hbar^2}{2m}\Delta + U(r,t) + g|\psi|^2\right]\psi, \tag{1}$$

where r is the set of single particle spatial coordinates, m is the atom mass, U is the trapping potential and g is the coupling constant originating from the effective low energy interaction potential $V(r_1 - r_2) = g\delta(r_1 - r_2)$ and proportional to the s-wave scattering length a of the true interaction potential, $g = 4\pi\hbar^2 a/m$. Here, the crucial difference with respect to the usual Gross-Pitaevskii equation is that the field is now the whole matter field rather than the condensate field.

This procedure of evolving a set of random fields with the Gross-Pitaevskii equation is known as the classical field approximation, since equation (1) can be formally obtained from the Heisenberg equation of motion for the atomic field operator $\hat{\psi}$ by replacing the field operator by a c-number field. The classical field approximation has already been used in the Glauber-P representation to study the formation of the condensate [9, 10, 11, 12, 13]. We face here a different situation: we assume an initially existing condensate and we use the Wigner representation, rather than the Glauber-P representation. The Wigner representation is in fact known in quantum optics to make the classical field approximation more accurate than in the Glauber-P representation because the "right amount" of quantum noise is contained in the initial state [14]. For a single mode system with a Kerr type nonlinearity and an occupation number n, the term neglected in the Wigner evolution equation is a third order derivative which is $1/n^2$ times smaller than the classical field term, whereas the term neglected in the Glauber-P evolution equation is a second order derivative, which is only $1/n$ times smaller than the classical field term. In the case of Bose-Einstein condensates however, we face a highly multimode problem and, therefore, the accuracy of the truncated Wigner approach needs to be revisited. We approach this problem in the second part of the paper. The strategy we adopt is to compare the predictions of the truncated Wigner method with existing well-established results: first with the time-dependent Bogoliubov approach and then with the Landau-Beliaev damping of a collective excitation in a spatially homogeneous condensate.

2 Basic notations and assumptions

2.1 Model Hamiltonian on a discrete grid

Let us express a simple quantity like the mean atomic density using the Wigner representation:

$$\langle\hat{\psi}^\dagger(r)\hat{\psi}(r)\rangle = \langle\psi^*(r)\psi(r)\rangle_W - \frac{1}{2}\langle[\hat{\psi}(r),\hat{\psi}^\dagger(r)]\rangle, \tag{2}$$

where $\langle\ldots\rangle_W$ represents the average over the Wigner quasi-distribution function. This shows that the discretisation of the problem on a finite grid is necessary to avoid infinities: in the continuous version of the problem, $[\hat{\psi}(r),\hat{\psi}^\dagger(r)] = \delta(0) = +\infty$. Physically this divergence comes from the fact that, in the Wigner point of view, some noise is included in each mode of the classical field ψ to mimic quantum noise; this extra noise adds up to infinity for a system with an infinite number of modes. Therefore we use, from the beginning, a discrete formulation of our problem which will make it also suitable for numerical simulations.

We consider a discrete spatial grid forming a box of length L_ν along the direction $\nu = x, y, z$ with an even number n_ν of equally spaced points. We denote $\mathcal{N} \equiv \prod_\nu n_\nu$ the number of points on the grid, $V \equiv \prod_\nu L_\nu$ the volume of the grid and $dV \equiv V/\mathcal{N}$ the volume of the unit cell of the grid. We take periodic boundary conditions in the box [15]. We can then expand the field operator over plane waves

$$\hat{\psi}(r) = \sum_k \hat{a}_k \frac{1}{\sqrt{V}} e^{ik\cdot r}, \tag{3}$$

where $\hat{a}_k$ annihilates a particle of momentum k and where the components of k are $k_\nu = 2\pi j_\nu/L_\nu$ with the integers j_ν running from $-n_\nu/2$ to $n_\nu/2 - 1$. We then have the inverse formula:

$$\hat{a}_k = dV \sum_r \frac{1}{\sqrt{V}} e^{-ik\cdot r}\hat{\psi}(r). \tag{4}$$

For each node r_i on the spatial grid, we find the commutation relations for the field operator:

$$[\hat{\psi}(r_i),\hat{\psi}^\dagger(r_j)] = \frac{1}{dV}\delta_{i,j} \tag{5}$$

and the discretised model Hamiltonian that we use is:

$$\hat{H} = \sum_k \frac{\hbar^2k^2}{2m}\hat{a}_k^\dagger\hat{a}_k + dV\sum_r U(r)\hat{\psi}^\dagger(r)\hat{\psi}(r) + \frac{g}{2}dV\sum_r \hat{\psi}^\dagger(r)\hat{\psi}^\dagger(r)\hat{\psi}(r)\hat{\psi}(r)\,. \tag{6}$$

The first term in (6) is the kinetic energy, which is easy to calculate in the momentum representation. In the position representation, the kinetic energy is a matrix that couples the $\mathcal{N}$ points of the grid. In the following we will write it as $p^2/2m$. The second term is the trapping potential. The last term represents the atomic interactions modeled by a discrete Kronecker δ potential

$$V(r_1 - r_2) = \frac{g}{dV}\delta_{r_1,r_2}, \tag{7}$$

with a coupling constant $g = 4\pi\hbar^2a/m$, where a is the s-wave scattering length of the true interaction potential.

We indicate briefly some requirements for the discrete Hamiltonian to be a good representation of reality. First, the spatial step of the grid should be smaller than the macroscopic physical scales of the problem:

$$dx_\nu \ll \xi \quad \text{and} \quad dx_\nu \ll \lambda, \tag{8}$$

where $\xi = 1/\sqrt{8\pi\rho|a|}$ is the healing length for the maximal atomic density ρ and $\lambda = \sqrt{2\pi\hbar^2/mk_BT}$ is the thermal de Broglie wavelength at temperature T. Secondly, the spatial step of the grid should be larger than the absolute value of the scattering length a:

$$dx_\nu \gg |a|, \tag{9}$$

so that the scattering amplitude of the model potential (7) is indeed very close to a. Another way of saying this is that the model potential (7) can be treated in the Born approximation for the low energy waves. A more precise treatment, detailed in the appendix A, is to replace in (7) the coupling constant g by its bare value g_0 adjusted so that the scattering length of the model potential on the grid is exactly equal to a.

2.2 Wigner representation

The Wigner quasi-distribution function associated with the N-body density operator $\hat{\sigma}$ is defined as the Fourier transform of the characteristic function χ:

$$W(\psi) \equiv \int \prod_r \frac{d\mathrm{Re}\,\gamma(r)\, d\mathrm{Im}\,\gamma(r) dV}{\pi^2}\, \chi(\gamma)\, e^{dV \sum_r \gamma^*(r)\psi(r) - \gamma(r)\psi^*(r)} \tag{10}$$

$$\chi(\gamma) = \mathrm{Tr}\left[\hat{\sigma} e^{dV \sum_r \gamma(r)\hat{\psi}^\dagger(r) - \gamma^*(r)\hat{\psi}(r)}\right], \tag{11}$$

where $\gamma(r)$ is a complex field on the spatial grid and $\hat{\sigma}$ is the density operator of the system. With this definition the Wigner function is normalised to unity:

$$\int \prod_r d\mathrm{Re}\psi(r) d\mathrm{Im}\psi(r) dV\, W(\psi) = 1. \tag{12}$$

We recall that the moments of the Wigner function correspond to totally symmetrised quantum expectation values, i.e.,

$$\langle O_1 \dots O_n \rangle_W = \frac{1}{n!} \sum_P \mathrm{Tr}\left[\hat{O}_{P(1)} \dots \hat{O}_{P(n)} \hat{\sigma}\right], \tag{13}$$

where the sum is taken over all the permutations P of n objects, O_k stands for ψ or ψ^* in some point of the grid and $\hat{O}_k$ is the corresponding field operator.

The equation of motion for the density operator $\hat{\sigma}$

$$\frac{d}{dt}\hat{\sigma} = \frac{1}{i\hbar}[\hat{H}, \hat{\sigma}] \tag{14}$$

can be written exactly as the following equation of motion for the Wigner distribution:

$$i\hbar \frac{\partial W}{\partial t} = \sum_r \frac{\partial}{\partial \psi(r)}(-f_\psi W) + \frac{g}{4(dV)^2} \frac{\partial^3}{\partial^2 \psi(r) \partial \psi^*(r)} (\psi(r) W) - \text{c.c.}, \tag{15}$$

with a drift term

$$f_\psi = \left[\frac{p^2}{2m} + U(r,t) + g\psi^*\psi - \frac{g}{dV}\right] \psi. \tag{16}$$

The truncated Wigner approximation consists in neglecting the cubic derivatives in the equation for W. The resulting equation reduces to the drift term whose effect amounts to evolving the field ψ according to an equation which resembles the Gross-Pitaevskii equation (1). The constant term $-g/dV$ inside the brackets of the above equation can be eliminated by a redefinition of the global phase of ψ, which has no physical consequence for observables conserving the number of particles.

3 Sampling the Wigner functional for a Bose condensed gas in thermal equilibrium

In [3] we derive an expression of the Wigner functional for a Bose condensed gas in thermal equilibrium in the frame of the $U(1)$ symmetry-preserving Bogoliubov approach [5, 6], in which the gas has a fixed total number of particles equal to N. We first introduce the approximate condensate wavefunction $\phi(r)$, which is a solution of the time-independent Gross-Pitaevskii equation:

$$H_{\mathrm{gp}}\phi \equiv \left[\frac{p^2}{2m} + U(r, t=0) + Ng|\phi|^2 - \mu\right] \phi = 0. \tag{17}$$

We then split the classical field $\psi(r)$ into components orthogonal and parallel to the condensate wavefunction $\phi(r)$:

$$\psi(r) = a_\phi \phi(r) + \psi_\perp(r) \tag{18}$$

$$a_\phi \equiv dV \sum_r \phi^*(r)\psi(r). \tag{19}$$

The Wigner functional provides us with the joint probability distributions of the transverse classical field $\psi_\perp(r)$, that we call the noncondensed field, and of the complex amplitude a_ϕ. Due to the $U(1)$ symmetry-preserving character of the theory, the final Wigner functional is of the form [3]

$$W(\psi) = \int \frac{d\theta}{2\pi}\, W_0(e^{-i\theta}\psi). \tag{20}$$

This means that one can sample the distribution $W(\psi)$ by (i) choosing a random field ψ according to the distribution $W_0(\psi)$, (ii) choosing a random global phase θ uniformly distributed between 0 and 2π, and (iii) forming the total atomic field as $\psi_{\rm tot}(r) = e^{i\theta}\psi(r)$. In practice, the global phase factor $e^{i\theta}$ is unimportant to calculate the expectation value of observables that conserve the number of particles. Since the other observables have a vanishing mean value, we can limit ourselves to the sampling of the $\theta = 0$ component of the Wigner functional, $W_0(\psi)$.

3.1 Sampling the distribution of the noncondensed field

The first step of the sampling procedure consists in generating a set of noncondensed fields $\{\psi_\perp\}$ according to the probability distribution

$$P(\psi_\perp) \propto \exp\left[-dV\ (\psi_\perp^*, \psi_\perp)\cdot M \begin{pmatrix} \psi_\perp \\ \psi_\perp^* \end{pmatrix}\right], \tag{21}$$

where we have collected all the components of $\psi_\perp$ and $\psi_\perp^*$ in a single vector with $2\mathcal{N}$ components, M is the $2\mathcal{N}\times 2\mathcal{N}$ matrix:

$$M = \eta \tanh\frac{\mathcal{L}}{2k_BT} \tag{22}$$

with

$$\eta = \begin{pmatrix} 1 & 0 \\ 0 & -1 \end{pmatrix}, \tag{23}$$

and where $\mathcal{L}$ is a $2\mathcal{N}\times 2\mathcal{N}$ matrix, which is the discretised version of the Bogoliubov operator of [5]:

$$\mathcal{L} = \begin{pmatrix} H_{\rm gp} + Ng\mathcal{Q}|\phi|^2\mathcal{Q} & Ng\mathcal{Q}\phi^2\mathcal{Q}^* \\ -Ng\mathcal{Q}^*\phi^{*2}\mathcal{Q} & -H_{\rm gp}^* - Ng\mathcal{Q}^*|\phi|^2\mathcal{Q}^* \end{pmatrix}. \tag{24}$$

In this expression the $\mathcal{N}\times\mathcal{N}$ matrix $\mathcal{Q}$ projects orthogonally to the condensate wavefunction ϕ in the discrete spatial grid $\{r_i\}$ representation,

$$\mathcal{Q}_{ij} = \delta_{ij} - dV\phi(r_i)\phi^*(r_j). \tag{25}$$

Note that the matrix M can be shown to be Hermitian from the fact that $\mathcal{L}^\dagger = \eta\mathcal{L}\eta$.

3.1.1 Direct diagonalisation of $\mathcal{L}$

If the eigenvectors of $\mathcal{L}$ are known, we can use the following modal expansion:

$$\begin{pmatrix} \psi_\perp \\ \psi_\perp^* \end{pmatrix} = \sum_k b_k \begin{pmatrix} u_k \\ v_k \end{pmatrix} + b_k^* \begin{pmatrix} v_k^* \\ u_k^* \end{pmatrix}, \tag{26}$$

where the sum is to be taken over all eigenmodes (u_k, v_k) of $\mathcal{L}$ normalisable as $\langle u_k|u_k\rangle - \langle v_k|v_k\rangle = 1$, with corresponding eigenvalues ϵ_k. Since the condensate is assumed to be in a thermodynamically stable or metastable state, all the ϵ_k are positive [16]. The probability distribution (21) is then a simple product of Gaussian distributions for the complex amplitudes b_k:

$$P_k(b_k) = \frac{2}{\pi}\tanh\left(\frac{\epsilon_k}{2k_BT}\right)\exp\left[-2|b_k|^2\tanh\left(\frac{\epsilon_k}{2k_BT}\right)\right]. \tag{27}$$

Each Gaussian distribution is easily sampled numerically [17]. Note that, even at zero temperature, the Gaussian distribution has a nonzero width: this is a signature of the extra noise introduced in the Wigner representation to mimic quantum noise.

3.1.2 Brownian motion simulation

The sampling of the distribution (21) can actually be performed without diagonalisation of $\mathcal{L}$ (an advantage for spatially inhomogeneous Bose condensates in the absence of rotational symmetry [4]) by means of a Brownian motion simulation for the noncondensed field:

$$d\begin{pmatrix} \psi_\perp \\ \psi_\perp^* \end{pmatrix} = -\alpha\, dt \begin{pmatrix} \psi_\perp \\ \psi_\perp^* \end{pmatrix} + Y \begin{pmatrix} d\xi \\ d\xi^* \end{pmatrix}, \tag{28}$$

where the field $d\xi$ is the noise term. The time t here is a purely fictitious time with no physical meaning and will be taken to be dimensionless. On our discrete grid, $\psi_\perp$ is a vector with $\mathcal{N}$ components, $d\xi$ is a Gaussian random vector of $\mathcal{N}$ components with zero mean and a covariance matrix $\langle d\xi_i d\xi_j^* \rangle$ equal to $(2dt/dV)\delta_{i,j}$, while α, Y are $2\mathcal{N} \times 2\mathcal{N}$ matrices. To ensure that the Brownian motion relaxes towards the correct probability distribution (21) we require that the drift matrix α and the diffusion matrix $D \equiv Y(Y^\dagger)$ satisfy a generalised Einstein's relation [4]:

$$D^{-1}\alpha = \alpha^\dagger D^{-1} = 2M, \tag{29}$$

where M is the matrix (22). There is, of course, no unique choice for α and Y. With respect to our previous work [4], we have largely improved the efficiency of our simulation by a different choice of α, Y and by the use of a second order integration scheme of the stochastic differential equation (28), more efficient than the usual first order Euler's scheme. In the appendix B we give a detailed description of these improvements, useful to the reader who is interested in implementing the numerical algorithm.

3.2 Sampling the condensate amplitude

We now have to sample the condensate amplitude a_ϕ from the Wigner functional W_0. This amplitude turns out to be real, and can be written as

$$a_\phi = \sqrt{N_0} \qquad \text{where} \qquad N_0 = a_\phi^* a_\phi\,. \tag{30}$$

Since we already know how to generate the noncondensed part of the field $\psi_\perp$, we have to sample the conditional distribution $P(N_0|\psi_\perp)$.

Due to a first approximation that we have performed in [3], which consists in treating "classically" the condensate mode and neglecting its quantum fluctuations in the limit of a large number of condensate particles, the probability distribution $P(N_0)$, that we will obtain by averaging $P(N_0|\psi_\perp)$ over the stochastic realisations of the noncondensed field $\psi_\perp$, actually coincides with the probability distribution of the number of condensed particles $\hat{a}_\phi^\dagger \hat{a}_\phi$ so that within this approximation we have:

$$\langle N_0 \rangle = \langle \hat{a}_\phi^\dagger \hat{a}_\phi \rangle, \tag{31}$$

$$\mathrm{Var}(N_0) = \mathrm{Var}(\hat{a}_\phi^\dagger \hat{a}_\phi), ... \tag{32}$$

Note that this should not be the case for the exact Wigner distribution as, e.g., the average $\langle N_0 \rangle$ should be equal to $\langle \hat{a}_\phi^\dagger \hat{a}_\phi \rangle + 1/2$ and the variance of N_0 should exceed the variance of $\hat{a}_\phi^\dagger \hat{a}_\phi$ by $1/4$.

We show in [3] that, when the number of thermally populated modes is much larger than one, the width in N_0 of the conditional distribution $P(N_0|\psi_\perp)$ is much narrower than the width of the distribution $P(N_0)$, so that we can replace the distribution $P(N_0|\psi_\perp)$ by a delta function centered on its mean value. With this second, more severe, approximation we get for the sampling:

$$N_0 \simeq \mathrm{Mean}(N_0|\psi_\perp) = C - \frac{1}{2} dV (\psi_\perp^*, \psi_\perp) \cdot \left[\mathrm{Id} - M^2\right] \begin{pmatrix} \psi_\perp \\ \psi_\perp^* \end{pmatrix}, \tag{33}$$

where the constant C is finite only in the discretised version and is given by

$$C = N - \frac{1}{4}\mathrm{Tr}\, M + \frac{1}{2}\mathrm{Tr}\, \mathcal{Q}. \tag{34}$$

Here, the trace of the projector $\mathcal{Q}$ is simply the number of modes in the simulation minus one.

The second approximation (33) does not introduce errors in the average $\langle N_0 \rangle$. We are able to verify a posteriori that the error introduced in the variance $\langle N_0^2 \rangle - \langle N_0 \rangle^2$ is small in the following way: on one hand we calculate the variance of N_0 ($\mathrm{Var}(N_0)$), by using (33). On the other hand we calculate the variance $\mathrm{Var}(\delta\hat{N})$ of the number of noncondensed particles by using directly the ensemble of noncondensed fields

$\{\psi_\perp\}$. Since the total number of particles is fixed one should have $\mathrm{Var}(N_0) = \mathrm{Var}(\hat{a}_\phi^\dagger \hat{a}_\phi) = \mathrm{Var}(\hat{\psi}_\perp^\dagger \hat{\psi}_\perp)$, and deviation from this identity gives us the error of $\mathrm{Var}(N_0)$.

We are now ready to form the total field:

$$\psi(r) = \sqrt{N_0}\left(\phi(r) + \frac{\phi_\perp^{(2)}(r)}{N}\right) + \psi_\perp(r). \tag{35}$$

The function $\phi_\perp^{(2)}$ is a correction to the condensate wavefunction including the condensate depletion neglected in the Gross-Pitaevskii equation (17) and the mean field effect of the noncondensed particles. This correction can be calculated from the ensemble of noncondensed fields $\{\psi_\perp\}$ as explained in [4]. As we will see in section 4.1 its contribution to the one-body density matrix is of the same order as that of $\psi_\perp$ and therefore has to be included.

3.3 Tests and applications: Distribution of the number of condensate particles

We can use the sampling procedure described above to calculate some equilibrium properties of the Bose condensed gas. Recently, the variance of the number of particles in the condensate has drawn increasing attention [18, 19, 20]. In our case we have access to the whole probability distribution for N_0 by applying equation (33) to the ensemble of stochastic noncondensed fields $\{\psi_\perp\}$.

3.3.1 Ideal Bose gas

As a test we check our probability distribution for the number of condensate particles against the exact one for the ideal Bose gas ($g = 0$) in one and two dimensions. The results are in figure 1.

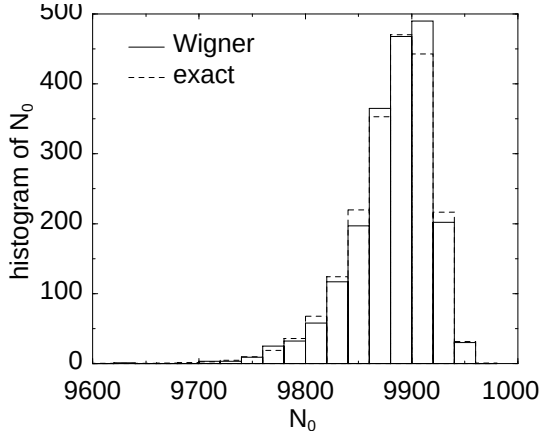

Figure 1: Probability distribution in the canonical ensemble of the number of condensate particles for the ideal Bose gas in thermal equilibrium in an isotropic harmonic potential $U(r) = \frac{1}{2}m\omega^2 r^2$. (a) In a 1D model for $k_B T = 30\hbar\omega$, and $N = 10\,000$. For the Wigner simulation 2000 realisations have been performed on a grid with 128 points. For the exact Bogoliubov rejection method described in the end of this subsection on the ideal gas, 400 000 realisations have been performed so that the statistical error is less than one per cent for the most populated channels of the histogram. (b) In a 2D model for $k_B T = 30\hbar\omega$, and $N = 8\,000$. For the Wigner simulation 500 realisations have been performed on a grid with 128×128 points. For the exact sampling 100 000 realisations have been performed.

The distributions of the number of condensed particles N_0 are clearly not Gaussian. To characterise them, besides the mean and the variance of N_0 one can introduce the skewness defined as:

$$\mathrm{skew}(N_0) = \frac{\langle (N_0 - \langle N_0 \rangle)^3 \rangle}{(\langle N_0^2 \rangle - \langle N_0 \rangle^2)^{3/2}}. \tag{36}$$

For the parameters of figure 1 we give the mean, the standard deviation and the skewness of N_0 obtained from the simulation, together with their exact values:

	1D simulation	1D exact	2D simulation	2D exact
$\langle N_0 \rangle$	9882.	9880.	6403.	6415.
ΔN_0	37.5	38.3	75.9	77.1
skew(N_0)	-1.20	-1.16	-0.40	-0.334

In what follows we explain in some detail how the exact probability distribution for the ideal Bose gas is obtained. Let $\hat{\sigma}$ be the density operator for the ideal Bose gas in the canonical ensemble:

$$\hat{\sigma} = \frac{1}{Z}\, e^{-\beta \hat{H}}\, p_N. \tag{37}$$

The operator p_N projects onto the subspace with N particles, and $\hat{H} = \sum_k \epsilon_k \hat{a}_k^\dagger \hat{a}_k$ is written in the eigenbasis of the trapping potential. In the spirit of the number conserving Bogoliubov method, we eliminate the condensate mode by writing

$$\hat{a}_0^\dagger \hat{a}_0 = \hat{N} - \sum_{k \neq 0} \hat{a}_k^\dagger \hat{a}_k \,. \tag{38}$$

Since the total number of particles is fixed we can replace the operator $\hat{N}$ by the c-number N in (38). Furthermore we establish a one to one correspondence between (i) each configuration of excited modes $\{n_k, k > 0\}$ having a number of excited particles $N' = \sum_k n_k$ lower than N and (ii) each configuration of the whole system with n_k particles in excited mode k and $N - N'$ particles in the condensate. We then obviously have to reject the configurations of excited modes for which the number of particles in the excited states N' is larger than N. This amounts to reformulating the effect of the projector p_N in terms of an Heaviside function Y. We then rewrite $\hat{\sigma}$ as:

$$\hat{\sigma} = \frac{1}{Z}\, e^{-\beta \epsilon_0 N}\, e^{-\beta \sum_{k \neq 0} (\epsilon_k - \epsilon_0) \hat{a}_k^\dagger \hat{a}_k}\, Y\left(N - \sum_{k \neq 0} \hat{a}_k^\dagger \hat{a}_k \right). \tag{39}$$

For the sampling procedure we use a rejection method i.e. we sample the probability distribution of the number of particles n_k in each mode $k \neq 0$ without the constraint imposed by the Heaviside function and we reject configurations with $N' > N$. In this scheme we have to generate the n_k, $k = 1, \ldots, \mathcal{N}$, according to the probability distribution

$$p_k(n_k) = \lambda_k^{n_k}(1 - \lambda_k) \quad \text{with} \quad \lambda_k = e^{-\beta(\epsilon_k - \epsilon_0)}. \tag{40}$$

For each k we proceed as follows: in a loop over n_k starting from 0 we generate a random number ϵ uniformly distributed in the interval $[0, 1]$ and we compare it with λ_k: if $\epsilon < \lambda_k$, we proceed with the next step of the loop, otherwise we exit from the loop and the current value of n_k is returned.

The calculation can also be done in the Bogoliubov approximation, that is by neglecting the Heaviside function in (39). For the parameters of figure 1 this is actually an excellent approximation, as the mean population of the condensate mode is much larger than its standard deviation, and the corresponding approximate results are in practice indistinguishable from the exact ones. The predictions of this Bogoliubov approximation for the first three moments of N_0 involve a sum over all the excited modes of the trapping potential:

$$\begin{aligned} \langle N_0 \rangle &= N - \sum_{k \neq 0} \bar{n}_k \\ \mathrm{Var}(N_0) &= \sum_{k \neq 0} \bar{n}_k (1 + \bar{n}_k) \\ \langle (N_0 - \langle N_0 \rangle)^3 \rangle &= \sum_{k \neq 0} 2\bar{n}_k^3 + 3\bar{n}_k^2 + \bar{n}_k \end{aligned} \tag{41}$$

where $\bar{n}_k = 1/(\exp(\beta(\epsilon_k - \epsilon_0)) - 1)$ is the mean occupation number of the mode k. In the limit $k_B T \gg \hbar\omega$ for an isotropic harmonic trap an analytical calculation, detailed in the appendix C, shows that the skewness tends to a constant in 1D, tends to zero logarithmically in 2D and tends to zero polynomially in 3D [21]:

$$\mathrm{skew}_{1\mathrm{D}}(N_0) \simeq -\frac{2\zeta(3)}{\zeta(2)^{3/2}} = -1.139547\ldots$$

$$\begin{aligned} \mathrm{skew}_{2\mathrm{D}}(N_0) &\simeq -\frac{2(\zeta(2)+\zeta(3))}{(\log(k_BT/\hbar\omega)+1+\gamma+\zeta(2))^{3/2}} \\ \mathrm{skew}_{3\mathrm{D}}(N_0) &\simeq -\frac{\log(k_BT/\hbar\omega)+\gamma+\frac{3}{2}+3\zeta(2)+2\zeta(3)}{(k_BT/\hbar\omega)^{3/2}\{\zeta(2)+(3\hbar\omega/2k_BT)[\log(k_BT/\hbar\omega)+\gamma+1-\zeta(2)/3]\}^{3/2}} \end{aligned} \quad (42)$$

where ζ is the Riemann Zeta function and $\gamma = 0.57721\ldots$ is Euler's constant.

3.3.2 Interacting case

As an example we show in figure 2 the probability distribution for the number of condensate particles in the interacting case to demonstrate that the large skewness of N_0 in 1D can even be enhanced in presence of interaction: the skewness of N_0 in figure 2 is equal to -2.3. We have been able [22] to calculate $P(N_0)$ in the Bogoliubov approximation in the interacting case starting from the sampling of the Wigner distribution of the noncondensed field (21). We compare the results with the Wigner approach in the same figure. As expected the agreement is excellent in the regime $k_BT = 30\hbar\omega \gg \hbar\omega$.

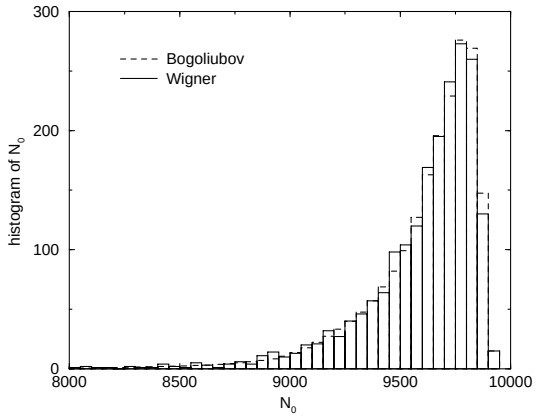

Figure 2: Probability distribution of the number of condensate particles in the canonical ensemble for a 1D interacting Bose gas in thermal equilibrium in a harmonic trap $U(x) = \frac{1}{2}m\omega^2x^2$, with $k_BT = 30\hbar\omega$, $\mu = 14.1\hbar\omega$ and $N = 10\,000$, corresponding to a coupling constant $g = 0.01\hbar\omega(\hbar/m\omega)^{1/2}$. The results have been obtained with the Wigner method using 2000 realisations on a grid with 128 points. The dashed line is the histogram of the probability distribution of N_0 in the Bogoliubov approximation generated using the same 2000 realisations, obtained with a method described in [22].

4 The truncated Wigner method for a time-dependent Bose condensed gas

In this section we investigate the conditions of validity of the truncated Wigner approach for time-dependent Bose-Einstein condensates. The strategy that we adopt is to compare the predictions of the truncated Wigner approach to well-established theories: the time-dependent Bogoliubov approach in section 4.1 and the Landau-Beliaev damping of a collective excitation in a spatially homogeneous condensate, in section 4.2.

4.1 The truncated Wigner method vs the time-dependent Bogoliubov method

In this section we investigate analytically the equivalence between the time-dependent Bogoliubov approach of [5] and the truncated Wigner method in the limit in which the noncondensed fraction is small.

We begin by sketching the number conserving Bogoliubov method of Ref. [5]. We split the atomic field operator into components parallel and orthogonal to the exact time-dependent condensate wavefunction ϕ_{ex} [23] (omitting for simplicity the time label for the field operators and for the condensate wavefunction):

$$\hat{\psi}(r) = \hat{a}_{\phi_{\mathrm{ex}}}\phi_{\mathrm{ex}}(r) + \hat{\psi}_\perp(r) \quad (43)$$

and we consider the limit

$$N \to \infty \qquad N\,g = \text{constant} \qquad T = \text{constant} \qquad \mathcal{N} = \text{constant}. \tag{44}$$

In [5] one performs a formal systematic expansion in powers of $1/\sqrt{N}$ of the exact condensate wavefunction $\phi_{\rm ex}$

$$\phi_{\rm ex}(r) = \phi(r) + \frac{\phi^{(1)}(r)}{\sqrt{N}} + \frac{\phi^{(2)}(r)}{N} + \dots \tag{45}$$

and of the noncondensed field

$$\hat{\Lambda}_{\rm ex}(r) \equiv \frac{1}{\sqrt{N}} \hat{a}^\dagger_{\phi_{\rm ex}} \psi_\perp(r) = \hat{\Lambda}(r) + \frac{1}{\sqrt{N}} \hat{\Lambda}^{(1)}(r) + \dots . \tag{46}$$

Note that in the lowest order approximation to $\hat{\Lambda}_{\rm ex}$ the exact condensate wavefunction $\phi_{\rm ex}$ is replaced by the solution ϕ of the time-dependent Gross-Pitaevskii equation

$$i\hbar\partial_t \phi = \left[p^2/2m + U(r,t) + Ng|\phi|^2\right]\phi \tag{47}$$

and $\hat{a}_\phi/\sqrt{N}$ is replaced by the phase operator $\hat{A}_\phi = \hat{a}_\phi (\hat{a}^\dagger_\phi \hat{a}_\phi)^{-1/2}$ so that

$$\hat{\Lambda}(r) = \frac{1}{\sqrt{\hat{a}^\dagger_\phi \hat{a}_\phi}} \hat{a}^\dagger_\phi \left[\hat{\psi}(r) - \phi(r)\hat{a}_\phi\right] \tag{48}$$

and $\hat{\Lambda}(r)$ satisfies bosonic commutation relations

$$[\hat{\Lambda}(r), \hat{\Lambda}^\dagger(s)] = \frac{1}{dV}\mathcal{Q}_{r,s} \tag{49}$$

where the matrix $\mathcal{Q}_{r,s} = \delta_{r,s} - dV\phi(r)\phi^*(s)$ projects orthogonally to ϕ. To the first two leading orders in $1/\sqrt{N}$ one obtains an approximate form of the one-body density matrix:

$$\begin{aligned} \langle r|\rho|s\rangle \equiv \langle \hat{\psi}^\dagger(s)\hat{\psi}(r)\rangle &= (N - \langle\delta\hat{N}\rangle)\phi(r)\phi^*(s) \\ &+ \langle \hat{\Lambda}^\dagger(s)\hat{\Lambda}(r)\rangle \\ &+ \phi^*(s)\phi^{(2)}_\perp(r) + \phi(r)\phi^{(2)*}_\perp(s) \\ &+ O(\frac{1}{\sqrt{N}}). \end{aligned} \tag{50}$$

We call the first term "parallel-parallel" because it originates from the product of two parts of the field both parallel to the condensate wavefunction; it describes the physics of a pure condensate with $N - \langle\delta\hat{N}\rangle$ particles. The second term, which we call "orthogonal-orthogonal" because $\hat{\Lambda}$ is orthogonal to ϕ, describes the noncondensed particles in the Bogoliubov approximation. The third term, called "orthogonal-parallel", describes corrections to the Gross-Pitaevskii condensate wavefunction due to the presence of noncondensed particles [5]. In (50) $\langle\delta\hat{N}\rangle$ is the average number of noncondensed particles in the Bogoliubov approximation:

$$\langle\delta\hat{N}\rangle = \sum_r dV\,\langle\hat{\Lambda}^\dagger(r)\hat{\Lambda}(r)\rangle. \tag{51}$$

The evolution equations for $\hat{\Lambda}$ and $\phi^{(2)}_\perp$ are given in appendix D.

Having described the Bogoliubov method, let us now consider the truncated Wigner approach in the limit (44). We expand the classical field in powers of $1/\sqrt{N}$:

$$\psi = \sqrt{N}\psi^{(0)} + \psi^{(1)} + \frac{1}{\sqrt{N}}\psi^{(2)} + \dots \tag{52}$$

where the $\psi^{(j)}$ are of the order of unity. We immediately note that the leading term of this expansion corresponds to a pure condensate with N particles so that $\psi^{(0)}$ is simply the solution of the time-dependent

Gross-Pitaevskii equation (47), $\psi^{(0)} = \phi$. This physically clear fact will be checked explicitly in what follows. In the initial thermal equilibrium state at time $t = 0$ we expand (35) in powers of $1/\sqrt{N}$:

$$\sqrt{N_0} \equiv \sqrt{N - \delta N} = \sqrt{N} - \frac{1}{2}\frac{\delta N}{\sqrt{N}} + \dots \tag{53}$$

so that we can identify explicitly:

$$\psi^{(0)}(t=0) = \phi \tag{54}$$
$$\psi^{(1)}(t=0) = \psi_\perp \tag{55}$$
$$\psi^{(2)}(t=0) = -\frac{\delta N}{2}\phi + \phi_\perp^{(2)}. \tag{56}$$

Following the same procedure as in the quantum case, we split each term of the expansion into a component along ϕ and a component orthogonal to ϕ:

$$\psi^{(j)}(r) = \xi^{(j)}\phi(r) + \psi_\perp^{(j)}. \tag{57}$$

We calculate now the one-body density matrix ρ. Since we are using the Wigner representation for the atomic field on a finite spatial grid we have:

$$\langle r|\hat{\rho}|s\rangle = \langle \psi^*(s)\psi(r)\rangle - \frac{1}{2dV}\delta_{r,s} \tag{58}$$

where dV is the unit cell volume of the spatial grid and $\delta_{r,s}$ is a Kronecker δ. Note that to simplify the notation we have omitted the subscript W on the right hand side of the equation since the quantum and Wigner averages can be readily distinguished by the hats on the operators. We insert the expansions (52) and (57) into (58) and we use the fact that $\psi^{(0)} = \phi$ to obtain:

$$\begin{aligned}
\langle r|\hat{\rho}|s\rangle_{TW} &= \phi^*(s)\phi(r)\left[N + \sqrt{N}\langle \xi^{(1)} + \xi^{(1)*}\rangle + \langle|\xi^{(1)}|^2\rangle + \langle \xi^{(2)} + \xi^{(2)*}\rangle - \frac{1}{2}\right] \\
&+ \langle \psi_\perp^{(1)*}(s)\psi_\perp^{(1)}(r)\rangle - \frac{1}{2dV}\mathcal{Q}_{r,s} \\
&+ \phi^*(s)[\sqrt{N}\langle\psi_\perp^{(1)}(r)\rangle + \langle \xi^{(1)*}\psi_\perp^{(1)}(r)\rangle + \langle\psi_\perp^{(2)}(r)\rangle] + \{r \leftrightarrow s\}^* \\
&+ O\left(\frac{1}{\sqrt{N}}\right)
\end{aligned} \tag{59}$$

where we have collected the terms "parallel-parallel" in the first line, the terms "orthogonal-orthogonal" in the second line and the terms "orthogonal-parallel" in the third line, and where the matrix $\mathcal{Q}_{r,s}/dV = \delta_{r,s}/dV - \phi(r)\phi^*(s)$ is the discrete version of the projector $Q = 1 - |\phi\rangle\langle\phi|$. As we show in appendix E, by using the evolution equation of the field (1) and the initial conditions (54), (55) and(56) the following identities hold at all times:

$$\psi^{(0)} = \phi \tag{60}$$
$$\sqrt{N}\langle \xi^{(1)} + \xi^{(1)*}\rangle + \langle|\xi^{(1)}|^2\rangle + \langle \xi^{(2)} + \xi^{(2)*}\rangle = -\langle\delta\hat{N}\rangle \tag{61}$$
$$\langle \psi_\perp^{(1)*}(s)\psi_\perp^{(1)}(r)\rangle - \frac{1}{2dV}\mathcal{Q}_{r,s} = \langle\hat{\Lambda}^\dagger(s)\hat{\Lambda}(r)\rangle \tag{62}$$
$$\sqrt{N}\langle\psi_\perp^{(1)}(r)\rangle + \langle \xi^{(1)*}\psi_\perp^{(1)}(r)\rangle + \langle\psi_\perp^{(2)}(r)\rangle = \phi_\perp^{(2)}(r). \tag{63}$$

As we have already mentioned the first identity (60) reflects the fact that at zero order in the expansion we have a pure condensate with N particles evolving according to the time-dependent Gross-Pitaevskii equation. At time $t = 0$ the three other identities are easily established since we have simply $\langle\psi_\perp^{(1)}\rangle = 0$, $\xi^{(1)} = 0$ and $\xi^{(2)} = -\delta N/2$. At later times the mean value $\langle\psi_\perp^{(1)}\rangle$ remains equal to zero while $\xi^{(1)}$ develops a nonzero imaginary part corresponding to phase change of ψ in the mode ϕ due to the interaction with the noncondensed particles

$$\psi = \sqrt{N}\phi + \xi^{(1)}\phi + \dots \simeq \sqrt{N}e^{\xi^{(1)}/\sqrt{N}}\phi + \dots \tag{64}$$

After averaging over all stochastic realisations, this random phase change contributes to the condensate depletion in (61) and to the correction $\phi^{(2)}$ to the condensate wavefunction in (63) [24]. As a consequence

of the purely imaginary character of $\xi^{(1)}$ the quantity proportional to $\sqrt{N}$ in (61) vanishes. The identity (62) reflects the fact that in the linearised regime quantum fluctuations (here $\hat{\Lambda}$) and classical fluctuations (here $\psi_\perp^{(1)}$) around the Gross-Pitaevskii condensate field $\sqrt{N}\phi$, evolve according to the same equations. We find interestingly that the average $\langle\psi_\perp^{(2)}\rangle$ in (63) evolves under the influence of the mean field of the noncondensed particles, i.e. the Hartree-Fock term and the anomalous average contribution. In the Wigner representation the Hartree-Fock mean field term $2g\langle\psi_\perp^{(1)*}\psi_\perp^{(1)}\rangle$ differs from the physical mean field $2g\langle\hat{\Lambda}^\dagger\hat{\Lambda}\rangle$ by the term $g(1-|\phi|^2dV)/dV \simeq g/dV$. We note however that this brings in a global phase change of the condensate wavefunction having no effect on the one-body density matrix, and which is compensated anyway by the $-g/dV$ term in the Wigner drift term (16). In our calculations this is reflected by the fact that this term does not contribute to $\phi_\perp^{(2)}$.

With the identities (60-63) we identify line by line the quantum expression (50) and the truncated Wigner expression (59) for the one-body density matrix of the system up to terms of $O(1)$: these two expressions coincide apart from the term $1/2$ in the occupation number of the mode ϕ. This slight difference ($1/2 \ll N$) comes from the fact that in the initial sampling of the Wigner function in thermal equilibrium we have treated classically the condensate mode. These results establish the equivalence between the truncated Wigner method and the time-dependent Bogoliubov approach of [5] up to neglected terms $O(1/\sqrt{N})$ in the limit (44).

Let us however come back to the expansions performed in the limit (44). We have mentioned that the small formal parameter is $1/\sqrt{N}$ but we now wish to identify the small physical parameter of the expansion. In the quantum theory of [5] one gets the small parameter

$$\epsilon_{\rm quant} = \left(\frac{\langle\delta\hat{N}\rangle}{N}\right)^{1/2} \tag{65}$$

where $\langle\delta\hat{N}\rangle$ is the Bogoliubov prediction for the number of noncondensed particles. In the expansion (52) of the evolving classical field we compare the norm of the first two terms, ignoring the field phase change $\xi^{(1)}\phi$:

$$\epsilon_{\rm wig} = \left(\frac{\langle dV\sum_r|\psi_\perp^{(1)}|^2\rangle}{N}\right)^{1/2} = \left(\frac{\langle\delta\hat{N}\rangle+(\mathcal{N}-1)/2}{N}\right)^{1/2}. \tag{66}$$

The validity condition of the expansion (52) in the truncated Wigner approach is then:

$$N \gg \langle\delta\hat{N}\rangle\ ,\ \mathcal{N}/2 \tag{67}$$

which is more restrictive than in the quantum case. What indeed happens in the regime $\langle\delta\hat{N}\rangle \ll N < \mathcal{N}/2$? We expect the truncated Wigner approach not to recover the predictions of the Bogoliubov approach of [5] which are correct in this limit. We therefore set a necessary condition for the validity of the truncated Wigner approach:

$$N \gg \mathcal{N}/2. \tag{68}$$

We interpret this condition as follows: the extra noise introduced in the Wigner representation (see discussion after (27)) contributes to the nonlinear term $g|\psi|^2$ in the evolution equation for the field; (68) means that this fluctuating additional mean field potential of order $g/(2dV)$ should be much smaller than the condensate mean field of order gN/V where $V = \mathcal{N}dV$ is the volume of the system. Condition (68) is also equivalent to $\rho dV \gg 1$, where ρ is the atomic density, i.e. there should be on average more than one particle per grid site. We note that it is compatible with the conditions (8) on the spatial steps of the grid in the regime of a degenerate ($\rho\lambda^3 \gg 1$) and a weakly interacting ($\rho\xi^3 \gg 1$) Bose gas. Condition (68) is therefore generically not restrictive.

A last important point for this subsection is that the time-dependent Bogoliubov approach, relying on a linearisation of the field equations around a pure condensate solution, is usually restricted to short times in the case of an excited condensate, so it cannot be used to test the condition of validity of the truncated Wigner approach in the long time limit. It was found indeed in [25] that nonlinearity effects in the condensate motion can lead to a polynomial or even exponential increase in time of $\langle\delta\hat{N}\rangle$ which eventually invalidates the time-dependent Bogoliubov approach. The truncated Wigner approach in its full nonlinear version does not have this limitation however, as we have checked with a time-dependent 1D model in [3].

4.2 Beliaev-Landau damping in the truncated Wigner approach

In this section we consider a spatially homogeneous Bose condensed gas in a cubic box in three dimensions with periodic boundary conditions. We imagine that with a Bragg scattering technique we excite

coherently a Bogoliubov mode of the stationary Bose gas, as was done experimentally at MIT [26, 27], and we study how the excitation decays in the Wigner approach due to Landau and Beliaev damping.

4.2.1 Excitation procedure and numerical results

We wish to excite coherently the Bogoliubov mode of wavevector $k_0 \neq 0$. With a Bragg scattering technique using two laser beams with wave vector difference q and frequency difference ω we induce a perturbation potential

$$W = \int d^3r \left(\frac{W_0}{2} e^{i(q\cdot r - \omega t)} + c.c. \right) \tag{69}$$

We match the wavevector and frequency of the perturbation to the wavevector k_0 and the eigenfrequency $\omega_0 = \epsilon_0/\hbar$ of the Bogoliubov mode we wish to excite:

$$q = k_0 \qquad\qquad \omega = \epsilon_0/\hbar = \omega_0. \tag{70}$$

During the excitation phase, we expect that two Bogoliubov modes are excited from the condensate, the modes with wavevectors k_0 and $-k_0$. We anticipate the perturbative approach of next subsection which predicts that the mode of wavevector k_0, being excited resonantly, has an amplitude growing linearly with time, while the mode with wavevector $-k_0$, being excited off-resonance, has an oscillating amplitude vanishing periodically when t is a multiple integer of π/ω_0. In the truncated Wigner simulation we therefore stop the excitation phase at

$$t_{\rm exc} = \frac{\pi}{\omega_0}\,. \tag{71}$$

We introduce the amplitudes of the classical field ψ of the Bogoliubov modes. We first define the field

$$\Lambda_{\rm static}(r) \equiv \frac{1}{\sqrt{N}} a_\phi^* \psi_\perp(r) \tag{72}$$

where a_ϕ and $\psi_\perp$ are the components of ψ orthogonal and parallel to the static condensate wavefunction $\phi(r) = 1/L^{3/2}$ (see (18)). The component along the Bogoliubov mode with wavevector k is then

$$b_k = dV \sum_r u_k^*(r)\Lambda_{\rm static}(r) - v_k^*(r)\Lambda_{\rm static}^*(r)\,. \tag{73}$$

The functions u_k and v_k are plane waves with wavevector $k \neq 0$

$$u_k(r) = \frac{1}{\sqrt{L^3}} U_k e^{ik\cdot r} \qquad\qquad v_k(r) = \frac{1}{\sqrt{L^3}} V_k e^{ik\cdot r} \tag{74}$$

and the real coefficients U_k and V_k are normalised to $U_k^2 - V_k^2 = 1$:

$$U_k + V_k = \frac{1}{U_k - V_k} = \left(\frac{\hbar^2 k^2/2m}{\hbar^2 k^2/2m + 2\mu} \right)^{1/4} \tag{75}$$

where the chemical potential is $\mu = gN/L^3$.

We denote by b_0 the amplitude of the field $\Lambda_{\rm static}$ along the Bogoliubov mode of wavevector k_0, and b_{-0} the amplitude along the mode with opposite wavevector. We show the mean values of these amplitudes as function of time obtained from the truncated Wigner simulation in figure 3. In the initial thermal state these mean values vanish, and they become nonzero during the excitation phase due to the coherent excitation procedure. At later times they decay to zero again [28].

4.2.2 Perturbative analysis of the truncated Wigner approach: Beliaev-Landau damping

In the appendix F we report the exact equations of motion of the classical field $\Lambda_{\rm static}$ defined by (72) in the truncated Wigner approach. We now make the assumption that $\Lambda_{\rm static}$ is small compared with $\sqrt{N}\phi$, implying that

$$N \gg \langle \delta\hat{N} \rangle \,,\ \frac{\mathcal{N}}{2} \tag{76}$$

where $\langle \delta\hat{N} \rangle$ represents here the mean number of particles in the excited modes of the cubic box. In this regime we neglect terms which are at least cubic in $\Lambda_{\rm static}$ in (163) and we replace the number of particles

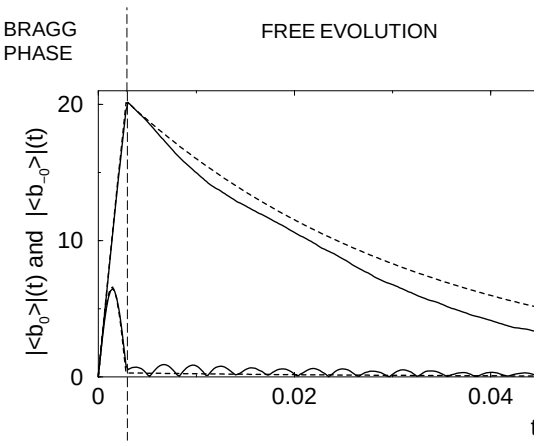

Figure 3: Bragg excitation of a Bogoliubov mode of wavevector k_0 and frequency ω_0 for a finite temperature Bose condensed gas in a cubic box. The vertical dashed line at time $t = \pi/\omega_0$ indicates the time after which the perturbation W is discontinued. Solid lines: evolution of the field amplitudes of the Bogoliubov modes with wavevectors $k_0 = (12\pi/L, 0, 0)$ (upper curve) and $-k_0$ (lower curve) in the Wigner simulation after averaging over 100 realizations. Only the mode k_0 is excited resonantly by Bragg scattering. After the coherent excitation Bragg phase, the amplitudes of the two modes are damped. Dashed line: perturbative approach of subsection 4.2.2. The truncated Wigner approach and the perturbation theory give comparable results. $N = 5 \times 10^4$, $k_B T = 3\mu$, $\hbar\omega_0 = 2.2\mu$, $W_0 = 0.175\mu$, $\mu = 500\hbar^2/mL^2$. In the Wigner simulation a grid with 22 points per dimension is used, so that $\mathcal{N} = 22^3 = 10648 \ll N$. In the perturbative approach a grid of 48 points per dimension is used to avoid truncation effects. The initial mean number of noncondensed particles is $N - \langle N_0 \rangle \simeq 5000$.

in the ground state of the box by the total number of particles N, except in the zeroth order term in $\Lambda_{\rm static}$ where we replace it by its initial mean value $\langle N_0 \rangle$. We then find:

$$i\hbar \frac{d}{dt}\Lambda_{\rm static} \simeq \sqrt{\langle N_0\rangle}\mathcal{Q}h_0\phi + \mathcal{Q}h_0\Lambda_{\rm static} + \frac{Ng}{L^3}(\Lambda^*_{\rm static} + 2\Lambda_{\rm static}) + \frac{g\sqrt{N}}{\sqrt{L^3}}\mathcal{Q}(\Lambda_{\rm static}\Lambda_{\rm static} + 2\Lambda^*_{\rm static}\Lambda_{\rm static}) - \frac{1}{\sqrt{NL^3}}\Lambda_{\rm static}(r)dV\sum_s W_0\cos(q\cdot s - \omega t)\Lambda^*_{\rm static} \quad (77)$$

where W_0 is non zero only during the excitation phase. In this equation $h_0 = p^2/2m + W_0\cos(q\cdot r - \omega t)$ is the one-body part of the Hamiltonian including the kinetic energy and the Bragg excitation potential, and $\mathcal{Q}$ projects orthogonally to the static condensate mode ϕ. The term of zeroth order in $\Lambda_{\rm static}$ is a source term which causes $\Lambda_{\rm static}$ to acquire a nonzero mean value during the evolution. The terms of first order in $\Lambda_{\rm static}$ in (77) describe the evolution in the static Bogoliubov approximation. Terms of second order provide the damping we are looking for. We project equation (77) over the static Bogoliubov modes (74) by using:

$$\Lambda_{\rm static}(r) = \sum_{k\neq 0} b_k u_k(r) + b^*_k v^*_k(r) \quad (78)$$

with the mode functions $u_k(r)$ and $v_k(r)$ defined in (74). Terms nonlinear in $\Lambda_{\rm static}$ in (77) then correspond to an interaction between the Bogoliubov modes.

We assume that the excitation phase is much shorter than the damping time of the coherently excited mode. As a consequence we can neglect in this phase the processes involving interaction among the Bogoliubov modes. Also in the action of the perturbation W we keep only the term acting on the condensate mode, that is the first term on the right hand side of (77), which is $\sqrt{\langle N_0\rangle}$ larger than the terms acting on the noncondensed modes. For the choice of parameters (70) only the two modes with wavevectors k_0 and $-k_0$ are excited from the condensate by the perturbation W; the amplitudes of the field in these modes evolve according to

$$i\hbar\frac{d}{dt}b_0 = \hbar\omega_0 b_0 + \sqrt{\langle N_0\rangle}\frac{W_0}{2}(U_0 + V_0)\, e^{-i\omega_0 t} \quad (79)$$

$$i\hbar\frac{d}{dt}b_{-0} = \hbar\omega_0 b_{-0} + \sqrt{\langle N_0\rangle}\frac{W_0}{2}(U_0 + V_0)\, e^{i\omega_0 t}\,. \quad (80)$$

By integrating these equations we realise that the mean amplitude $\langle b_0 \rangle$ grows linearly in time, since the mode is excited resonantly, while the mean amplitude $\langle b_{-0} \rangle$ oscillates and vanishes at $t = \pi/\omega_0$.

After the excitation phase we include the second order terms that provide damping:

$$i\hbar \frac{d}{dt} b_0 = \epsilon_0 b_0 + \sum_{i,j} A^0_{i,j} b_i b_j + (A^j_{i,0} + A^j_{0,i}) b^*_i b_j + \sum_{i,j} (B_{i,j,0} + B_{0,i,j} + B_{i,0,j}) b^*_i b^*_j \tag{81}$$

with

$$A^i_{j,k} = \frac{g\sqrt{N}}{L^3} [U_i(U_j + V_j)U_k + (U_i + V_i)V_j U_k + V_j(U_k + V_k)V_i] \delta_{i,j+k} \tag{82}$$

$$B_{i,j,k} = \frac{g\sqrt{N}}{L^3} V_i (U_j + V_j) U_k \delta_{-i,j+k} \, . \tag{83}$$

and where i, j, k denote momenta. The last terms with the B's in (81) do not conserve the Bogoliubov energy and we can neglect them here for the calculation of the damping rate since we are going to use second order perturbation theory; we would have to keep them in order to calculate frequency shifts. In the terms with the A's we recognise two contributions: the term with $A^0_{i,j}$ describes a Beliaev process where the excited mode can decay into two different modes while the term with $A^j_{i,0} + A^j_{0,i}$ describes a Landau process where the excited mode by interacting with another mode is scattered into a third mode [29]. We introduce the coefficients $\tilde{b}$ in the interaction picture

$$\tilde{b}_j = b_j \, e^{i\epsilon_j \, t/\hbar} \tag{84}$$

where ϵ_j is the Bogoliubov eigenenergy of the mode with wavevector j, and we solve (81) to second order of time-dependent perturbation theory to obtain:

$$\begin{aligned} \langle \tilde{b_0}(t) - \tilde{b_0}(0) \rangle \simeq & -\frac{1}{\hbar^2} \sum_{i,j} A^0_{i,j} (A^0_{i,j} + A^0_{j,i}) \, I_t(\epsilon_0 - \epsilon_i - \epsilon_j)(1 + \bar{n}_i + \bar{n}_j) \langle \tilde{b_0}(0) \rangle \\ & -\frac{1}{\hbar^2} \sum_{i,j} (A^j_{i,0} + A^j_{0,i}) \, I_t(\epsilon_0 + \epsilon_i - \epsilon_j)(\bar{n}_i - \bar{n}_j) \langle \tilde{b_0}(0) \rangle \\ & -\frac{1}{\hbar^2} 2 (A^{0+0}_{0,0})^2 \, I_t(\epsilon_0 + \epsilon_0 - \epsilon_{0+0}) \langle \tilde{b^*_0}(0) \tilde{b_0}(0) \tilde{b_0}(0) \rangle \end{aligned} \tag{85}$$

where $0 + 0$ represents the mode of wavevector $2k_0$ and where

$$I_t(\nu) = \int_0^t d\tau \, e^{i\nu\tau/\hbar} \, f_\tau(\nu) \tag{86}$$

$$f_\tau(\nu) = \int_0^\tau d\theta \, e^{-i\nu\theta/\hbar} . \tag{87}$$

The $\bar{n}_j$'s are the occupation numbers of the Bogoliubov modes in thermal equilibrium given by the Bose formula

$$\bar{n}_j = \frac{1}{e^{\epsilon_j / k_B T} - 1} \tag{88}$$

where ϵ_j is the energy of the Bogoliubov mode. In the language of nonlinear optics the last line in (85) describes a χ_2 effect or a second harmonic generation which can be important if the conservation of energy condition $\epsilon_{2k_0} = 2\epsilon_{k_0}$ is satisfied and if the initial amplitude $\langle \tilde{b_0}(0) \rangle = \beta$ is large since one has

$$\langle \tilde{b^*_0}(0) \tilde{b_0}(0) \tilde{b_0}(0) \rangle = |\beta|^2 \beta + \bar{n}_0 2\beta \, . \tag{89}$$

We have checked that the χ_2 effect is negligible for the low amplitude coherent excitations considered in the numerical examples of this paper: ϵ_0 is larger than μ so that k_0 is not in the linear part of the Bogoliubov spectrum and therefore the second harmonic generation process is not resonant. By using the fact that:

$$\text{Re} \, I_t(\nu) = \frac{1}{2} |f_t(\nu)|^2 = \frac{2\hbar^2}{\nu^2} \sin^2 \frac{\nu\tau}{2\hbar} \equiv \pi\hbar t \delta_t(\nu) \tag{90}$$

where $\delta_t(\nu)$ converges to a Dirac delta distribution in the large t limit, we calculate the evolution of the modulus of the Bogoliubov mode amplitude

$$\begin{aligned} \frac{|\langle b_0(t) \rangle| - |\langle b_0(0) \rangle|}{|\langle b_0(0) \rangle|} \simeq & -\frac{\pi t}{\hbar} \sum_{i,j} A^0_{i,j} (A^0_{i,j} + A^0_{j,i}) \, \delta_t(\epsilon_0 - \epsilon_i - \epsilon_j)(1 + \bar{n}_i + \bar{n}_j) \\ & -\frac{\pi t}{\hbar} \sum_{i,j} (A^j_{i,0} + A^j_{0,i})^2 \, \delta_t(\epsilon_0 + \epsilon_i - \epsilon_j)(\bar{n}_j - \bar{n}_i) \, . \end{aligned} \tag{91}$$

This formula can be applied to a finite size box as it contains finite width δ's. By plotting equation (91) as a function of time we can identify a time interval over which it is approximately linear in time, and we determine the slope $-\gamma_{\rm perturb}$ with a linear fit [30]. Heuristically we then compare $\exp(-\gamma_{\rm perturb}t)$ to the result of the truncated Wigner simulation, see figure 3 and we obtain a good agreement for this particular example [31].

In the thermodynamic limit, when the Bogoliubov spectrum becomes continuous, the discrete sums in (91) can be replaced by integrals and the finite width δ_t is replaced by a Dirac δ distribution. In this case an analytical expression for the damping rate can be worked out and we recover *exactly* the expression for the Beliaev and Landau damping rate obtained in the quantum field theory [32, 33, 34].

4.2.3 Validity condition of the truncated Wigner approach

We now investigate numerically the influence of the grid size on the predictions of the truncated Wigner simulation. The line with squares in figure 4 shows the damping rate obtained from the Wigner simulation, defined as the inverse of the $1/e$ half-width of $|\langle b_0(t)\rangle|$, as a function of the inverse grid size $1/\mathcal{N}$. For small grids the results of the simulations reach a plateau close to the perturbative prediction $\gamma_{\rm perturb}$. For large grids the damping rate in the simulation becomes significantly larger than $\gamma_{\rm perturb}$. Since the perturbative prediction reproduces the known result for Beliaev-Landau damping, we conclude that the results of the truncated Wigner simulation become incorrect for large grid sizes. The reason of such a *spurious* damping appearing in the Wigner simulation for large $\mathcal{N}$ will become clear below.

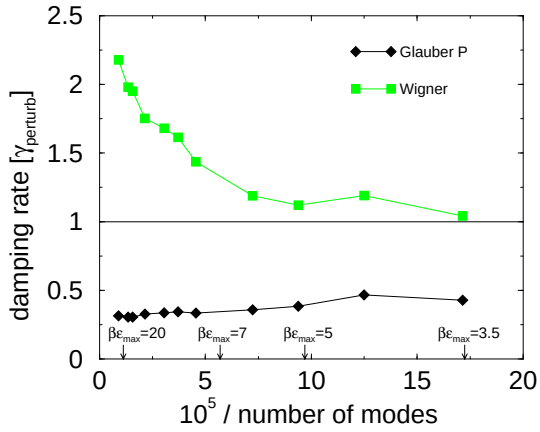

Figure 4: Damping rate of the coherent excitation in the Bogoliubov mode of wavevector $k_0 = (12\pi/L, 0, 0)$ and of frequency ω_0 as a function of the inverse number of modes in the grid $1/\mathcal{N}$ for the Glauber-P and the Wigner distributions. Each disk represents the average over 100 realisations of the simulation and the lines are a guide to the eye. $N = 10^5$, $k_BT = 3\mu$, $\mu = 500\hbar^2/mL^2$, so that $\hbar\omega_0 = 2.2\mu$, $\gamma^{-1}_{\rm perturb} = 0.061mL^2/\hbar$, $W_0 = 0.0874\mu$. The damping rate is expressed in units of $\gamma_{\rm perturb}$. Arrows indicate some values of $\epsilon_{\rm max}/k_BT$ where $\epsilon_{\rm max}$ is the maximal Bogoliubov energy on the grid.

It is tempting to conclude from the perturbative calculation of subsection 4.2.2 that the validity condition of the truncated Wigner approach is dictated only by the condition $\mathcal{N} \ll N$. To check this statement we have performed a second set of simulations (not shown) for a particle number N reduced by a factor of two keeping the size of the box L, the chemical potential $\mu = Ng/L^3$ and the temperature fixed. If the condition of validity of the truncated Wigner approach involves only the ratio $N/\mathcal{N}$ the plateaux in the damping time should start at the same value of $N/\mathcal{N}$ for the two sets of simulations. However this is not the case, and we have checked that on the contrary, the two curves seem to depend on the number of modes only.

Another way to put it is that the condition to have agreement between the truncated Wigner simulation and the perturbation theory of section 4.2.2 is not (or not only) that the number of particles should be larger than the number of modes. There is in fact another "hidden" condition in the perturbative calculation which is the hypothesis that the occupation numbers of the Bogoliubov modes are constant during the evolution. In reality, even in absence of the Bragg perturbation, our initial state which reproduces the correct thermal distribution for the quantum Bose gas, is not stationary for the classical field evolution (1). The perturbative expression (91) holds indeed in the limit $N/\mathcal{N} \gg 1$, but the occupation

numbers of the Bogoliubov modes, initially equal to the Bose formula $\bar{n}_j$, change in the course of the time evolution in the simulation and this affects the damping rate. This effect is neglected in the perturbative formula (91) and it is found numerically to take place on a time interval comparable to the damping time of the Bogoliubov coherent excitation as we show in figure 5.

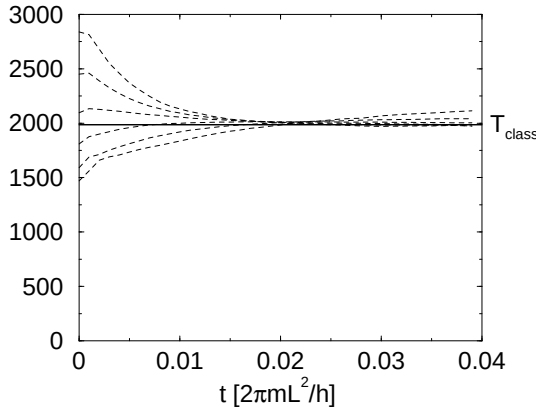

Figure 5: Evolution of the squared amplitudes $\langle b_k^* b_k \rangle$ of the classical field Bogoliubov modes multiplied by the corresponding Bogoliubov energy ϵ_k in the truncated Wigner simulation in the absence of the Bragg perturbation. We have collected the Bogoliubov modes in energy channels of width 2μ, so that the plotted quantity is the average among each channel of $\epsilon_k \langle b_k^* b_k \rangle$, with increasing energy from top to bottom at initial time $t = 0$. The thick horizontal line is the expected temperature $T_{\rm class}$ of the equilibrium classical field distribution as given by (94). Parameters are: $N = 5 \cdot 10^4$, $k_B T = 3\mu$, $\mu = 500\hbar^2/mL^2$ and the vertical axis of the figure is in units of $\hbar^2/mL^2$, where L is the cubic box size. The number of modes is 22 per spatial dimension so that the maximum Bogoliubov energy allowed on the grid is $\epsilon_{\rm max} = 15.3\mu$. The averaging in the simulation is performed over 500 realisations.

What it is expected to happen in the absence of external perturbation is that the classical field equation (1), in the three-dimensional cubic box geometry considered here, displays an ergodic behaviour leading to thermalisation of the classical field ψ towards its equilibrium distribution [11, 12]. In the regime where the noncondensed fraction is small and the number of modes is smaller than N, we can approximately view the classical field as a sum of Bogoliubov oscillators b_k weakly coupled by terms leading to the nonlinearities in (163). In the equilibrium state for the classical field dynamics we then expect the occupation numbers of the Bogoliubov modes to be given by the equipartition formula:

$$\langle b_k^* b_k \rangle_{\rm class} = \frac{k_B T_{\rm class}}{\epsilon_k} \tag{92}$$

attributing a mean energy of $k_B T_{\rm class}$ to each of the Bogoliubov mode. The classical field equilibrium temperature $T_{\rm class}$ can then be deduced from the approximate conservation of the Bogoliubov energy [35]:

$$\begin{aligned} k_B T_{\rm class} &= \frac{1}{\mathcal{N}-1} \sum_{k \neq 0} \epsilon_k \langle b_k^* b_k \rangle (t=0) \\ &= \frac{1}{\mathcal{N}-1} \sum_{k \neq 0} \left[\frac{\epsilon_k}{\exp(\beta \epsilon_k) - 1} + \frac{1}{2} \epsilon_k \right] \qquad (93) \\ &= \frac{1}{\mathcal{N}-1} \sum_{k \neq 0} \frac{\epsilon_k}{2 \tanh(\beta \epsilon_k / 2)} \, . \qquad (94) \end{aligned}$$

The thermalisation of the Bogoliubov modes to the new temperature $T_{\rm class}$ is nicely demonstrated in figure 5. One sees that $\epsilon_k \langle b_k^* b_k \rangle$ indeed converges to a constant value almost independent of k. From the fact that $\tanh x < x$ for any $x > 0$ we deduce that the classical equilibrium temperature $T_{\rm class}$ is always larger than the real physical temperature T of the gas. In the regime $k_B T \gg \mu$ this 'heating' increases the squared amplitudes $\langle b_k^* b_k \rangle$ of the modes of energy $\sim \mu$ by a factor $\simeq T_{\rm class}/T$. Since the Landau damping rate is approximately proportional to the populations of these modes [32, 33, 34] the damping rate is increased roughly by a factor $T_{\rm class}/T$, an artifact of the truncated Wigner approximation.

It is clear that $T_{\rm class}$ will remain very close to T as long as the maximum Bogoliubov energy allowed in the simulation remains smaller than k_BT. One can indeed in this case expand (94) in powers of $\beta\epsilon_k$. One has to expand the hyperbolic tangent up to cubic order to get a nonzero correction:

$$\frac{T_{\rm class}}{T} \simeq 1 + \frac{1}{\mathcal{N}-1}\sum_{k\neq 0}\frac{(\beta\epsilon_k)^2}{12}. \tag{95}$$

The absence of terms of order $\beta\epsilon_k$ in (95) is a fortunate consequence of the noise added to the field in the Wigner representation. This added noise shifts the average $\langle b_k^* b_k\rangle(t=0)$ by 1/2 with respect to the Bose formula.

When the maximum Bogoliubov energy becomes much larger than k_BT we expect $T_{\rm class}$ to become significantly larger than T. This is illustrated in figure 6 obtained by a numerical calculation of the sum in (94) for increasing grid sizes. We have also plotted in this figure the value that one would obtain for $T_{\rm class}$ in the absence of the added Wigner noise (i.e. in a Glauber-P approach), that is by removing the terms $\epsilon_k/2$ in (93). The Glauber-P distribution for the field ψ in the sense of [36] is given by

$$\psi = N_0\phi + \sum_{k\neq 0} b_k u_k + b_k^* v_k^* \tag{96}$$

where the b_k are chosen from a Gaussian distribution such that $\langle b_k^* b_k\rangle = 1/(\exp(\beta\epsilon_k)-1)$ and the value of N_0 is dictated by the normalisation condition $||\psi||^2 = N$. In this case $T_{\rm class}$ is always smaller than T, and deviates from T for smaller grid sizes, since the fortunate cancellation of the order $\beta\epsilon_k$ obtained in (95) does not occur anymore. We expect in this case a spurious reduction of the damping rate. We have checked it by evolving an ensemble of fields of the form (96) with the Gross-Pitaevskii equation and we found that the damping rate is always smaller than half of the correct result even for the smallest grids that we tested, see the line with diamonds in figure 4.

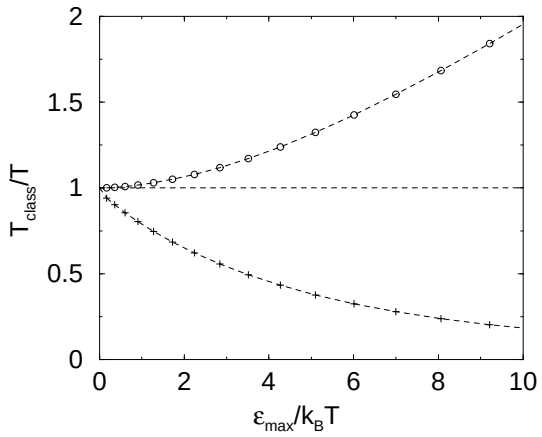

Figure 6: Equilibrium temperature $T_{\rm class}$ of the classical gas as function of the maximum energy $\epsilon_{\rm max}$ of the Bogoliubov modes on the momentum grid with the assumption of equipartition of the energy in the Bogoliubov modes. Circles: the initial field distribution is the Wigner distribution for the quantum gas at temperature T. Crosses: Glauber-P distribution defined in [36], amounting to the removal of the added Wigner noise from the initial field distribution. The dashed lines are a guide to the eye. The number of momentum components along each dimension of space goes from 2 to 30 in steps of 2. The chemical potential is $\mu = 500\hbar^2/mL^2$ and the temperature is $k_BT = 3\mu$.

5 Conclusion

We have considered a possible way of implementing the truncated Wigner approximation to study the time evolution of trapped Bose-Einstein condensates perturbed from an initial finite temperature equilibrium state. First a set of random classical fields ψ is generated to approximately sample the initial quantum thermal equilibrium state of the gas, in the Bogoliubov approximation assuming a weakly interacting and almost pure Bose-Einstein condensate. Then each field ψ is evolved in the classical field approximation,

that is according to the time-dependent Gross-Pitaevskii equation, with the crucial difference with respect to the more traditional use of the Gross-Pitaevskii equation that the field ψ is now the whole matter field rather than the field in the mode of the condensate.

The central part of this paper is the investigation of the validity conditions of this formulation of the truncated Wigner approximation.

For short evolution times of the fields ψ the dynamics of the noncondensed modes, i.e. the components of the field orthogonal to the condensate mode, is approximately linear; we can then use the time-dependent Bogoliubov approximation, both for the exact quantum problem and for the truncated Wigner approach. A necessary condition for the truncated Wigner approach to correctly reproduce the quantum results is then

$$N \gg \mathcal{N}/2 \tag{97}$$

where $\mathcal{N}$ is the number of modes in the Wigner approach and N is the total number of particles in the gas. This condition can in general be satisfied in the degenerate and weakly interacting regime without introducing truncation effects due to a too small number of modes.

For longer evolution times the nonlinear dynamics of the noncondensed modes comes into play. When the classical field dynamics generated by the Gross-Pitaevskii equation is ergodic, e.g. in the example of a three dimensional gas in a cubic box considered in this paper, the set of Wigner fields ψ evolves from the initial distribution mimicking the thermal state of the quantum gas at temperature T to a classical field equilibrium distribution at temperature $T_{\rm class}$. Since noise is added in the Wigner representation in all modes of the classical field to mimic quantum fluctuations it turns out that $T_{\rm class}$ is always larger than T. If $T_{\rm class}$ deviates too much from T the truncated Wigner approximation can give incorrect predictions. For example we have found that the Beliaev-Landau damping of a Bogoliubov mode in the box, taking place with a time scale comparable to that of the 'thermalisation' of the classical field, is accelerated in a spurious way as the classical field 'warms up'. A validity condition for the truncated Wigner approach in this long time regime is therefore

$$|T_{\rm class} - T| \ll T. \tag{98}$$

This condition sets a constraint on the maximum energy of the Bogoliubov modes $\epsilon_{\rm max}$ in the Wigner simulation: $\epsilon_{\rm max}$ *should not exceed a few* $k_B T$. More precisely one can use the following inequality to estimate the error [37]:

$$\frac{|T_{\rm class} - T|}{T} < \frac{1}{12}\frac{\langle \epsilon_k^2 \rangle}{(k_B T)^2} < \frac{1}{12}\left(\frac{\epsilon_{\rm max}}{k_B T}\right)^2 \tag{99}$$

where $\langle \epsilon_k^2 \rangle$ is the arithmetic mean of the squares of all the Bogoliubov energies in the Wigner simulation.

The fact that the initial set of Wigner fields is nonstationary under the classical field evolution could be a problem: the time-dependence of the observables could be affected in an unphysical way during the thermalisation to a classical distribution of the ensemble. To avoid this, we could *start* directly from the thermal equilibrium classical distribution [11, 13], restricting to the regime $\epsilon_{\rm max} < k_B T$.

A remarkable feature of the Wigner simulation is that $T_{\rm class}$ deviates from T at low values of $\epsilon_{\rm max}$ only *quadratically* in $\epsilon_{\rm max}/k_B T$. This very fortunate feature originates from the added noise in the Wigner representation. It explains why for $\epsilon_{\rm max}$ as high as 3.5 $k_B T$ the truncated Wigner approach can still give very good results for the Beliaev-Landau damping time (see Fig. 4). In contrast, if we remove the Wigner added noise, in the so-called Glauber-P representation, or if we add more noise, in the so-called Q representation, $T_{\rm class}$ deviates from T *linearly* in $\epsilon_{\rm max}/k_B T$. In this case we expect that the condition of validity of the classical Gross-Pitaevskii equation will be that all modes in the problem must be highly occupied, resulting in the stringent condition $\epsilon_{\rm max} < k_B T$. We therefore conclude that the Wigner representation is the most favorable representation of the quantum density operator with which to perform the classical field approximation. This fact, known in quantum optics for few mode systems, was not obvious for the highly multimode systems that are the finite temperature Bose gases.

Still, condition (98) is a serious limitation of the truncated Wigner method for simulating general ergodic three dimensional systems. One possibility to overcome this limitation is to proceed as in [38, 39] i.e. to treat the high energy modes as a reservoir, which leads to the inclusion of a stochastic term in the Gross-Pitaevskii equation. The advantage of this treatment is that the additional term has dissipative effects and thermalises the system to the correct quantum field thermal distribution in the stationary state as opposed to the classical one. However, one of the conceptual advantages of the truncated Wigner method and of classical field methods in general [9, 10, 11, 12] which we would like to keep is that apparent damping and irreversibility arise from the dynamics of a *conservative* equation (the Gross-Pitaevskii or nonlinear Schrödinger equation) as is the case in the original Hamiltonian equations for the quantum field.

Laboratoire Kastler Brossel is a research unit of École Normale Supérieure and of Université Pierre et Marie Curie, associated to CNRS. We acknowledge very useful discussions with Crispin Gardiner. This work was partially supported by National Computational Science Alliance under DMR 9900 16 N and used the NCSA SGI/CRAY Origin2000.

A Bare vs effective coupling constant

In this appendix we describe how to adjust the potential $\mathcal{V}(r)$ defined on the grid in the simulation in order to reproduce correctly the low energy scattering properties of the true interatomic potential.

We start with the Schrödinger equation for a scattering state $\phi(r)$ of the discrete delta potential $\mathcal{V}(r) \equiv (g_0/dV)\delta_{r,0}$ on the spatial grid of size L_ν and volume V:

$$\epsilon\phi(r) = \left(\frac{p^2}{m}\phi\right)(r) + \frac{g_0}{dV}\phi(r)\delta_{r,0} \tag{100}$$

where m is twice the reduced mass and where $\phi(0)$ is different from zero. We project this equation on plane waves of momentum k:

$$\tilde{\phi}(k) = \frac{g_0}{V^{1/2}}\frac{\phi(0)}{\epsilon - \hbar^2k^2/m}, \tag{101}$$

where $\tilde{\phi}(k)$ is the component of ϕ on the plane wave $e^{ik\cdot r}/\sqrt{V}$. Fourier transforming back gives $\phi(0)$; dividing the resulting equation by $\phi(0)$ leads to the quantization condition

$$1 = \frac{1}{V}\sum_k \frac{g_0}{\epsilon - \hbar^2k^2/m}. \tag{102}$$

We define the effective coupling constant $g_{\rm eff}$ in such a way that the energy of the lowest scattering state of the pseudopotential $g_{\rm eff}\delta(r)\partial_r(r\,\cdot)$ in the box is the same as the energy of the lowest scattering state solution of (102).

We now restrict ourselves to the case where the size of the box is much larger than the scattering length associated with $g_{\rm eff}$. In this case the energy of the lowest scattering state for the continuous theory with the pseudopotential is very close to $g_{\rm eff}/V$, so that we can calculate $g_{\rm eff}$ from the equation $\epsilon = g_{\rm eff}/V$. In this large box case, one can then check that the energy ϵ is negligible as compared to $\hbar^2k^2/m$ except if $k = 0$. This gives

$$g_{\rm eff} = \frac{g_0}{1 + \frac{1}{V}\sum_{k\neq 0}\frac{g_0}{\hbar^2k^2/m}} \tag{103}$$

which allows us to adjust g_0 in order to have $g_{\rm eff} = g \equiv 4\pi\hbar^2a/m$ where a is the scattering length of the true interatomic potential.

The sum over k in the denominator can be estimated by replacing the sum by an integral over k and is found to be on the order of $k_{\rm max}a_0$ where $g_0 = 4\pi\hbar^2a_0/m$ and $k_{\rm max}$ is the maximum momentum on the grid. g_0 is therefore very close to $g_{\rm eff}$ when condition (9) is satisfied, so that we can set $g_0 \simeq g_{\rm eff} = g$. In the opposite limit of a grid step size tending to zero one gets $g_{\rm eff} \to 0$, and we recover the known fact that a delta potential does not scatter in the continuous limit. We would have to increase g_0 continuously up to infinity as the grid step size tended to zero, if we wanted to get a finite $g_{\rm eff}$ in this limit.

B An improved Brownian motion simulation

A better choice for α and Y – In our previous work [4] the drift matrix α and the noise matrix Y were the hyperbolic sine and cosine of $\mathcal{L}/(2k_BT)$, which imposed a time step dt in the simulation which was exponentially small in the parameter $\epsilon_{\rm max}/(k_BT)$, where $\epsilon_{\rm max}$ is the largest eigenvalue of $\mathcal{L}$ allowed on the spatial grid of the simulation. We have now identified a choice that does not have this disadvantage:

$$\alpha = 2M \tag{104}$$

$$Y = \begin{pmatrix} \mathcal{Q} & 0 \\ 0 & \mathcal{Q}^* \end{pmatrix}, \tag{105}$$

where the projector $\mathcal{Q}$ is defined in (25). With this new choice for α and Y both the friction matrix and the noise matrix are bounded from above by unity, which allows a much larger dt in the case $\epsilon_{\rm max} > k_BT$.

To calculate the action of matrix α on the vector $(\psi_\perp, \psi_\perp^*)$ we write the hyperbolic tangent as:

$$\tanh x = x \frac{\tanh x}{x} \equiv x F(x^2). \tag{106}$$

The function $F(u)$ is then expanded on Chebyshev polynomials in the interval $u \in [0, (\epsilon_{\max}/(2k_BT))^2]$ and approximated by a polynomial of a given degree, typically 15 for $\epsilon_{\max}/(2k_BT) = 3$ and 25 for $\epsilon_{\max}/(2k_BT) = 6$, obtained by truncating a Chebyshev expansion of degree 50 [40].

An improved integration scheme – Initially we set $\psi_\perp = 0$. Since the noise $d\xi$ is Gaussian, and because the stochastic differential equation (28) is linear, the probability distribution of $\psi_\perp$ is guaranteed to be Gaussian at any step of the integration so that the issue of the convergence of the distribution to the correct steady state distribution (21) can be discussed in terms of the convergence of the covariance matrix of the distribution to its right steady state value. Two issues in particular should be addressed: the error introduced by the discretisation in time (finite time step dt of integration), and the error introduced by the integration over a finite time interval (approach to the steady state distribution).

We now explain how to face the first problem with an efficient integration scheme yielding an error on the steady state covariance matrix of the distribution scaling as dt^2, rather than dt for the simple Euler scheme. In the numerical scheme the vector $\vec{X} \equiv (\psi_\perp, \psi_\perp^*)$ that stores the values of the field $\psi_\perp$ and of its complex conjugate $\psi_\perp^*$ on the discrete grid obeys the recursion relation:

$$\vec{X}_{[t=(n+1)dt]} = (1 - \alpha_{\rm num} dt)\vec{X}_{[t=n\,dt]} + Y_{\rm num} \begin{pmatrix} d\xi_{[t=n\,dt]} \\ d\xi^*_{[t=n\,dt]} \end{pmatrix} \tag{107}$$

with the initial condition $\vec{X}_{[t=0]} = 0$. In this recursion relation the friction matrix $\alpha_{\rm num}$ and the noise matrix $Y_{\rm num}$ may differ from α and Y of the continuous stochastic differential equation (28) by terms linear in dt that remain to be determined in order to achieve an error scaling as dt^2.

As we have already mentioned $\vec{X}_{[t=n\,dt]}$ is a Gaussian vector for any step n of the iteration so that its probability distribution is characterised by the covariance matrix $C_{ij}^{(n)} = \langle X_i X_j^* \rangle$, with indices i, j ranging from 1 to $2\mathcal{N}$. From (107) the covariance matrices are shown to obey the recursion relation:

$$C^{(n+1)} = (1 - \alpha_{\rm num} dt) C^{(n)} (1 - \alpha_{\rm num}^\dagger dt) + \frac{2dt}{dV} Y_{\rm num} Y_{\rm num}^\dagger. \tag{108}$$

For a small enough time step dt this matrix sequence converges to a finite covariance matrix solving

$$C^{(\infty)} = (1 - \alpha_{\rm num} dt) C^{(\infty)} (1 - \alpha_{\rm num}^\dagger dt) + \frac{2dt}{dV} Y_{\rm num} Y_{\rm num}^\dagger. \tag{109}$$

We now try to choose the friction matrix and the noise matrix in order to minimise the deviation of $C^{(\infty)}$ from the desired value, which is the covariance matrix of the exact distribution (21), equal to $(2M\,dV)^{-1}$. We look for $\alpha_{\rm num}$ and $Y_{\rm num}$ differing from the theoretical values (104,105) by terms linear in dt, and leading to a covariance matrix different from the theoretical one by terms quadratic in dt:

$$\alpha_{\rm num} = 2M + \alpha_1 dt \tag{110}$$

$$Y_{\rm num} = \begin{pmatrix} \mathcal{Q} & 0 \\ 0 & \mathcal{Q}^* \end{pmatrix} + Y_1 dt \tag{111}$$

$$C^{(\infty)} = \frac{1}{2M\,dV} + O(dt^2). \tag{112}$$

Equation (109) is satisfied up to order dt irrespectively of the choice of α_1, Y_1. Requiring that equation (109) is satisfied up to order dt^2 leads to the condition

$$-\alpha_1 \frac{1}{4M} - \frac{1}{4M}\alpha_1 + Y_1 \begin{pmatrix} \mathcal{Q} & 0 \\ 0 & \mathcal{Q}^* \end{pmatrix} + \begin{pmatrix} \mathcal{Q} & 0 \\ 0 & \mathcal{Q}^* \end{pmatrix} Y_1^\dagger + M = 0. \tag{113}$$

A particular solution of this equation is provided by $\alpha_1 = 0$ and $Y_1 = Y_1^\dagger = -M/2$. Our improved integration scheme is therefore

$$\alpha_{\rm num} = 2M \tag{114}$$

$$Y_{\rm num} = \begin{pmatrix} \mathcal{Q} & 0 \\ 0 & \mathcal{Q}^* \end{pmatrix} - \frac{1}{2} M dt. \tag{115}$$

The analysis of the recursion relation (108) is easily performed for our improved integration scheme (114,115) since $\alpha_{\rm num}$, $\alpha^\dagger_{\rm num}$, $Y_{\rm num}$ and hence $C^{(n)}$ are polynomials of M and commute with M. As a consequence $C^{(\infty)}$ also commutes with M.

Let us first estimate the deviation of $C^{(\infty)}$ from the exact covariance matrix $(2M\,dV)^{-1}$:

$$C^{(\infty)} = \left[1-(1-\alpha_{\rm num}dt)^2\right]^{-1}\frac{2dt}{dV}Y_{\rm num}Y^\dagger_{\rm num} \quad (116)$$

$$\simeq \frac{1}{2M\,dV}\left[1+\frac{dt^2}{4}M^2+O(dt^3)\right]. \quad (117)$$

Because M is bounded from above by unity we take in practice $dt = 1/8$ so that the error is less than 0.5 percent.

Let us finally estimate the convergence time of the covariance matrices. The recursion relation (108) can be rewritten as

$$C^{(n+1)}-C^{(\infty)} = (1-\alpha_{\rm num}dt)^2\left[C^{(n)}-C^{(\infty)}\right] \quad (118)$$

so that the relative deviation of $C^{(n)}$ from its asymptotic value evolves as $(1-2M_{\rm min}dt)^{2n}$ where $M_{\rm min}$ is the smallest eigenvalue of M, that can be evaluated along the lines of [4]. We choose the number of time steps n so that the relative deviation of $C^{(n)}$ from $C^{(\infty)}$ is less than 0.5 percent.

C Moments of N_0 of a harmonically trapped ideal Bose condensed gas

We explain how to calculate the approximate expressions (42) for the moments of the number of condensed particles for an ideal Bose gas in an isotropic harmonic potential of frequency ω in the temperature regime $k_BT \gg \hbar\omega$ and in the Bogoliubov approximation. The calculation of the moments involves sums over the excited harmonic levels, see (41). By using the known degeneracy of the harmonic eigenstate manifold of energy $n\hbar\omega$ above the ground state energy the calculation reduces to the evaluation of sums of the form

$$S_{p,q}(\epsilon) = \sum_{n=1}^{\infty}\frac{n^p}{(\exp(n\epsilon)-1)^q} \quad (119)$$

where $\epsilon = \hbar\omega/k_BT$ is tending to zero, and the exponents p and q are positive integers.
First case: $q-p>1$: In the limit $\epsilon\to 0$ the sum is dominated by the contribution of small values of n. Replacing $\exp(\epsilon n)-1$ by its first order expression we obtain:

$$S_{p,q}(\epsilon) \simeq \frac{1}{\epsilon^q}\sum_{n=1}^{\infty}\frac{1}{n^{q-p}} = \frac{1}{\epsilon^q}\zeta(q-p) \quad (120)$$

where $\zeta(\alpha) = \sum_{n\geq 1} 1/n^\alpha$ is the Riemann Zeta function.
Second case: $q-p<1$: In the limit $\epsilon\to 0$ the contribution to the sum is dominated by large values of n. We then replace the discrete sum by an integral over n from 1 to $+\infty$. Taking as integration variable $u=\epsilon n$ we arrive at

$$S_{p,q}(\epsilon) \simeq \frac{1}{\epsilon^{p+1}}\int_\epsilon^{+\infty} du\,\frac{u^p}{(\exp(u)-1)^q}. \quad (121)$$

We can take the limit $\epsilon\to 0$ in the lower bound of the integral since $q-p<1$:

$$S_{p,q}(\epsilon) \simeq \frac{1}{\epsilon^{p+1}}I_{p,q}. \quad (122)$$

To calculate the resulting integral $I_{p,q}$ we expand the integrand in series of $\exp(-u)$ and integrate term by term over u:

$$I_{p,q} \equiv \int_0^{+\infty} du\,\frac{u^p}{(\exp(u)-1)^q} = \sum_{k=0}^{\infty}\frac{p!}{(k+q)^{p+1}}\frac{(k+q-1)!}{k!(q-1)!} \quad (123)$$

which can be expressed in terms of the Riemann Zeta function, e.g. $I_{2,2} = 2(\zeta(2)-\zeta(3))$.
Third case: $q-p=1$: In the limit $\epsilon\to 0$ both the small values of n and the large values of n contribute to the sum. We introduce a small parameter $\nu \ll 1$ that will be put to zero at the end of the calculation. For the summation indices $n<\nu/\epsilon$ we keep a discrete sum and we approximate each term of the sum by its first order expression in ϵ, which is correct as $n\epsilon<\nu\ll 1$. For the summation indices $n>\nu/\epsilon$ we

replace the sum by an integral, which is correct in the limit $\epsilon \to 0$ for a fixed ν, since we then recognise a Riemann sum of a function with a converging integral. This leads to

$$S_{p,p+1} \simeq \frac{1}{\epsilon^{p+1}} \left[\sum_{n=1}^{\nu/\epsilon} \frac{1}{n} + \int_{\nu}^{+\infty} du \, \frac{u^p}{(\exp(u)-1)^{p+1}} \right]. \tag{124}$$

In the limit $\epsilon \to 0$ the discrete sum is approximated by

$$\sum_{n=1}^{\nu/\epsilon} \frac{1}{n} \simeq \log(\nu/\epsilon) + \gamma \tag{125}$$

where γ is Euler's constant. In the integral we remove and add $1/(\exp(u)-1)$ to the integrand in order to get a convergent integrand which facilitates the calculation of the $\nu \to 0$ limit. The integral of $1/(\exp(u)-1)$ can be calculated explicitly from the primitive $\log(1-\exp(-u))$ so that in the small ν limit

$$\int_{\nu}^{+\infty} du \, \frac{u^p}{(\exp(u)-1)^{p+1}} = \log \frac{1}{1-\exp(-\nu)} + \int_{\nu}^{+\infty} du \, \left[\frac{u^p}{(\exp(u)-1)^{p+1}} - \frac{1}{\exp(u)-1} \right] \tag{126}$$

$$\simeq -\log \nu + J_p \tag{127}$$

where

$$J_p = \int_0^{+\infty} du \, \left[\frac{u^p}{(\exp(u)-1)^{p+1}} - \frac{1}{\exp(u)-1} \right]. \tag{128}$$

The $-\log\nu$ term coming from the integral compensates the $\log\nu$ term coming from the sum in (125) so that in the limit $\nu \to 0$ we get the ν-independent estimate

$$S_{p,p+1} \simeq \frac{1}{\epsilon^{p+1}} \left[-\log\epsilon + \gamma + J_p \right]. \tag{129}$$

The quantity J_p for $p > 0$ can be calculated from a recursion relation obtained in the following way: we use the identity

$$\frac{u^p}{(\exp(u)-1)^{p+1}} = -\frac{u^p}{(\exp(u)-1)^p} + u^p \frac{\exp(u)}{(\exp(u)-1)^{p+1}}. \tag{130}$$

The first term of the above expression leads to an integral already calculated in (123) and called $I_{p,p}$. We then integrate the second term of the above expression by parts, taking the derivate of u^p with respect to u. This finally leads to

$$J_p = J_{p-1} + \frac{1}{p} - I_{p,p}. \tag{131}$$

We get in particular $J_1 = 1 - \zeta(2)$ and $J_2 = 3/2 - 3\zeta(2) + 2\zeta(3)$.

Finally we collect the approximations for the $S_{p,q}$ relevant for the calculation of the skewness of the number of condensed particles N_0 in 1D, 2D, 3D:

$$\begin{array}{lll} S_{0,1} \simeq \dfrac{-\log\epsilon+\gamma}{\epsilon} & S_{0,2} \simeq \dfrac{\zeta(2)}{\epsilon^2} & S_{0,3} \simeq \dfrac{\zeta(3)}{\epsilon^3} \\ S_{1,1} \simeq \dfrac{\zeta(2)}{\epsilon^2} & S_{1,2} \simeq \dfrac{-\log(\epsilon)+\gamma+1-\zeta(2)}{\epsilon^2} & S_{1,3} \simeq \dfrac{\zeta(2)}{\epsilon^3} \\ S_{2,1} \simeq \dfrac{2\zeta(3)}{\epsilon^3} & S_{2,2} \simeq \dfrac{2\zeta(2)-2\zeta(3)}{\epsilon^3} & S_{2,3} \simeq \dfrac{-\log\epsilon+\gamma+J_2}{\epsilon^3} \end{array} \tag{132}$$

D Equations of the number conserving Bogoliubov approach

In this appendix we give the equations of motion for the operator $\hat{\Lambda}$ and for $\phi_\perp^{(2)}(r)$ from [5]. The evolution equation for $\hat{\Lambda}$ is:

$$i\hbar\partial_t \begin{pmatrix} \hat{\Lambda}(r,t) \\ \hat{\Lambda}^\dagger(r,t) \end{pmatrix} = \mathcal{L}(t) \begin{pmatrix} \hat{\Lambda}(r,t) \\ \hat{\Lambda}^\dagger(r,t) \end{pmatrix} \tag{133}$$

with $\mathcal{L}$ given by (24). The evolution equation for $\phi_\perp^{(2)}(r)$ is:

$$\left(i\hbar\frac{d}{dt} - \mathcal{L}(t) \right) \begin{pmatrix} \phi_\perp^{(2)}(t) \\ \phi_\perp^{(2)*}(t) \end{pmatrix} = \begin{pmatrix} \mathcal{Q}(t)S(t) \\ -\mathcal{Q}^*(t)S^*(t) \end{pmatrix} \tag{134}$$

where

$$\begin{aligned} S(r) &= -gN|\,\phi(r)\,|^2\phi(r)\langle 1+\sum_s dV\,\hat\Lambda^\dagger(s)\hat\Lambda(s)\rangle \\ &+ 2gN\phi(r)\langle\hat\Lambda^\dagger(r)\hat\Lambda(r)\rangle + gN\phi^*(r)\langle\hat\Lambda(r)\hat\Lambda(r)\rangle \\ &- gN\sum_s dV\,|\,\phi(s)\,|^2\langle\Big[\hat\Lambda^\dagger(s)\phi(s)+\hat\Lambda(s)\phi^*(s)\Big]\,\hat\Lambda(r)\rangle\,. \end{aligned} \tag{135}$$

E Truncated Wigner approach in the Bogoliubov regime

In this appendix we demonstrate the equivalences (60-63). For convenience we change in this appendix the phase reference of the field ψ which now evolves according to

$$i\hbar\partial_t\psi = \left[p^2/2m + U(r,t) + g|\psi|^2 - \mu\right]\psi \tag{136}$$

where μ is the chemical potential in the time-independent Gross-Pitaevskii equation for the condensate wavefunction (17).

1. **Identification of the pure condensate wavefunction**

   At $t=0$ equation (60) is satisfied. By keeping only terms of order $\sqrt{N}$ in (136), in the limit (44), we obtain

   $$i\hbar\partial_t\psi^{(0)} = (h_0 + g|\psi^{(0)}|^2 - \mu)\psi^{(0)} \tag{137}$$

   where h_0 is the one-body part of the Hamiltonian. This shows that (60) holds at all times.

2. **"Orthogonal-orthogonal" contribution**

   We wish to prove (62). To this aim we expand $\hat\Lambda$ and $\psi_\perp^{(1)}$ over the Bogoliubov modes:

   $$\hat\Lambda = \sum_k \hat b_k u_k + \hat b_k^\dagger v_k^* \tag{138}$$

   $$\psi_\perp^{(1)} = \sum_k b_k u_k + b_k^* v_k^* \tag{139}$$

   At $t=0$ the same mode functions u_k and v_k^* appear in the expansions of $\hat\Lambda$ and $\psi_\perp^{(1)}$. We wish to show that (138-139) hold at any time, or equivalently that $\hat\Lambda$ and $\psi_\perp^{(1)}$ have the same equations of motion. If we keep only terms of order $O(1)$ in (136) we get

   $$i\hbar\partial_t\begin{pmatrix}\psi^{(1)}\\ \psi^{(1)*}\end{pmatrix} = \mathcal{L}_{GP}\begin{pmatrix}\psi^{(1)}\\ \psi^{(1)*}\end{pmatrix} \tag{140}$$

   where $\mathcal{L}_{GP}$ is the usual Bogoliubov operator obtained from (24) by eliminating all the projectors. By using the fact that

   $$\begin{pmatrix}\psi_\perp^{(1)}\\ \psi_\perp^{(1)*}\end{pmatrix} = \begin{pmatrix}\mathcal{Q} & 0\\ 0 & \mathcal{Q}^*\end{pmatrix}\begin{pmatrix}\psi^{(1)}\\ \psi^{(1)*}\end{pmatrix} \tag{141}$$

   and

   $$\begin{pmatrix}\xi^{(1)}\phi\\ \xi^{(1)*}\phi^*\end{pmatrix} = \begin{pmatrix}\mathcal{P} & 0\\ 0 & \mathcal{P}^*\end{pmatrix}\begin{pmatrix}\psi^{(1)}\\ \psi^{(1)*}\end{pmatrix} \tag{142}$$

   with the matrices

   $$\mathcal{P}_{r,s} = dV\,\phi(r)\phi^*(s) \qquad \mathcal{Q}_{r,s} = \delta_{r,s} - dV\phi(r)\phi^*(s) \tag{143}$$

   we get

   $$i\hbar\partial_t\begin{pmatrix}\psi_\perp^{(1)}\\ \psi_\perp^{(1)*}\end{pmatrix} = \mathcal{L}\begin{pmatrix}\psi_\perp^{(1)}\\ \psi_\perp^{(1)*}\end{pmatrix} + (\xi^{(1)}+\xi^{(1)*})\begin{pmatrix}\mathcal{Q} & 0\\ 0 & \mathcal{Q}^*\end{pmatrix}\begin{pmatrix}gN|\phi|^2\phi\\ -gN|\phi|^2\phi^*\end{pmatrix} \tag{144}$$

   $$i\hbar\frac{d}{dt}\xi^{(1)} = dV\sum_r gN|\phi(r)|^2[\phi^*(r)\psi^{(1)}(r) + \psi^{(1)*}(r)\phi(r)]. \tag{145}$$

The fact that the derivative of $\xi^{(1)}$ is purely imaginary and the initial condition $\xi^{(1)} = 0$ guarantee that $(\xi^{(1)} + \xi^{(1)*}) = 0$ for all times, which proves that $\hat{\Lambda}$ and $\psi_\perp^{(1)}$ have the same equations of motion. At all times we then have

$$\langle \hat{\Lambda}^\dagger(s)\hat{\Lambda}(r)\rangle = \sum_k u_k(r)u_k^*(s)\langle \hat{b}_k^\dagger \hat{b}_k\rangle + v_k^*(r)v_k(s)\langle \hat{b}_k \hat{b}_k^\dagger\rangle \tag{146}$$

and

$$\langle \psi_\perp^{(1)*}(s)\psi_\perp^{(1)}(r)\rangle = \langle \hat{\Lambda}^\dagger(s)\hat{\Lambda}(r)\rangle + \frac{1}{2}\sum_k u_k(r)u_k^*(s) - v_k^*(r)v_k(s) \tag{147}$$

where the amplitudes b_k are time-independent and the u_k, v_k are time-dependent modes evolving according to

$$i\hbar\partial_t \begin{pmatrix} u_k \\ v_k \end{pmatrix} = \mathcal{L} \begin{pmatrix} u_k \\ v_k \end{pmatrix} . \tag{148}$$

By using the decomposition of unity, equation (61) of reference [5]:

$$\sum_k u_k(r)u_k^*(s) - v_k^*(r)v_k(s) = \frac{1}{dV}\mathcal{Q}_{r,s} \tag{149}$$

we prove (62).

3. **"Parallel-parallel" contribution**

We wish to prove (61). We use the fact that $\langle dV \sum_r |\psi(r)|^2\rangle$ is a constant of motion order by order in $1/\sqrt{N}$. To order $\sqrt{N}$ we get

$$\frac{d}{dt}N = 0 \tag{150}$$

To order N^0 we get

$$\frac{d}{dt}\langle \xi^{(1)} + \xi^{(1)*}\rangle = 0 \tag{151}$$

which we verified directly in (145). To order $1/\sqrt{N}$ we get

$$\frac{d}{dt}\left[\langle \xi^{(2)} + \xi^{(2)*}\rangle + \langle |(\xi^{(1)}|^2\rangle + \langle dV \sum_r |\psi_\perp^{(1)}(r)|^2\rangle\right] = 0\,. \tag{152}$$

Using (62) we then obtain

$$\langle \xi^{(2)} + \xi^{(2)*}\rangle + \langle |(\xi^{(1)}|^2\rangle + \langle \delta\hat{N}\rangle + \frac{\mathcal{N}-1}{2} = \text{constant}\,. \tag{153}$$

At $t = 0$ from (55), (56) we deduce

$$\text{constant} = \frac{\mathcal{N}-1}{2} \tag{154}$$

so that at any time

$$\langle \xi^{(2)} + \xi^{(2)*}\rangle + \langle |(\xi^{(1)}|^2\rangle = -\langle \delta\hat{N}\rangle\,. \tag{155}$$

Note that without the approximation in [3] we would have at $t = 0$ constant $= \frac{\mathcal{N}}{2}$ and as a consequence $\langle \xi^{(2)} + \xi^{(2)*}\rangle + \langle |(\xi^{(1)}|^2\rangle = -\langle \delta\hat{N}\rangle + \frac{1}{2}$. The contribution of the $1/2$ compensates exactly the term $-\frac{1}{2}\phi^*(s)\phi(r)$ in (59). We neglect here this contribution.

4. **Term "parallel-orthogonal"**

The last step consists in proving (63). We first remark that at $t = 0$ $\langle \psi_\perp^{(1)}\rangle = 0$, and for linearity reasons $\langle \psi_\perp^{(1)}\rangle = 0$ at all times. At $t = 0$ (63) is satisfied by construction. We then have to deduce the equation of motion for

$$\langle \chi\rangle \equiv \langle \xi^{(1)*}\psi_\perp^{(1)} + \psi_\perp^{(2)}\rangle \tag{156}$$

and show that it coincides with the equation of motion for $\phi_\perp^{(2)}$. By keeping only terms of order $1/\sqrt{N}$ in (136) we get

$$i\hbar\partial_t \begin{pmatrix} \psi^{(2)} \\ \psi^{(2)*} \end{pmatrix} = \mathcal{L}_{GP} \begin{pmatrix} \psi^{(2)} \\ \psi^{(2)*} \end{pmatrix} + \begin{pmatrix} gN[\phi^*\psi^{(1)2} + 2\phi|\psi^{(1)}|^2] \\ -gN[\phi\,\psi^{(1)*2} + 2\phi^*|\psi^{(1)}|^2] \end{pmatrix} . \tag{157}$$

With a calculation analogous to the one we performed to obtain the derivative of $(\psi_\perp^{(1)}, \psi_\perp^{(1)*})$, using (153) to eliminate $\xi^{(2)}$ and replacing $\psi^{(1)}$ by $\xi^{(1)}\phi + \psi_\perp^{(1)}$, we obtain:

$$i\hbar\partial_t \begin{pmatrix} \psi_\perp^{(2)} \\ \psi_\perp^{(2)*} \end{pmatrix} = \mathcal{L} \begin{pmatrix} \psi_\perp^{(2)} \\ \psi_\perp^{(2)*} \end{pmatrix} - \langle \delta\hat{N} \rangle \begin{pmatrix} gN\mathcal{Q}|\phi|^2\phi \\ -gN\mathcal{Q}^*|\phi|^2\phi^* \end{pmatrix} \tag{158}$$

$$+ \begin{pmatrix} gN\mathcal{Q}[2|\psi_\perp^{(1)}|^2\phi + 2\xi^{(1)}\phi^2\psi_\perp^{(1)*} + \phi^*(\psi_\perp^{(1)})^2] \\ -gN\mathcal{Q}^*[2|\psi_\perp^{(1)}|^2\phi + 2\xi^{(1)}\phi^2\psi_\perp^{(1)*} + \phi^*(\psi_\perp^{(1)})^2]^* \end{pmatrix}. \tag{159}$$

In particular, we find that the terms involving $|\xi^{(1)}|^2$ disappear because $(\xi^{(1)})^2 = -|\xi^{(1)}|^2$. By using (144) and (145) we can calculate the derivative of $\langle\chi\rangle$:

$$i\hbar\partial_t \begin{pmatrix} \langle\chi\rangle \\ \langle\chi^*\rangle \end{pmatrix} = \mathcal{L} \begin{pmatrix} \langle\chi\rangle \\ \langle\chi^*\rangle \end{pmatrix} + \begin{pmatrix} \mathcal{Q}\,R \\ -\mathcal{Q}^*\,R^* \end{pmatrix} \tag{160}$$

with

$$\begin{aligned} R(r) &= -\langle\delta\hat{N}\rangle gN|\phi(r)|^2\phi(r) + 2gN\phi(r)[\langle\hat{\Lambda}^\dagger\hat{\Lambda}\rangle - \frac{1}{2}|\phi(r)|^2] \\ &+ gN\phi^*\langle\hat{\Lambda}^2\rangle - gN\left\{\frac{1}{2}\phi(r)|\phi(r)|^2 + dV\sum_s |\phi(s)|^2\langle[\hat{\Lambda}^\dagger(s)\phi(s) + \phi^*(s)\hat{\Lambda}(s)]\hat{\Lambda}(r)\rangle\right\} \end{aligned} \tag{161}$$

which is identical to (135), except for the contribution of the term 1/2 neglected in [3] as discussed after (155). In order to obtain (161) we used the identity (62) and the fact that all terms proportional to $\phi(r)$ are killed by the projector $\mathcal{Q}$ in (160). Summarising, (160) and (161) together with $\langle\psi_\perp^{(1)}\rangle = 0$ prove (63).

F Equation for the noncondensed field in the Wigner approach

In the truncated Wigner approach, we define the field $\Lambda_{\rm ex}(r) = a_\phi^*\psi_\perp(r)/\sqrt{N}$ where ϕ is at this stage an arbitrary wave function normalised to unity, $\psi_\perp$ is the component of ψ orthogonal to ϕ, and a_ϕ is the coefficient of ψ along ϕ. When ψ solves the time-dependent Gross-Pitaevskii equation, the equation of motion for $\Lambda_{\rm ex}$ is given by:

$$i\hbar\frac{d\Lambda_{\rm ex}}{dt} = \frac{1}{\sqrt{N}}i\hbar\frac{d}{dt}\left(a_\phi^*\psi_\perp(r)\right) = dV\sum_s\sum_{k=0}^{4}\frac{R_k(r,s)}{N^{(k-1)/2}} \tag{162}$$

where we have collected the terms of the same power in $\Lambda_{\rm ex}$:

$$\begin{aligned} R_0(r,s) &= \frac{N_\phi}{N}\frac{\mathcal{Q}_{r,s}}{dV}[-i\hbar\partial_t + h_0 + gN_\phi|\,\phi(s)\,|^2]\phi(s) \\ R_1(r,s) &= \frac{\mathcal{Q}_{r,s}}{dV}\left[h_0 + 2gN_\phi|\,\phi(s)\,|^2\right]\Lambda_{\rm ex}(s) - \phi(r)(i\hbar\partial_t\phi^*(s))\Lambda_{\rm ex}(s) \\ &+ \frac{\mathcal{Q}_{r,s}}{dV}gN_\phi\phi^2(s)\Lambda_{\rm ex}^*(s) - \Lambda_{\rm ex}(r)\phi^*(s)(-i\hbar\partial_t + h_0 + gN_\phi|\,\phi(s)\,|^2)\phi(s) \\ R_2(r,s) &= -\frac{N}{N_\phi}\Lambda_{\rm ex}^*(s)\Lambda_{\rm ex}(r)(-i\hbar\partial_t + h_0 + 2gN_\phi|\,\phi(s)\,|^2)\phi(s) \\ &+ gN\frac{\mathcal{Q}_{r,s}}{dV}\left[\Lambda_{\rm ex}^2(s)\phi^*(s) + 2\Lambda_{\rm ex}^*(s)\Lambda_{\rm ex}(s)\phi(s)\right] \\ &- gN\phi^*(s)|\,\phi(s)\,|^2\Lambda_{\rm ex}(s)\Lambda_{\rm ex}(r) \\ R_3(r,s) &= gN\frac{N}{N_\phi}\left[\frac{\mathcal{Q}_{r,s}}{dV}\Lambda_{\rm ex}^*(s)\Lambda_{\rm ex}^2(s) - \Lambda_{\rm ex}^{*2}(s)\Lambda_{\rm ex}(r)\phi^2(s)\right] \\ &- 2gN\frac{N}{N_\phi}|\,\phi(s)\,|^2\Lambda_{\rm ex}^*(s)\Lambda_{\rm ex}(s)\Lambda_{\rm ex}(r) \\ R_4(r,s) &= -gN\left(\frac{N}{N_\phi}\right)^2\Lambda_{\rm ex}^{*2}(s)\Lambda_{\rm ex}(s)\Lambda_{\rm ex}(r)\phi(s) \end{aligned} \tag{163}$$

where $N_\phi = a_\phi^* a_\phi$, $h_0 = p^2/2m + U(r,t)$ is the one-body part of the Hamiltonian and $\mathcal{Q}_{r,s} = \delta_{r,s} - dV\phi(r)\phi^*(s)$ projects orthogonally to ϕ. In the case of a uniform wavefunction $\phi(r) = 1/L^{3/2}$ we have

the following simplifications: (i) $\partial_t \phi$ is equal to zero, (ii) the constant terms like $|\phi(s)|^2\phi(s)$ are killed by the projectors, (iii) for terms having a vanishing spatial sum, $\frac{\mathcal{Q}_{r,s}}{dV}$ can be replaced by $\delta_{r,s}$, (iv) the sum over s of $\psi_\perp(s)$ and therefore of $\Lambda_{\rm ex}(s)$ is zero. For this value of ϕ, $\Lambda_{\rm ex}$ coincides with $\Lambda_{\rm static}$ defined in (72) and N_ϕ is equal to N_0 of equation (77).

References

[1] M. J. Steel, M. K. Olsen, L. I. Plimak, P. D. Drummond, S. M. Tan, M. J. Collett, D. F. Walls, and R. Graham, Phys. Rev. A **58**, 4824 (1998).

[2] D. F. Walls and G. J. Milburn, *Quantum Optics*, Springer-Verlag, Berlin (1994).

[3] A. Sinatra, C. Lobo and Y. Castin, Phys. Rev. Lett. **87**, 210404 (2001).

[4] A. Sinatra, Y. Castin and C. Lobo, Jour. of Mod. Opt. **47**, 2629-2644 (2000).

[5] Y. Castin and R. Dum, Phys. Rev. A **57** 3008-3021 (1998).

[6] C. Gardiner, Phys. Rev. A **56** 1414-1423 (1997).

[7] About the solution of the exact problem see e.g. I. Carusotto, Y. Castin, and J. Dalibard, Phys. Rev. A **63**, 023606 (2001) and L. I. Plimak, M. K. Olsen, M. Fleischhauer and M. J. Collett, Europhys. Lett. **56**, 372-378 (2001).

[8] Actually the equation for ψ obtained in the truncated Wigner approach differs from the usual Gross-Pitaevskii equation by a term involving a sum over all modes $\phi_k(r)$ of the field. In this paper we restrict ourselves to the case where $\sum_k \phi_k(r)\phi_k^*(r)$ is a constant independent of the position r. In this case the mean field term in the truncated Wigner point of view differs from the one $g|\psi|^2$ of the usual Gross-Pitaevskii equation by a constant term involving the number of modes, see [1] and our section 2 below.

[9] Yu. Kagan and B. Svistunov, Phys. Rev. Lett. **79** 3331 (1997) and references therein.

[10] K. Damle, S. Majumdar, and S. Sachdev, Phys. Rev. A **54**, 5037 (1996).

[11] M.J. Davis, S.A. Morgan and K. Burnett, Phys. Rev. Lett. **87**, 160402 (2001).

[12] K. Góral, M. Gajda, K. Rzążewski, Opt. Express **8**, 82 (2001).

[13] M.J. Davis, S.A. Morgan and K. Burnett, cond-mat/0201571.

[14] C. Gardiner, *Quantum Noise*, Springer-Verlag Berlin Heidelberg (1991), chapter 4 "Phase space methods".

[15] In the case of a harmonically trapped gas we assume that the box is large enough so that the atomic density is small close to the boundaries.

[16] Y. Castin, lectures in: Coherent Atomic Matter Waves, Les Houches Summer School Session LXXII in 1999, edited by R. Kaiser, C. Westbrook, and F. David (Springer, New York, (2001), and cond-mat/0105058.

[17] William H. Press, Brian P. Flannery, Saul A. Teukolsky, William T. Vetterling, *Numerical Recipes*, §7.2, Cambridge University Press (1986).

[18] M. Wilkens, C. Weiss, Opt. Expr **1**, 272 (1997).

[19] S. Giorgini, L. P. Pitaevskii, S. Stringari, Phys. Rev. Lett. **80**, 5040, (1998).

[20] V.V. Kocharovsky, Vl. V. Kocharovsky, and Marlan O. Scully, Phys. Rev. Lett. **84**, 2306 (2000).

[21] We have included not only the leading terms but also higher order terms in the denominator of the 3D formula since we have observed numerically that this dramatically improves the accuracy of the formula for moderately high values of $k_B T/\hbar\omega$.

[22] see I. Carusotto and Y. Castin (in preparation).

[23] exact in the sense of O. Penrose and L. Onsager, Phys. Rev. **104**, 576 (1956).

[24] We find at last the physical interpretation of a component of $\phi^{(2)}$ that was unexplained in [5].

[25] Y. Castin and R. Dum, Phys. Rev. Lett. **79**, 3553 (1997).

[26] D. Stamper-Kurn, A. Chikkatur, A. Görlitz, S. Inouye, S. Gupta, D. Pritchard, W. Ketterle, Phys. Rev. Lett. **82**, 4569 (1999).

[27] W. Ketterle, Spinor Condensates and Light Scattering from Bose-Einstein Condensates, in Les Houches Summer School 1999, Session LXXII, eds. R. Kaiser and C. Westbrook (cond-mat/0005001)

[28] In the simulation we observe damping in each single realisation, which indicates that this damping is a true relaxation phenomenon and not a collapse due to dephasing among different stochastic realisations. This was not the case in the 1D model of [3].

[29] We note that exactly the same procedure from the beginning of this subsection can be followed in the quantum treatment. The evolution equation for $\hat{\Lambda}_{\rm ex}$ can in fact be obtained from (163) by putting hats on a_ϕ and $\psi_\perp$ and by changing stars into daggers (see equation (A3) of [5]).

[30] For the parameters of figure (3) we perform a linear fit of the perturbative prediction for $|\langle b_0(t)\rangle|$ on the time interval $(0.0075, 0.015)$ in units of $mL^2/\hbar$ for a grid size 48^3. The slope is -0.328 with a linear correlation coefficient -0.99998. The results are the same for a grid size 64^3.

[31] In the perturbative calculation for the figure we have actually included the effect of the interaction between Bogoliubov modes which provides damping also in the excitation phase, simply by adding a term $-i\hbar\gamma_{\rm perturb}b_0$ and $-i\hbar\gamma_{\rm perturb}b_{-0}$ to the right hand side of (79) and of (80) respectively. This damping term is not totally negligible indeed since $\gamma_{\rm perturb}t_{\rm exc} \simeq 0.1$.

[32] Vincent Liu, Phys. Rev. Lett. **79**, 4056 (1997).

[33] L. P. Pitaevskii, and S. Stringari, Phys. Lett. A **235**, 398 (1997).

[34] P. O. Fedichev and G. V. Shlyapnikov, Phys. Rev. A **58**, 3146 (1998).

[35] We have checked with the particular example $\mathcal{N} = 22^3$, $N = 5\times10^4$, $k_BT = 3\mu$ and $\mu = 500\hbar^2/mL^2$, that the mean Bogoliubov energy (after averaging over 100 realisations) is conserved during the course of the time evolution at the 2% level.

[36] Michele Modugno, Ludovic Pricoupenko, and Yvan Castin, cond-mat/0203597.

[37] We have used the inequality $x/\tanh x < 1 + x^2/3$.

[38] H. T. C. Stoof, J. Low Temp. Phys. **114**, 1 (1999).

[39] C. W. Gardiner, J. R. Anglin, and T. I. A. Fudge, cond-mat/0112129.

[40] Ibidem [17], §5.6.

4.4.4 Cristallisation d'un réseaux de vortex

Dans les expériences effectuées à l'ENS, le condensat est piégé dans un potentiel cigare légèrement anisotrope et tournant autour de son axe. Dans la seconde vérsion de ces expériences, la fréquence de rotation est augmentée adiabatiquement de zéro à une valeur finale Ω_r. Pour des valeurs de Ω_r supérieures à un seuil $\simeq 0.7\omega$ où ω est la fréquence d'oscillation dans le plan transverse, la formation et successivement la cristallisation d'un réseau de vortex a été observée. Notre simulation 3D de champ classique a permis de montrer que : (*i*) Contrairement à ce qui état affirmé dans toutes les publications sur ce sujet, et même pour une température initialement nulle du condensat, il n'est pas nécessaire d'introduire à la main des termes dissipatifs dans l'équation de Gross-Pitaevskii pour observer la cristallisation du réseau de vortex. C'est en effet le régime turbulent qui suit une instabilité dynamique du système qui peuple des modes du champ initialement vides qui peuvent soustraire de l'énergie au réseaux de vortex. (*ii*) L'instabilité dynamique prédite analytiquement dans un précédent travail de S. Sinha et Y. Castin donne effectivement naissance à un réseau de vortex. (*iii*) Pour des fréquences de rotation $\Omega_r > 0.7\omega$ le scénario dépend peu de la température initiale du condensat. Enfin, nous avons mis en évidence un nouveau régime, pas encore observé expérimentalement, où, pour un condensat initialement à température non nulle, des vortex peuvent apparaître à une fréquence de rotation plus basse que 0.7ω mais supérieure à la fréquence de Landau pour laquelle le condensat sans vortex cesse d'être un minimum local d'énergie à l'équilibre thermodynamique.

4.4.5 Publication jointe

VOLUME 92, NUMBER 2 PHYSICAL REVIEW LETTERS week ending 16 JANUARY 2004

Vortex Lattice Formation in Bose-Einstein Condensates

Carlos Lobo, Alice Sinatra, and Yvan Castin
Laboratoire Kastler Brossel, Ecole Normale Supérieure, 24 rue Lhomond, 75231 Paris CEDEX 05, France
(Received 30 January 2003; published 15 January 2004)

We show that the formation of a vortex lattice in a weakly interacting Bose condensed gas can be modeled with the nonlinear Schrödinger equation for both $T = 0$ and finite temperatures without the need for an explicit damping term. Applying a weak rotating anisotropic harmonic potential, we find numerically that the turbulent dynamics of the field produces an effective dissipation of the vortex motion and leads to the formation of a lattice. For $T = 0$, this turbulent dynamics is triggered by a rotational dynamic instability of the condensate. For finite temperatures, noise is present at the start of the simulation and allows the formation of a vortex lattice at a lower rotation frequency, the Landau frequency. These two regimes have different vortex dynamics. We show that the multimode interpretation of the classical field is essential.

DOI: 10.1103/PhysRevLett.92.020403 PACS numbers: 03.75.Lm

Vortex lattices exist in many domains of physics, from neutron stars to superconductors or liquid helium. In none of these systems has the formation of the lattice been understood at the level of a microscopic theory. Several groups have recently observed the formation of a vortex lattice in weakly interacting Bose gases [1–4] and are able to monitor this formation in real time. This gives us the chance to understand the problem of lattice formation in a relatively simple system. Indeed there have been theoretical attempts to understand the formation process [5–8] with simulations of the Gross-Pitaevskii equation for the condensate wave function. All of them stress the need for explicitly including a damping term representing the noncondensed modes to which the vortices have to give away energy to relax to a lattice configuration. In this Letter, we consider this problem in the framework of the classical theory of a complex field [9] whose exact equation of motion is the nonlinear Schrödinger equation (NLSE). First, we show that lattice formation is predicted within this framework without the addition of damping terms. Second, we provide two distinct scenarios of vortex lattice formation (dynamics, temperature dependence of the formation time, and critical rotation frequency) that can be directly compared with the experiments. We study the formation of the lattice in 3D from an initially nonrotating Bose condensed gas both at $T = 0$ and at finite temperature. Contrary to the common belief, we find that the dynamic instability, which was predicted in [10] to occur above a certain threshold value of the trap rotation frequency, leads to the formation of a vortex lattice. The formation time is in this case only weakly dependent of the temperature and the observed scenario and time scales are comparable to those seen in present experiments. For a lower trap rotation frequency corresponding to the Landau frequency, but only at finite temperature, we identify a new scenario not yet observed experimentally in which the vortices enter a few at a time and gradually spiral towards the center.

We start our simulations with the nonrotating classical field in thermal equilibrium. For $T = 0$, the system initially is a pure condensate and the field is proportional to the condensate wave function ϕ given by the Gross-Pitaevskii equation in the absence of rotation, $\psi = \sqrt{N_0}\phi$, where N_0 is the condensate atom number. For finite temperatures, we sample the initial thermal equilibrium in the Bogoliubov approximation at a given temperature T for a fixed number N_0 of condensate particles. In this approximation, the classical field is given by $\psi(\mathbf{r}, 0) = \sqrt{N_0}\phi(\mathbf{r}) + \psi_\perp(\mathbf{r})$. The random field $\psi_\perp(\mathbf{r})$ orthogonal to ϕ [11] representing the thermal noise is given by

$$\psi_\perp(\mathbf{r}) = \sum_n b_n u_n(\mathbf{r}) + b_n^* v_n^*(\mathbf{r}), \tag{1}$$

where u_n and v_n are the Bogoliubov mode functions associated with ϕ and b_n are independent random c numbers taken from a Gaussian distribution that obeys the classical equipartition formula, $\langle b_n^* b_n \rangle = k_B T/\epsilon_n$, ϵ_n being the Bogoliubov energy of mode n. In practice, to sample this distribution we use the Brownian motion method described in [11]. In our work, the field ψ is to be interpreted not as the condensate wave function but as the whole matter field. We present here results from single realizations of the field ψ which experimentally correspond to single runs. We have checked that different realizations lead to similar results.

In our simulations, we consider a Bose condensed gas initially trapped in a cigar-shaped harmonic potential with oscillation frequencies whose ratio is 1:1:0.25, with 10^5 atoms of mass m and a coupling constant $g = 0.0343$ in units of $\hbar\omega a_0^3$, where ω is the radial frequency and $a_0 = \sqrt{\hbar/m\omega}$ is the oscillator length. The corresponding chemical potential is $\mu = 8\hbar\omega$. We start each simulation with the gas in thermal equilibrium. We abruptly turn on the trap anisotropy which leads to a change in the radial frequencies: $\omega_{x,y}^2 = \omega^2(1 \mp \epsilon)$, where $\epsilon = 0.025$. Then

 © 2004 The American Physical Society

the rotation frequency $\Omega(t)$ of this anisotropy is slowly increased from zero to a final value Ω_f over $500\omega^{-1}$, to follow Procedure I in [10]. After that, we let the gas evolve in the presence of the rotating anisotropy until the angular momentum of the gas reached a steady state.

The calculation is performed in the rotating frame so that the NLSE takes the form

$$i\hbar\partial_t\psi = \left[-\frac{\hbar^2}{2m}\Delta + U(\mathbf{r}) + g|\psi|^2 - \Omega(t)L_z\right]\psi, \quad (2)$$

where L_z is the angular momentum operator along z, and U is the anisotropic harmonic potential. The field ψ is subject to periodic boundary conditions in the rotating frame [12]. Our grid size is $32 \times 32 \times 128$ corresponding to an energy cutoff of $32\hbar\omega$ per spatial direction, although we have also run simulations on a $64 \times 64 \times 256$ grid (see below).

Zero initial temperature.—This set of simulations can be divided into two groups: those for which the final rotation frequency is $\Omega_f/\omega \leq 0.7$ and those with $\Omega_f/\omega \geq 0.75$. Between these two values lies the threshold for the dynamic instability of the condensate which changes the subsequent dynamics dramatically [10,13]. In the first group, as the rotation frequency gradually increases with time, the condensate adiabatically follows a steady state, apart from excitations of the surface modes leading to a very small oscillation of the angular momentum [see curve for $\Omega_f = 0.7\omega$ in Fig. 2(a) (below)]. With increasing Ω_f, the condensate's final state becomes more and more elliptically deformed, surrounded by a ring of vortices which, however, never enter it. The second group shows a completely different behavior when $\Omega(t)/\omega \simeq 0.75$ (see left column of Fig. 1): The instability sets in; the condensate becomes slightly S-shaped at $t \simeq 450\omega^{-1}$ before being highly deformed and undergoing very turbulent motion [5]. This is accompanied by a large increase in angular momentum of the gas from almost zero when $\Omega(t) < 0.75\omega$ to between $5\hbar$–$7\hbar$ per particle [see Fig. 2(a)]. At this point ($t \simeq 670\omega^{-1}$) several vortices enter the high density region and, in less than $200\omega^{-1}$, settle down to form a well-defined lattice. After this, a period of relaxation of around $800\omega^{-1}$ begins with the initially rotating lattice finally stopping in the rotating frame. There remains a small random motion of the vortices around their equilibrium positions in the lattice together with density fluctuations in and around the condensate.

At the end of the simulation, damping of the vortex motion has occurred and the initial energy of the vortex motion has been transferred in an effectively irreversible way to other degrees of freedom of the field. A similar phenomenon has been observed for the relative motion of two condensates [15]. *If we assume that the field has reached a thermal distribution*, we can calculate the temperature of the system by taking the final state of the simulation and evolving it with the conjugate gradient method in a trap rotating at Ω_f. This reduces its energy

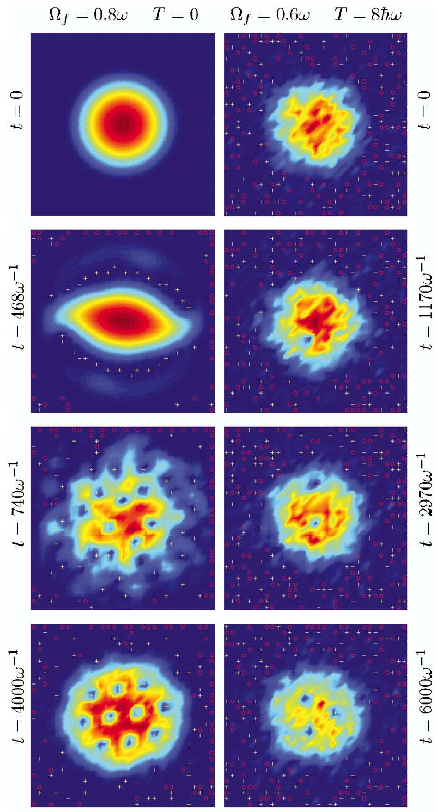

FIG. 1 (color online). Cut along the radial plane ($z = 0$) of the system spatial density at different times. Crosses (circles) indicate the position of vortices of positive (negative) charge [14]. Left column: $T = 0$, $\Omega_f = 0.8\omega$. Top to bottom: initial state; near instability; turbulent behavior; end of simulation. Right column: $k_BT = 8\hbar\omega$, $\Omega_f = 0.6\omega$. Top to bottom: initial state; entry of first vortex; entry of second vortex; end of simulation with a three-vortex lattice.

and takes it to the local minimum associated with the vortex lattice. We then calculate the energy difference ΔE between the final state of the simulation and the one at the minimum. Assuming that Bogoliubov theory is valid, ΔE must correspond to the energy of a classical thermal distribution of weakly coupled harmonic oscillators of amplitude b_n which obeys the equipartition formula $\langle b_n^* b_n\rangle\epsilon_n = k_BT$, with n being the Bogoliubov mode number. So, if $\mathcal{N}$ is the number of modes in the system (and keeping in mind that we have to subtract the one corresponding to the condensate), then we have

$$\Delta E = \sum_n \langle b_n^* b_n\rangle\epsilon_n = (\mathcal{N} - 1)k_BT. \quad (3)$$

The final temperature is $0.616\hbar\omega$ for $\Omega_f = 0.75\omega$ and $0.754\hbar\omega$ for $\Omega_f = 0.8\omega$, in other words it is extremely small, less than a tenth of the chemical potential.

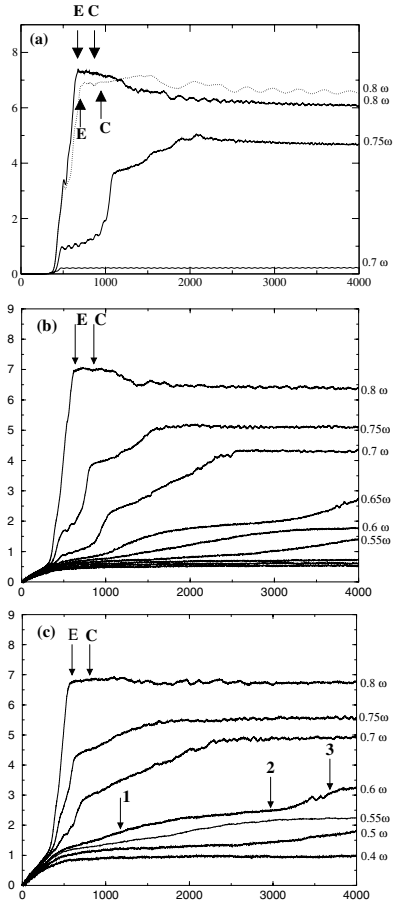

FIG. 2. Total angular momentum of the system in units of $\hbar$ per atom as a function of ωt. The arrows marked E and C indicate the entry of the vortices into the condensate and the crystallization of the lattice for $\Omega_f = 0.8\omega$. (a) $T = 0$, solid lines from bottom to top: $\Omega_f/\omega = 0.7(0), 0.75(7), 0.8(10)$; dashed line: $\Omega_f/\omega = 0.8(10)$ with a grid size of $64 \times 64 \times 256$. All other curves were done on a $32 \times 32 \times 128$ grid. In parenthesis is the number of vortices in the lattice at the end of the simulation. (b) $k_B T = 4\hbar\omega$, $\Omega_f/\omega = 0.4(0), 0.45(0), 0.5(0), 0.55(1), 0.6(1), 0.65(2), 0.7(6), 0.75(7), 0.8(10)$. (c) $k_B T = 8\hbar\omega$, $\Omega_f/\omega = 0.4(0), 0.5(1), 0.55(1), 0.6(3), 0.7(7), 0.75(7), 0.8(10)$. The arrows correspond to the approximate entry time of the vortices for $\Omega_f = 0.6\omega$ as shown in Fig. 1. Note that the total angular momentum shows no signature of the entries.

We have also carried out a simulation on a larger grid ($64 \times 64 \times 256$) to check the dependence on size. We chose $\Omega_f = 0.8\omega$ and compared it with the one on the $32 \times 32 \times 128$ grid. The vortex nucleation and crystallization phases are very similar and occur at roughly the same times. At longer times, two differences arise: First, there are large underdamped oscillations of the angular momentum [see Fig. 2(a)]. An analysis of the simulation suggests that these oscillations are those of the scissors mode. Second, the final temperature ($0.094\hbar\omega$) differs by the ratio of the number of modes as expected: At time $t = 500\omega^{-1}$ when $\Omega(t) = \Omega_f$, ψ had not yet reached the boundary in the smaller grid case and so the evolution of ψ on both grids was identical up to this time with the same total energy which was conserved at later times resulting in the same value of ΔE. This exemplifies the fact that, in classical field theories, the relationship between energy and temperature depends on the energy cutoff.

Since the thermal occupation of the modes is directly proportional to the temperature, we expect that all relaxation processes which involve scattering from or into those modes (such as Landau-Beliaev damping) will be reduced. We are thus led to the conclusion that, for our simulations starting at $T = 0$, relaxation rates in the period after the formation of the lattice could depend on the size of the grid. However, with the present numerical results, we were not able to demonstrate this.

Finite initial temperature.—We performed simulations starting with $k_B T = 4\hbar\omega$ and $k_B T = 8\hbar\omega$. Now not only the condensate but also other modes are occupied in the initial state, with a thermal distribution. For a final rotation frequency below that of the dynamic instability, the situation is quite different from that of the zero temperature case: The condensate is never deformed and the vortices do enter the condensate if $\Omega_f \geq 0.55\omega$ for $k_B T = 4\hbar\omega$ and if $\Omega_f \geq 0.5\omega$ for $k_B T = 8\hbar\omega$. In contrast to the $T = 0$ case at a frequency below that of the dynamic instability, all the noncondensed modes are now thermally occupied allowing the condensate to exchange particles, energy, and angular momentum with the noncondensed cloud. Therefore, as soon as Ω_f is greater than the Landau frequency (at which the vortex-free condensate is no longer a minimum of the energy [6]), the condensate moves gradually toward an energy minimum with one or more vortices. We have found numerically by imaginary time evolution that the Landau frequency is 0.51ω. During the real time evolution corresponding to $\Omega_f = 0.6\omega$ (right column of Fig. 1), we find that the vortices enter only one at a time. That is, as the angular momentum of the cloud increases, one vortex out of the group of vortices that surrounds the condensate will enter it and spiral slowly clockwise towards the center on a time scale of hundreds of ω^{-1}. After that vortex has reached the center, a second one enters slowly, repeating the trajectory of the first until it starts to interact with it, and the two orbit around each other for a while after which a third will enter. At the end of the simulation, coinciding with the achievement of the plateau in angular momentum, the lattice becomes stationary in the rotating frame and no further vortex enters the condensate. For $\Omega_f = 0.7\omega$, we find that the condensate deforms itself elliptically after which three vortices enter at the same time and form a rotating lattice. After that, and spaced by

several hundred ω^{-1}, a fourth and then a fifth vortex enter. Finally, two further vortices enter simultaneously to form the final seven vortex lattice. At each intermediate stage there is always a well-defined lattice present although it is not stationary in the rotating frame. We should contrast this with the scenario of [6,7], where a large number of vortices enter all at once into the condensate in a ring configuration and then some of them form a lattice while others are shed and leave the condensate.

For Ω_f above the dynamic instability frequency, the situation is quite similar to the corresponding one at $T = 0$. Once the instability has set in the lattice is formed for both temperatures in about $200\omega^{-1}$ as in the $T = 0$ case [see Figs. 2(b) and 2(c)]. This weak temperature dependence was also found experimentally [16]. We find a time for the lattice to stop rotating on the order of $100\omega^{-1}$, much shorter than at $T = 0$.

It is important to emphasize the multimode interpretation of the field. Transposing Penrose and Onsager's definition to the classical field theory, the condensate wave function is defined as the eigenvector corresponding to the largest eigenvalue of the one-body density matrix $\langle\psi^*(\mathbf{r}')\psi(\mathbf{r})\rangle$ where the average is over an ensemble of initial states. If the system becomes turbulent because it encounters an instability, the trajectories of the neighboring realizations will diverge exponentially. However, after averaging, we believe that the condensate wave function will not be a turbulent function. For $T = 0$, there is only one initial state and so we replace ensemble averaging by one over time in the steady state regime [17]. In our simulations with $\Omega_f = 0.8\omega$, the system must therefore be understood as becoming intrinsically multimode even though we started at $T = 0$ with a pure condensate. This shows that any theoretical model which singles out the condensate mode for separate treatment with a Gross-Pitaevskii–type equation could run into trouble in turbulent situations since the separation between condensed and noncondensed modes would be hard to keep.

Conclusions.—We have identified two very different scenarios for the crystallization of the vortex lattice in the classical field model. In the first one, the vortex and the subsequent lattice formation are triggered by a dynamic instability which sets in for a threshold value of the rotation frequency of the trap. Many vortices enter the condensate at the same time and settle into a lattice in about $200\omega^{-1}$. In this scenario, the lattice formation time is essentially the same for both $T = 0$ and finite temperatures in agreement with experimental observation [16]. In the second scenario, observed only at finite temperatures, vortices appear for a lower value of the rotation frequency corresponding to the Landau frequency, and so no dynamic instability occurs. The vortices enter one by one into the condensate and settle into a lattice before the entry of the following one. Thus far, there has been no experimental check of this second scenario.

We thank B. Durin, L. Carr, I. Carusotto, G. Shlyapnikov, and J. Dalibard for useful contributions. C. L. acknowledges support from the Fundação para a Ciência e Tecnologia of Portugal. We acknowledge financial support from Région Ile de France. L. K. B. is a unit of ENS and of Université Paris 6 associated to CNRS.

Note added.—We have been informed that crystallization of the vortex lattice has also been observed in a simulation without a damping term by the group of Bigelow [18].

[1] K. W. Madison, F. Chevy, W. Wohlleben, and J. Dalibard, Phys. Rev. Lett. **84**, 806 (2000).
[2] J. R. Abo-Shaeer, C. Raman, J. M. Vogels, and W. Ketterle, Science **292**, 476 (2001).
[3] P. C. Haljan, I. Coddington, P. Engels, and E. A. Cornell, Phys. Rev. Lett. **87**, 210403 (2001).
[4] E. Hodby, G. Hechenblaikner, S. A. Hopkins, O. M. Maragó, and C. J. Foot, Phys. Rev. Lett. **88**, 010405 (2002).
[5] D. L. Feder, A. A. Svidzinsky, A. L. Fetter, and C. W. Clark, Phys. Rev. Lett. **86**, 564 (2001).
[6] M. Tsubota, K. Kasamatsu, and M. Ueda, Phys. Rev. A **65**, 023603 (2002); K. Kasamatsu, M. Tsubota, and M. Ueda, Phys. Rev. A **67**, 033610 (2003).
[7] A. A. Penckwitt, R. J. Ballagh, and C. W. Gardiner, Phys. Rev. Lett. **89**, 260402 (2002).
[8] E. Lundh, J.-P. Martikainen, and K.-A. Suominen, Phys. Rev. A 67, 063604 (2003).
[9] K. Damle, S. N. Majumdar, and S. Sachdev, Phys. Rev. A **54**, 5037 (1996); Yu. Kagan and B. Svistunov, Phys. Rev. Lett. **79**, 3331 (1997); M. J. Davis, S. A. Morgan, and K. Burnett, Phys. Rev. Lett. **87**, 160402 (2001).
[10] S. Sinha and Y. Castin, Phys. Rev. Lett. **87**, 190402 (2001).
[11] A. Sinatra, C. Lobo, and Y. Castin, J. Phys. B **35**, 3599 (2002).
[12] Periodic boundary conditions (PBC) in the lab frame would stop the rotation of the noncondensed gas. We checked that PBC in the rotating frame do not set a pure condensate into rotation as the condensate density is negligible at the grid borders. The harmonic trap anisotropy is then crucial for the vortex formation at $T = 0$ by triggering the dynamic instability of [10].
[13] K. Madison, F. Chevy, V. Bretin, and J. Dalibard, Phys. Rev. Lett. **86**, 4443 (2001).
[14] Vortex positions are found by integrating the gradient of the phase around each grid square in the plane.
[15] A. Sinatra, P. Fedichev, Y. Castin, J. Dalibard, and G. V. Shlyapnikov, Phys. Rev. Lett. **82**, 251 (1998).
[16] J. R. Abo-Shaeer, C. Raman, and W. Ketterle, Phys. Rev. Lett. **88**, 070409 (2002).
[17] L. D. Landau and E. M. Lifshitz, *Statistical Physics* (Pergamon, Oxford, 1980), 3rd ed., Pt. 1, Sect. 1; K. Góral, M. Gajda, and K. Rzążewski, Phys. Rev. A **66**, 051602(R) (2002).
[18] N. Bigelow, 2002 Summer Session on Atomic Gases in Benasque, Spain.

4.5 Activité expérimentale sur le piégeage et le refroidissement d'atomes

Pendant ma deuxième année de séjour post doctoral à l'ENS, j'ai été initiée à la physique expérimentale des atomes froids. J'ai participé pendant quatre mois à une expérience sur le piégeage et le refroidissement des isotopes 6 et 7 (fermion et boson respectivement) du lithium, dans le groupe de Christophe Salomon, et j'ai travaillé pendant un an sur l'expérience de condensation de l'hélium métastable de Michèle Leduc.

4.5.1 Piégeage simultané Li^6+Li^7

En 1999 l'expérience de gaz de Fermi dégénéré dans l'équipe de Christophe Salomon démarrait. A cause de la difficulté de réaliser le refroidissement par évaporation sur des fermions polarisés (les collisions dans l'onde s sont supprimées pour des fermions dans le même état interne), le projet était de le refroidir le ^{6}Li (fermion) par thermalisation avec un nuage de ^{7}Li bosonique. J'ai "atterri" dans une équipe très performante formée de Mark Oliver-Mewes, Florien Schrek et Gabriele Ferrari. Fabrice Gerbier (maintenant permanent du Laboratoire) était en stage de DEA dans l'équipe à ce moment-là.

Selon un montage maintenant "standard" dans les expériences d'atomes froids, les deux isotopes du lithium sortant d'un four sont ralentis par la pression de radiation d'une onde laser dans un champ magnétique inhomogène (ralentisseur Zeeman), avant d'être capturés et refroidis par un piège magnéto-optique dans une cellule en verre. Pour ralentir et piéger chacun des deux isotopes, nous avions besoin de quatre fréquences : un faisceau principal et un repompeur pour le piège, et un faisceau principal et un repompeur pour le ralentisseur. En tout, il nous fallait huit fréquences autour de la longueur d'onde 671 nm dans un intervalle de fréquence d'environ 10 GHz. Le système laser fournissant les fréquences et la puissance nécessaires était constitué de *dix* diodes laser dont deux lasers maîtres stabilisés en fréquence et huit lasers esclaves, et un amplificateur à semiconducteur (MOPA). Injecté par quatre lasers esclaves, le MOPA délivre 140 mW de puissance dans le même mode spatial (gaussien) et de polarisation, avec un spectre de fréquence contenant les quatre composantes nécessaires au piégeage des deux isotopes [12].

J'ai donc participé à la mise en œuvre de l'optique pour le ralentissement et le piégeage simultané des deux isotopes du système d'imagerie pour les deux isotopes.

Je me souviendrai longtemps de l'émotion éprouvée en voyant le double piège ^{6}Li + ^{7}Li pour la première fois (les transitions utilisées sont dans le visible pour le lithium et l'on voit la fluorescence du piège magnéto-optique très bien à l'œil nu). Le double piège une fois obtenu, nous l'avons optimisé pour augmenter la densité en vue du refroidissement évaporatif.

A la fin de la phase de compression, nous avions typiquement : 3×10^8 atomes de ^{6}Li fermionique avec 6×10^9 atomes de ^{7}Li bosonique à des températures de l'ordre de 0.6 mK, et des densités de 4×10^{11} atomes/cm^3 pour le ^{7}Li et 6.5×10^{10} atomes/cm^3 pour le ^{6}Li. Plus de détails sur le montage expérimental et sur les résultats sont donnés dans la référence [12].

4.5.2 Vers un condensat d'hélium métastable

Au cours de l'année 1999-2000, j'ai travaillé sur une expérience dont le but était d'obtenir un condensat de Bose-Einstein d'hélium métastable He* (2^3S_1). L'intérêt d'un tel

condensat est que ses atomes peuvent être détectés avec une très bonne résolution spatiale et temporelle (MCP, channeltron, ...) et une grande efficacité puisque l'énergie interne de He^* (2^3S_1) est de 20 eV. L'équipe était dirigée par Michèle Leduc et Claude Cohen-Tannoudji et je bénéficiais à l'époque d'un poste temporaire de maître de conférence au Collège de France attaché à la chaire du professeur Cohen-Tannoudji.

Pour cette expérience, on utilise l'état métastable triplet 2^3S_1 de longue durée de vie comme l'état "fondamental" d'une transition dans l'infrarouge ($2^3S_1 - 2^3P_2$) permettant de manipuler les atomes par laser et de les détecter. Après avoir informatisé l'expérience, et mis au point un système d'imagerie compliqué par la faible efficacité quantique de notre caméra infrarouge et la faible masse de l'He, nous avons mené une série de mesures systématiques destinées à caractériser le taux de pertes à deux corps dans notre piège magnéto-optique, essentiellement dues aux collisions de Penning autoionisantes.

$$2^3S_1 + 2^3S_1 \rightarrow 1S_0 + \mathrm{He}^+ + e^- \tag{4.5}$$
$$2^3S_1 + 2^3P_2 \rightarrow 1S_0 + \mathrm{He}^+ + e^- \tag{4.6}$$

Ce sont ces collisions en effet qui limitent la densité maximale d'atomes métastables dans le piège magnéto-optique à quelques 10^{10} at/cm^3. Comme la section efficace de collision de Penning impliquant un atome excité (4.6) est environ 100 fois plus élevée que celle impliquant deux atomes métastables, le taux de pertes à deux corps dépend des conditions d'accord et d'intensité des faisceaux de piégeage. Nous avons donc mesuré le taux de pertes en fonction de l'intensité et du désaccord tout en étendant le domaine des mesures préexistantes à des désaccord plus importants. En utilisant un modèle simple et en mesurant la fraction d'atomes excités pour chaque expérience, nous avons pu déduire de nos mesures la constante de taux (section efficace $\times$ vitesse moyenne) pour les collisions de Penning dominantes (4.6) avec une précision significativement accrue par rapport aux résultats disponibles [15]. Les détails expérimentaux sur notre piège magnéto-optique pour l'hélium métastable sont donnés dans [16].

Du point de vue de l'obtention d'un gaz dégénéré, on veut obtenir idéalement un nuage avec beaucoup d'atomes et très dense a fin d'augmenter la densité et le taux de collisions pour démarrer le refroidissement par évaporation. La suppression des collisions de Penning pour un gaz polarisé dans le piège magnétique permettra d'atteindre au but. L'équipe de Michèle Leduc et Claude Cohen-Tannouji a été la deuxième (à distance de quelques semaines de l'équipe d'Alain Aspect à Orsay) à condenser l'hélium métastable en 2001.

Chapitre 5

Pompage optique de l'^{3}He pour l'imagerie médicale

Les numéros entre crochets font référence à la liste de mes publications, disponible en fin de document.

5.1 Imagerie avec des gaz (hyper)polarisés

Il y a quelques années sont apparues les premières images de poumons obtenues avec de l'hélium 3 polarisé par pompage optique. Les spins nucléaires de l'hélium, préalablement orientés par laser, et précessant dans un champ magnétique typiquement de 1.5 Tesla, sont utilisés à la place des protons présents dans les tissus pour faire les images par résonance magnétique. Une fois inhalé, l'hélium reste confiné dans les cavités pulmonaires. On obtient alors des images complémentaires aux images "en proton" (voir figure 1).

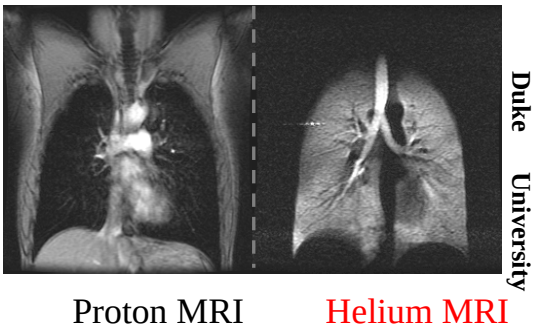

FIG. 5.1 – Image du torse humain "en proton" et "en hélium polarisé".

5.2 Rappel : Structure atomique de l'hélium 3

En champ nul

L'état fondamental 1^1S_0 de l'hélium 3 est un état singlet ($S = 0$) avec moment angulaire orbital nul $J = 0$. Le noyau a un moment angulaire $I = 1/2$, ce qui donne naissance à deux sous-niveaux magnétiques dans le fondamental $m_I = \pm 1/2$. L'état triplet 2^3S_1 est métastable. Il comporte deux niveaux hyperfins $F = 3/2$ et $F = 1/2$, séparés de 6.74 GHz, et six sous-niveaux Zeeman. L'autre état qui nous intéresse est l'état triplet 2^3P. Il comporte 5 niveaux et 18 sous-niveaux Zeeman. De la structure des niveaux 2^3S et 2^3P

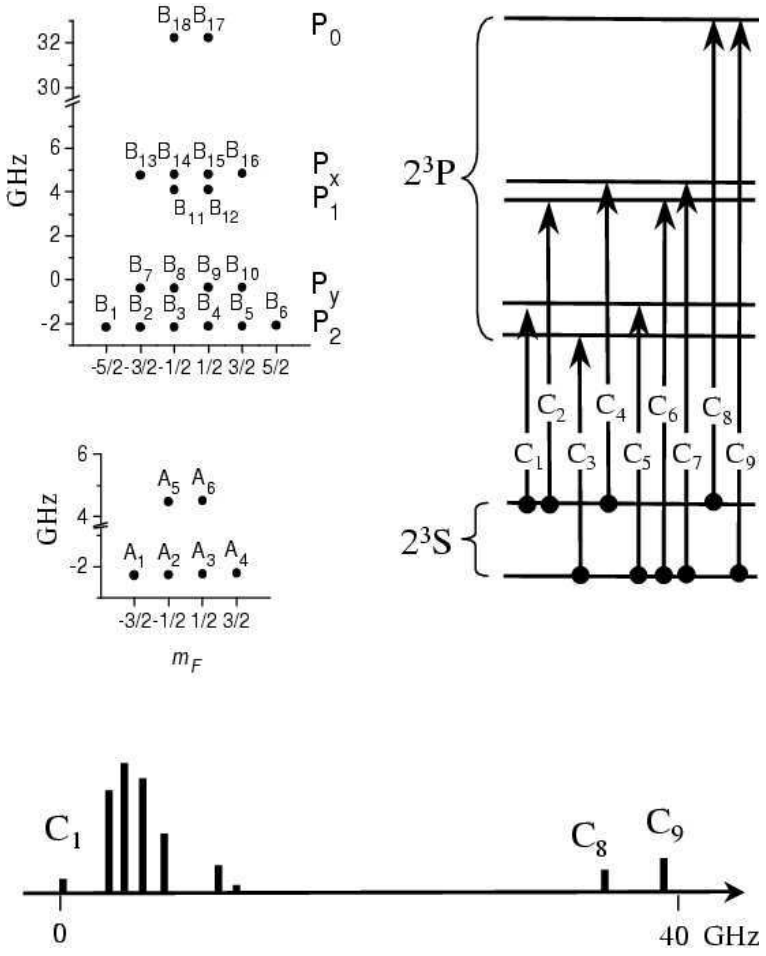

FIG. 5.2 – Structure de la raie atomique 2^3S-2^3P de l'hélium 3 en champ nul et spectre correspondant.

résultent 9 raies appelées C_1-C_9 par ordre d'énergie croissante. Les raies isolées C_8 et C_9 sont celles habituellement utilisées pour le pompage optique de l'hélium à bas champ. La largeur Doppler est de 1.2 GHz à température ambiante.

À 1.5 Tesla

À 1.5 Tesla les niveaux de l'état métastable 2^3S et de l'état 2^3P s'étalent sur plusieurs dizaines de GHz (Fig.5.3). Les sous-niveaux $A_1 - A_6$ du métastable sont proches des états de la base découplée $|m_J, \pm\rangle$, où $m_J = -1, 0, 1$ est le nombre quantique magnétique du moment angulaire électronique et $\pm$ dénote le nombre quantique magnétique du spin nucléaire $m_I = \pm 1/2$. En introduisant les angles de mélange $\theta_\pm$ on a :

$$\begin{aligned}
\mathrm{A}_1 &= |-1,-\rangle \\
\mathrm{A}_2 &= \cos\theta_- \,|-1,+\rangle + \sin\theta_- \,|0,-\rangle \\
\mathrm{A}_3 &= \cos\theta_+ \,|0,+\rangle + \sin\theta_+ \,|1,-\rangle \\
\mathrm{A}_4 &= \cos\theta_- \,|0,-\rangle - \sin\theta_- \,|-1,+\rangle \\
\mathrm{A}_5 &= |1,+\rangle \\
\mathrm{A}_6 &= \cos\theta_+ \,|1,-\rangle - \sin\theta_+ \,|0,+\rangle
\end{aligned} \tag{5.1}$$

avec, à 1.5 Tesla,

$$\sin\theta_+ = 0.07128 \quad \text{and} \quad \sin\theta_- = 0.07697. \tag{5.2}$$

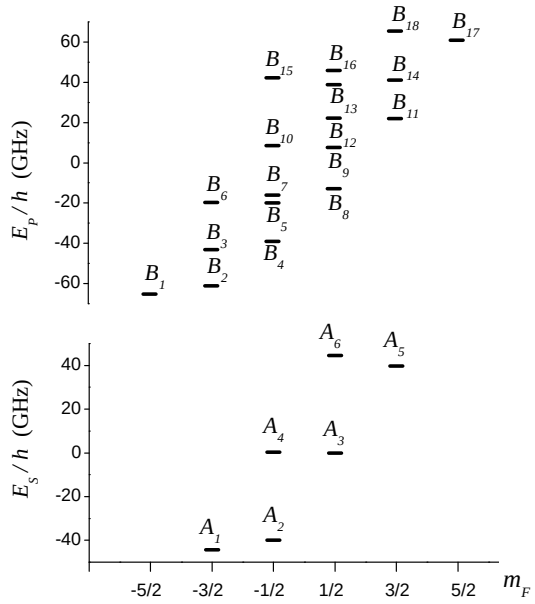

FIG. 5.3 – Structure de la raie atomique 2^3S-2^3P de l'hélium 3 à 1.5 T.

5.3 Pompage optique dans un champ de 1.5 Tesla

La technique de pompage optique par échange de métastabilité repose sur des collisions aux cours desquelles un atome métastable et un atome fondamental échangent leurs variables électroniques. Ces collisions unies au couplage hyperfin dans le niveau métastable sont chargées de transférer l'orientation créée par le laser dans le niveau métastable, au niveau fondamental. Cette technique permet d'obtenir des polarisations nucléaires allant jusqu'à 80%. Toutefois, la méthode marche seulement pour une faible pression d'hélium de l'ordre du millibar. Une compression du gaz sans perte de polarisation est alors nécessaire pour que le gaz puisse être inhalé. Bien que des méthodes de compression efficaces aient été développées dans quelques laboratoire dans le monde, la préparation du gaz polarisé à la pression atmosphérique reste pour l'instant un obstacle à la diffusion à grande échelle de cette nouvelle technique d'imagerie. Polariser le gaz à une plus forte pression simplifierait considérablement l'étape de compression et donc la préparation des échantillons pour l'imagerie. En particulier, l'idée de Pierre-Jean Nacher était de travailler en fort champ magnétique où le partiel découplage hyperfin dans les différents états excités atomiques et moléculaires entrant en jeu, supprime les canaux importants de relaxation pour la polarisation nucléaire qui rendent habituellement le pompage par échange de métastabilité inefficace à forte pression. Mon projet démarré au sein du groupe en 2001 était donc d'explorer expérimentalement et de modéliser le pompage optique dans des conditions nouvelles, de champ magnétique intense et de forte pression. Pendant quatre ans, j'ai travaillé avec Marie Abboud que j'ai (co)encadrée (avec Pierre-Jean Nacher), pour son stage de DEA et ensuite sa thèse dans le groupe, et en collaboration avec Xavier Maître du laboratoire U2R2M à Orsay.

5.3.1 Dispositif expérimental

Pour mener cette expérience nous avons construit un dispositif compact, portable et amagnétique pour polariser le gaz que nous venions placer lors des créneaux libres (souvent les week-ends) à l'intérieur d'un imageur IRM hospitalier qui nous fournissait

un champ magnétique homogène de 1.5 Tesla. Un schéma du dispositif expérimental est montré en Fig.5.4. Un premier laser, le laser pompe polarisé σ^- ou σ^+, parallèle au champ

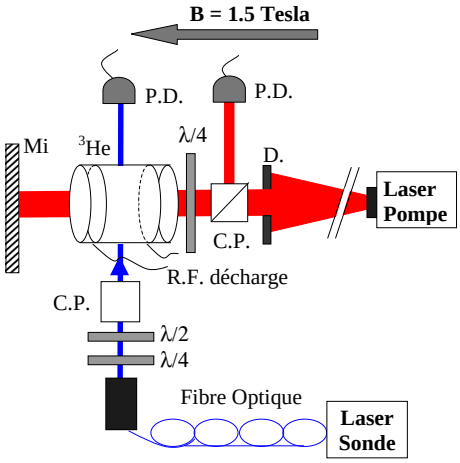

FIG. 5.4 – Schéma du montage expérimental. C.P., $\lambda/2$ et $\lambda/4$ sont respectivement des cubes polariseurs et des lames retardatrices demi-onde et quart d'onde. Mi est un miroir ; D est un diaphragme circulaire de diamètre 1.5 cm P.D. sont des photo diodes pour l'infra-rouge.

magnétique, est utilisé pour polariser l'hélium. Il s'agit d'une diode laser amplifiée dans une fibre dopée Yb qui delivre un demi Watt. Un deuxième laser, le laser sonde (dans une superposition de polarisations σ^- et σ^+), est utilisé pour mesurer les populations des sous-niveaux métastables et déduire ainsi la polarisation nucléaire. Le gaz est contenu dans une cellule en Pyrex (Fig.5.5). Des électrodes en cuivre fixées aux parois externes de la cellule et reliées à un circuit oscillant à 3 MHz, entretiennent un plasma dans le gaz qui maintient une petite fraction d'atomes $\sim 10^{-6}$ dans l'état métastable. Une vue d'ensemble est montrée en Fig.5.6.

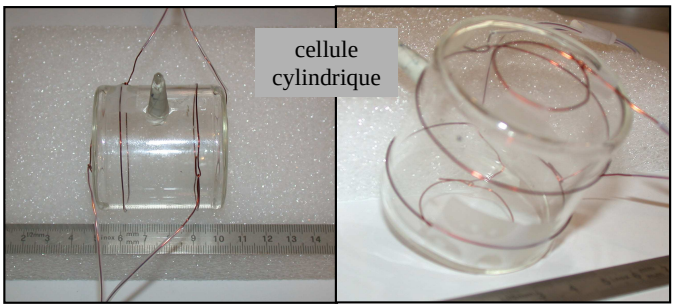

FIG. 5.5 – Photo de la cellule cylindrique (de dimensions internes 4.6 cm×4.6 cm) avec deux paires d'électrodes circulaires ; deux petites électrodes sont posées contre les fenêtres optiques de la cellule, les deux autres de diamètre 5 cm sont enroulées sur la cellule. Les électrodes sont connectées deux à deux au même potentiel, de sorte que deux électrodes successives ont des potentiels de polarité opposée.

5.3.2 Résultats

Nous avons mené une étude expérimentale systématique sur différentes cellules entre 1 et 67 mbar et nous avons déterminé les meilleures conditions de fonctionnement du

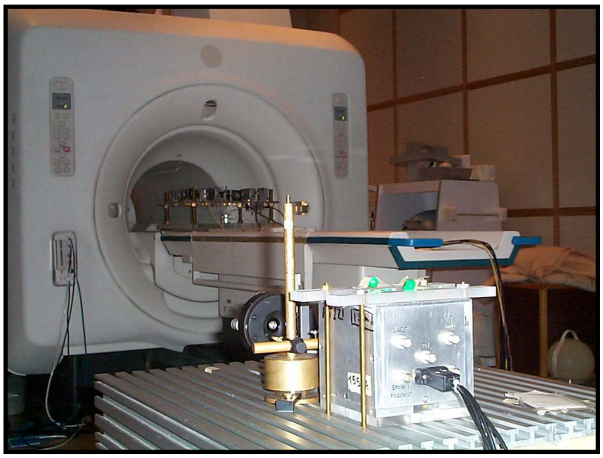

FIG. 5.6 – Vue d'ensemble. Les lasers (dont la diode sonde au premier plan), les appareils électroniques et le système d'acquisition informatique restent dans une région de faible champ magnétique.

pompage à fort champ et forte pression (paramètres de décharge, intensité et désaccord du laser pompe, choix de la raie de pompage).

Nos meilleurs résultats à haut champ pour la polarisation nucléaire stationnaire sont montrés sur la Fig.5.7. Les polarisations obtenues à bas champ pour les mêmes pressions sont montrées sur la même figure pour comparaison. À basse pression d'hélium (1.33 mbar) nous retrouvons une polarisation très elevée (82%). Il y a pourtant des différences importantes par rapport aux pompage à bas champ. (i) La dynamique de pompage est intrinsèquement ralentie par le découplage hyperfin dans le niveau métastable, ce qui rend le taux de production de gaz polarisé à fort champ et basse pression non compétif : on perd environ un facteur 10 par rapport aux meilleurs taux de pompage à bas champ. En augmentant la pression, la polarisation stationnaire obtenue par le pompage traditionnel s'effondre. Par contre, le pompage à haut champ donne des polarisations élevées ($\sim 40\%$) jusqu'à la pression la plus importante que nous avons étudiée systematiquement, 67 mbar. Bien que la dynamique soit ralentie, le gain en pression fait remonter les taux de production de l'aimantation à des valeurs compétitives [21,22] avec seulement 0.5 W de puissance laser utilisée.

Les polarisations nucléaires et les taux de pompage obtenus montrent la possibilité d'étendre le domaine d'applicabilité du pompage optique par échange de métastabilité aux fortes pressions. Étant donné que 1.5 Tesla est la valeur du champ la plus courante dans les imageurs médicaux, ce nouveau schéma de pompage ouvre la voie, pour les applications médicales, au développement d'un polariseur de gaz à haut champ, avec une simplification considérable de la procédure de compression (1 : 30 ou 1 : 15 au lieu de 1 : 1000). Un deuxième avantage du pompage à haut champ par rapport au pompage optique standard est dû aux fait que la sélection de la raie de pompage se fait en fréquence *et* polarisation (plutôt qu'en polarisation seulement), ce qui allège énormément les contraintes sur la qualité de la polarisation du faisceau pompe.

5.3.3 Modélisation et comparaison théorie-expérience

Un travail de fond de modélisation théorique du pompage optique et du processus de collision d'échange à haut champ nous a permis de comprendre en détail la physique, les potentialités et les limites de ce nouveau schéma de pompage à 1.5 Tesla. Les principales

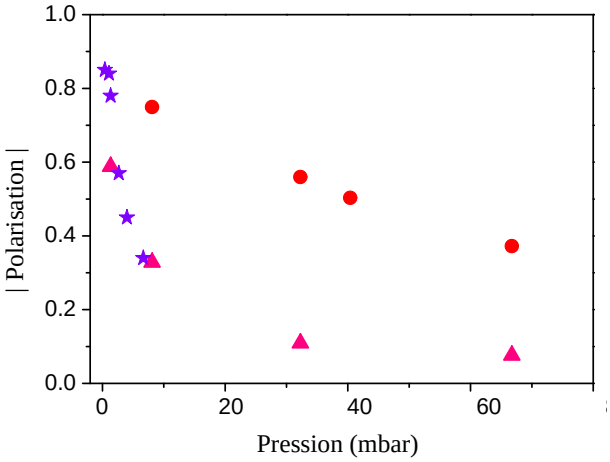

FIG. 5.7 – Polarisation nucléaire à l'état stationnaire M_{stat} en fonction de la pression du gaz. Étoiles et triangles : pompage habituel à bas champ, mesures données dans la littérature (étoiles) ou effectuées dans les mêmes cellules utilisées à haut champ (triangles). Cercles : pompage à 1.5 Tesla. La puissance du faisceau pompe utilisé est de $2W$ et $5W$ pour les triangles et les étoiles respectivement à bas champ, et de $0.5W$ pour les cercles à haut champ.

différences par rapport au pompage à bas champ viennent du découplage hyperfin important qui change radicalement la structure des niveaux de l'état métastable et affecte les collisions d'échange de métastabilité. À 1.5 Tesla, l'effet Zemann étant dominant, les 6 sous-niveaux de l'état métastable 2^3S_1 se groupent en trois paires de niveaux quasi-dégénérés correspondant (dans la limite $B \to \infty$) à $m_j = 1$, $m_j = 0$ et $m_j = -1$). Une intensité de laser pompe relativement faible peut transférer efficacement les atome d'une paire à l'autre par pompage optique car le couplage entre paires donné par les collisions d'échange est faible. Par contre, le couplage à l'intérieur d'une paire est très fort et, même en présence du laser pompe, les populations relatives à l'intérieur d'une paire donnée sont en première approximation données par la température de spin imposée par les collisions d'échange. Cette vision simple permet de quantifier le ralentissement de la dynamique de pompage et d'estimer le "rendement quantique" (nombre d'atomes polarisés sur nombre de photons absorbés) pour les différentes raies de pompage à fort champ. La bonne surprise confirmée par l'expérience est que, en dépit du découplage hyperfin important à 1.5 Tesla, le pompage optique conserve les propriétés de haut rendement quantique qui le caractérisent à bas champ.

Avec l'aide du modèle théorique que nous avons développé, nous avons montré que l'application d'un champ magnétique réduit sensiblement la relaxation de la polarisation nucléaire, et en particulier la relaxation en présence du laser de pompage, qui limite la polarisation obtenue à forte pression et bas champ. Un taux de relaxation résiduel, qui augmente avec la densité d'atomes dans le niveau excité 2^3P et avec la pression, a aussi été mis en évidence.

5.3.4 Publications jointes

EUROPHYSICS LETTERS 15 November 2004

Europhys. Lett., **68** (4), pp. 480–486 (2004)
DOI: 10.1209/epl/i2004-10237-y

High nuclear polarization of ^{3}He at low and high pressure by metastability exchange optical pumping at 1.5 tesla

M. Abboud[1](*), A. Sinatra[1](**), X. Maître[2], G. Tastevin[1] and P.-J. Nacher[1]

[1] *Laboratoire Kastler Brossel, Ecole Normale Supérieure*
24 rue Lhomond, 75005 Paris, France(***)
[2] *U2R2M, Université Paris-Sud and CIERM, Hôpital de Bicêtre*
94275 Le Kremlin-Bicêtre Cedex, France(**)

received 19 July 2004; accepted in final form 21 September 2004
published online 22 October 2004

PACS. 32.80.Bx – Level crossing and optical pumping.
PACS. 67.65.+z – Spin-polarized hydrogen and helium.
PACS. 87.61.-c – Magnetic resonance imaging.

Abstract. – Metastability exchange optical pumping of helium-3 is performed in a strong magnetic field of 1.5 T. The achieved nuclear polarizations, between 80% at 1.33 mbar and 25% at 67 mbar, show a substantial improvement at high pressures with respect to standard low-field optical pumping. The specific mechanisms of metastability exchange optical pumping at high field are investigated, advantages and intrinsic limitations are discussed. From a practical point of view, these results open the way to alternative technological solutions for polarized helium-3 applications and in particular for magnetic-resonance imaging of human lungs.

Introduction. – A gas of ground-state ^{3}He atoms in which a high degree of nuclear polarization is achieved offers an incredibly rich playground in various fields of science, from statistical or nuclear physics to biophysics and medicine [1]. Depending on the targeted application, the degree of nuclear polarization, the sample density, or the production rate of polarized atoms should be optimized. A recent application, which may have an important impact on the diagnosis of pulmonary diseases, is the polarized-gas magnetic-resonance imaging (MRI) [2]. Clinical studies to demonstrate the relevance of this new tool are under way in Europe and in the United States. Yet, if a wide expertise exists in MRI to adapt the existing imaging techniques to the case of polarized gases, the gas preparation remains a critical stage to be transferred from physics laboratories to hospitals. Two methods are presently used to polarize ^{3}He: spin-exchange with optically pumped alkali atoms [3] and pure-He metastability exchange optical pumping (MEOP) [4]. In standard conditions, MEOP is performed at

(*) E-mail: marie.abboud@lkb.ens.fr
(**) E-mail: alice.sinatra@lkb.ens.fr
(***) Laboratoire Kastler Brossel is a unité de recherche de l'Ecole Normale Supérieure et de l'Université Pierre et Marie Curie, associée au CNRS (UMR 8552).
(**) U2R2M (Unité de Recherche en Résonance Magnétique Médicale) is a unité de recherche de l'Université Paris-Sud, associée au CNRS (UMR 8081).

© EDP Sciences

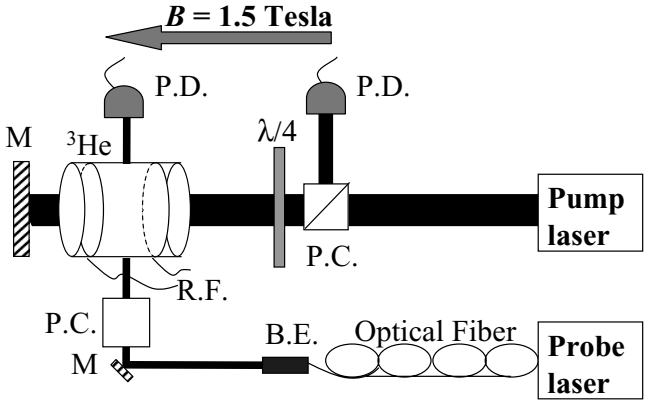

Fig. 1 – Experimental setup. The nuclear polarization is measured by the absorption of a transverse probe beam. B: static magnetic field, P.D.: photodiode, P.C.: polarizing beam-splitter, B.E: beam expander, $\lambda/4$: quarter wave plate, M: mirror, R.F.: radio-frequency to excite the discharge.

low pressures (1 mbar) in a guiding magnetic field of the order of 1 mT. Circularly polarized light at 1083 nm, corresponding to the 2^3S-2^3P transition of ^{3}He, is used to transfer angular momentum to the atoms and nuclear polarization is created by hyperfine coupling in the metastable 2^3S state. Through metastability exchange collisions, nuclear polarization builds up in the ground state. The steady-state nuclear polarization obtained by MEOP in standard conditions rapidly decreases if the pressure of the sample exceeds a few mbar (see below, fig. 5a) [5–7]. Therefore, a delicate polarization-preserving compression stage is necessary for MRI where the gas should be at atmospheric pressure for inhalation, and for all applications needing a dense sample. In this letter, the MEOP scheme is shown to withstand large hyperfine decoupling. A strong magnetic field of 1.5 T actually improves its performances with respect to standard low-field optical pumping. At 1.33 mbar, high nuclear polarizations of the order of 80% are routinely obtained with much lighter experimental constraints. At higher pressures, the achieved nuclear polarizations are dramatically increased compared to published low-field results. An elementary model with simple rate equations is used to account for these results.

Experimental setup and methods. – Experiments are performed in the bore of the 1.5 T superconducting magnet of a clinical MRI system. The experimental apparatus is sketched in fig. 1. The helium gas is enclosed in a sealed cylindrical Pyrex cell (diameter 5 cm, length 5 cm). Four cells filled with 1.33 mbar, 8 mbar, 32 mbar and 67 mbar of pure ^{3}He are used. A radio-frequency discharge at 3 MHz is sustained in the gas by external electrodes, leading to metastable atom densities n_{m} in the 0.3–3×10^{10} atoms/cm^3 range, depending on the applied voltage and on the gas pressure. The optical pumping laser is either a 50 mW single-mode laser diode amplified to 0.5 W [8], or a broad-band fiber laser (1.63 GHz FWHM) delivering 2 W [9]. The pump beam is back-reflected to enhance its absorption, which is monitored on the transmitted beam with a photodiode. At the entrance of the cell, the Gaussian transverse intensity profile of the pump beam has a FWHM of the order of 2 cm. A weak probe beam from a single-mode laser diode is used to measure the nuclear polarization. It is linearly polarized perpendicularly to the magnetic field (σ polarization). The discharge intensity is modulated at 133 Hz, and the probe absorption is measured with a lock-in amplifier. Laser sources and electronics remain several meters away from the magnet bore, in a low-field region.

At 1.5 T, due to Zeeman splitting, the energy levels of the 2^3S and 2^3P states are spread over 80 and 160 GHz, respectively (fig. 2a). Hyperfine decoupling in the 2^3S state is significant,

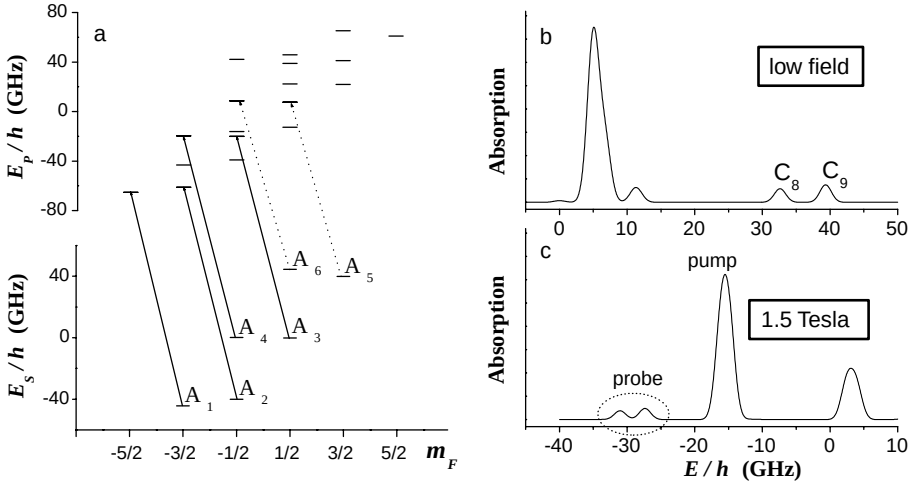

Fig. 2 – (a) Energies of the ^{3}He sublevels at 1.5 T for the metastable 2^3S state (E_S) and the 2^3P state (E_P). The transitions induced by the σ^--polarized pump (solid lines) and probe (dotted lines) are displayed. Each pump transition has a matrix element T_{ij} close to 1 [10]. (b) Absorption spectrum at low magnetic field. (c) Absorption spectrum for σ^- light at 1.5 T. Vertical and horizontal scales are identical in (b) and (c). Level names A_1 to A_6, energy zeros and spectral line positions are defined as in ref. [10].

so that the eigenstates of the Hamiltonian show only little mixing between different eigenstates $|m_J, m_I\rangle$ of the decoupled spin system, where m_J, m_I, and m_F denote the magnetic quantum numbers for the electronic, nuclear, and total angular momentum, respectively. As shown in fig. 2a, the 2^3S sublevels are arranged into three pairs of quasi-degenerate levels of increasing energies (A_1, A_2), (A_3, A_4), and (A_5, A_6) that correspond, respectively, to $m_J = -1$, 0, and 1 in the completely decoupled limit $B \to \infty$. For more details about the 2^3S level structure and the analytical expressions of eigenstates and energies, we refer the reader to ref. [10]. The absorption spectra at low magnetic field and at 1.5 T are displayed in figs. 2b and c, respectively. In standard MEOP, very high nuclear polarizations are obtained using C_8 or C_9 lines [6, 11]. Comparable polarizations are achieved at 1.5 T using the σ^--strong pump line displayed in fig. 2c. All the results presented in this work are obtained with this pump transition. The performances and efficiencies of other optical-pumping transitions at 1.5 T will be reported elsewhere. The pump simultaneously addresses the four 2^3S sublevels A_1 to A_4. Population transfer into the pair (A_5, A_6) is achieved by the following sequence: laser excitation, collisional redistribution in the 2^3P state and spontaneous emission. The ground-state nuclear polarization M is defined as $M = (n_+ - n_-)/(n_+ + n_-)$, where n_+ and n_- denote populations of the $m_I = 1/2$ and $m_I = -1/2$ nuclear spin states, respectively. In the absence of optical pumping, metastability exchange collisions impose a spin temperature distribution for the 2^3S sublevel populations, proportionally to $e^{\beta m_F}$, where $e^\beta = n_+/n_- = (1+M)/(1-M)$ [10]. The populations of sublevels A_5 and A_6, not addressed by the pump, are probed to measure M. Examples of probe absorption spectra for an unpolarized and an optically pumped steady-state situation are shown in fig. 3a. M is inferred from the relative heights of the absorption peaks. The build-up of the polarization, as well as its decay when the pump is turned off, are monitored by tuning the probe laser frequency on the probe transition starting from the A_5 ($m_F = 3/2$) sublevel (fig. 3b). These measurement procedures operate at arbitrary magnetic field and pressure [10].

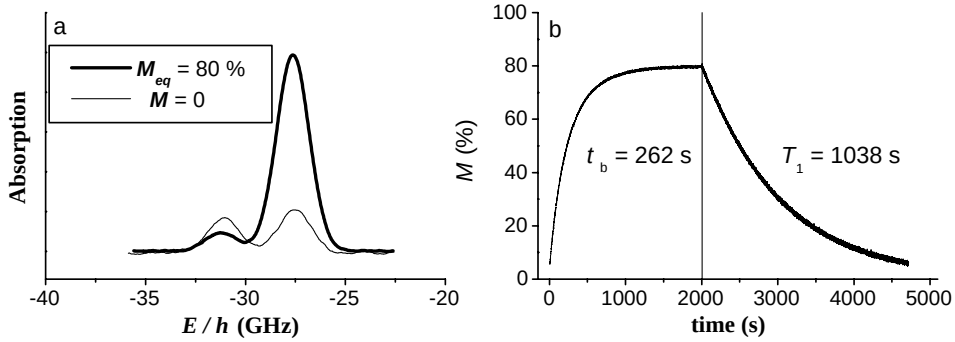

Fig. 3 – Examples of recorded signals in the 1.33 mbar cell: (a) absorption measurements on transitions from sublevels A_5 ($E/h = -27.36$ GHz) and A_6 ($E/h = -31.04$ GHz) at thermal equilibrium ($M \simeq 0$) and at steady-state nuclear polarization ($M = M_{\rm eq}$) in an optically pumped gas. (b) Polarization build-up and discharge-induced decay deduced from changes of light absorption in sublevel A_5. Pump laser is applied at time $t = 0$, and turned off after 2000 s.

Results. – The steady-state polarization $M_{\rm eq}$ and the polarization build-up time constant $t_{\rm b}$ in the 1.33 mbar cell are shown in figs. 4a and b as a function of the discharge-induced decay time T_1. Over a wide range of moderate-to-weak discharges (T_1 ranging from 300 s to 1500 s), $t_{\rm b}$ (ranging from 60 to 350 s) is proportional to T_1 and the polarization achieved with the broad-band 2 W laser is high, about 80%, independently of T_1. This behavior is specific to the high-field optical pumping, and contrasts with the standard low-field situation where a very weak discharge is required to obtain such large nuclear polarizations. For the strongest discharges, build-up times decrease ($t_{\rm b}$ ranging from 15 to 55 s) and steady-state polarizations

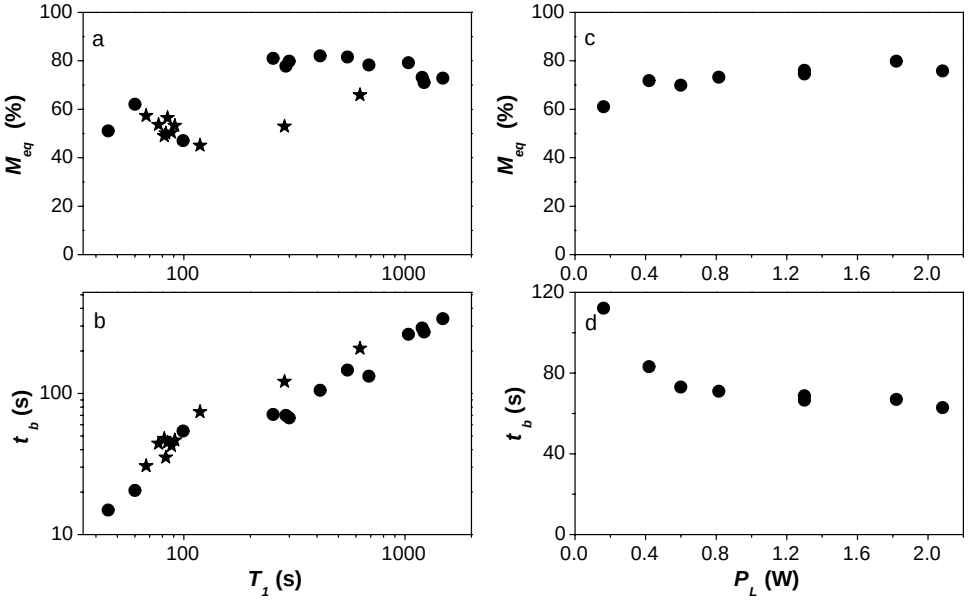

Fig. 4 – Results obtained at 1.5 T in the 1.33 mbar cell. (a) Steady-state polarization, and (b) polarization build-up time constant, as a function of the discharge-induced decay time of the polarization T_1. Circles and stars: broad-band (2 W) and single-mode (0.5 W) pump lasers, both running at full power. (c) Steady-state polarization, and (d) polarization build-up time constant, as a function of incident laser power $\mathcal{P}_{\rm L}$. Data are obtained with the broad-band pump laser and for $T_1 = 300$ s.

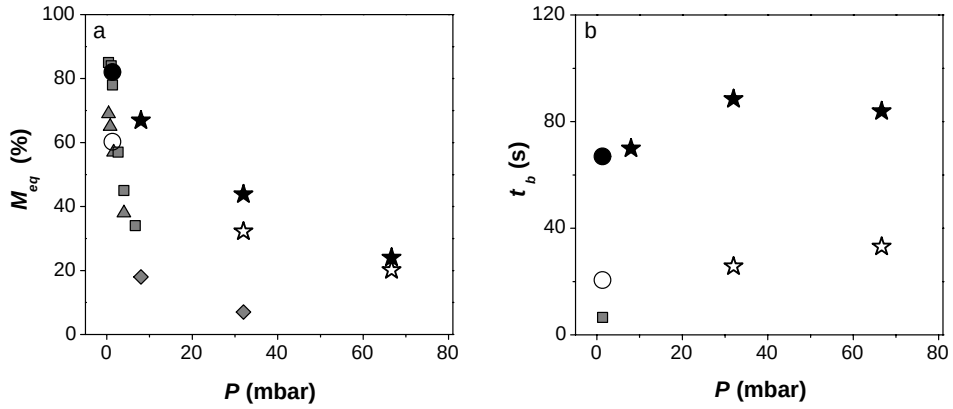

Fig. 5 – (a) Steady-state polarization, and (b) polarization build-up time constant, as a function of ^{3}He pressure P, at high and low magnetic fields. Circles and stars are 1.5 T data obtained with a broad-band (2 W) and single-mode (0.5 W) pump lasers, respectively. Filled (open) symbols are for weak (strong) discharge: T_1 = 300 (60), 2600, 1600 (325), and 1300 (700) s for 1.33, 8, 32, and 67 mbar, respectively. Triangles, squares, and diamonds are low-field data published in [5,6], and [7], respectively (all for weak discharges).

are lower. Figures 4c and d show the influence of the pump laser power for a given discharge ($T_1 = 300$ s). A laser power as low as 0.5 W is sufficient for the polarization and the build-up time to almost reach their asymptotic values. Similar studies of MEOP have been performed at higher pressures, where T_1 between 300 and 2600 s are measured. Selected results for a weak and a strong discharge at full laser power are shown in fig. 5 together with published low-field results. The polarizations obtained at high pressures are, to our knowledge, record MEOP values. The polarization build-up times weakly depend on ^{3}He pressure, in contrast with low-field MEOP [6, 12].

Discussion. – An extension of the detailed model for standard MEOP [11] to high-field conditions [10] is required to compute the populations of all atomic sublevels. Here, for simplicity, an elementary model is used to account for the main observed features. We assume that i) atoms are fully pumped into the (A_5, A_6) pair, and ii) the populations of sublevels not addressed by the pump laser are imposed by the ground-state spin temperature which only depends on M: $a_5 = (1 + M)/2$ and $a_6 = (1 - M)/2$. The sublevel A_5 is totally oriented ($m_J = 1$, $m_I = 1/2$) and carries a nuclear angular momentum $\langle I_z \rangle = \hbar/2$, while A_6 has a small component on ($m_J = 0$, $m_I = 1/2$) and a large component on ($m_J = 1$, $m_I = -1/2$) and thus carries a nuclear angular momentum $\langle I_z \rangle = \hbar(\epsilon - 1)/2$ with $\epsilon = 1 \times 10^{-2}$ at 1.5 T [13]. The rate equation for M, resulting from relaxation and metastability exchange, is then

$$\frac{\mathrm{d}M}{\mathrm{d}t} = \frac{2\langle I_z \rangle/\hbar - M}{T_\mathrm{e}} - \frac{M}{T_1} \qquad \text{with } \langle I_z \rangle = \frac{\hbar}{2}\left(M + \epsilon\frac{1-M}{2}\right),$$

where $1/T_\mathrm{e}$ is the metastability exchange collision rate for a ^{3}He atom in the ground state ($1/T_\mathrm{e} = n_\mathrm{m} \times 1.53 \times 10^{-10}\,\mathrm{cm}^3/\mathrm{s}$), and $2\langle I_z \rangle/\hbar$ is the nuclear polarization in the 2^3S state. One infers a steady-state polarization $M_\mathrm{eq} = (1 + 2T_\mathrm{e}/(\epsilon T_1))^{-1}$ and a build-up time $t_\mathrm{b} = 2T_\mathrm{e}M_\mathrm{eq}/\epsilon$. Using values of n_m and T_1 measured in the absence of pumping beam, the predicted polarization is $M_\mathrm{eq} \simeq 1$, at all pressures. The build-up times are in the range 20–300 s for the low-pressure cell, and in the range 15–40 s for the three high-pressure cells. Although this elementary model is clearly not sufficient to predict M_eq, it accounts reasonably well for

Table I – *Steady-state polarizations $M_{\rm eq}$, build-up times $t_{\rm b}$ and production rates $R_{\rm a}$ (see text) vs. gas pressure P and laser power $\mathcal{P}_{\rm L}$ for the data in fig.* 5 *and other published data. Results in parenthesis correspond to strong discharges.*

Ref.	P (mbar)	$\mathcal{P}_L$ (W)	$M_{\rm eq}$ (%)	$t_{\rm b}$ (s)	T_1 (s)	$R_{\rm a}$ (mbar/s)
this work	1.33	2.0	80 (60)	67 (20)	300 (60)	0.016 (0.039)
this work	8	0.5	67	70	2600	0.076
this work	32	0.5	44 (32)	88 (26)	1600 (325)	0.159 (0.401)
this work	67	0.5	24 (20)	84 (33)	1300 (700)	0.191 (0.405)
[12]	1	0.05	50 (40)	40 (9)	270 (40)	0.013 (0.047)
[14]	1.33	1.1	56 (39)	11 (2)	400 (10)	0.066 (0.266)
[6]	1.33	4.5	78 (45)	6.5 (0.3)	900 (15)	0.160 (2)

the observed dynamics. Its domain of validity and accuracy are estimated from detailed rate equations for the six 2^3S-sublevel populations. We find that in our experimental conditions and for the observed range of nuclear polarization, $2\langle I_z\rangle/\hbar$ given by the simple model differs from the exact value by a factor not exceeding 2, depending on M and on the gas pressure. This difference results from incomplete population transfer into (A_5, A_6) as well as from deviations of the order of ϵ of the populations a_5 and a_6 from their assumed spin-temperature values. In spite of its simplicity, the model sheds light on two key features: i) The dynamics of optical pumping at 1.5 T is intrinsically limited by hyperfine decoupling. ii) The build-up time, at least in the explored range of parameters, weakly depends on pressure and is affected only through changes of $n_{\rm m}$ and T_1.

For application purposes, production rates of polarized atoms per unit volume $R_{\rm a} = PM_{\rm eq}/t_{\rm b}$ are compared to published results for standard MEOP conditions and similar sealed cells in table I. At low pressure, production rates at high field are lower than those obtained with low-field optical pumping. Nevertheless, one can take advantage of the weak-pressure dependence of $M_{\rm eq}$ and $t_{\rm b}$ at 1.5 T to efficiently perform MEOP at higher pressure. By increasing the pressure from 1.33 to 32 mbar, a factor of 10 in $R_{\rm a}$ is gained and good production rates are recovered. For instance, gas in a 250 cc cell at 32 mbar can be polarized at 40% within 3 minutes. This amount of gas is suitable for small-animal lung imaging after compression to atmospheric pressure. For human lung MRI, considerable scaling-up or accumulation of polarized gas remains necessary. However, optical pumping around 50 mbar would considerably simplify the compression stage by reducing the compression ratio from 1 : 1000 down to 1 : 20.

An intrinsic advantage of the high-field MEOP scheme is that, due to the large Zeeman splittings in the 2^3S-2^3P transition, the magnetic sublevels involved in optical pumping are selected by the frequency of the light, and not only by its polarization. High-field MEOP is therefore extremely robust against polarization impurity of the pumping light. This is a crucial issue for massive production of polarized ^{3}He using high laser power, since imperfect light polarization can severely limit achieved polarizations at low field [14].

Perspectives. – The nuclear polarization improvement observed at 1.5 T for high pressures is plausibly due to the inhibition by hyperfine decoupling of relaxation channels in atomic and/or molecular states in the plasma, as suggested by preliminary results at 0.1 T [7]. Further experiments at different magnetic-field intensities are planned to confirm this hypothesis. In this perspective, the present study provides a first set of data showing that, in spite of the large hyperfine decoupling in the 2^3S state, MEOP at high field i) still yields high nuclear polarizations at low pressures and ii) extends the domain of its applicability to higher pressures,

providing fair polarizations and high production rates. From a practical point of view, and in the perspective of a large-scale medical use of polarized gases, the development of a ^{3}He polarizer operating at 1.5 T (a widely used magnetic field in MRI), and at tens of mbar (for simplified compression) could be an attractive choice.

REFERENCES

[1] Becker J. *et al.*, *Nucl. Instrum. Methods A*, **402** (1998) 327.
[2] Möller H. *et al.*, *Magn. Res. Med.*, **47** (2002) 1029.
[3] Walker T. G. and Happer W., *Rev. Mod. Phys.*, **69** (1997) 629.
[4] Colegrove F. D., Schearer L. D. and Walters G. K., *Phys. Rev.*, **132** (1963) 2561.
[5] Leduc M., Crampton S. B., Nacher P.-J. and Laloë F., *Nucl. Sci. Appl.*, **1** (1983) 1.
[6] Gentile T. R. and McKeown R. D., *Phys. Rev. A*, **47** (1993) 456.
[7] Nacher P.-J. *et al.*, *Acta Phys. Pol. B*, **33** (2000) 2225.
[8] Chernikov S. V. *et al.*, *Electron. Lett.*, **33** (1997) 787.
[9] Tastevin G. *et al.*, *Appl. Phys. B*, **78** (2004) 145.
[10] Courtade E. *et al.*, *Eur. Phys. J. D*, **21** (2002) 25.
[11] Nacher P.-J. and Leduc M., *J. Phys. (Paris)*, **46** (1985) 2057.
[12] Stoltz E. *et al.*, *Appl. Phys. B*, **63** (1996) 629.
[13] With notations of ref. [10], $\epsilon = 2\sin^2\theta_+ = 1 \times 10^{-2}$ at 1.5 T.
[14] Leduc M., Nacher P.-J., Tastevin G. and Courtade E., *Hyperline Interact.*, **127** (2000) 443.

Preprint

March 10, 2006

Metastability exchange optical pumping of helium-3 at high pressure and high magnetic field: experiments

M. Abboud, A. Sinatra, G. Tastevin, and P.-J. Nacher
Laboratoire Kastler Brossel, Ecole Normale Supérieure, 24 rue Lhomond, 75005 Paris, France

X. Maître
U2R2M, Université Paris-Sud and CIERM, Hôpital de Bicêtre, 94275 Le Kremlin-Bicêtre Cedex, France

Metastability exchange optical pumping in the pressure range 8-67 mbar is performed in the 1.5 T magnetic field of a full-body scanner. Stationary polarizations, production rates, photon efficiency of this new optical pumping scheme are investigated experimentally. Results are interpreted and nicely reproduced using a theoretical model for optical pumping adapted to our high field and high pressure conditions. Despite the important hyperfine decoupling in the 2^3S metastable state at 1.5 T, metastability exchange optical pumping retains its high photon efficiency (one or two according to the pumping line). High nuclear polarizations and production rates are obtained at high pressure making this scheme promising for applications.

PACS numbers: 03.75.Be - 32.60.+i - 32.80.Bx - 67.65.+z - 87.61.-cg

I. INTRODUCTION

Highly polarized helium-3 is used in various fields of science, spanning from magnetic resonance imaging (MRI) of air spaces in human lungs [1, 2], to nuclear physics to prepare spin filters for neutrons [3] and polarized targets [4]. The most successful methods presently used to polarize helium-3 are spin-exchange optical pumping using alkali atoms [5], and pure-helium metastability exchange optical pumping [6]. The applications have driven research towards improvement in terms of photon efficiency, stationary polarization, and production rate, both for spin exchange optical pumping [7], and metastability exchange optical pumping [8, 9]. The metastability exchange technique was demonstrated by Colegrove, Schearer, and Walters over forty years ago [6]. In standard conditions, metastability exchange optical pumping is performed at low pressure (1 mbar) in a guiding magnetic field up to a few mT. Metastable 2^3S-state atoms are produced using a radiofrequency discharge. They are optically pumped using the 2^3S-2^3P transition at 1083 nm. The electronic polarization is transferred to the nuclei by hyperfine interaction. Through metastability exchange collisions, nuclear polarization is transferred to ground-state helium-3 atoms. Metastability exchange optical pumping in standard conditions provides, in a few seconds, high nuclear polarizations (up to 0.9 at 0.7 mbar [10]). Unfortunately, the achieved nuclear polarization rapidly drops down when the helium-3 pressure exceeds a few mbar [9, 11]. Therefore, a delicate polarization-preserving compression stage is necessary for all applications needing a dense sample. Recently, we demonstrated that the applicability domain of metastability exchange optical pumping can be extended to higher pressure provided the optical pumping (OP) is performed in a high magnetic field [12–14].

In this paper, we present the experimental results of a systematic study of OP at 1.5 T and we compare them with a theoretical model.

In section II, we describe our setup, the OP schemes we have explored at 1.5 T, and we explain in detail the experimental methods, in particular the measurement of the nuclear polarization in stationary and non stationary conditions.

In section III, we present our results obtained at 1.5 T in various experimental conditions including the discharge intensity, the pump laser power, the atomic line chosen for OP, and the gas pressure. We also compare in this section the high field OP performances with results obtained in standard conditions.

In section IV, we do a quantitative comparison between our results and the predictions of an optical pumping model in the spirit of [18], adapted to our high field and high pressure conditions [14]. We show that the metastable atom density within the pump beam is strongly affected by the electronic orientation of the metastable atoms. The measured pumping rates and photon efficiencies are nicely reproduced by the theory. Results for the stationary polarizations obtained at high pressure indicate the existence of a relaxation process for nuclear polarization whose rate is enhanced by the population of excited state. A clear reduction of this effect is nevertheless observed at 1.5 T with respect to low field conditions.

II. EXPERIMENTAL

A. Experimental Setup

Experiments are performed in the homogeneous 1.5 T field of the superconducting magnet of a clinical full-body scanner. The experimental apparatus is sketched

in Fig.1. The helium-3 gas is enclosed in a sealed cylin-

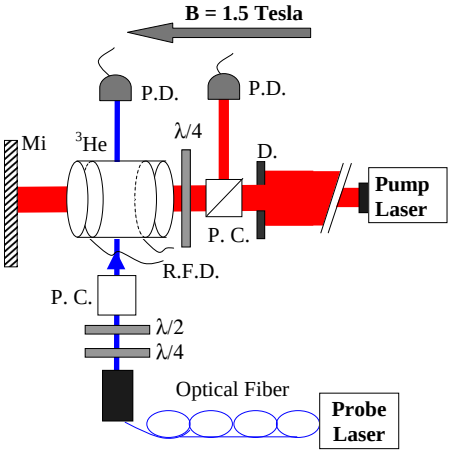

FIG. 1: Experimental setup scheme. P.C.=polarizing cube, P.D.=photodiode, Mi=mirror, R.F.D.=radiofrequency discharge, D.=diaphragm, $\lambda/2$=half wave plate, $\lambda/4$=quarter wave plate.

drical Pyrex cell, 5 cm in external diameter and 5 cm in external length. Cells are filled after a cleaning procedure: baking at 700 K under high vacuum for many days, followed by microwave discharges with several gas changes until only helium atomic lines are detected. In our study, we use cells filled with pressure P=1.33 mbar (low pressure regime), 8 mbar, 32 mbar, and 67 mbar (high pressure regime) of pure helium-3.

An electrical discharge generated by radiofrequency high voltage applied to external electrodes is used to populate the 2^3S state and maintain a metastable atom density n_m^0 in the range 10^{10}-10^{11} atoms/cm^3, depending on the applied voltage and the gas pressure. Experimentally, aligning the radiofrequency electric field with the static magnetic field provides a higher metastable density and better OP results.

The OP laser is a DBR single mode laser diode (50 mW) amplified using an ytterbium doped fiber amplifier (0.5 W) in the so-called MOPFA configuration (master oscillator power fiber amplifier) allowing fine frequency tuning and spectral width control [15]. The laser diode beam is coupled into the single mode fiber using a combination of two collimating lenses. The operational wavelength of the laser diode can be tuned by temperature over the entire structure of the lines of the metastable helium atoms. At the entrance of the OP cell, the Gaussian transverse intensity profile of the pump beam reaches a waist of 1.3 cm (1.53 cm FWHM). Some experiments are performed using a circular diaphragm (1.5 cm diameter) to select the central fraction of the beam. Others are performed with the entire divergent pump beam (0.5 W) which matches the spatial plasma distribution in the cell. The polarization of the pump beam is adjusted using combination of polarizing cube and quarter-wave retarding plate. The pump beam is back-reflected to enhance its absorption and collected by a photodiode to monitor its tuning to atomic resonance.

The probe beam is provided by another single mode laser diode. It is expanded, attenuated to provide a laser intensity on the order of 1 μW/cm^2, and linearly polarized perpendicularly to the magnetic field.

The absorption of the probe and the pump lasers are measured using a modulation technique. The discharge intensity is modulated at 133 Hz and the absorptions are measured with lock-in amplifiers. The average values of the transmitted probe and pump intensities are also recorded. Laser sources and all the electronics remain several meters away from the magnet bore in a low-field region.

B. OP scheme at high field

The spectrum of helium-3 at 1.5 T over the infrared transition 2^3S-2^3P is shown in Fig.2 for circularly polarized light. The first four peaks on the left are observed

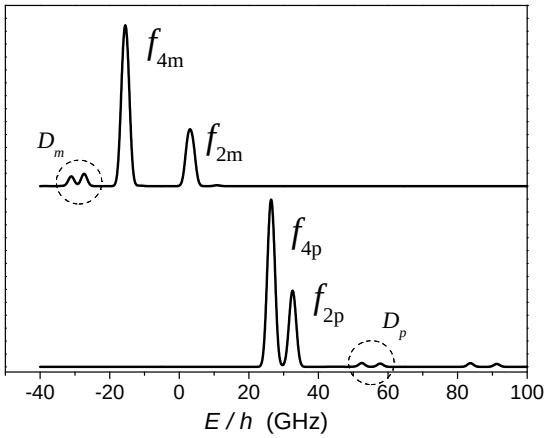

FIG. 2: Helium-3 spectrum over the 2^3S-2^3P transition at 1.5 T for circularly polarized light. The σ_- (top curve) and σ_+ (bottom curve) spectra are completely resolved. Efficient OP is obtained on the f_{4m}, f_{4p}, f_{2m} or f_{2p} peaks. Doublets of atomic lines D_m or D_p are used for the measurement of the nuclear polarization.

with σ_- light and the others with σ_+ light. At this magnetic field value, the σ_+ and σ_- spectra are completely resolved; this is very advantageous for OP as all the stringent requirements on polarization purity of the pumping light (encountered in low field [10, 16]) are eliminated. The most efficient transitions for pumping, in the pressure and laser power domains that we have experimentally explored (1-67 mbar and up to 125 mW/cm^2), are the four intense lines that we label f_{4m}, f_{2m}, f_{4p} and f_{2p}. The doublets labelled D_m or D_p are used for

detection and measurement of the nuclear polarization, when pumping on f_{4m} and f_{2p} or f_{2m} and f_{4p} respectively as we explain in detail in the subsection II C. In Fig.3, we show the energetic positions of the 2^3S and 2^3P sublevels, and transitions we use when pumping with σ_- light on the f_{4m} or on the f_{2m} line. The six 2^3S sublevels are grouped into three quasi-degenerate pairs (A_1,A_2), (A_3,A_4), (A_5,A_6) corresponding respectively to electronic angular momentum projections $m_J = -1, 0, 1$ in the completely decoupled limit $B \to \infty$. The f_{4m} (f_{2m}) line addresses four (two) transitions (full arrows in Fig.3) which are not resolved due to room temperature Doppler broadening in the vapor. Two other transitions (dashed arrows in Fig.3) are addressed by the probe lasers and are used to measure the nuclear polarization.

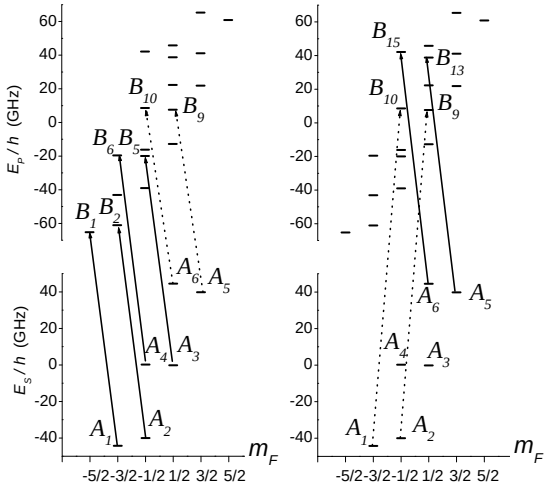

FIG. 3: Optical pumping schemes: f_{4m} (left) and f_{2m} (right). Solid (dashed) arrows correspond to transitions addressed by the pump (probe) laser. When we pump with σ_- light on four lines (f_{4m}), we probe with σ_- light the pair of sublevels (A_5,A_6). When we pump with σ_- light on two lines (f_{2m}), we probe with σ_+ light the pair of sublevels (A_1,A_2).

C. Stationary polarization measurements

In our experiments, we use an optical detection method based on absorption measurements to determine quantitatively the nuclear polarization. This absorption technique does not need any calibration and is reliable for arbitrary magnetic field and pressure [13, 14, 17]. It relies on the fact that in fast spin exchange conditions, and in the absence of OP and important relaxation processes, the relative populations of metastable sublevels a_{m_F} follow a Boltzmann-like distribution in angular momentum:

$$a_{m_F} \propto e^{\beta m_F} \qquad \text{with} \qquad M = \frac{e^\beta - 1}{e^\beta + 1} \qquad (1)$$

where M is the nuclear polarization in the ground-state and $1/\beta$ is the spin temperature. The spin temperature distribution for metastable helium sublevels populations was explicitly verified in previous works [13, 17, 18]. An example for our data is given in Fig.4; in the lower panel, we show deviations of a measured absorption spectrum from a calculation assuming spin temperature distribution, for $M_{stat} \simeq 0.5$. In practice, to measure the nuclear polarization in stationary conditions we record the probe absorption signal while sweeping the probe frequency along two neighboring detection peaks. Peaks amplitudes are precisely measured by a fit to a Gaussian or Voigt absorption profile (according to the sample pressure) and normalized to their $M = 0$ values in order to eliminate constant factors. From the ratio of the two amplitudes and using the field-dependent computed transition probabilities, we deduce the population ratio of the two probed hyperfine sublevels. We finally use Eq.(1) to calculate the spin temperature and M.

In our OP configurations f_{4m} or f_{2m}, we probe the populations of the two sublevels A_5 and A_6, or A_1 and A_2 respectively (see Fig.3), so that in both configurations we probe sublevels that *(i)* are not addressed by the pump and *(ii)* belong to the same quasi-degenerate pair of sublevels. An example of the influence of the pump laser on the absorption spectrum is shown in the upper panel of Fig.4.

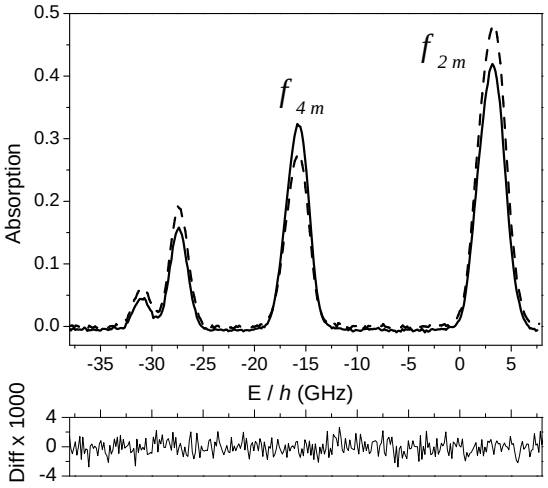

FIG. 4: Top panel: Probe absorption signals recorded with pump laser ON (dashed line) and OFF (solid line). The first two peaks on the left are the D_m detection doublet used to deduce nuclear polarization. Measurements are performed in the 8 mbar cell with 0.25 W pump laser for f_{4m} pumping after reaching $M_{stat} = 0.51$. Bottom panel: residual plot showing the difference between the solid line (top panel) and a computed spin temperature distribution spectrum.

Although the absorption profile is considerably modified (compare solid and thin lines in Fig.4), we verified that

the ratio of the probed populations remains unaffected; it can thus be used to infer the polarization M even in the presence of the pump laser. This experimental observations confirm the arguments detailed in [14]; metastability exchange collisions remain the dominant process within each pair of quasi-degenerate metastable sublevels with respect to other physical processes so that the ratio of the intra-pair populations is still correctly described by the spin temperature distribution.

D. Dynamic measurements

Due to OP, nuclear polarization builds-up in our samples in tens or hundreds of seconds. In the absence of the pumping beam and in presence of the discharge, nuclear polarization decays typically in thousands of seconds.

1. *Build-up of the polarization*

To monitor the build-up time of polarization we record probe absorption as we scan back and forth the frequency of the probe beam along a detection doublet (1 GHz/s). The detection doublets D_m or D_p and the corresponding transitions are illustrated in Figs.2 and 3. An example of raw data is shown in Fig.5. The amplitudes of the

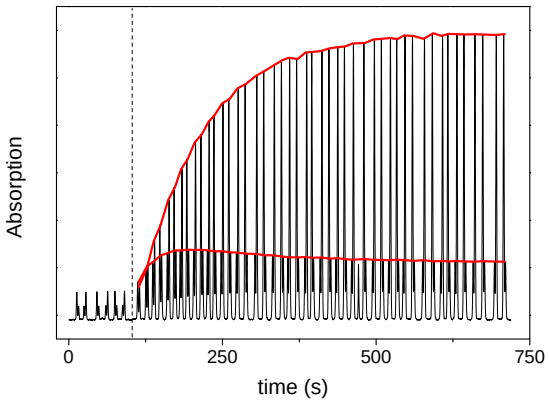

FIG. 5: Probe absorption signal when the laser frequency is swept back and forth along the detection doublet D_m during a polarization build-up. The envelope lines show the time-evolution of the populations of the probed sublevels A_5 and A_6 .

two detection peaks for the same time value are obtained by linear interpolation, and the nuclear polarization at that time is inferred as described in subsection II C. An example of result including the errors coming from the interpolation procedure is shown in Fig.6. The obtained function $M(t)$ is non exponential. To extract a build-up time and the polarization derivative at $M = 0$, we fit the first part of the curve by an exponential of time

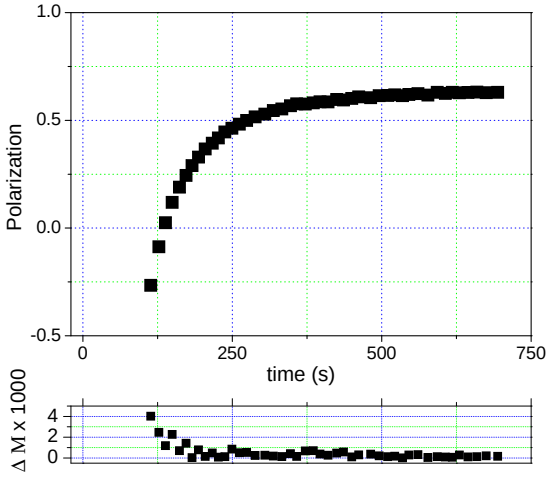

FIG. 6: Top panel: Polarization build-up in the 8 mbar cell; the pump laser is tuned on f_{4m} OP line and released at t=100 s. Bottom panel: Errors coming from the interpolation procedure in time described in the text.

constant t_b, fixing the asymptote to the correct value M_{stat}, deduced from the tail of the curve or measured in stationary conditions (see Fig.7). We have in this case by construction:

$$\left(\frac{dM}{dt}\right)_{(M=0)} = \frac{M_{stat}}{t_b} \quad . \tag{2}$$

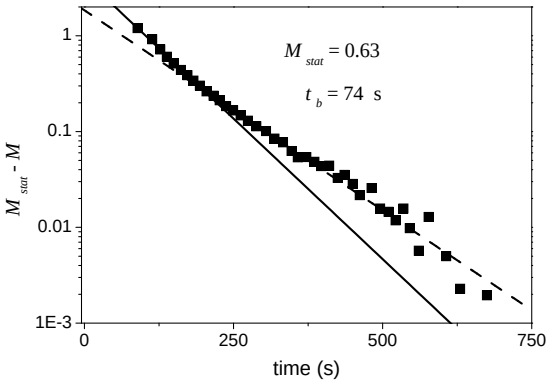

FIG. 7: Non exponential build-up of the polarization. Squares correspond to experimental data, the line corresponds to an exponential fit to obtain t_b as explained in the text.

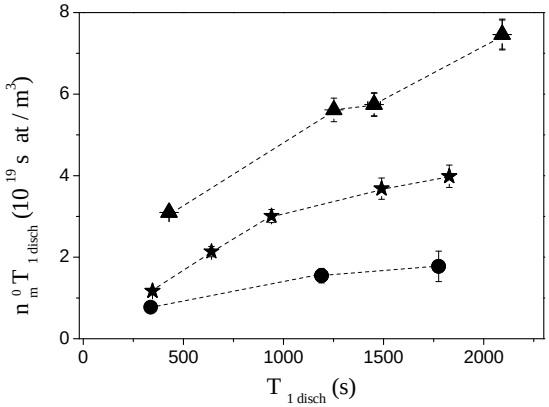

FIG. 8: Product $n_m^0 \times T_{1disch}$ as a function of the polarization decay constant in the absence of pumping beam T_{1disch}. Triangles: 8 mbar, stars: 32 mbar, circles: 67 mbar.

TABLE I: Stationary polarization M_{stat} and build-up time t_b for the two OP lines and in the different discharge conditions illustrated in Fig.8.

			$f_{4\,m}$		$f_{2\,m}$	
P	$T_{1\ dech}$	n_m^0	M_{stat}	t_b	M_{stat}	t_b
mbar	s	10^{10} at/cm^3		s		s
8	428	7.2	0.41	31	-0.62	84
	1453	4.0	0.53	80	-0.66	122
	2092	3.6	0.60	85	-0.71	118
32	346	3.4	0.25	56	-0.37	120
	1490	2.5	0.35	101	-0.49	214
	1828	2.2	0.37	218	-0.47	243
67	1190	1.3	0.26	195	-0.28	301
	1775	1.0	0.30	277	-0.36	364

2. *Discharged induced decay*

With the same technique, and in the absence of the pumping beam, we monitor the decay of polarization in the presence of the discharge. The observed decay is exponential and we call $T_{1disch} = 1/\Gamma_{1disch}$ the corresponding time constant.

III. EXPERIMENTAL RESULTS

We investigated systematically OP performances in the f_{4m} and the f_{2m} schemes for different configurations of radiofrequency discharge and pumping laser power.

A. Influence of the discharge intensity

Two global parameters are used to characterize the discharge: the metastable atom density n_m^0 in the pump beam measured at weak pump power and when the sample is not polarized ($M = 0$), and the nuclear polarization decay constant T_{1disch}. Ideally, we would like to maximize the product $n_m^0 T_{1disch}$ in order to have high polarization production rate (proportional to n_m^0) and a long relaxation time. We present the discharge parameters that we typically obtain in the three pressure cells in Fig.8. The weak discharge regime (that corresponds to the longest T_{1disch}) maximizes the product $n_m^0 T_{1disch}$ at all pressures. We were not able to obtain such long T_{1disch} in low magnetic field in the same cells. We report the OP results (stationary polarization and build-up time) in these discharges and for the two OP schemes (f_{4m} and f_{2m}) in Table I.

As the T_{1disch} increases for weak discharges, the stationary polarization increases and the build-up time gets longer. Highest polarizations are obtained for the longest T_{1disch} we could obtain (on the order of 2000 s) and can be as high as -0.7 at 8 mbar (f_{2m} OP) with a build-up time on the order of 300 s. The polarization can be further increased and the build-up time reduced by increasing the pump laser power. The f_{2m} line gives systematically higher polarization results at these pressures, contrarily to what we have observed at 1.33 mbar where f_{4m} gives the best results.

B. Influence of the pump laser power

An example of the laser power dependence of results is shown in Fig.9 for the f_{2m} OP line. We notice a clear saturation in the shrinkage of the build-up times as the power increases only for the 8 mbar cell. The saturation of the build-up times is accompanied by a saturation of the stationary polarization. A numerical calculation shows that this saturation is due to the fact that the pumping light can effectively transfer population from the pumped quasi-degenerate pairs to the other pairs of sublevels [14]. A higher laser power would be necessary to observe saturation, both in build-up times and stationary polarization, in higher pressure cells. For the two higher pressure cells, we observed a different behavior when pumping on the atomic line f_{4m}: a saturation of the stationary polarization is observed while the build-up times continue to shrink as the pumping laser power is increased. This behavior is mainly related to additional relaxation processes in the presence of the pump laser as we discuss later on in the paper.

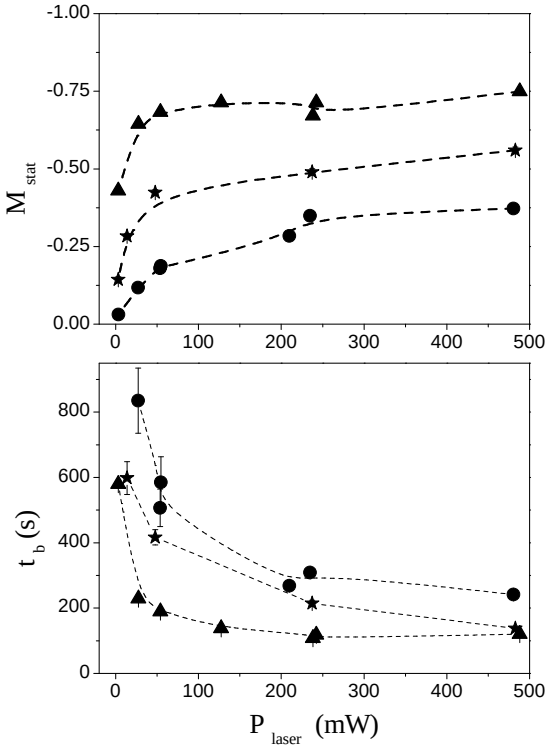

FIG. 9: Stationary polarization (top panel) and polarization build-up time (bottom panel) as a function of the incident pump laser power when pumping on the f_{2m} line. Triangles: 8 mbar ($T_{1disch} = 2092$ s and $n_m^0 = 3.49 \times 10^{16}$ at/m^3), stars: 32 mbar ($T_{1disch} = 1490$ s and $n_m^0 = 2.47 \times 10^{16}$ at/m^3), circles: 67 mbar ($T_{1disch} = 1090$ s and $n_m^0 = 1.31 \times 10^{16}$ at/m^3).

C. High field *versus* low field OP performances

We summarize the best results obtained in high field and we compare them to standard low field OP results in Fig.10. High field data are obtained with 0.5 W of pumping laser power on the f_{2m} transition and low field include results in the literature [9] and data that we obtained in the same cells used for the experiments at 1.5 T with a 2 W pump laser power [14]. A dramatic improvement is obtained at high field for high pressure samples. A more complete compilation of the results on the two lines f_{2m} and f_{4m} is reported in Table II where results in the literature of metastability exchange optical pumping in standard low-field and low-pressure conditions are listed for comparison. An important parameter for applications is the polarization production rate:

$$R_a = P\frac{M_{stat}}{t_b} \quad . \tag{3}$$

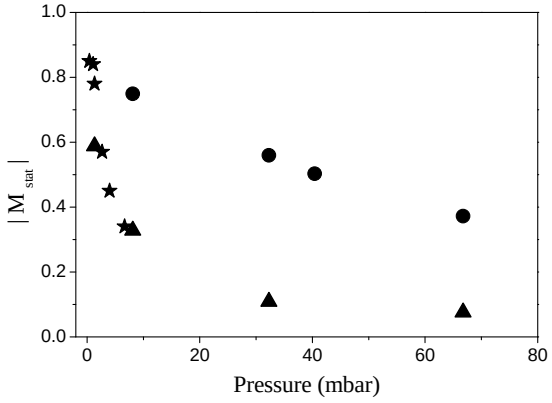

FIG. 10: Best results for stationary polarization versus the gas pressure. Circles: 1.5 T data obtained with a f_{2m} OP, stars: low field results of [9], triangles: low field data obtained pumping on C_9 line with 2 W in the same cells as for the 1.5 T study.

As shown in Table II, interesting production rates can be obtained with relatively small laser power.

IV. THEORY AND EXPERIMENT

In this section, we use the OP model developed in [14] in the complete collisional redistribution limit in the 2^3P state in order to interpret our results. Most of the input parameters of the model namely the gas pressure, the pump laser frequency and intensity, and the polarization relaxation rate in the absence of pumping beam $1/T_{1disch}$ are experimentally measured. However, there are two crucial parameters which we cannot measure directly and which we deduce with the help of our theoretical model. The first one is the metastable atom density within the pump beam in OP conditions n_m. In order to calculate n_m from an absorption measurement, one has to know the population of the probed sublevel. In the presence of the OP beam, the sublevels populations differ from the spin temperature distribution but can be calculated theoretically in each given OP condition. The second parameter is the total polarization relaxation rate during OP, in the presence of both the discharge and the pumping beam. This rate is in general larger than $\Gamma_{1\ disch}$ by a quantity that we name $\Gamma_{1\ laser} = 1/T_{1laser}$.

Our strategy consists in several steps. First, we deduce n_m using our model in order to reproduce the measured pump laser absorption at $M = 0$, and $M = M_{stat}$. Second, we compare the experimental and theoretical values of the pumping rates at $M = 0$ and the photon efficiency of our OP schemes. Finally, we compare the predicted stationary polarization values to the experimentally mea-

TABLE II: Stationary polarization M_{stat}, build-up time t_b and production rate R_a as a function of the gas pressure and pumping power in cylindrical cells 5 cm x 5 cm. The results refer to data in Fig.10.

line	P mbar	$T_{1\ dech}$ s	P_{laser} W	M_{stat}	t_b s	$\mid R_a \mid$ mbar/s
$f_{4\,m}$	8	2100	0.5	0.62	70	0.072
			0.25	0.59	85	0.056
$f_{4\,m}$	32	1490	0.5	0.40	96	0.134
			0.25	0.35	100	0.113
$f_{4\,m}$	67	1190	0.5	0.29	117	0.165
			0.25	0.26	203	0.085
$f_{2\,m}$	8	2100	0.5	-0.75	120	0.051
			0.25	-0.71	118	0.048
$f_{2\,m}$	32	1490	0.5	-0.56	138	0.131
			0.25	-0.49	214	0.074
$f_{2\,m}$	67	1190	0.5	-0.37	180	0.137
			0.25	-0.28	300	0.062
C_9 [8]	1	270	0.05	0.50	40	0.013
C_9 [16]	1.33	400	1.1	0.56	11	0.068
C_9 [9]	1.33	900	4.5	0.78	6.5	0.160
C_9	8	448	2	0.32	21	0.123
			0.25	0.21	79	0.021
C_9	67	280	2	0.07	32	0.146
			0.25	0.04	130	0.021

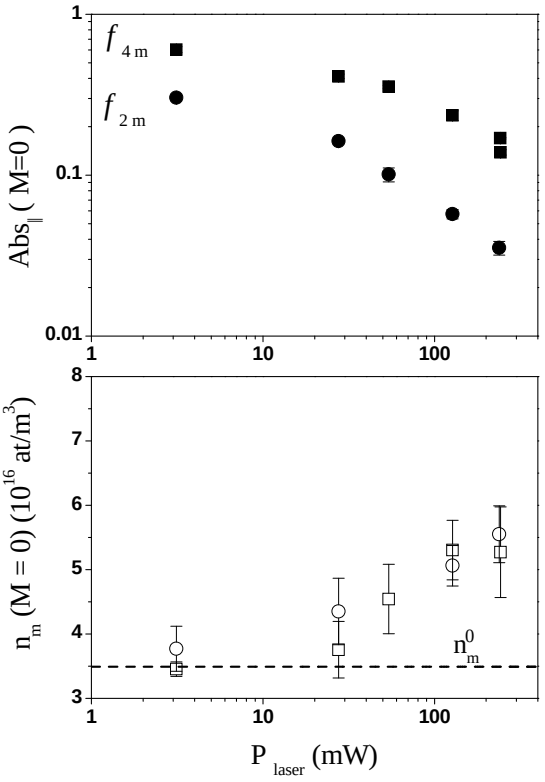

FIG. 11: 8 mbar cell, f_{4m} (squares) and f_{2m} (circles) OP. Pump laser absorption in OP conditions (top panel) as a function of the incident pump laser power, and metastable atoms density n_m deduced from our model in order to reproduce the measured absorptions (bottom panel).

sured ones and we deduce the $1/T_{1laser}$ values.

A. Determination of the metastable atom density

In Fig.11, we illustrate as a function of the incident laser power, the values of n_m (bottom panel) deduced with the help of our model from the measured pump absorptions (top panel) in the 8 mbar cell. Compatible values of n_m are obtained from the absorption of the pump in the two OP schemes (f_{4m} or f_{2m}). Notice that n_m increases with the pump laser power and is always *above* the value n_m^0 measured at $M = 0$ using a weak pump intensity (dashed line in Fig.11). A consistent interpretation of such variation is obtained by plotting the relative variation of n_m as a function of the electronic orientation of the metastable atoms in the beam as illustrated in Fig.12. In this figure, results corresponding to the three pressures are presented both for $M = 0$ and $M = M_{stat}$ and for the two OP lines f_{4m} and f_{2m}. The mean electronic orientation in the metastable state is calculated from the metastable sublevel populations a_i. In a high magnetic field:

$$\langle J_z^* \rangle \sim -(a_1 + a_2) + (a_5 + a_6) \qquad (4)$$

Note that even for $M = 0$ the metastable atoms within the OP beam can have an important electronic orientation. The increase in metastable atom density with the electronic polarization of the atoms can be interpreted as a consequence of a partial inhibition of Penning ionizing collisions in the sample [19, 20].

In a complementary experiment using another setup where the pump and the probe beams are collinear and spatially overlap in the cell, we verified directly the dependence of n_m with respect to $\langle J_z^* \rangle$ in the 8 mbar cell. In Fig.13, we plot the relative variation of n_m for three different experimental situations. The first one is during a discharge induced decay in the absence of pump laser (the populations of the metastable sublevels are then given by the spin temperature distribution and n_m is deduced from the weak probe absorption). The second and third

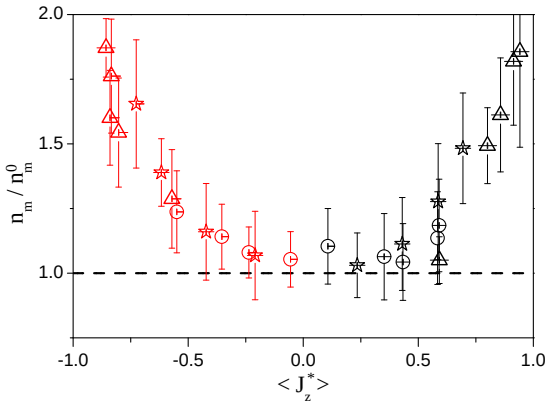

FIG. 12: Relative variation of n_m as a function of the electronic orientation of the metastable atoms in the beam. Data correspond to 8 mbar (triangles), 32 mbar (stars) and 67 mbar (circles) cells.

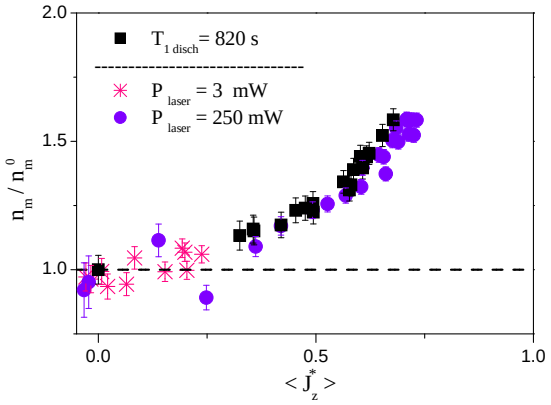

FIG. 13: Relative variation of n_m with respect to the value n_m^0 measured for a weak pump and at $M = 0$, for three experimental situations: during a discharge induced decay (squares), and during polarization builds-up with $P_{laser} = 3$ mW (stars) and with $P_{laser} = 250$ mW (circles).

ones are during polarization builds-up for two different pump laser intensities (here, we use the model to evaluate the populations in the metastable sublevels and we infer n_m from the probe absorptions). The observed variation in n_m is compatible with the one we have deduced from pump laser absorptions. Thus, these measurements validate the approach we used to determine the metastable atom density.

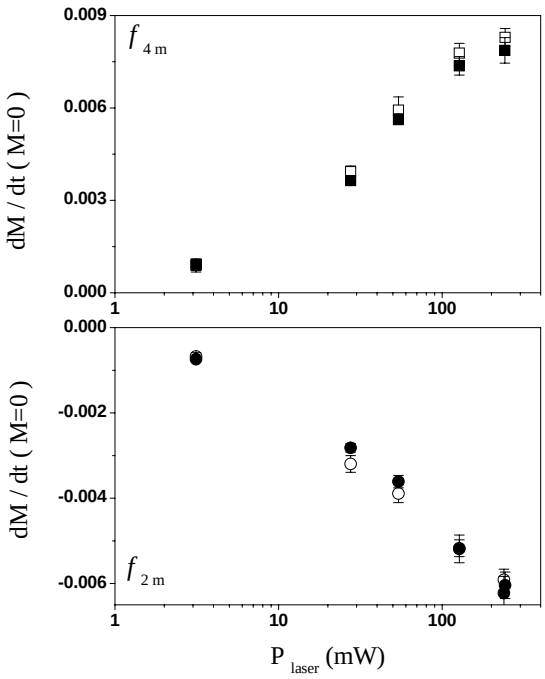

FIG. 14: Polarization pumping rate dM/dt at $M = 0$ as a function of the pumping incident laser power for the two OP lines f_{4m} or f_{2m} in the 8 mbar cell.

B. Pumping rate and photon efficiency

Using the metastable atom density deduced from pump absorption measurements, we compare theoretical and experimental results for the polarization pumping rates at $M = 0$ and the photon efficiency of our pumping schemes.

In Fig.14, we present for the 8 mbar cell the polarization pumping rate (derivative) dM/dt at $M = 0$ as a function of the pumping incident laser power for the two OP lines f_{4m} or f_{2m}. Good agreement is obtained between theory and experiment with no adjustable parameters. From those data and from pump absorption results of Fig.11, we can deduce the photon efficiency η defined as:

$$\eta = \frac{\text{number of polarized atoms/s}}{\text{number of absorbed photons/s}} \quad . \qquad (5)$$

The photon efficiency can be estimated in a very simple way assuming a complete collisional redistribution in the 2^3P state and that the relative population within each quasi-degenerate pair (A_1,A_2), (A_3,A_4), (A_5,A_6) obey the spin temperature distribution. Let us consider a f_{2m} pumping. During one cycle of absorption followed by spontaneous emission, one atom is transferred from sublevel A_6 or A_5, with equal probabilities if $M = 0$,

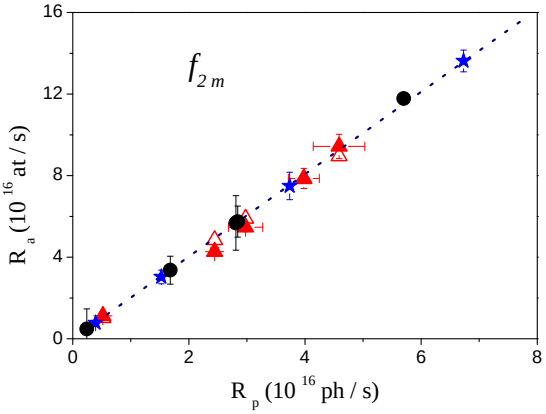

FIG. 15: Experimental and theoretical results for the photon efficiency on the f_{2m} OP line. Data correspond to 8 mbar (triangles), 32 mbar (stars) and 67 mbar (circles) cells.

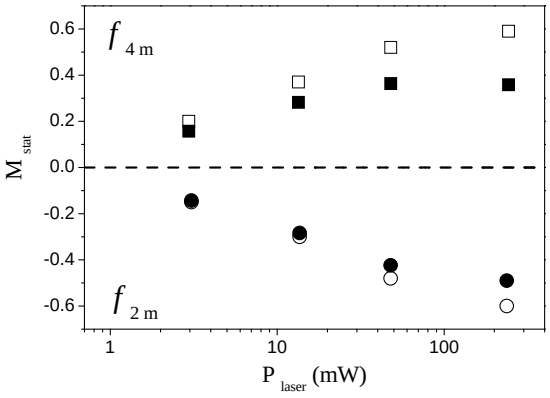

FIG. 16: Experimental (full symbols) and theoretical (empty symbols) values of M_{stat} in the 32 mbar cell as a function of the incident laser power.

towards any of the 6 sublevels of the metastable state (again with equal probabilities). The net change in angular momentum is $\langle \Delta F_z \rangle = -1$. This angular momentum is transferred to the vapor and it finally ends-up in the ground-state polarizing two $F = 1/2$ atoms. We then expect a photon efficiency approximately equals 2 for f_{2m} pumping and 1 for f_{4m} pumping (using a similar reasoning). Theoretical and experimental results for the photon efficiency on the f_{2m} line are illustrated in Fig.15. Full triangles are experimental data for the 8 mbar cell. As we did not measure systematically pump absorption at $M = 0$ for the other pressures, R_a is experimentally measured while R_p is calculated using the OP model under corresponding experimental conditions. The results for the photon efficiency for the two lines in the 8 mbar cell are summarized in Table III. These results

TABLE III: Experimental and theoretical values of photon efficiency for the two OP lines in the 8 mbar cell.

	η^{exp}	η^{th}
$f_{2\,m}$	1.96 ± 0.06	2.00 ± 0.03
$f_{4\,m}$	0.74 ± 0.05	0.82 ± 0.04

show that despite the important hyperfine decoupling at 1.5 T, and although many metastability exchange collisions are required to transfer the angular momentum to the ground-state, metastability exchange optical pumping retains its high photon efficiency characteristics with respect to standard low field results.

C. Stationary polarization and relaxation processes

The nuclear polarization achieved in stationary conditions results from a balance between a source term coming form metastability exchange collisions with polarized metastable atoms and relaxation [14]. In Fig.16 we compare, for the 32 mbar cell, the measured values of M_{stat} to theoretical predictions. The relaxation taken into account in the model is the one measured in the absence of the pumping beam (T_{1disch}). Experimental values of stationary polarizations $|M_{stat}|$ are systematically lower than theoretical values for higher pressures especially for f_{4m} OP meaning that additional relaxation processes should be taken into account during the pumping, *i.e.* in the presence of the OP beam. Similar results are obtained for the 67 mbar cell while the disagreement is less important in the 8 mbar cell. For the three pressures, we computed the additional relaxation rate that we should put in our model in order to recover the experimental results for the stationary polarizations. We call Γ_{1laser} this additional relaxation of polarization in the presence of the OP beam. For all pressures, Γ_{1laser} increases as a function of the population in the 2^3P state n_P. By forcing a linear dependence, we obtain the slopes in the table IV which depend in general on the pumping line $f_{4\,m}$ or $f_{2\,m}$. In Fig.17, we plot Γ_{1laser} as a function of the population in the 2^3P state in the 32 mbar pressure cell in which the most important relaxation was measured. For comparison we show Γ_{1laser} in low field in the same cell, where we used the low-field optical pumping model [18] to infer Γ_{1laser} from the measured steady state polarization. Both Γ_{1laser} and Γ_{1disch} are largely reduced (by approximately one order of magnitude) in high magnetic field. It is precisely this reduction in relaxation which explains the spectacular improvement in OP performances at high pressure shown in Fig.10.

TABLE IV: Slopes obtained from the linear fits of the relaxation rate $\Gamma_{1\ laser}$ as a function of the excited state population n_P.

	$f_{4\,m}$ 10^{-17} s^{-1}/(at/m^3)	$f_{2\,m}$ 10^{-17} s^{-1}/(at/m^3)
8 mbar	0.5	1.8
32 mbar	2.4	2.2
67 mbar	1.3	

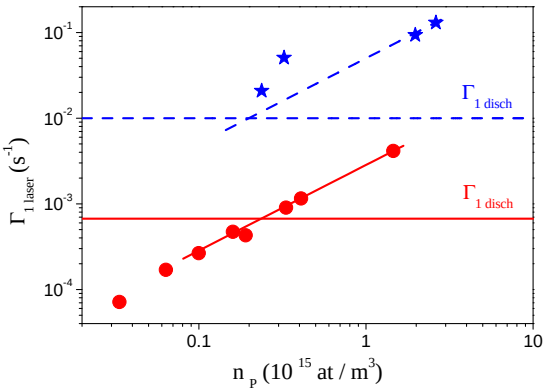

FIG. 17: Additional relaxation rate Γ_{1laser} as a function of the population in the 2^3P state n_P in the 32 mbar cell at high (circles) low (stars) magnetic field. For high field we plotted together results from the $f_{4\,m}$ and $f_{2\,m}$ lines. The horizontal lines represent the discharge contribution to the polarization relaxation rate Γ_{1disch}. We assume in this figure that the relaxation mechanism responsible for Γ_{1laser} is active in the entire volume of the cell.

In what follows we consider a possible interpretation of the observed relaxation in terms of metastable helium molecules. Three body processes involving two ground-state atoms and an excited atom in the 2^3S or in the 2^3P state can give rise to homonuclear metastable helium-3 molecules in the $a^3\Sigma_u^+$ or in the $b^3\Pi_g^+$ state respectively [21, 22]. We argue that such molecules could perform metastability exchange collisions with ground-state atoms and dissipate angular momentum in their external degrees of freedom. The cross-section of the creation process is almost 100 times higher from the 2^3P state [21, 22], which could explain an increase of the population of molecules, and of relaxation, in the presence of the pumping laser. The angular momentum dissipation rate for molecules Γ_1^{mol} and the metastability exchange collision time with molecules τ_e^{mol} are not known for metastable helium. There are however two possible regimes to be considered: a strong dissipation regime $\Gamma_1^{mol}\tau_e^{mol} \gg 1$ and a weak dissipation where $\Gamma_1^{mol}\tau_e^{mol} \ll 1$. Assuming that metastable molecules density is proportional to the creation rate of molecules and inversely proportional to the gas pressure (the lifetime of the molecules being limited by diffusion towards the cell walls), on gets for the density of molecules $n_{mol} \propto P^3$ where P is the gas pressure. In the strong dissipation case, where $M^{*mol} \simeq 0$, one then expects a relaxation rate proportional to P^3. In the weak dissipation case on the contrary $M^{*mol} \simeq M$ and the relaxation rate "brought back" to the ground-state is proportional to $\Gamma_1^{mol} n_{mol}/n_g$ which shows a linear dependence on pressure (if we assume $\Gamma_1^{mol} \propto 1/P$ [23]). The fact that we observed a reduction of relaxation at high field (figure 17) together with the rather weak pressure dependence of our relaxation rates Γ_{1laser} (table IV), seems to exclude the strong dissipation regime and indicate that Γ_1^{mol} is modified in high field. Although this scenario is suggestive, a direct measurement of metastable molecules and the determination of their density in each case would be necessary to validate all the hypothesis. Measurements in different magnetic fields would then possibly allow an experimental determination of Γ_1^{mol} and quantify the effect of hyperfine decoupling in molecular states in high field.

V. CONCLUSIONS

We have presented a systematical investigation of a new scheme for metastability exchange optical pumping in a high magnetic field which allows to obtain important nuclear polarization at pressures which are almost two orders of magnitude higher than those usually employed in traditional low-field metastability exchange optical pumping. For three pressure cell: 8, 32 and 67 mbar, stationary polarization and pumping rates were measured for different parameters of the discharge and pumping field intensity on $f_{4\,m}$ and $f_{2\,m}$: the two lines of the σ^- spectrum which were identified to be the most efficient at high field. A quantum efficiency of approximately 1 for $f_{4\,m}$ and of approximately 2 for $f_{2\,m}$ was demonstrated in good agreement with the predictions of our high-field optical pumping model. Using the model we could also prove that the large improvement in the obtained polarization at high pressure with respect to low field is due to a substantial reduction in the relaxation rates both in the absence and in the presence of the optical pumping laser. An interpretation of this fact based on the formation of metastable helium molecules is sketched.

[1] M.S. Albert, G.D. Cates, B. Driehuys, W. Happer, B. Saam, C.S. Springer Jr, and A. Wishnia; Nature **370** 199 (1994).

[2] H.E. Möller, X.J. Chen, B. Saam, K.D. Hagspiel, G.A. Johnson, T.A. Altes, E.E. de Lange, and H.U. Kauczor; Magn. Res. in Medicine **47** 1029 (2002).

[3] J. Becker, J. Bermuth, T. Grossmann, W. Heil, D. Hofmann, M. Leduc, E.W. Otten, D. Rohe, and R. Surkau; Nucl. Instrum. Methods A **402** 327 (1998).

[4] W. Xu et al. Phys. Rev. Lett. **8**5 2900 (2000).

[5] W. Happer; Rev. Mod. Phys. **44** 169 (1972).

[6] F.D. Colegrove , L.D. Schearer, and G.K. Walters; Phys. Rev. **132** 2561 (1963).

[7] E. Babcock, I. Nelson, S. Kadlecek, B. Driehuys, L.W. Anderson, F.W. Hersman, and T.G. Walker; Phys. Rev. Lett. **91** 123003 (2003).

[8] E. Stoltz, M. Meyerhoff, N. Bigelow, M. Leduc, P.-J. Nacher, and G. Tastevin; Appl. Phys. B **63** 629 (1996).

[9] T.R. Gentile, R.D. McKeown; Phys. Rev. A **47** 456 (1993).

[10] M. Wolf, Ph.D.Thesis, Gutenberg-Universität Mainz, (2004), http://ubm.opus.hbz-nrw.de/volltexte/2005/655/

[11] P.-J. Nacher, E. Courtade, M. Abboud, A. Sinatra, G. Tastevin, and T. Dohnalik; Acta Phys. Pol. B **33** 2225 (2002).

[12] M. Abboud, A. Sinatra, X. Maître, G. Tastevin, and P.-J. Nacher, Europhys. Lett. **68**, 480 (2004).

[13] M. Abboud, A. Sinatra, G. Tastevin, P.-J. Nacher, and X. Maître, Las. Phys. Jour. **15**, 475 (2005).

[14] M. Abboud, Ph.D.Thesis, Université Pierre et Marie Curie, Paris, (2005), http://tel.ccsd.cnrs.fr/documents/archives0/00/01/10/99

[15] S.V. Chernikov, J.R. Taylor, N.S. Platonov, V.P. Gapontsev, P.-J. Nacher, G. Tastevin, M. Leduc, and M.J. Barlow; Electronics Lett. **33** 787 (1997).

[16] M. Leduc, P.-J. Nacher, G. Tastevin, and E. Courtade; Hyperfine Interactions **127** 443 (2000).

[17] E. Courtade, F. Marion, P.-J. Nacher, G. Tastevin, K. Kiersnowski, and T. Dohnalik; Eur. Phys. J. D **21** 25 (2002).

[18] P.-J. Nacher, M. Leduc; J. Physique **46** 2057 (1985).

[19] G.V. Shlyapnikov, J.T.M. Walraven, U.M. Rahmanov, and M.W. Reynolds; Phys. Rev. Lett. **73** 3247 (1994).

[20] N. Herschbach, P.J.J. Tol, W. Hogervorst, and W. Vassen; Phys. Rev. A **61** 050702 (2000).

[21] F. Emmert, H.H. Angermann, R. Dux, and H. Langhoff; J. Phys. D - Appl. Phys. **21** 667 (1988).

[22] X. Zhao, P.A. Soletsky, W.H. Bryan, F.B. Dunning, and G.K. Walters; Phys. Rev. A **48** 4350 (1993).

[23] A. Abragam, *The Principles of Nuclear Magnetism*, Oxford University Press, p.319 (1961).

Chapitre 6

Perspectives et projets

Dans ce dernier chapitre je décris brièvement des suites possibles aux travaux exposés dans ce mémoire et j'expose quelques orientations futures de mes recherches, spécialement dans la section sur les gaz dégénérés.

Les numéros entre crochets font référence à la liste de mes publications, disponible en fin de document.

6.1 Optique quantique : de la compression de la lumière à celle des spins

L'intrication entre atomes et photons et la possibilité de transférer des corrélations quantiques d'un champ à l'autre sont au cœur de plusieurs idées centrales du traitement quantique de l'information comme par exemple celle de "mémoire quantique".

Il serait intéressant dans cette optique de revisiter certains schémas de génération d'états comprimés et de mesures QND du champ électromagnétique, dans le but cette fois de contrôler les fluctuations quantiques du champ *atomique* ainsi que les corrélations entre le champ atomique et champ électromagnétique. Pour donner un exemple, le schéma de deux champs près des conditions de piégeage cohérent de population décrit dans ce mémoire [25], a été très récemment proposé indépendamment par le groupe d'optique quantique de Michel Pinard et Élisabeth Giacobino, dans le cas particulier de deux champs d'intensité égale en cavité, pour produire des états comprimés de spin[1].

En ce qui concerne l'utilisation des spins nucléaires de l'hélium 3 comme mémoire quantique à longue durée de vie, je vois deux voies possibles de développement.

Nous avons analysé assez en détail la possibilité de se servir de l'état métastable 2^3S et de transférer les corrélations quantiques de la lumière aux spins nucléaires grâce à l'effet conjoint de l'interaction laser-atomes et des collisions d'échange de métastabilité. Si l'on voulait continuer dans cette direction, une vérification expérimentale s'imposerait notamment pour valider notre description des collisions d'échange de métastabilité, dont la validité (bien qu'elle paraisse raisonnable et cohérente) n'a pas été démontrée par un traitement rigoureux de la physique à plusieurs corps des collisions d'échange. Dans ce but on pourrait par exemple mesurer le spectre de bruit des atomes métastables, par l'intermédiaire de mesures de bruit sur un champ laser comme dans l'expérience de Polzik[2] pour différentes concentrations d'atomes fondamentaux et comparer à nos prédictions (équations (20) et (21) dans [24]).

[1] A. Dantan, J. Cviklinski, E. Giacobino, M. Pinard, Phys. Rev. Lett. **97** (2006) 023605.

[2] B. Julsgaard, A. Kozhekin, E.S. Polzik, Nature **413**, 400 (2001).

La mise en œuvre d'une expérience de mémoire quantique sur une vapeur d'hélium selon le schéma que nous avons proposé paraît faisable et avait été en effet considérée par le groupe d'optique quantique du LKB Jussieu. Pour les premiers essais de transfert de corrélations quantiques de la lumière aux atomes et inversement, on pourrait initialement utiliser de la lumière ayant du bruit dépendant de la quadrature, ce qui ne nécessite pas le développement d'une source de lumière comprimée.

Un autre volet intéressant à explorer, consiste en la manipulation des spins nucléaires au niveau quantique par RMN (Résonance Magnétique Nucléaire). Cette vois offrirait l'avantage de ne pas nécessiter une décharge (potentielle source de bruit) ni un plasma pour peupler l'état métastable. Un spin macroscopique polarisé devrait avoir une composante transverse de nature quantique susceptible de donner un signal RMN. Si l'on arrivait à avoir la sensibilité pour détecter un tel signal (qui croît en $\sqrt{N}$ avec le nombre d'atomes), ce qui constituerait la toute première étape d'un tel projet, on pourrait imaginer différents schémas pour mettre en œuvre une rétroaction[3] pour manipuler et réduire le bruit quantique du spin. On peut aussi se demander si, au moyen de courants électriques et bobines (en utilisant le signal de détection provenant d'un échantillon comme input pour créer un champ magnétique vu par le deuxième échantillon) on ne pourrait pas créer des corrélations quantiques entre deux spins macroscopiques séparés.

6.2 Gaz dégénerés : production d'états non classiques du champ atomique

Onze ans après leur obtention en laboratoire, les condensats de Bose-Einstein gazeux sont devenus un "outil" précieux pour de nombreuses expériences bénéficiant d'une source d'atomes ultrafroids et denses. L'utilisation des condensats en métrologie, en physique non linéaire, ou encore pour réaliser des modèles de la matière condensée est à présent l'objet d'un travail de recherche très actif.

Ce qui m'intéresse particulièrement est d'utiliser des condensats de Bose-Einstein pour la production d'états quantiques non triviaux ; pour l'investigation des frontières entre le monde quantique et le monde classique ainsi que pour le traitement quantique de l'information. C'est bien dans cette direction que je vais orienter mes recherches futures. J'entends mener une activité théorique et j'espère entamer au même temps une collaboration fructueuse avec le groupe expérimental "Microcircuits à atomes" dirigé par Jakob Reichel.

6.2.1 Compression de spin avec les condensats de Bose-Einstein

Un premier thème sur lequel je vais travailler est la dynamique de spin des condensats de Bose-Einstein à 2 composantes dans le but de produire des états fortement comprimés

[3]Voir par exemple J.M. Geremia, J.K. Stockton, H. Mabuchi Science **304**, 270 (2004).

de spin[4]. Il a été montré théoriquement[5] et expérimentalement[6] que la sensibilité des horloges atomiques est fondamentalement limitée par le bruit quantique de l'état atomique utilisé, qui a son origine dans la non commutativité des trois composantes du spin S selon trois directions orthogonales n_1, n_2, n_3. Pour définir les états comprimés de spin[7] on introduit un *paramètre de squeezing*

$$\xi^2 = \frac{N\Delta S_{n_1}^2}{\langle S_{n_2}\rangle^2 + \langle S_{n_3}\rangle^2} \tag{6.3}$$

qui est directement lié à la sensibilité maximale que l'on peut obtenir dans une mesure de "spectroscopie de population" (franges de Ramsey pour les horloges atomiques) d'une part[8], et à l'intrication dans le système d'autre part[9]. Pour les états comprimés de spin $\xi^2 < 1$. En 2001 il a été proposé d'utiliser la non linéarité intrinsèque du champ atomique pour produire des état intriqués et fortement comprimés de spin ($\xi^2 \sim 10^{-3}$ avec $N = 10^5$ atomes) avec des condensats de Bose-Einstein[10]. Dans cet article les auteurs proposent d'utiliser l'atome de sodium.

Avec Jakob Reichel et Li Yun, qui démarre sa thèse sur ce sujet, nous nous proposons d'analyser la faisabilité d'une expérience de compression de spin avec un condensat de rubidium. Le rubidium est l'élément le plus courant dans les expérience de condensats et aussi un bon candidat pour les horloges atomiques.

Si l'on veut limiter la sensibilité aux fluctuations de champ magnétique, il y a deux choix possibles d'états internes. Le premier choix est celui des états $|F = 1, m_F = -1\rangle$ et $|F = 2, m_F = 1\rangle$ piègeables magnétiquement. Ce choix impose la contrainte (ou l'avantage) de devoir séparer les deux composantes de spin pendant un temps d'interaction bien choisi car la symétrie particulière des interactions entre atomes dans ces états fait que la dynamique de spin est quasiment "gelée" lorsque les deux composantes sont superposées. Le deuxième choix, plus compliqué à mettre en œuvre, consiste à utiliser les états $|F = 1, m_F = 1\rangle$ et $|F = 2, m_F = -1\rangle$, qu'il faut piéger optiquement, et pour lesquels il y a une résonance de Feshbach à bas champ qui permet de changer la force de l'interaction entre espèces.

En 1999 j'ai déjà étudié la dynamique de phase (c'est-à-dire la dynamique du spin moyen $\langle S_x\rangle$) en tenant compte de (*i*) la dynamique spatiale des condensats dans le régime de gros condensats où le mode du condensat dépend du nombre d'atomes via le potentiel de champ moyen, (*ii*) les fluctuations du nombre total de particules et (*iii*) l'effet des pertes de particules. Avec Yvan Castin, suite à des expérience faites au JILA, nous avons

[4]Il s'agit du spin collectif (observable à 1 corps) obtenu en faisant la somme des spins 1/2 de chaque atome. Par exemple pour S_x en première quantification

$$S_x = \sum_i (|a\rangle\langle b|_i + |b\rangle\langle a|_i)/2 \tag{6.1}$$

où $|a\rangle$ et $|b\rangle$ sont deux états orthogonaux à une particule, par exemple 2 états internes différents. En deuxième quantification

$$S_x = (a^\dagger b + b^\dagger a)/2\,. \tag{6.2}$$

[5]D.J. Wineland, J.J. Bollinger, W.M. Itano, D.J. Heinzen, Phys. Rev. A, **50**, 67 (1994).

[6]G. Santarelli, Ph. Laurent, P. Lemonde, A. Clairon, A.G. Mann, S. Chang, A.N. Luiten, C. Salomon, Phys. Rev. Lett. **82**, 4619 (1 999).

[7]M. Kitagawa, M. Ueda Phys. Rev. A **47**, 5138 (1993).

[8]D.J. Wineland, J.J. Bollinger, W.M. Itano, D.J. Heinzen, Phys. Rev. A, **50**, 67 (1994).

[9]A. Sorensen, K. Molmer, Phys. Rev. Lett. **86**, 4431 (2001).

[10]A. Sorensen, L.-M. Duan, J.I.Cirac, P.Zoller, Nature, **404**, 63 (2001).

développé une méthode pour étudier ce système numériquement et, dans certains cas, analytiquement [11]. Il paraît donc naturel d'étendre ces études aux fluctuations du spin c'est-à-dire à la compression de spin, avec une attention particulière à ce qui peut être réalisé expérimentalement dans l'équipe Microcircuits à atomes.

6.2.2 Décohérence à température non nulle

Un effet que nous avions négligé à l'époque dans notre étude sur la cohérence de phase, et qui pourrait expliquer le désaccord entre la prédiction théorique du temps de cohérence et l'expérience du JILA, est la présence d'une fraction d'atomes non condensés. Le problème de la cohérence d'un condensat de Bose-Einstein à température non nulle est par ailleurs un problème fondamental et intéressant en soi, qui n'a pas encore été bien exploré expérimentalement.

Effet de la température sur la cohérence de phase d'un condensat

Avec Emilia Witkowska que j'ai eu la possibilité d'accueillir à Paris pendant 5 mois, avec un contrat européen QuFAR, nous avons commencé le programme d'étude de la dynamique de phase à température non nulle.

Notre premier objectif simple est de déterminer le temps au bout duquel la phase accumulée par un condensat à l'équilibre thermique est brouillée, en fonction de la température du gaz. Nous voulons aussi savoir si la phase du condensat "diffuse" (variance qui croît linéairement en temps), comme prédit dans la littérature avec des modèles inspirés par l'optique quantique[11], ou si elle présente une autre dépendance temporelle[12]. La stratégie que nous utilisons est d'une part un calcul analytique basé sur la théorie "Number conserving" de Castin et Dum, d'autre part des simulations de champ classique [17], [18], [20].

À terme, après une première étude fondamentale et "théorique" pour un condensat homogène à l'équilibre, nous voulons analyser des situation plus réalistes sur des condensats à deux composantes, mêlant donc les effet de la température aux effet de brouillage de phase, ou dynamique de spin, et éventuellement de dynamique spatiale.

Limites ultimes de la compression de spin

Une analyse à température nulle suggère qu'avec les condensats on peut réduire le paramètre de squeezing d'un facteur proportionnel à $N^{-2/3}$ où N est le nombre d'atomes. Toutefois, d'un point de vue fondamental mais aussi pratique, il est important d'établir les limitations ultimes du spin squeezing que l'on peut obtenir avec les condensats découlant du fait que le gaz n'est pas à température nulle.

Un premier travail a été fait par Sorensen[13] dans l'approximation de Bogoliubov. Ils serait à mon avis intéressant de vérifier numériquement ses résultats et d'essayer d'aller au delà de Bogoliubov en incluant les interactions entres modes de Bogoliubov (comme les processus de Beliaev-Landau) pour avoir une prédiction fiable aux temps longs.

Petits condensats et chats de Schrödinger

Un régime différent mais non moins intéressant, concerne des petits condensats dans lesquels le nombre de particules perdues pendant la durée de l'expérience est inférieur

[11] D. Jaksch, C. W. Gardiner, K. M. Gheri, P. Zoller, Phys. Rev. A **58**, 1450 (1998) ; R. Graham Phys. Rev. Lett. **81**, 5262 (2001) ; R. Graham, Phys. Rev. A **62**, 023609 (2000).

[12] A.B. Kuklov, J.L. Birman, Phys. Rev. A **63**, 013609 (2001).

[13] A. Sorensen, Phys. Rev. A, **65**, 043610 (2002).

à un. Comme nous l'avons vu dans ce mémoire, deux condensats qui sont initialement préparés dans un état de phase relative bien définie, voient aux cours du temps leur phase relative s'étaler à cause des interactions entre atomes qui constituent une non linéarité pour le champ atomique. L'effet de la non linéarité uni à la nature discrète de l'observable "nombre d'atomes" donne lieu comme nous l'avons vu à des brouillages et résurgences de la phase relative. On peut facilement montrer qu'à l'instant médian entre deux résurgences de phase, le système se trouve dans une superposition de deux états de phase relative opposée, donc dans un état de type chat de Schrödinger[14]. Nous avons montré la grande sensibilité de ces états aux pertes de particules [8] et on s'attend à ce qu'une température de l'ordre de $\hbar\omega/k_B$ où $\omega/2\pi$ est la fréquence d'oscillation des atomes dans leur piège, soit suffisante pour les détruire.

6.3 Suite des expérience de pompage optique en champ fort

Le projet de pompage optique à fort champ se poursuit à Cracovie dans le groupe de Tomasz Dohnalik en collaboration avec Pierre-Jean Nacher et Geneviève Tastevin. Les attrait de cette "suite" sont la possibilité de varier la valeur du champ de zéro à 2 Tesla et de tester des nouvelles cellules de diamètre plus faible, ce qui devrait mieux localiser le plasma dans le centre du faisceau pompe. Avec Marie Abboud pendant deux séjours de quelques semaines à Cracovie en 2004 et 2005, nous avons aidé à démarrer ce projet qui, nous l'espérons, donnera des résultats bientôt.

Si je devais continuer dans ce projet dont pour moi l'intérêt est avant tout pratique, je serais tentée, à des fins de démonstration, d'explorer les limites ultimes de la méthode sur des cellules de pression plus élevée. Il faudrait alors prévoir un laser pompe plus puissant que celui de 0.5 W avec lequel tous nos résultats à forte pression ont été obtenus (et qui est maintenant à Cracovie). Par exemple un laser de 5 W comme celui que notre groupe emploie habituellement pour du pompage optique "traditionnel" à faible pression. En effet, nos résultats expérimentaux et théoriques montrent que pour la cellule à 50 torr (67 mbar) nous sommes déjà limités en puissance pour le taux de production d'aimantation et pour la polarisation stationnaire. Toujours dans la même lignée, Xavier Maître du Laboratoire U2R2M, a le projet de construire un prototype de polariseur à fort champ.

[14] Voir par exemple Y. Castin, Lecture Notes of Les Houches Summer School 1999, cond-mat/0105058.

Chapitre 7

Curriculum vitæ

Renseignements personnels

Nom et prénom	Sinatra Alice
Lieu et date de naissance	Rome, 23 septembre 1968
Nationalité	italienne

Formation

Laurea in Fisica, Université de Milan, Italie, mai 1993. 110/110 *cum laude*.

Doctorat en Physique, Université de Milan Italie, féevrier 1997
Directeur de thèse : Prof. Luigi Lugiato
"Contrôle du bruit quantique en optique à l'aide de transitions à deux photons."

Bourse Marie Curie Individuelle, Lab. LKB ENS Paris, 1997-1999

Maître de Conférence au Collège de France (chaire de Claude Cohen Tannoudji), 1999-2000

Enseignant chercheur, Université Pierre et Marie Curie, Paris VI, 2000-présent

(Co)encadrement

"Tesi di Laurea" : Davide Zibetti 1995, Maria Guerzoni 1996, Université de Milan.

Stage de Recherche : Hann Nguyen, magistère de physique fondamentale (2001).

Stages de DEA : Marie Abboud 2002, DEA laser et matière, Gaël Reinaudi 2004, DEA laser et matière.

Thèse de doctorat : Marie Abboud, 2002-2005, Paris VI.

Visiteur étranger : Emilia Witkowska février-juillet 2006.

Enseignement (2000-2005)

Physique générale (travaux dirigés et pratiques) en L1 à Paris VI.

Introduction à la physique quantique (cours) en L1 et L2, à Paris VI.

Ondes acoustiques et lumineuses (travaux dirigés et pratiques) en L2, à Paris VI.

Physique Statistique et Mécanique Quantique (travaux dirigés) en M1, Magistère Phytem, ENS Cachan-Paris VI.

Mécanique quantique (travaux dirigés) en M2 de physique quantique de l'École Normale Supérieure.

Exposés invités à des conférences (ou ateliers) internationales

1. KITP progam on Bose Einsein condensation, Santa Barbara, "Dynamics of two interacting BECs", juin-juillet 1998

2. Condensed Quantum Systems, University of Urbana Champaign, Illinois, "Dynamics of two components Bose-Einstein Condensates", novembre 1999

3. Quantum degeneracy in trapped gases, Gif sur Yvette, France "Semi-classical field approach to finite temperature Bose-Einstein Condensates", février 2000.

4. Theory of Quantum gases and quantum coherence, Salerno, Italy, "A classical field approach for finite temperature Bose condensed gases", juin 2001.

5. BEC Euroconference on the Physics of Atomic gases at low temperature, San Feliu de Guixols, Spain, "A classical field method for time-dependent Bose-Einstein condensed gases", septembre 2001.

6. ESF Quantum Optics, San Feliu de Guixols, Spain, "Quantum Optics Methods for BEC", octobre 2001.

7. Physics of Ultracold Dilute Atomic Gases, Benasque Center for Science, Spain, "The truncated Wigner method for Bose-Einstein condensed gases : advantages and limits of validity", juin 2002.

8. HELION02, at Oppenheim, Germany "Metastability exchange optical pumping of helium3 at high pressure and magnetic field", septembre 2002.

9. Quantum Optics VI, Krynica, Poland, "Long-Lived quantum memory with nuclear spins", juin 2005.

10. XI International Conference on Quantum Optics, Minsk, Belarus, "Quantum fluctations of two optical fields close to electromagnetically induced transparency", mai 2006.

Organisation de séminaires

Séminaires de Physique Atomique et Moléculaire 1999/2000 au Collège de France.

Autre

Depuis 2005 je fais partie de la commission de spécialistes CSE section 30 de l'Université Pierre et Marie Curie.

Depuis 2005 je perçois la prime PEDR pour l'encadrement doctoral et la recherche.

Chapitre 8

Liste des publications

Articles dans des révues à comité de lecture

1. "Back-Action induced Squeezed Light in a detuned Quantum Non-Demolition scheme"
   P. Grangier, J.Ph.Poizat, P.Grelu, F.Castelli, L.A.Lugiato, A.Sinatra, J. Mod. Opt. **41**, 2241-2257 (1994).

2. "Effective Two-Level Model for Three-Level Atoms in an Optical Cavity : a Test of its validity in the Quantum Domain"
   A.Sinatra, F.Castelli, L.A.Lugiato, P. Grangier, J.Ph.Poizat, Appl. Phys. B **60**, S39-S48 (1995), Special Issue "quantum optics"

3. "Effective Two-Level Model versus Three-Level Model"
   A.Sinatra, F.Castelli, L.A.Lugiato, P. Grangier, J.Ph.Poizat, Quantum Semiclass. Opt. **7**, 405-421 (1995).

4. "Nearly Ideal Squeezing in Degenerate Two-photon Optical Bistability"
   A.Sinatra, D.Zibetti, L.A.Lugiato, F.Castelli, Quantum Semiclass. Opt. **8**, 1189-1204 (1996).

5. "Quantum Non Demolition measurements using cold trapped atoms"
   J.-F. Roch, K.Vigneron, Ph.Grelu, A.Sinatra, J.-Ph.Poizat and P. Grangier, Phys. Rev. Lett. **78**, 634-637 (1997).

6. "Quantum Nondemolition Measurements using Cold Atoms in an Optical Cavity"
   A. Sinatra, J.-F. Roch, K.Vigneron, Ph.Grelu, J.-Ph.Poizat and P. Grangier, J. Mod. Opt. **44** 1967-1984 (1997).

7. "Quantum Non Demolition measurements using cold trapped atoms : comparison between theory and experiment"
   A. Sinatra, J.-F. Roch, K. Vigneron, Ph. Grelu, J.-Ph.Poizat, Kaige Wang, and P. Grangier, Phys. Rev. A **57**, 2980-2995 (1998).

8. "Phase Dynamics of Bose-Einstein condensates : Losses vs. Revivals"
   A. Sinatra, Y. Castin, Eur. Phys. J. D **4**, 247-260 (1998).

9. "Dynamics of two interacting Bose-Einstein condensates"
A. Sinatra, P.O. Fedichev, Y. Castin, J. Dalibard and G. Shlyapnikov, Phys. Rev. Lett **82**, 251 (1999).

10. "Spatial pump-meter quantum correlations in a vectorial Kerr medium model"
M. Hoyuelos, A. Sinatra, P. Collet, L.Lugiato and M. San Miguel, Phys. Rev. A **59**, 1622-1632 (1999).

11. "Binary Mixtures of Bose-Einstein condensates : Phase dynamics and Spatial Dynamics"
A. Sinatra, Y. Castin, Eur. Phys. J. D **8**, 319-332 (2000).

12. "Simultaneous Magneto-Optical Trapping of Two Lithium Isotopes"
M.-O. Mewes, G. Ferrari, F. Schreck, A. Sinatra, and C. Salomon, Phys. Rev. A **61**, 011403(R), 1-4 (2000).

13. "Calculation of quantum correlation spectra using the regression theorem"
Kaige Wang, A. Sinatra, L. Lugiato, Eur. Phys. J. D **12**, 339-349 (2000).

14. "A Monte Carlo formulation of the Bogolubov theory"
A. Sinatra, Y. Castin, C. Lobo, Journal of Mod. Opt. **47**, 2629-2644 (2000).

15. "Penning collisions of laser-cooled metastable helium atoms"
Dos Santos, F. Perales, J. Leonard, A. Sinatra, J. Wang, F. S. Pavone, E. Rasel, C. S. Unnikrishnan, M. Leduc, Eur. Phys. J. D **14**, 15-22 (2001).

16. "Efficient magneto-optical trapping of a metastable helium gas"
Dos Santos, F. Perales, J. Leonard, A. Sinatra, J. Wang, F. S. Pavone, E. Rasel, C. S. Unnikrishnan, M. Leduc, Eur. Phys. J. AP **14**, 69-76 (2001).

17. "Classical field method for time-dependent Bose-Einstein condensed gases"
A. Sinatra, C. Lobo, Y. Castin, Phys. Rev. Lett. **87**, 210404 (2001).

18. "The truncated Wigner method for Bose-Condensed gases : limits of validity and applications"
A. Sinatra, C. Lobo, Y. Castin, J. Phys. B **35**, 3599-3631 (2002).

19. "Optical pumping of helium-3 at high pressure and magnetic field" P.J. Nacher, E. Courtade, M. Abboud, A. Sinatra, G. Tastevin,T. Dohnalik Acta Phys. Pol. B **33**, 225-2236 (2002).

20. "Vortex Lattice Formation in Bose-Einstein Condensates"
C. Lobo, A. Sinatra and Y. Castin, Phys. Rev. Lett. **92**, 020403 (2004).

21. "High nuclear polarization of helium-3 at low and high pressure by metastability exchange optical pumping at 1.5 Tesla"
M. Abboud, A. Sinatra, X. Maître, G. Tastevin, P.-J. Nacher, Europhysics Letters, **68** n.4, 480-486 (2004).

22. "High nuclear polarization of helium-3 at low and high pressure by metastability exchange optical pumping at 1.5 Tesla"
M. Abboud, A. Sinatra, X. Maître, G. Tastevin, P.-J. Nacher, Laser Physics, **15** n.4, 475-479 (2005).

23. "Long-lived quantum memory with nuclear atomic spins"
A. Dantan, G. Reinaudi, A. Sinatra, F. Laloë, E. Giacobino, M. Pinard, Phys. Rev. Lett. **95**, 123002 (2005). Seleclet for Virtual Journal of Quantum Information 2005.

24. "Squeezing and entangling nuclear spins in helium 3"
G. Reinaudi, A. Sinatra, A. Dantan, M. Pinard, *to appear in Jour. Mod. Opt.* quant-ph/0512186A.

25. "Quantum fluctuations of two optical fields close to Electromagnetically Induced Tranparency", *accepté in Phys. Rev. Lett.* quant-ph/0603016.

Articles de vulgarisation

1. "Bose condensates make quantum leaps and bounds"
Y. Castin, R. Dum and A. Sinatra, Physics World 12 n.8, August 1999.

2. "Quantum noise in optics"
L. Lugiato et A. Sinatra, Article of the Enciclopedia Treccani, edition of year 2000.

Actes de conférences

1. P. Grangier, J.Ph.Poizat, P.Grelu, F.Castelli, L.A.Lugiato, A.Sinatra, *'Quantum Non-Demolition Measurements and Back-Action-Induced Squeezing in Atomic Three-Level Systems'*, Springer Proceedings in Physics, vol.77 (123-133). Editors : D.F.Walls, J.D.Harvey. Springer-Verlag (Berlin, Heidelberg), 1994.

2. A. Sinatra, D. Zibetti, L. A. Lugiato, F. Castelli, *'Nearly Ideal Squeezing in Degenerate Two-photon Optical Bistability'* in 'Coherence and Quantum Optics VII', edited by J. Eberly, L. Mandel, E. Wolf, 7-10 June, Rochester.